ACTINOPTERYGIAN AND CHONDRICHTHYAN PALAEOCOMMUNITY RESPONSES TO EARLY CENOZOIC GLOBAL WARMING

by

HANNAH CHANTELLE BIRD

A thesis submitted to the University of Birmingham for the degree of

DOCTOR OF PHILOSOPHY

School of Geography, Earth and Environmental Sciences

College of Life and Environmental Sciences

University of Birmingham

September 2024

ABSTRACT

Climate change in the geological past can be a valuable tool for assessing the context of current and future global warming, with numerous warming events punctuating the early Paleogene (~48 to 66 Ma) greenhouse world considered partially analogous to today's anthropogenic climate change. The Palaeocene-Eocene Thermal Maximum (PETM, ~56 Ma), Early Eocene Climate Optimum (EECO, ~49 to 53 Ma) and Middle Eocene Climate Optimum (MECO, ~40.1 to 40.5 Ma) are three key intervals of environmental change, during which atmospheric carbon dioxide peaked at levels akin to predictions by the Intergovernmental Panel on Climate Change for 2100 under worst-case emissions scenarios. Consequently, the interplay of the atmosphere and ocean in response to global warming and environmental change is important to understand the ecological and biological impacts, with inferences on how this may translate to the modern day and the future.

Palaeontology is invaluable for exploring biotic responses to such climate events as fossils can indicate the abundance and diversity of palaeocommunities through time. To understand the response of the marine realm to early Paleogene climate perturbations, actinopterygian (bony fish) and chondrichthyan (shark) fossils are important as they comprised over half of all marine vertebrate diversity at this time, and fish radiated due to expansion of ecological niches after the end-Cretaceous mass extinction. Whilst complete articulated body fossils of fish and sharks are relatively rare, microfossils from them are considerably more abundant, with the possibility to generate higher temporal and spatial resolution records. Important microfossils are otoliths (calcareous components in vertebrate inner ears), teeth and

denticles (tooth-like scales external of cartilaginous sharks), collectively termed ichthyoliths, which enable reconstruction of fish and shark productivity and diversity.

Museum collections provide an important but often underutilised resource for palaeobiodiversity studies, partly due to poor data accessibility (particularly digitally) but also because the value of such collections in large-scale analyses is highly dependent upon the quality of the information associated with them. Here, the potential of the largest public early Eocene (~48 to 56 Ma) actinopterygian otolith collection in the United Kingdom (housed in the Natural History Museum, London) is evaluated to reconstruct the shallow marine bony fish palaeocommunity from southern England and test if there is a true radiation post-Cretaceous or if sampling and museum curatorial biases are impacting the signal.

Turning to the response of deeper marine fish and shark palaeocommunities to climate change, fish teeth and shark denticles extracted from Indian and South Atlantic Ocean cores are assessed to understand productivity and diversity responses to short-lived PETM warming, long-term EECO warming and intermediate MECO warming. Whilst fish productivity is often elevated during warming intervals, diversity responses fluctuate between these three climate events. Ultimately, the rate of environmental change over which the onset and termination of each event occurs is a major determinant of the ability of fish, in particular, to adapt to the ambient environmental perturbations. As such, fish turnover associated with the rapid onset of the PETM and termination of the MECO highlight the potential ‘short-term’ instability of fish communities responding to modern climate change, but the ‘longer-term’ ability to equilibrate for a thriving marine ecosystem in the future.

ACKNOWLEDGEMENTS

After almost a decade at the University of Birmingham, charting my undergraduate, masters and PhD, I have immense gratitude for all those who have played a part in my journey along the way, both professionally and personally. To achieve a PhD here is the culmination of a quarter of a century of education and it is with immense pride that I do so at the institution. Of course, thanks must be given to Dr Kirsty Edgar and Dr Elizabeth Sibert whose expertise have been invaluable as I explored micropalaeontology and coding software, as well as Professor Richard Twitchett and Emma Bernard for facilitating access to the fossil fish collections at the Natural History Museum, London. I also appreciate the numerous scientists who undertook the expeditions to obtain the cores from which my samples derive, and the International Ocean Discovery Program Bremen Core Repository for supplying them to me. Furthermore, this research was supported by a Central England Natural Environment Research Council Training Alliance Grant (NE/S007350/1).

The biggest thank you is extended to my family. My parents have spent decades encouraging me to value every moment of my education and the opportunities that privilege brings, as well as the importance of making the most of every moment along the way to enjoy life. Travelling the world with you has opened my eyes to the importance of climate research and I finally came back to my dream as a child of being both a published author and working in a marine biology-adjacent field.

To my twin, Charlotte, life with you by my side is joyous and I thank you for our competitive spirit always pushing me to be the best version of myself. From being my

sounding board for ideas, to my proofreader and occasional agony aunt over my love-hate relationship with coding, your help over the last four years of PhD (and 28 years of life!) is beyond anything I could have hoped for.

Finally, for my grandparents, most of whom I never had the privilege of knowing, but who I hope to have made proud with not only this achievement of the PhD, but of the person I have become along the way.

TABLE OF CONTENTS

	Page
Contribution statements	1
CHAPTER ONE: Introduction	3
1.1. Early Paleogene climate change	3
1.2. Significance of early Paleogene climate research for actinopterygians and chondrichthyans	6
1.3. Thesis outline	11
CHAPTER TWO: Materials and methods	13
2.1. Chapter Three: Early Paleogene UK otoliths	13
2.2. Chapter Four: IODP Site U1514 early Cenozoic ichthyoliths	14
2.2.1. Sample preparation and ichthyolith extraction methodology	14
2.2.1.1. Pre-processing	14
2.2.1.2. Acidifying the sample	15
2.2.1.3. Separating ichthyoliths using LST FastFloat heavy liquid	15
2.2.1.4. Ichthyolith processing	16
2.2.2. Ichthyolith morphotype coding	17
2.2.3. Ichthyolith analyses in R	19
2.3. Chapter Five: South Atlantic Ocean MECO ichthyoliths	19
CHAPTER THREE: Museum collections and palaeocommunity reconstruction biases: a case study of early Paleogene actinopterygians from the UK	20
3.1. Chapter introduction	20
3.2. Materials and methods	24

3.2.1. NHMUK otolith data collection 24
3.2.2. Data validation 25
3.2.3. Palaeontological analyses 26
3.3. Synthesis of UK early Paleogene strata 27
3.4. Results 30
3.4.1. UK Ypresian actinopterygian palaeocommunity 30
3.4.1.1 Taxonomic analysis 31
3.4.1.2. Palaeocommunity reconstruction 35
3.4.2. Sampling biases in the NHMUK otolith collection 39
3.4.2.1. Biases from outcrop availability 39
3.4.2.2. Biases from sampling localities 41
3.4.2.3. Biases from collectors and donators 45
3.5. Discussion 47
3.5.1. Early Eocene radiation or collection bias? 47
3.5.2. Challenges with the NHMUK collection 49
3.5.2.1. Geological bias 49
3.5.2.2. Taphonomic bias 50
3.5.2.3. Anthropogenic bias 51
3.5.3. Bias mitigation strategies 53
3.6. Chapter conclusions 56
CHAPTER FOUR: Actinopterygian and chondrichthyan productivity, community structure and evolutionary patterns across the early Cenozoic of the Mentelle Basin, Australia (IODP Site U1514) 58
4.1. Chapter introduction 58

4.2. Methods 63
4.2.1. Sampling site 63
4.2.2. Age model 66
4.2.3. Sample selection and preparation 68
4.2.4. Stable carbon and oxygen isotopes 69
4.2.5. X-ray fluorescence data 70
4.2.6. Ichthyolith accumulation rate 70
4.2.7. Ichthyolith morphotypes 71
4.2.8. R scripts 73
4.3. Results 73
4.3.1. Ichthyolith abundance through time 73
4.3.2. IAR in context of climate patterns and productivity 77
4.3.2.1. IAR and isotopic climate patterns 77
4.3.2.2. IAR and geochemical productivity proxies 84
4.3.3. Community composition metrics 90
4.3.4. Morphotype occurrences through time 96
4.3.5. Morphotype origination and extinction 100
4.3.6. Morphospace occupation 103
4.4. Discussion 106
4.4.1. Productivity at Site U1514 106
4.4.2. Open ocean fish diversity at Site U1514 110
4.4.3. Site U1514 productivity and diversity in context of global patterns 113
4.5. Chapter conclusions 117

CHAPTER FIVE: Actinopterygian productivity, community structure and evolutionary patterns in the South Atlantic Ocean during the Middle Eocene Climate Optimum 119

5.1. Chapter introduction 119

5.2. Methods 123

5.2.1. Sampling sites 123

5.2.2. Age model 126

5.2.3. Sample selection and preparation 128

5.2.4. Stable carbon and oxygen isotopes 128

5.2.5. X-ray fluorescence data 129

5.2.6. Ichthyolith accumulation rate 129

5.2.7. Ichthyolith morphotypes 130

5.2.8. R scripts 130

5.3. Results 130

5.3.1. Ichthyolith abundance and accumulation in the South Atlantic Ocean 130

5.3.2. Climate patterns 135

5.3.2.1. Carbon and oxygen isotopes 135

5.3.2.2. Environmental proxy data 137

5.3.3. Community composition 141

5.3.4. Morphotype occurrences through time 145

5.3.5. Morphotype origination and extinction 150

5.3.6. Morphospace occupation 152

5.4. Discussion 155

5.4.1. Productivity in the South Atlantic Ocean 155

5.4.2. Marine fish diversity in the South Atlantic Ocean 158

5.4.3. South Atlantic Ocean productivity and diversity compared to global patterns 159

5.4.4. Early Paleogene climate event comparisons 161

5.5. Chapter conclusions 162

CHAPTER SIX: Conclusions 165

6.1. Summary of research findings 165

6.2. Future Paleogene research 169

List of references 172

Appendices 201

Appendix 1: Supplementary material for Chapter 3 201

Appendix 2: Supplementary material for Chapter 4 214

Appendix 3: Supplementary material for Chapter 5 230

LIST OF FIGURES

Page

CHAPTER ONE

1.1. Late Palaeocene to late Eocene timeline defined by carbon and oxygen isotopes, with the intervals of study for each chapter indicated. 5

1.2. Examples of ichthyoliths (teeth, denticles and otoliths) from the study sites. 8

1.3. Early Eocene hyperthermals identified in calcium-iron record from Site U1514. 10

CHAPTER TWO

2.1. Character states used for coding fish teeth and identifying morphotypes. 18

CHAPTER THREE

3.1. Modern standardised Paleogene succession of the UK. 29

3.2. NHMUK otolith abundance from early Paleogene strata. 32

3.3. Family-level biostratigraphic range chart of NHMUK otolith taxa in the early Paleogene. 34

3.4. Diversity index for the early Paleogene NHMUK otolith collection. 36

3.5. Rarefaction curves of species richness according to stratigraphic unit. 38

3.6. Surface outcrop map of UK early Paleogene strata with otolith abundances by sampling site. 43

3.7. NHMUK cumulative otolith abundance and species richness by acquisition date and prominent contributors. 46

3.8. Flowchart of geologic, taphonomic and anthropogenic biases impacting museum collections. 55

CHAPTER FOUR

4.1. Palaeogeographic reconstruction of the Palaeocene-Eocene boundary at 56 Ma. 65

4.2. Age-depth model and sedimentation rates for Site U1514. 67

4.3. Example triangle and cone teeth from Site U1514 illustrating coding characteristics. 72

4.4. Total ichthyolith counts and abundance for the late Palaeocene to middle Eocene, PETM and EECO hyperthermal datasets. 75

4.5. Global and site-specific carbon and oxygen isotope curves matched to EECO hyperthermals and ichthyolith accumulation rate. 79

4.6. PETM carbon and oxygen isotopes for Site U1514 matched to ichthyolith accumulation rate. 81

4.7. Crossplots of ichthyolith accumulation rate against carbon and oxygen isotopes. 83

4.8. Ichthyolith accumulation rate and sedimentation rate correlated to palaeoenvironmental proxies of Ca/Fe, Si/Fe and Ba/Fe ratios. 87

4.9. Crossplots of ichthyolith accumulation rate against palaeoenvironmental proxies of Ca/Fe, Si/Fe and Ba/Fe ratios. 89

4.10. Example triangle and cone teeth of shape categories. 92

4.11. Tooth shape abundances by relative size fraction. 93

4.12. Relative abundance of teeth smaller than 63 μm to larger than 63 μm and cones to triangles. 95

4.13. Morphotype range chart plotted against morphotype richness and ichthyolith accumulation rate. 99

4.14. Examples of abundant tooth morphotypes at Site U1514. 100

4.15. Origination and extinction rates. 102

4.16. Morphotype morphospace occupation across three time bins (pre-EECO, EECO and post-EECO) for community similarity. 104

4.17. Morphotype morphospace occupation for characteristics of the tooth coding system. 105

CHAPTER FIVE

5.1. Palaeogeographic reconstruction of the middle Eocene at 40 Ma. 124

5.2. Age-depth model and average sedimentation rates for Sites 702 and 1263. 127

5.3. Total ichthyolith counts and abundance across the MECO for Sites 702 and 1263. 133

5.4. Ichthyolith accumulation rate and sedimentation rate across the MECO for Sites 702 and 1263. 134

5.5. Bulk carbon and oxygen isotopes for Sites 702 and 1263. 136

5.6. Ca/Fe ratios across the MECO interval for Site 702. 138

5.7. Benthic foraminifera (BFAR) and coarse fraction (CFAR) accumulation rates for Sites 702 and 1263. 140

5.8. Abundances of the four tooth shape categories (squat, medium, long and extra-long) across the MECO at Sites 702 and 1263. 143

5.9. Relative abundance of teeth 38 to 63 μm and 63 to 250 μm and cones to triangles and rectangles for Sites 702 and 1263. 144

5.10. Combined morphotype range chart for Sites 702 and 1263 ordered by first appearance. 147

5.11. Examples of abundant teeth and new morphotypes at Sites 702 and 1263. 148

5.12. Combined morphotype range chart for Sites 702 and 1263 ordered by last appearance. 149

5.13. Per capita origination and extinction rates combined for Sites 702 and 1263. 151

5.14. Morphospace occupation across pre-MECO, MECO and post-MECO time bins to assess community diversity. 153

5.15. Morphospace occupation for characteristics of the tooth coding system. 154

LIST OF TABLES

Page

CHAPTER THREE

3.1. Summary of surface outcrop, stratigraphic unit thickness and volume, otolith abundance and species richness by formation and basin. 40

CONTRIBUTION STATEMENTS

CHAPTER ONE

I produced all text and figures based upon literature reviews and my own photographs of samples.

CHAPTER TWO

Methodologies for all chapters are outlined. Those for Chapter Three were devised by myself with guidance from Emma Bernard, Fossil Fish Curator at the Natural History Museum, UK. Ichthyolith extraction processes and analyses in R for Chapters Four and Five were instructed by Dr Elizabeth Sibert as the leading expert on using fossil fish teeth and shark denticles for palaeocommunity research. All text was written by myself, with Figure 2.1 supplied by Dr Sibert as the standard for character states used in tooth morphotype coding.

CHAPTER THREE

Project conception was a collaboration between myself, Dr Kirsty Edgar, Dr Elizabeth Sibert, Dr Ivan Sansom, Professor Richard Butler and Professor Richard Twitchett. Data collection at the museum was conducted by myself, as was the production of all text, figures and tables for the analyses and discussion. Feedback on the results and discussion was provided by Drs Edgar and Sibert.

CHAPTER FOUR

This chapter was designed in collaboration with Drs Edgar and Sibert, using specimens provided by the former following International Ocean Drilling Programme

Expedition 369. Lab sample processing, analyses and discussion through production of text, figures and tables was conducted by myself. Guidance on tooth coding and scripts for use in R software was provided by Dr Sibert. Feedback on the results and discussion was provided by Drs Edgar and Sibert. I also co-supervised undergraduate student projects (Haf Nawsath, Lily Goddard and Zulaikha Sukerdi) alongside Drs Edgar and Sibert.

CHAPTER FIVE

This chapter was designed with Drs Edgar and Sibert, and sample preparation and analyses follow the same methodology as in Chapter Four. Sample selection and ordering from the International Ocean Discovery Program Bremen Core Repository was conducted by myself, with all lab work, analyses and discussion carried out by myself. Feedback on the results and discussion was provided by Drs Edgar and Sibert.

CHAPTER SIX

I wrote all of the thesis conclusions based upon prior discussion of individual chapters with Drs Edgar and Sibert.

CHAPTER ONE

Introduction

1.1. Early Paleogene climate change

The Paleogene (~23 to 66 Ma; Figure 1 of Westerhold *et al.*, 2020; Figure 1.1) is a pivotal period in Earth's history, when greenhouse conditions persisted for ~30 million years through the Palaeocene (~56 to 66 Ma) and Eocene (~34 to 56 Ma), before a climatic shift into the coolhouse world of the Oligocene (~23 to 34 Ma) when polar ice caps formed on Antarctica. Atmospheric carbon dioxide (pCO_2) levels peaked at ~1,500 parts per million (ppm; Rae *et al.,* 2021) in the early Eocene, where sea surface temperatures were elevated by a maximum of 10 to 23 °C at high latitudes (Cramwinckel *et al.*, 2018), with a 13.3 °C pole to equator thermal gradient (Eichenseer and Jones, 2024), and bottom waters were ~10 °C warmer than their modern counterparts (Zachos *et al.*, 2001). Such temperatures had consequences for the ambient marine environment, relating to ocean acidification (with shoaling of the carbonate compensation depth (the depth at which calcium carbonate supply from the surface equals dissolution below) by ~1,500 m in the early to middle Eocene; Bohaty *et al.*, 2009; Slotnick *et al.,* 2015), oxygen supply (contraction of open ocean oxygen depletion zones; Auderset *et al.*, 2022) and nutrient enrichment or depletion (linked to seasonality affecting weathering on land and nutrient input to oceans; Arimoto *et al.,* 2020). Furthermore, this time interval experienced significant tectonic movements with consequent impacts on oceanographic circulation, including: opening of the Tasman Gateway in the Eocene (beginning ~48 to 49 Ma; Bijl *et al.*, 2013), allowing throughflow of surface waters between the Pacific and

Indian Oceans; opening of the Drake Passage (beginning ~49 Ma; Scher and Martin, 2004), permitting polar waters to circulate into global southerly oceans; and narrowing of the Tethys Gateway affecting the northerly connection between the Atlantic and Pacific Oceans (Allen and Armstrong, 2008).

Superimposed on the greenhouse trend of the early Cenozoic are more than 20 transient enhanced warming events (Westerhold *et al.*, 2020; Vahlenkamp *et al.*, 2020) of different durations, magnitudes and rates of change. These include the Palaeocene-Eocene Thermal Maximum (PETM, ~56 Ma, lasting ~200 kyr; Aziz *et al*., 2008; Murphy *et al.*, 2010; Figure 1.1), Early Eocene Climatic Optimum (EECO, ~49 to 53 Ma; Vahlenkamp *et al*., 2020) and Middle Eocene Climatic Optimum (MECO, ~40 Ma, lasting ~400 to 700 kyr; Bohaty *et al.*, 2009). The differing timescales and warming patterns (in terms of the rapidity of onset and termination) of these events provide a valuable opportunity to explore atmosphere-ocean responses and their ecological and biological impacts. Investigating the responses of Earth's systems during these past warming intervals permits validation of climate models and whether they encapsulate the behaviour of the current climate system (Foster *et al*., 2018). In particular, the short-lived nature of the PETM and rapidity of change across the MECO, combined with elevated pCO_2 akin to the Intergovernmental Panel on Climate Change's projections of pCO_2 over 1,000 ppm by 2100 under worst-case scenario Representative Concentration Pathway 8.5 (IPCC, 2022), means these early Paleogene events are considered important partial analogues for assessing the impacts of global warming.

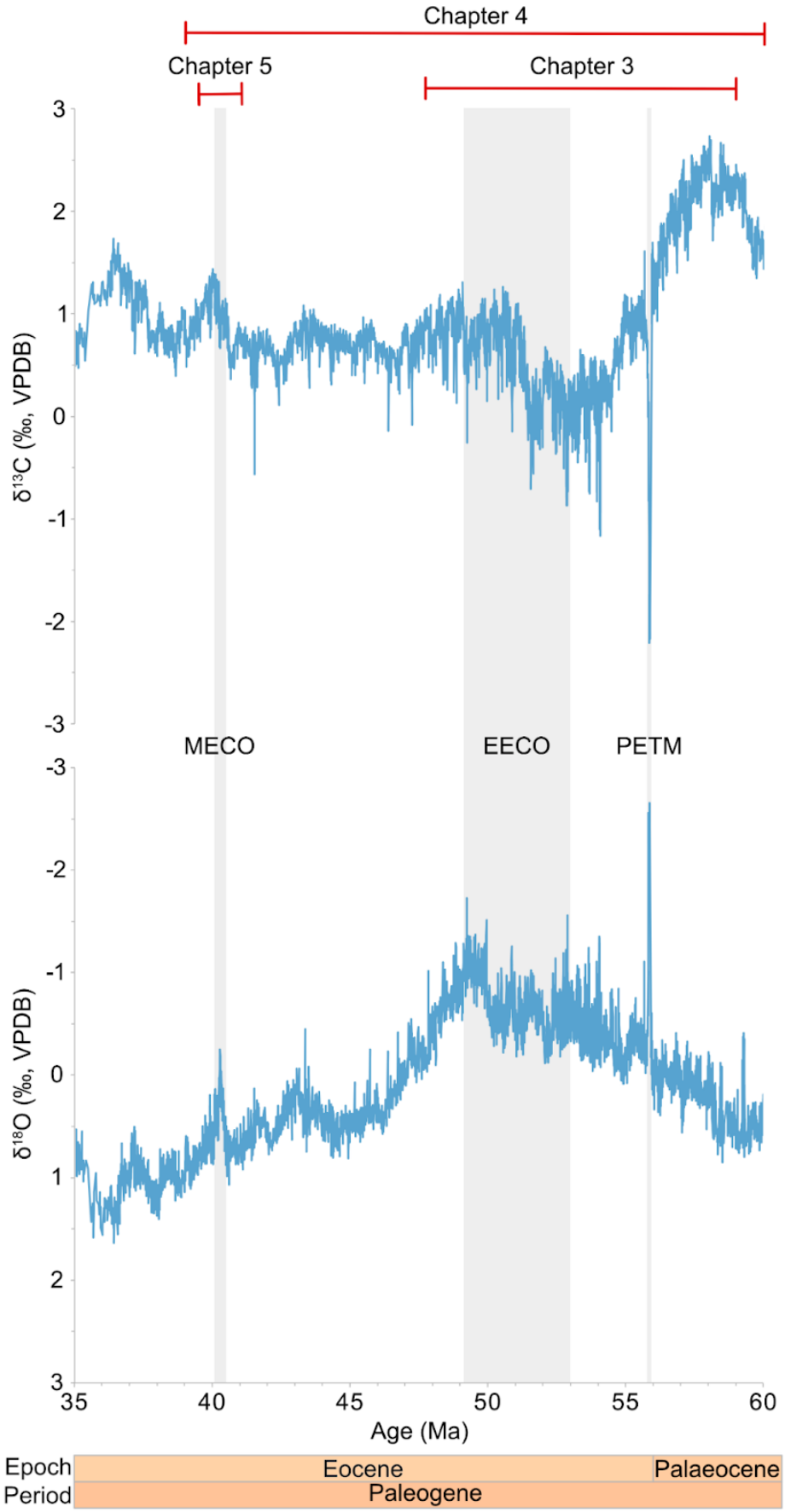
Chapter 4
Chapter 5
Chapter 3
MECO
EECO
PETM
δ13C (‰, VPDB)
δ18O (‰, VPDB)
Age (Ma)
Epoch
Period
Eocene
Palaeocene
Paleogene

Figure 1.1. *(Previous page)* Late Palaeocene to late Eocene segment of the Cenozoic Global Reference benthic foraminiferal carbon and oxygen Isotope Dataset (CENOGRID, referenced to Vienna Peedee Belemnite (VPDB) isotopes; Westerhold *et al*., 2020) with key warming events marked (PETM: Palaeocene-Eocene Thermal Maximum, EECO: Early Eocene Climate Optimum and MECO: Middle Eocene Climate Optimum). The time intervals studied in each of the thesis chapters are also indicated.

1.2. Significance of early Paleogene climate research for actinopterygians and chondrichthyans

Modern models have considerable uncertainty when predicting how marine vertebrates may react to continued climate warming in the future (for example, Heneghan *et al.*, 2021; Tittensor *et al*., 2021) and so looking to their responses during this time in Earth's history is of vital importance to help answer this knowledge gap. In particular, actinopterygians (bony fish) comprise almost half of all marine vertebrate diversity in the modern day (Nelson, 2006) and are an important global protein source (Boyd *et al.*, 2022), thus, understanding their role, alongside chondrichthyans (sharks), in a warmer world is significant to ensure stability of trophic webs in the ocean and food security for human populations on land.

Productivity (the production of new biomass) and diversity (in ecology referencing species abundance and richness) are two key parameters to consider when assessing fish response to climate change. In a warmer world, there are currently differing views on whether primary productivity increases or decreases (Savian *et al.*, 2014; Dalpadado *et al.*, 2021) with this having consequences on the available

biomass for consumers (such as fish), as well as oxygen supply at lower depths in the water column due to bacterial metabolism of organic matter. Meanwhile, diversity patterns in a greenhouse world are also unclear, and the rate of change into and out of these climate events may be a primary factor in how readily the marine ecosystem is able to adapt, and whether this leads to taxonomic originations and/or extinctions.

In order to determine fish and shark productivity and diversity in the past, body fossil records can provide valuable insights on form and function but are somewhat limited, being predominantly disarticulated, temporally discontinuous and biased towards lacustrine and shallow marine settings (Friedman, 2022; Sibert, 2016). However, there are some notable exceptions that form Lagerstätte, such as those in southern United Kingdom (Friedman *et al.*, 2015) and Monte Bolca, Italy (Friedman and Carnevale, 2018). Whilst these are unique sites, they cover discrete windows in time, hence microfossil remains become more useful as they can provide spatially and temporally continuous records in both shallower and deeper waters, being preserved in greater abundance and frequency than body fossils (Friedman, 2022). Common microfossils found in marine (and in some cases freshwater) sediments include teeth (Figures 1.2 a, b), otoliths (calcareous components in the inner ears of vertebrates for auditory and gravity detection purposes; Figure 1.2 d) and denticles (tooth-like scales on the outside of cartilaginous fish for hydrodynamics; Figures 1.2 c, e), collectively termed ichthyoliths. Such microfossil remains are dissolution-resistant across a variety of environments, hence can provide a high resolution (tens of thousands of years) proxy record for fish and shark community abundance and structure.

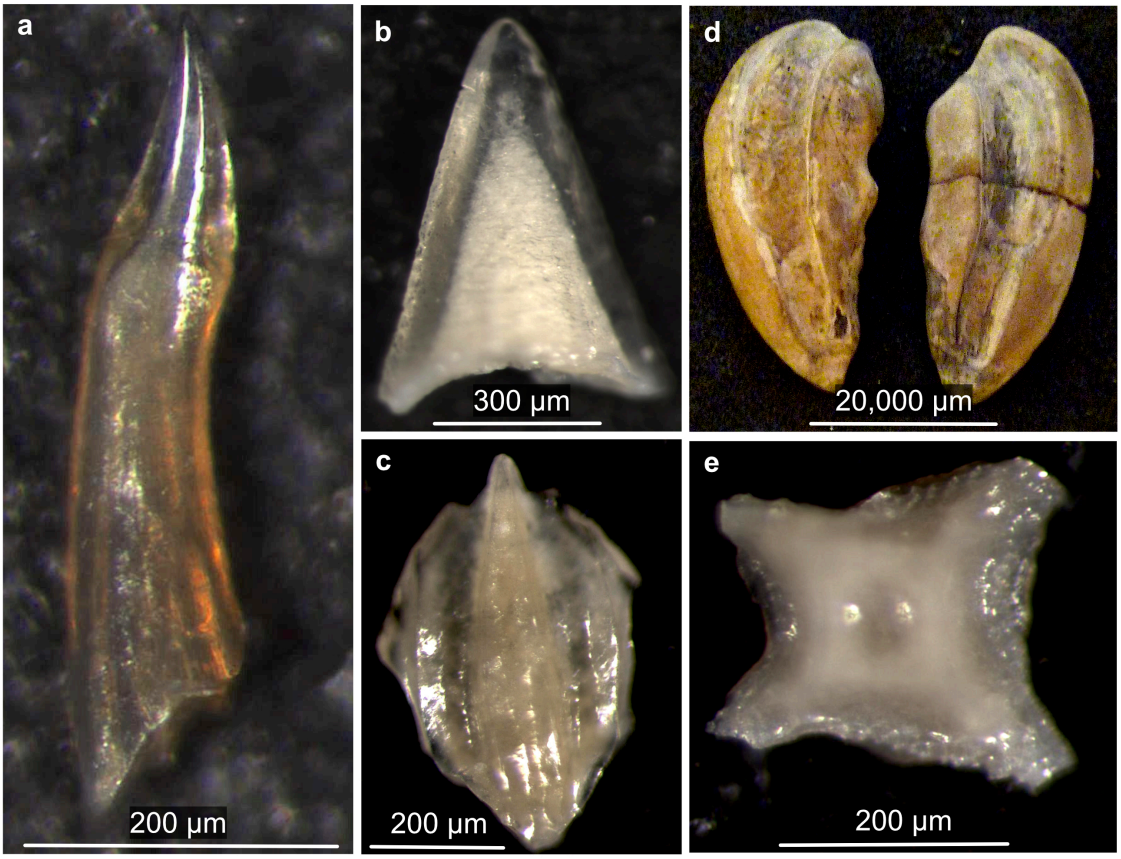

Figure 1.2. Examples of ichthyoliths in this study: cone tooth (**a**; Specimen ID: 369 U1514A 18H 3W 143-145 cm #9, over 63 µm), triangle tooth (**b**; Specimen ID: 369 U1514A 30X 2W 23-25 cm #19, over 63 µm), linear denticle (**c**; Specimen ID: 369 U1514A 22F 1W 110-112 cm #25, over 63 µm), otoliths (**d**; Specimen ID: NHMUK PV P 43145) and geometric denticle (**e**; Specimen ID: 208 U1263B 9H 1W 113-115cm #28, over 63 µm).

Otolith studies are prevalent globally, pertaining to modern taxonomic designations (for example, Paxton, 2000; Chang and Geffen, 2012; Echreshavi *et al.*, 2021; Stock *et al.*, 2021; Arroyo-Zúñiga *et al.*, 2022; Park *et al.*, 2023) but suffer from outdated and inconsistent taxonomies when considering those from the geological past (including Schubert, 1916; Frost, 1925, 1933, 1934; Stinton, 1975, 1977, 1978, 1980,

1983), which render comparisons across time intervals and locations complex. Consequently, comprehensive assessments of their abundance and diversity in response to warming events, such as those in the Paleogene, are lacking. Additionally, fish only produce six otoliths, with only two of these used in palaeontology, whereas fish may produce dozens to hundreds of teeth in their lifetime, hence the latter have the potential to be more useful for palaeontological studies. Furthermore, classically, ichthyolith work in deep marine sediments recovered by the International Ocean Drilling Program (IODP) and its predecessors has predominantly focused on their utility for palaeoceanographic or palaeoenvironmental reconstructions via geochemical isotopes (predominantly neodymium and strontium (for example, Scher and Martin, 2004; Huck *et al*., 2016; Tanaka *et al*., 2024) but also oxygen (MacLeod *et al.,* 2018)) rather than their taxonomic affinities (bar early work on macrofossil teeth (Johns *et al*., 2005) and more recent research on Mesozoic teeth and denticles (Tackett *et al*., 2022)). However, within the last decade, novel character coding systems for microfossil teeth and denticles from open ocean ecosystems have been developed by Sibert (2016), opening up research on their morphological ranges through time and permitting abundance and diversity analyses.

Primarily, these studies have focused on the Pacific Ocean across the Cretaceous-Paleogene boundary (Sibert *et al*., 2014; Sibert and Norris, 2015; Sibert *et al.*, 2018) and through the Miocene (Sibert and Rubin, 2021) to the modern day (Sibert *et al*., 2016). For those studies pertaining to the early Paleogene, an increase in ichthyoliths is observed post-Cretaceous, inferred to be expansion of fish into newly-opened niche spaces in the Palaeocene before beginning to stabilise in the Eocene (Sibert

and Norris, 2015; Sibert *et al.*, 2016; Sibert *et al.*, 2018). Specifically, this previous research has predominantly focused on pelagic fish, with ichthyoliths therefore representing the communities living down to mid-water depths and at a distance from coastal communities, likely including migratory species. These communities established during the Paleogene have continued through to the present day, with mid-water fish currently being the most abundant marine vertebrates, thus this research provides valuable exploration of past and potential future patterns of a rich component of the ocean realm.

Whilst broad patterns over millions of years have been identified, high-resolution datasets for short-lived warming events (such as EECO hyperthermals (generally less than ~200 kyr-long; Figure 1.3) and the MECO) are lacking, hence there is an opportunity to explore new ocean basins and transient climate change through this work.

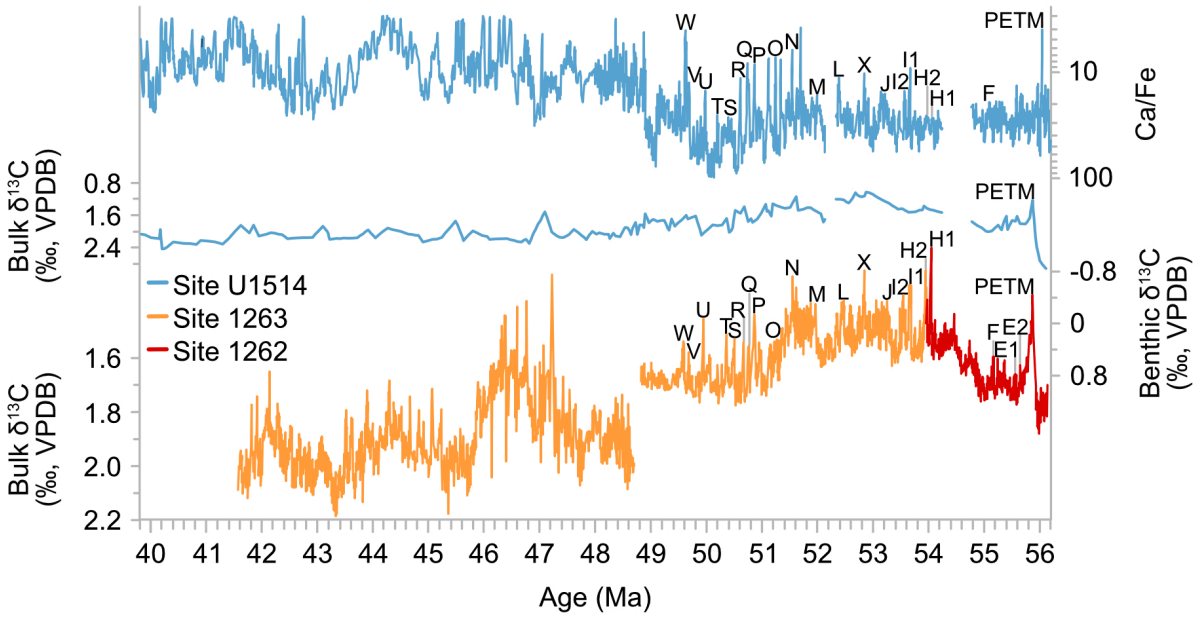

Figure 1.3. *(Previous page)* Early Eocene hyperthermals identified in calcium-iron (Ca/Fe) record from Site U1514 against bulk and benthic carbon isotopes from Sites U1514, 1262 and 1263 (reproduced from Vahlenkamp *et al.* (2020) based upon Westerhold *et al*. (2015) and Stap *et al.* (2010)).

1.3. Thesis outline

The overarching aim of this thesis is to utilise museum and deep-sea records to identify the response (specifically productivity and diversity) of bony fish and sharks to past global warming events of different durations, magnitudes and rates of change. Specifically, the rapidity of warming during hyperthermals has relevance for the abrupt nature of modern climate change, thus understanding the past is paramount to supporting marine fish and shark communities into the future.

Research methods are outlined in **Chapter Two**, with individual chapters further detailing project-specific techniques.

Chapter Three aims to assess the response of fish to warming in the late Palaeocene and early Eocene in shallower waters (up to 200 m; King, 1981) through study of the largest known otolith collection in the UK, housed at the Natural History Museum, UK. These historical archives are comprised of specimens collected across the south of England and permit reconstruction of fish palaeocommunities across the study interval. The chapter also investigates the geological and anthropogenic biases that have likely impacted the collection and offers suggestions on how these may be alleviated for future museums-based research.

Understanding the impact of warming on deep-sea fish and shark communities over shorter (less than 200 kyrs for the PETM) and longer timescales (millions of years for the EECO) is at the centre of **Chapter Four**. Here, teeth and denticles extracted from IODP Site U1514 (Mentelle Basin, Australia) cores spanning 39 to 62 Ma are analysed based upon a character coding system to generate a database of morphotypes that permit investigation of abundance through time, geological range and patterns of origination and extinction. This longer-term study is supplemented by additional data obtained from undergraduate students studying the abrupt PETM and R and S hyperthermal events within the EECO at the same site to provide insights into the effects of different rates of environmental change on fish and shark palaeocommunities.

Intermediate climate change on the scale of hundreds of thousands of years with a different warming pattern to the PETM and EECO is explored through study of the MECO in **Chapter Five**. The same methodologies and outputs as for Chapter Four are employed on samples derived from two locations in the South Atlantic Ocean, ODP Sites 702 (Islas Orcadas Rise) and 1263 (Walvis Ridge).

Finally, an assessment of the productivity and diversity responses of bony fish and sharks across these key temporal windows of climate change (PETM, EECO and MECO) are summarised in **Chapter Six**. Additionally, here are included suggestions of how this research can be further expanded to shine a light on fish and sharks in a warmer world, and how further closure of this knowledge gap allows us to have hope for a thriving marine realm as we continue to face climate change into the future.

CHAPTER TWO

Materials and methods

2.1. Chapter Three: Early Paleogene UK otoliths

Through consultation with the Fossil Fish Curator (Emma Bernard) at the Natural History Museum, London, I identified late Palaeocene and early Eocene otolith specimens for study to assess shallow marine fish abundance and diversity across the warming interval. I systematically photographed drawer labels with a Panasonic compact camera for collection references, as well as individual sample labels. The reference images are currently digitally accessible via the NHMUK's private collections database. For samples that had numerous otolith specimens in boxes and vials, these were carefully opened over black paper to enable ease of counting due to contrast, as well as return to the vials without loss.

Subsequently, the specimen labels were transcribed into a Microsoft Excel spreadsheet (Appendix Table 3.1) and a text colour coding system was established to identify information that was directly from the label (black), updated label notes from other researchers (green), and information gaps or updates that were filled by literature searches (blue). This included details on chronostratigraphy, lithostratigraphy, NHMUK collection reference, taxonomic identification, collector, collection or museum acquisition date, publication reference where available, and number of otoliths within the registered box or vial. To validate and, where necessary, update lithostratigraphy, a comparison table in Stinton (1975; Table 1 therein) was used to cross-reference earlier alphanumeric designations of the London Clay Formation (Thames Group) divisions, then further updated using King

(2016) as the most recent accepted lithostratigraphy. Meanwhile, taxonomic data was validated using otolith monographs (Stinton 1975-1983) followed by comparison to the most recent accepted taxonomies in Nolf (1985; 2013).

Statistical analyses were conducted in the free software Paleontological Statistics (PAST) version 4.11 for Mac (Hammer *et al.*, 2001; available from: https://www.nhm.uio.no/english/research/resources/past/). Raw taxonomic abundance data was input to the software to use diversity (Shannon *H*), richness, evenness, Bray-Curtis dissimilarity and rarefaction functions to produce figures.

2.2. Chapter Four: IODP Site U1514 early Cenozoic ichthyoliths

For site-specific details on location, age model generation, sample selection, isotope and X-ray fluorescence data and calculating ichthyolith accumulation rate, see section 4.2. The full ichthyolith processing methodology and coding system are outlined below.

2.2.1. Sample preparation and ichthyolith extraction methodology

2.2.1.1. Pre-processing

1. Transfer samples to a beaker of known weight, retaining a ~1 cm^3 piece for bulk analyses and scraping the sample rind to remove loose material potentially transferred from other units during core extraction.
2. Weigh sample in beaker, then place in the oven at 30 °C and weigh every day until a constant weight is achieved to remove residual moisture.

2.2.1.2. Acidifying the sample

1. Produce 10% acetic acid solution by mixing 100 ml glacial acetic acid with 900 ml deionised water.
2. Transfer the sample into a labelled beaker.
3. Wet sample with deionised water to prevent clays seizing with acid interaction.
4. Pour acetic acid solution onto the sample in 25 to 50 ml increments, checking every 10 to 20 minutes and letting the sample bubble to completion each time.
5. Thoroughly wash with deionised water using a 250 µm protector sieve over a 38 µm sieve, then transfer to Fisherbrand general purpose filter paper to dry in an oven overnight at 30 °C.
6. Samples insufficiently broken down can be soaked in sodium metaphosphate before a second round of acid, but must be thoroughly washed between.

2.2.1.3. Separating ichthyoliths using LST FastFloat heavy liquid

1. Transfer the sample into 15 ml tubes labelled with the sample ID. If the sample reaches over 1.5 cm up the base of the tube, then split the sample across multiple tubes to allow space for LST heavy liquid separation.
2. Check the density of the LST using a calibrated pipette (the average of five density tests), adding small amounts of deionised water if necessary to dissolve crystals and ensure a density of 2.75 to 2.85 g cm^{-3}, allowing separation from bioapatite ichthyoliths with a density of ~3.1 g cm^{-3}.
3. Squirt LST around the tube inside to rinse the sample down, filling to ~6 ml, then add two vigorous squirts straight down into the tube up to ~12 ml to break up the initial clump of sediment rising to the top.

4. Leave to settle overnight ideally, but a minimum of 6 hours.
5. To separate the sediment floats, circle the top layer with a pipette and syphon off into labelled filter paper. Once most of the sediment is removed, gently pierce through the top layer and draw up some LST to rinse down the insides. Expel residue into filter paper with force to avoid clogging and ensure it mixes with deionised water also being added. Continue until ~1 cm of LST remains above the ichthyolith and residual sediment grain sinks at the base of the tube.
6. Rinse the tube and lid into a separate labelled filter paper to retrieve the sinks.
7. Continue adding deionised water as necessary until filters are unclogged.
8. Filter the sample to remove LST by attaching a flask to a vacuum line and running ~400 ml deionised water through the separate floats and sinks filter papers sitting inside a funnel lined with 0.4 µm filter paper.
9. Place the samples in an oven at 30 °C and dry overnight.
10. Collect LST for reuse by using a glass beaker on a hot plate up to 110 °C to boil off the deionised water and impurities, using a continuous magnetic stirrer or stirring manually every 10 minutes. When nearing completion, check density frequently to reach 2.75 to 2.85 g cm^{-3} using the aforementioned calibrated pipette system.

2.2.1.4. Ichthyolith processing

1. Transfer weighed sinks residue into a sieve stack (38 to 63 µm and 63 to 250 µm size fractions) and pick through each set under a reflected light microscope, transferring into separate areas of a labelled microscope slide.

2. Use a water soluble glue to paint onto a glass slide, allowing ichthyoliths to adhere when transferred with a wet brush but permitting movement if reorientation of the tooth is required at a later point. Aim to align the tooth flat to enable visualisation of as many features as possible.
3. Return remaining sinks residue back to vials for storage.
4. Image ichthyoliths, in this study conducted via Leica M205 C microscope using Image Pro Premiere Software Version 9.3.1.

2.2.2. Ichthyolith morphotype coding

Morphotype coding of teeth as a proxy for fish diversity followed the system of Sibert (2016) and Sibert *et al.* (2018), updated to version v0.4. Tooth images in JPEG format were observed and compared to a coding spreadsheet with dropdown menus (Sibert, 2023; 2024) that considers 47 characteristics pertaining to size in three dimensions and overall shape; surface texture; curvature; symmetry, size, length and location of blades and barbs; pulp cavity shape and size; base shape; tip shape and material (Figure 2.1). The coded tooth was then compared to a PowerPoint database (Sibert, 2023; 2024) of images of past coded teeth to identify a relevant morphotype, or to designate a new morphotype where necessary. Alongside the morphotype name, the coding spreadsheet also generated a numerical code used to produce a matrix for subsequent analyses in R coding software. Novel morphotype names were assigned for teeth with unique combinations of character states.

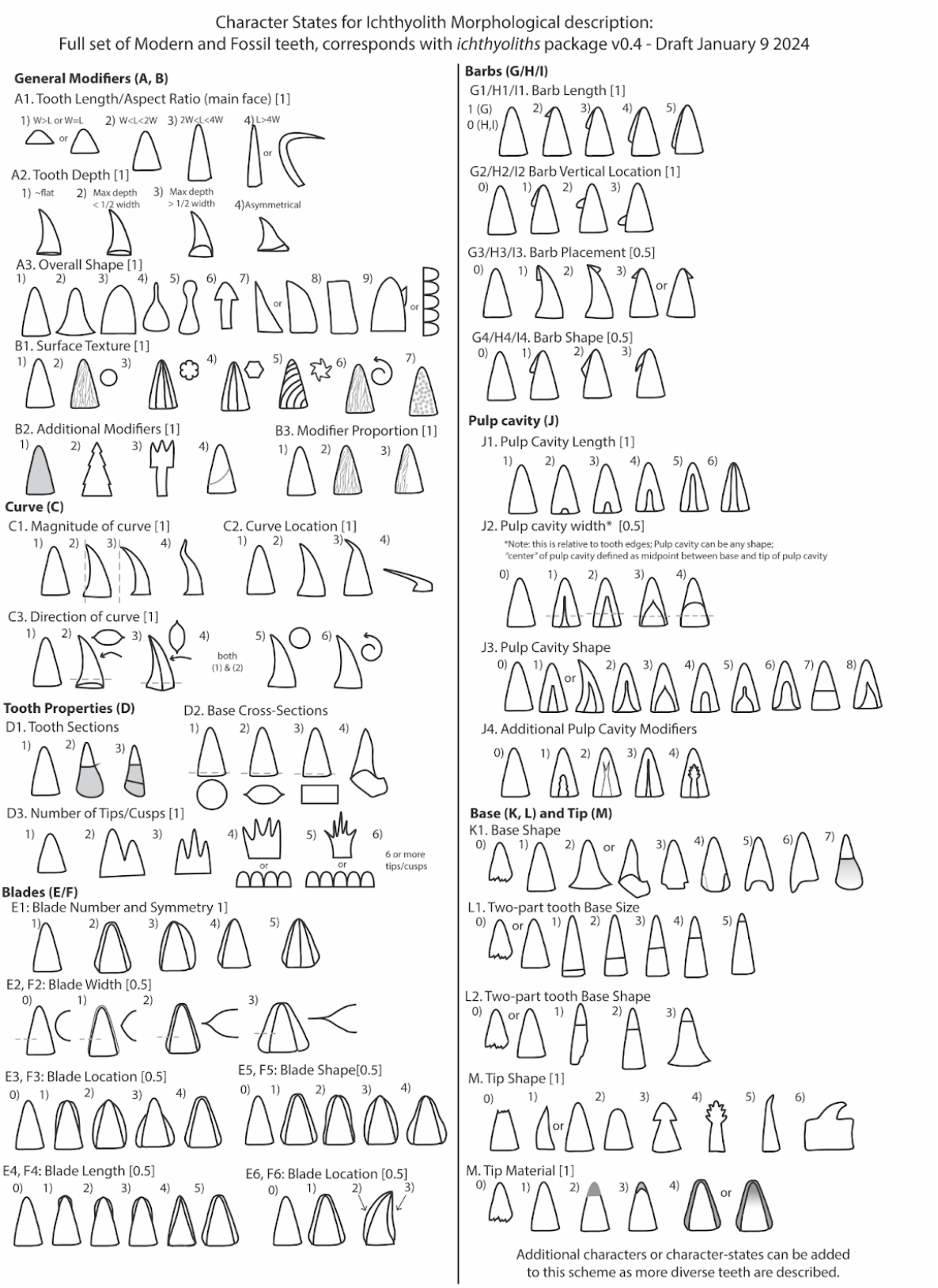

Figure 2.1. Character states used for coding teeth and identifying morphotypes (Sibert, 2024).

2.2.3. Ichthyolith analyses in R

The tooth morphotype coding spreadsheet was downloaded as a csv file to permit upload to R Studio (version 4.3.2; R Core Team, 2023) to produce a matrix for manipulation using the *ichthyoliths* R package v0.4 developed by Dr Elizabeth Sibert (available from: https://github.com/esibert/ichthyoliths). The R code for producing range charts was only modified to order by first and last appearance to explore the impact on data patterns. Furthermore, the data matrix was subset by time interval (preceding, during and after each respective warming event) to observe morphotype changes through time via non-metric multi-dimensional scaling (NMDS) ordination plots. The latter script was modified in the *vegan* R package (Oksanen *et al.*, 2022) to produce NMDS figures for particular coded characteristics, such as number of parts, curvature and blade and barb type. To produce origination and extinction plots, the R code of Foote (2000; using a script provided by Sibert, 2024) was used on a counts table, produced based upon specimen ages and morphotypes, to calculate turnover rates as well as observed and estimated standing diversity in the tooth morphotype community.

2.3. Chapter Five: South Atlantic Ocean MECO ichthyoliths

For site-specific details on location, age model, sample selection, isotope and X-ray fluorescence data and ichthyolith accumulation rate, see section 5.2, plus the full ichthyolith processing methodology and coding system outlined in section 2.2.

CHAPTER THREE

Museum collections and palaeocommunity reconstruction biases: a case study of early Paleogene actinopterygians from the UK

3.1. Chapter introduction

Global temperatures increased from the mid-Palaeocene through early Eocene, culminating in the Early Eocene Climatic Optimum (EECO, ~49 to 53 Ma; Hollis *et al*., 2019), the warmest interval of the Cenozoic (last 66 million years), excluding a number of short-lived hyperthermal events, such as the Palaeocene-Eocene Thermal Maximum (PETM, 55.71 to 55.93 Ma; Westerhold *et al*., 2017; Westerhold *et al.*, 2020). Mean global surface palaeotemperature for the EECO was 27 °C (Inglis *et al.*, 2020), ~14 °C warmer than present, with reduced pole to equator latitudinal gradients of ~17 °C to 21 °C (Cramwinckel *et al.*, 2018) compared to approximately -22 °C to 31 °C today (Zhang *et al.*, 2019), and atmospheric carbon dioxide (pCO_2) concentrations of ~1,500 parts per million (ppm; Rae *et al.*, 2021). Climate modelling suggests that Eocene-like temperature and pCO_2 conditions could be reached by 2100 under the most extreme Intergovernmental Panel on Climate Change Representative Concentration Pathway 8.5 projection (Westerhold *et al.*, 2020; IPCC, 2022). However, the EECO is not a strict analogue for modern conditions given that anthropogenic climate change is occurring at a significantly more rapid rate than past warming, plus background conditions and ecological communities also differ. Nevertheless, early Cenozoic community and ecosystem responses of marine fauna to a major climatic perturbation and significantly higher global temperatures may hold insights for present and future impacts of global warming.

In the early Eocene (Ypresian, ~48 to 56 Ma), the UK was situated ~11.5 ° further south at a palaeolatitude of ~42 °N (Smith *et al.*, 1994) which today corresponds to locations around the Mediterranean. Sea levels were elevated ~75 m to 140 m globally (Sluijs *et al*., 2008; Miller *et al*., 2020), leading to extensive marine deposits of the Lambeth and Thames Groups across the south of England, particularly the London Clay Formation within the Thames Group (Aldiss, 2014). These Ypresian-aged shallow to deeper marine deposits are globally significant for palaeoichthyology (fossil fish studies), as they yield exceptionally-preserved and highly diverse articulated actinopterygian (ray-finned bony fish) skulls in pyritic, phosphatic or calcitic concretions, hence the London Clay Formation is designated a Lagerstätte (Friedman *et al.*, 2015). Whilst other countries, such as Belgium, Peru and Denmark, also yield exceptionally preserved early Eocene fossil fish (totalling ~80 known bony fish species; Friedman *et al.*, 2015), their taxonomic richness individually is lower than that of the UK, focused on skeletal material and some teeth. A notable exception is Monte Bolca, Italy, which has provided at least 20 species of chondrichthyans (sharks and rays), 30 species of non-acanthomorph ray-finned fishes and over 150 actinopterygian species, though again this is mostly based upon skeletal material (Friedman and Carnevale, 2018). The three-dimensional preservation of the London Clay Formation specimens provides a unique opportunity to study form and function that can elucidate further details of ecological niches within this palaeocommunity. The London Clay Formation also preserves a diverse community of non-vertebrate macrofossils such as corals, echinoderms, bivalves, gastropods and crustaceans, as well as (sub)tropical and temperate plants (Quayle,

1987; Collinson, 2000; Tracey *et al.*, 2002), which together help to provide a more complete picture of marine and terrestrial communities of the time.

The early Cenozoic was a time of rapid actinopterygian diversification capitalising on the opening of shallow continental shelf and marginal marine niches following the Cretaceous-Paleogene mass extinction (Alfaro *et al.*, 2018; Sibert and Norris, 2015; Friedman *et al*., 2015), when most modern higher-order diversity was established. Whilst actinopterygian diversification is well-known from this time, and is one of the most abundant and diverse marine groups of vertebrates in the Paleogene (~23 to 66 Ma) through to the modern day (Nelson *et al.*, 2016), whether this is a closely coupled response to elevated temperatures is less well-defined.

Actinopterygian palaeocommunities can be reconstructed using skeletal remains, teeth and otoliths (calcareous components in vertebrate inner ears). Whilst body fossils may be easily identifiable taxonomically and provide a wealth of anatomical and ecological information, teeth and otolith microfossils are far more abundant in the geological record than complete body fossils. They are also preserved in a wider range of sedimentary environments (coral reefs through to deep sea; Doyle and Riedel, 1979; Zhuang *et al.*, 2015; Lin *et al.*, 2016; Sibert *et al.*, 2017) so can offer a much richer view of ancient ecosystem diversity and ecology. This is aided by the specificity in taxonomic identifications of otoliths in particular, making them a valuable, if somewhat underused, resource for palaeocommunity reconstructions.

Otoliths are calcareous mineralised components of the static-acoustic organs in the ears of actinopterygian fish, primarily used for auditory and vestibular functions (gravity detection for movement and body positioning; Schulz-Mirbach *et al.*, 2019).

Each fish has three pairs of otoliths (sagittae, asterisci and lapilli) with sagittae being the most commonly used for taxonomy due to being the largest (see example in Figure 1.2 d), more robust and having characteristic identifiable species-level morphology. However, despite their widespread use in the fossil record, only ~2,000 otolith-based taxa are named and described (Nolf, 1985; 2013), yet there are ~30,000 recognised extant bony fish species spanning marine and freshwater environments (Nelson *et al.*, 2016), thus otoliths are not known for many morphological species.

There is a rich history of research on UK Eocene bony fish communities (particularly otoliths) extending back into the 1800s (Whitaker, 1866; Schubert, 1916; Frost, 1925, 1933, 1934; White, 1931; Casier, 1966; Stinton, 1975, 1977, 1978, 1980, 1983), but these studies were largely taxonomy-focused, with outdated taxonomic concepts and lacking wider diversity or ecological synthesis. Furthermore, given the age of these studies and lack of recent research into UK otoliths of this age, the fossils are not well integrated into online community databases, such as the Paleobiology Database (PBDB), routinely used in evolutionary studies. Difficulty in synthesis is also exacerbated by a lack of digital catalogues of specimens from museum collections.

The PBDB has relatively sparse records for bony fish occurrences during the early Eocene globally and for the UK (1,944 and 162 species respectively, excluding the dataset of this chapter; PBDB, 2024), and is largely based on skeletal remains from a breadth of contributors, thus lacks consistency. Therefore, historical collections of otoliths and body fossils (with less robust geographic, stratigraphic and taxonomic data) challenge palaeocommunity reconstructions during a critical period of fish

diversification, yet holds the potential to offer a significant window into their response to a climate perturbation if these concerns are addressed.

Here, a taxonomically and stratigraphically updated, comprehensive and digital record of the early Paleogene otolith collection (over 8,200 specimens) housed within the Natural History Museum, UK (NHMUK), is provided. Whilst this has not included complete redescription and identification of each otolith, existing taxonomic designations provided in the museum's collections have been updated and synonymised with the most recent literature. Samples span the late Palaeocene to early Eocene Thanet, Montrose and Lambeth Groups that include the rise of and peak greenhouse conditions. The relative value of this collection for accurately reconstructing bony fish palaeocommunities is discussed, as well as the impact of various environmental, preservational and sampling biases on this.

3.2. Materials and methods

3.2.1. NHMUK otolith data collection

The NHMUK houses the largest (~20,000 individual specimens) palaeontological otolith repository in the UK spanning the Cenozoic (Bernard, 2022). Whilst an internal catalogue of scans for registered specimen papers and isolated data sheets by individual researchers exists, there is no openly accessible, fully collated digital catalogue yet, providing challenges for use in research to feed into online community biodiversity databases. To determine the stratigraphic coverage and species richness of the collection, all otolith vials and sample labels from the Palaeocene and early Eocene were photographed using a Panasonic compact camera, with specimen label data subsequently transcribed into a Microsoft Excel spreadsheet (Appendix Table

3.1). Transcribed label information typically included: chronostratigraphy, lithostratigraphy, sample location in the NHMUK collection, taxonomic identification, collector, collection or museum acquisition date, publication reference where available, and number of otoliths within the registered box or vial. Where possible, any information gaps were filled via literature searches, and lithostratigraphy, chronostratigraphy and taxonomy were updated as necessary. The details and images of specimens from the study are included in the NHMUK's digital collections database with accompanying photographs of specimen labels, though this is not currently publicly accessible.

3.2.2. Data validation

Taxonomic identifications were taken as assigned on the specimen labels with no independent re-evaluation of the taxonomy undertaken. Instead, where applicable, these names were updated to currently accepted and synonymised taxa, based on Nolf's (1985; 2013) identification of "true otolith genus" and Stinton's (1975-1983) otolith monographs from southern England. Where higher systematic palaeontology was contentious, or the species was absent from Nolf (2013) and Stinton (1975-1983), the more recent compendium 'Fishes of the World' (Nelson *et al.*, 2016) was used. Multiple specimens within a single box or vial were assumed to have the same taxonomic identification and thus considered a single collection object. Therefore, rather than registering each individual otolith within the boxes and vials, of which there were over 8,200 in the Palaeocene and early Eocene collection, only 180 boxes and vials were registered within the NHMUK database (with a note on the number of specimens in each).

Lithostratigraphic information for each specimen was updated as per Appendix Figure 3.1 to enable more accurate comparison of occurrence data within units and through time, and thus the timing of evolutionary events. This was most important for specimens from the London Clay Formation, which form most of the collection, because there have been multiple iterations of sub-divisions of this unit over the last ~100 years and various name changes between numerical and alphabetical designations (Wrigley, 1924; Ward, 1978; Stinton, 1975; King, 1981; Ellison *et al.*, 2004; Aldiss, 2014; King, 2016). Many specimen labels cite the sampling unit as "London Clay", thus further refining them to the most recently published 13 London Clay sub-divisions (A2 to F; King, 2016) is not possible. However, for the specimens that are referenced within Stinton's (1975-1983) five-part monograph, it was possible to correlate earlier numerical or alphabetical division designations with the broader Divisions A to F of King (2016).

Geographical data is mostly well-constrained to a locality and/or town, though very few specimens include grid references or GPS coordinates. There are some instances where county boundaries have changed since the sample's collection and addition to the NHMUK archive, with specimens now falling within the Greater London area, so only minor updates were necessary for this metadata type.

3.2.3. Palaeontological analyses

Standard palaeontological diversity analysis including diversity, richness, evenness, cluster and rarefaction analyses were conducted in the free software Paleontological Statistics (PAST) version 4.11 for Mac (Hammer *et al.*, 2001).

3.3. Synthesis of UK early Paleogene strata

Early Paleogene outcrops of the Lambeth and Thames Groups included in this study occur throughout southeast England, in the London and Hampshire Basins, extending into the southern North Sea Basin and throughout northern Europe (Paris Basin, Belgium, Germany, Holland and Denmark; King, 1981). Though geographically separated, the London and Hampshire Basins formed a single synformal depositional basin (King, 2006). Throughout the Paleogene, the seemingly continuous stratigraphic record in these basins was predominantly marine, but sensitive to changes in eustatic sea level and North Sea Basin tectonic movement, resulting in multiple regression-transgression cycles (King, 1981; Knox, 1996).

The oldest unit studied here is the late Palaeocene Thanet Formation (Montrose Group; Figure 3.1, Appendix Figure 3.1). The Thanet Formation predominantly comprises fine-grained sands, representing shallowing from inner to outer marine shelf above fair-weather wave base (up to 15 m water depth where the seabed is affected by daily waves during calm weather; Ellison *et al.*, 1994). Shallowing continued into the overlying Upnor Formation (Lambeth Group) deposited in a high-energy, tidally-influenced nearshore marine environment. This is followed by the interleaved coastal floodplain deposits of the overlying Reading Formation and marginal marine environments at the land-sea boundary (with transient freshwater incursions) of the Woolwich Formation (Aldiss, 2014). Within the Woolwich and Reading Formations interleaves, the Cobham Lignite of the Shorne Member is where the boundary between the Palaeocene and Eocene (and the PETM) is inferred based upon the identification of a pronounced negative carbon isotope excursion (Collinson *et al.*, 2003).

The overlying early Eocene Harwich Formation represents sublittoral (continental shelf below low tide) or marginal marine environments, sometimes within storm-wave base (depth to seabed affected by storm waves). These units are indicative of progressive deepening of the environment from the shelly shoreface (where waves move particles on the shoreline) deposits of the Blackheath Member and sandier nearshore marine Oldhaven Member to the inner marine shelf of the Swanscombe Member. The Ypresian stratigraphic succession culminates in the deeper marine environments of the overlying London Clay Formation.

The London Clay Formation's divisions currently use two classification systems that split the units into either five divisions (Walton, Ockenden, Aveley, Sheppey and Claygate Members; Aldiss, 2014) or six (A to F; King, 2016). The latter further splits the strata into 13 sub-divisions that represent multiple transgressive cycles on the inner to outer marine shelf, where water depths ranged from ~20 m to 200 m (King, 1981). These divisions vary from clay, silt and silty sands, to laminated clays, coarse sands and pebble beds, forming the thickest succession in south Essex at 150 m (King, 1981). Divisions A to F are represented within the London Basin, but only partial exposure of Divisions A to C are present in the Hampshire Basin (King, 2016). These marine shelf conditions persisted into the overlying Bracklesham Group (not included here).

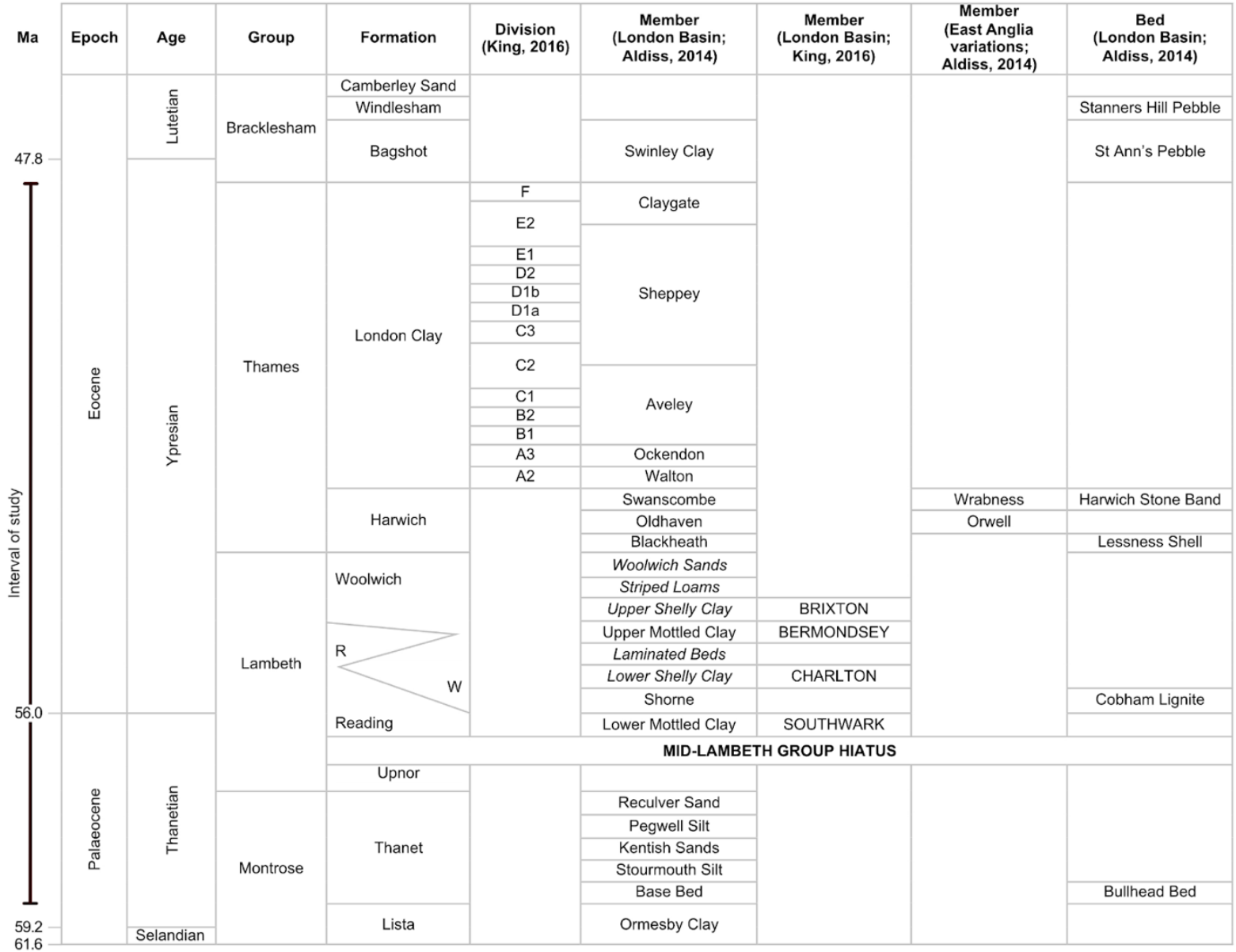
Ma
Epoch
Age
Group
Formation
Division (King, 2016)
Member (London Basin; Aldiss, 2014)
Member (London Basin; King, 2016)
Member (East Anglia variations; Aldiss, 2014)
Bed (London Basin; Aldiss, 2014)
47.8
56.0
59.2
61.6
Interval of study
Eocene
Palaeocene
Lutetian
Ypresian
Thanetian
Selandian
Bracklesham
Thames
Lambeth
Montrose
Camberley Sand
Windlesham
Bagshot
London Clay
Harwich
Woolwich
R
W
Reading
Upnor
Thanet
Lista
F
E2
E1
D2
D1b
D1a
C3
C2
C1
B2
B1
A3
A2
Claygate
Sheppey
Aveley
Ockendon
Walton
Swanscombe
Oldhaven
Blackheath
Woolwich Sands
Striped Loams
Upper Shelly Clay
Upper Mottled Clay
Laminated Beds
Lower Shelly Clay
Shorne
Lower Mottled Clay
MID-LAMBETH GROUP HIATUS
Reculver Sand
Pegwell Silt
Kentish Sands
Stourmouth Silt
Base Bed
Ormesby Clay
BRIXTON
BERMONDSEY
CHARLTON
SOUTHWARK
Wrabness
Orwell
Stanners Hill Pebble
St Ann's Pebble
Harwich Stone Band
Lessness Shell
Cobham Lignite
Bullhead Bed

Figure 3.1. *(Previous page)* Modern standardised Paleogene succession of the UK, compiled from Aldiss (2014; 2021) and King (2016). Units in italics are informal sub-divisions recognised by the British Geological Survey (BGS), whilst King's (2016) members in capitals are often cited but yet to be formalised by the BGS. W/R indicate Woolwich and Reading Formation(s) respectively where they interleave. Ages from the British Geological Survey (2020).

3.4. Results

3.4.1. UK Ypresian actinopterygian palaeocommunity

There are 1,163 otolith entries in the NHMUK physical (paper) database for the early Paleogene (Thanetian and Ypresian) of the UK, corresponding to 8,202 individual otoliths. 158 otolith species are named in the NHMUK dataset, 128 of which are found within the London Clay Formation. Both body fossil (Friedman, 2010) and otolith diversity increase from the Palaeocene through Eocene but it is unclear if this is a real radiation related to climate change (either the long-term Palaeocene-Eocene warming or PETM hyperthermal), or the result of collection biases, owing to the significantly higher number of samples from the London Clay Formation compared to any other surrounding formations. Here, the power of the NHMUK otolith collection is evaluated to address evolutionary and ecological change across the early Paleogene, with consideration of biases introduced by variations in sampling date, locality, collector, stratigraphy and taphonomy.

3.4.1.1 Taxonomic analysis

Within the fauna housed in the NHMUK, there are 26 orders, 64 families, 112 genera and 158 species represented by otoliths. Ophidiiformes dominate the collection (45%, 3,612 otoliths), with Ophidiidae (cusk-eels, modern temperate and tropical marine ecology; Nelson *et al.*, 2016) being most abundant and comprising over 29% of the whole otolith population (2,364 otoliths; Figure 3.2). Together with Ophidiiformes, Aulopiformes (13% of the dataset, 1,058 otoliths; lizardfishes, whose extant species are benthic tropical/subtropical; Nelson *et al.*, 2016), Gadiformes (11% of the dataset, 916 otoliths; cods and hakes, which are mostly temperate but ranging into subtropical and Arctic realms; Nelson *et al.*, 2016) and Perciformes (6% of the dataset, 470 otoliths; perches, found in benthic tropical waters; Nelson *et al.*, 2016) form ~75% of the fauna. Of the 64 families in the dataset, 20 fall within the 3% of rarer taxa, including Apogonidae peaking at 74 specimens across four species, whilst 13 families have less than 15 specimens in the collection. Compared to the 75 actinopterygian species of 26 orders attributed to body fossils in a summary of London Clay skeletal specimens housed at NHMUK (Friedman *et al.*, 2015), otoliths capture twice the species diversity.

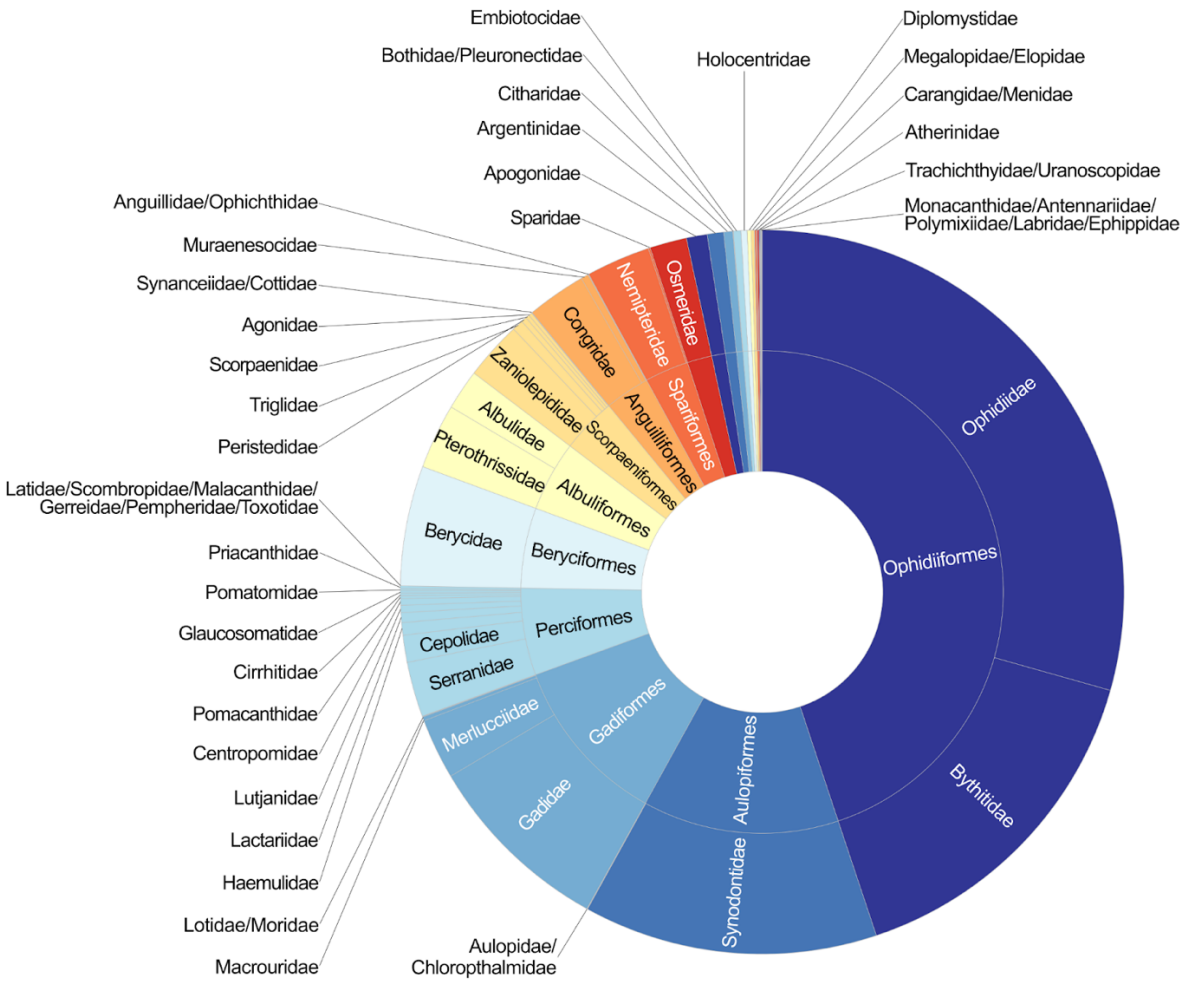

Figure 3.2. NHMUK otolith abundance from early Paleogene strata, with segments proportional to the number of specimens for each order (inner ring) and family (outer ring). Colour-coded by order for visual purposes only.

The late Palaeocene is represented by only six species, all of which occur in the oldest unit in this study, the Thanet Formation (Figure 3.3, Appendix Figure 3.2). Of these six species, five are distinct to the Thanet Formation (*Primaevomesus tricrenulatus*, *Archemacrouroides ornatus*, *Nemopteryx trigonus*, *Gadus thanetensis* and *Ampheristus retusus*) and do not appear elsewhere in the studied NHMUK collection; other representatives of the families to which these six species belong

(Osmeridae, Macrouridae, Merlucciidae, Gadiidae and Ophidiidae, which are all extant) do however occur through the succession. No otoliths occur in the overlying late Palaeocene to earliest Eocene Upnor and Reading Formations within the NHMUK collection. The early Eocene Woolwich Formation has only three species represented in the collection, one being the upper preserved limit of *Argentina planulata*, following on from its appearance in the Thanet Formation, whereas *Platysepta prima* and *Polyperca serranoides* occur only in this unit. Meanwhile, the overlying Harwich Formation shows a large increase to 21 species, with all except one (*Microgadus subnotus*) exclusive to this formation and not continuing into the overlying London Clay Formation.

The most abundant otolith-bearing unit in this study is the London Clay Formation, yielding 81% of the otoliths and 128 species, of which all except one (*M. subnotus*) are unique to the formation. Of the 128 taxa, 64 can be confidently assigned to either Division B or C, whilst an additional 28 taxa can likely be assigned to those units (and a further 16 likely assigned to Division E) based upon cross-referencing with literature (Stinton 1975-1983). 22 taxa could not be assigned to division level, thus were designated to the entirety of the London Clay Formation. Sub-division C1 has the most taxa (50 species) definitively assigned, whilst units A2 to A3 and D1a to F have few specimens and species (Figure 3.3, Appendix Figure 3.2).

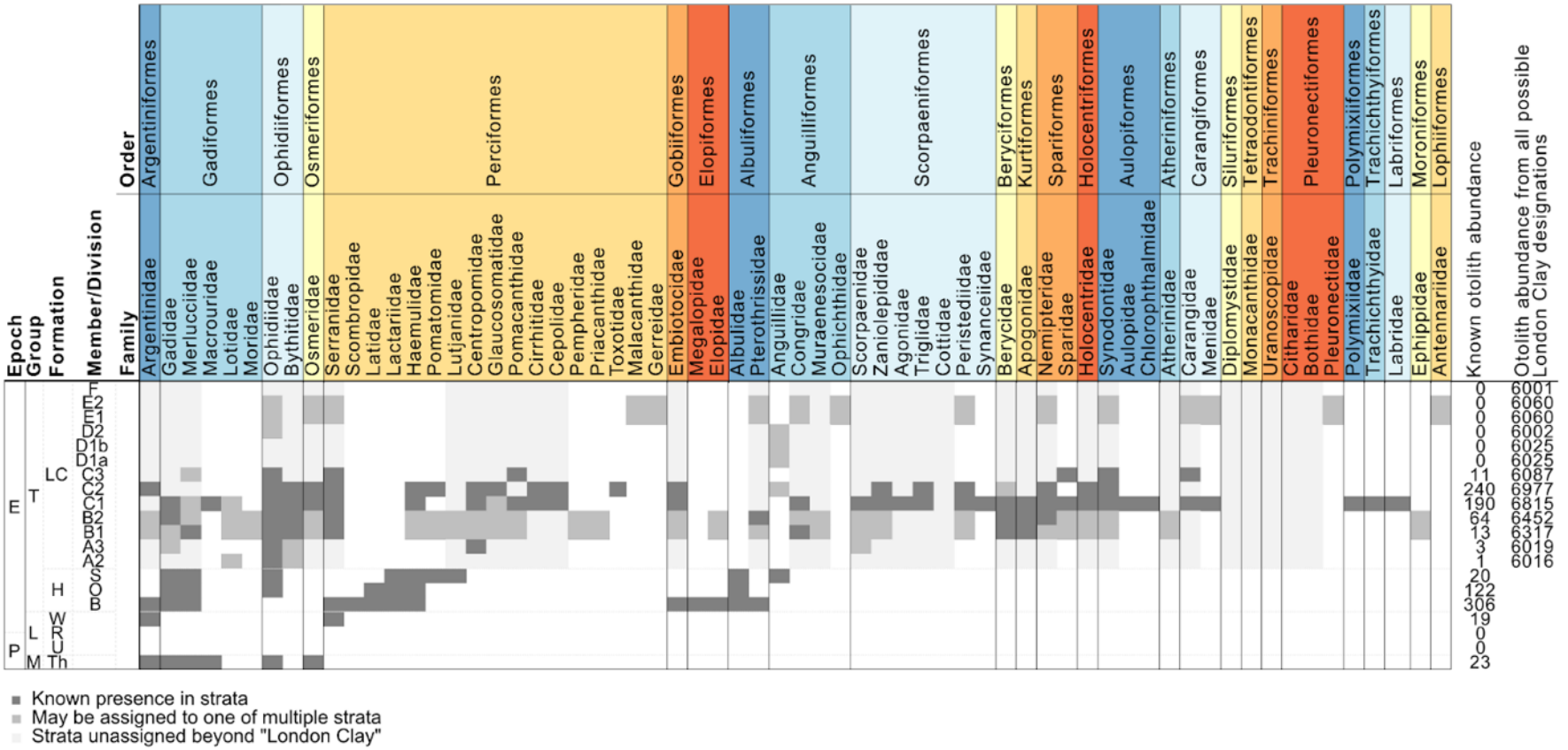

Figure 3.3. Family-level biostratigraphic range chart of NHMUK otolith taxa in the early Paleogene. Dark grey boxes indicate definitive presence of taxa in the lithostratigraphic unit, whilst the medium grey corresponds to taxa that may be assigned to one of multiple London Clay Formation sub-divisions. The palest grey represents taxa known from the London Clay Formation but for which further stratigraphic detail is uncertain. Colour coding of taxonomic names is for illustrative purposes only.

(Figure 3.3 caption continued from previous page): Chronostratigraphic abbreviations: Eocene (E), Palaeocene (P), Thames (T), Lambeth (L), Montrose (M), London Clay (LC), Harwich (H), Woolwich (W), Reading (R), Upnor (U), Thanet (Th), Swanscombe (S), Oldhaven (O), Blackheath (B).

3.4.1.2. Palaeocommunity reconstruction

The lack of stratigraphic information for many London Clay Formation samples necessitates considering diversity indices at three levels (Figure 3.4): [1] the stratigraphic units to formation or group level, [2] individual London Clay divisions (A to F) where specimens are from a particular division, and [3] all London Clay Formation specimens that may be assigned to one of multiple divisions (though here individual otolith abundance counts are duplicated across divisions). Overall, diversity indices show temporal patterns when samples are assigned to specific time bins (scenario 1 and 2), however this pattern is based on a significantly reduced otolith dataset, meaning resulting analyses may be heavily biased. When otoliths with uncertain temporal affinity are included, diversity curve structures become less defined.

Shannon's *H* index (Shannon and Weaver, 1949) is a diversity measure that can balance occurrences of rare species against the relative abundance of common species. Sample diversity (Figure 3.4) varies significantly across early Paleogene units, with higher *H* values corresponding to greater diversity. The London Clay Formation has the highest Shannon's *H*-derived diversity (2.83), closely followed by the Swanscombe Member (2.21), with diversity in the other units being lower (0.87 to 1.80).

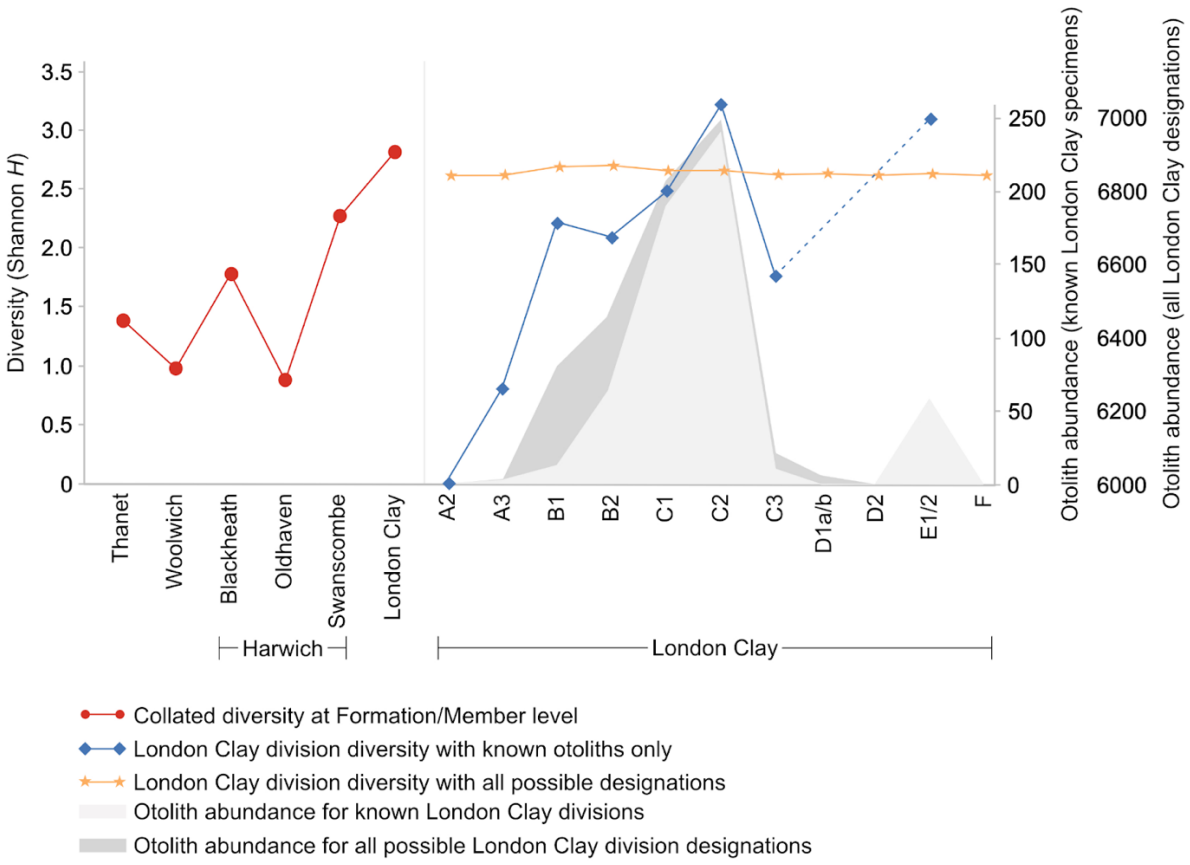

Figure 3.4. Diversity (Shannon *H*) index for the early Paleogene NHMUK otolith collection. The left panel shows diversity for all stratigraphic units as a whole (where London Clay Formation divisions are collated) and the right panel has diversity indices calculated where [1] otoliths can be definitively assigned to a division of the London Clay Formation (blue diamonds) and [2] assignment of specimens to all possible divisions (orange stars), with extrapolation across absent data points for units D1a/b and D2. Indeterminate species are removed to avoid skewing data (especially as they dominate divisions E1 and E2). The known and all possible designation otolith abundances for London Clay specimens are also shown in grey.

Within the London Clay Formation, there is very low diversity in divisions A2 and A3 (Division A2 has a *H* value of zero as only one species is recorded, *Neobythites*

obtusus) with higher diversity in the remainder of the unit (1.77 to 3.23) when samples were definitely assigned, peaking in divisions C2 (3.23) and E1 to E2 (3.11, with E divisions containing numerous singular occurrences of species, many of which are holotypes). These diversity patterns are also reflected in Bray-Curtis dissimilarity analyses (Appendix Figure 3.3), which consistently plot the London Clay divisions separate to all other formations. Dominance and evenness tests (Appendix Figure 3.4) were also run as they are strongly impacted by diversity, but as the otoliths were 'cherry-picked' by collectors, the dataset does not have standardised sampling to draw appropriate conclusions beyond highlighting collection bias.

Rarefaction tests the impact of sample size on species diversity and the likelihood of capturing a relatively complete community. When only known specimens are included (Figure 3.5 a), the units with over 25 specimens (29 to 305 across the Woolwich Formation, Blackheath and Oldhaven Members, plus London Clay sub-division C2) show the characteristic initial rapid rise in richness with increasing sample number and then the line begins to plateau, indicating relatively more complete sampling in these sections. Whereas, units with less than 25 specimens (Thanet Formation, Swanscombe Member and all London Clay sub-divisions excluding C2; Figure 3.5 b), suggest that these units are considerably under-sampled. It is important to note that rarefaction curve extrapolation is constrained by the largest sample size, hence scaling units with fewer than 25 specimens to those with greater than 300 specimens introduces bias in itself, whilst the undetected species in the largest sample will also not be considered.

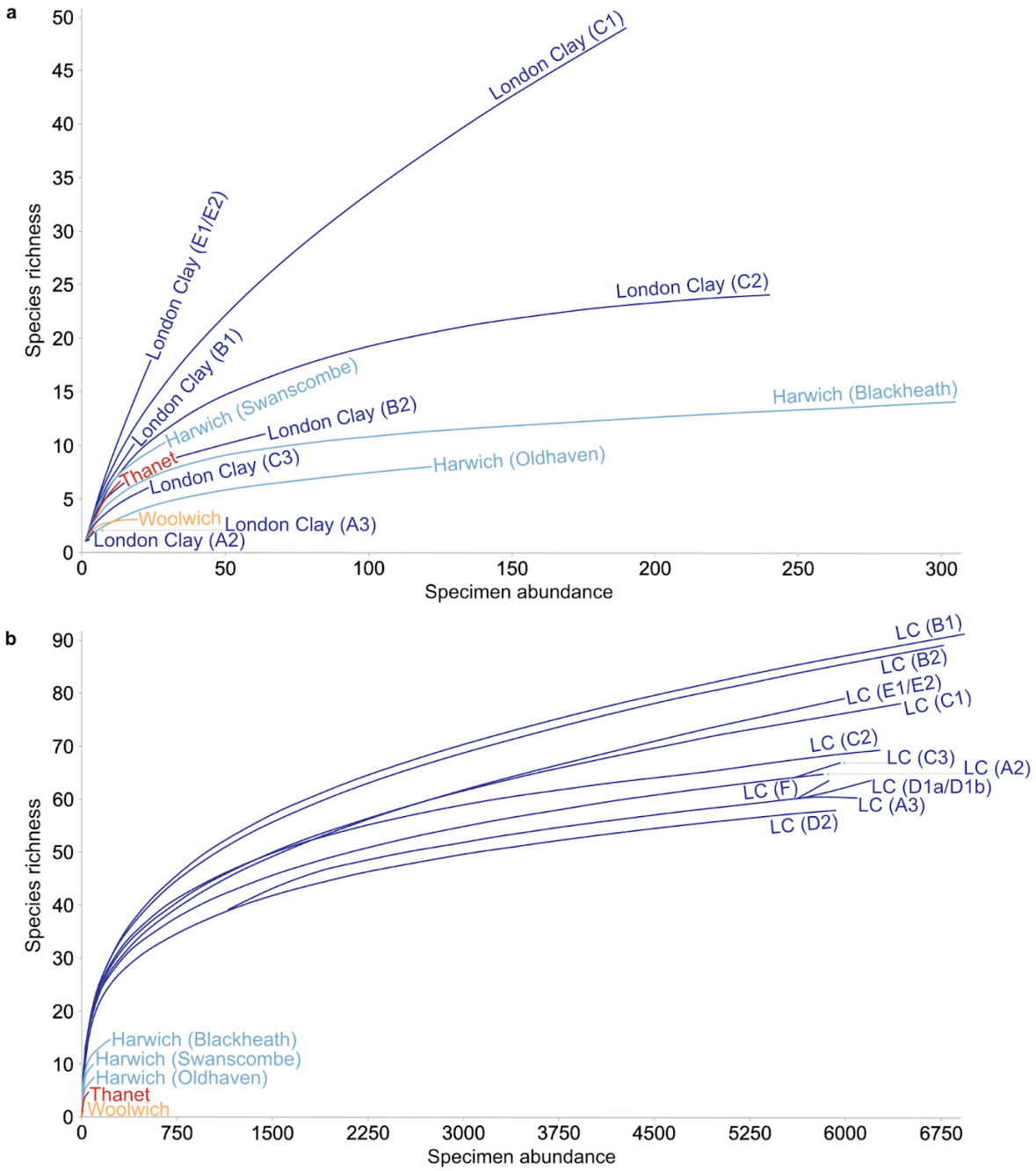

Figure 3.5. Rarefaction curves for all members and London Clay sub-divisions with known specimens only (**a**) and all members and London Clay sub-divisions with all possible designations of the specimens (**b**; London Clay abbreviated to LC).

3.4.2. Sampling biases in the NHMUK otolith collection

Biases that impact palaeodiversity reconstructions can be divided into two broad themes: geological (primarily referencing stratigraphy, taphonomy and availability of rock outcrop and exposure) and anthropogenic sampling (such as location accessibility and human interest). Here, each is discussed in the context of this dataset.

3.4.2.1. Biases from outcrop availability

Availability of accessible surface outcrop, cliff sections, boreholes and road cuttings for sampling sites depends upon the basin structure and therefore the thickness and area over which the relevant strata occur. All of the units thin westwards towards the Hampshire Basin and neighbouring counties, resulting in smaller surface outcrop in this basin relative to the London Basin (Table 3.1). The Thames Group strata (including the London Clay Formation) yield the largest surface outcrop area, and highest otolith abundances and richness, whereas both the Lambeth and Montrose Groups have lower surface areas and low otolith abundances and species richness (Appendix Figure 3.5). However, the Lambeth Group has a much larger unit area than the Montrose Group, yet the collection yields the same number of specimens and similarly low richness, perhaps indicating uneven sampling effort. Notably, there is a much smaller area of late Palaeocene rocks in the UK than early Eocene (the Thanet Formation is only present at the surface in the London Basin) hindering Palaeocene sampling.

Table 3.1. Estimated unit thicknesses of early Paleogene strata exposed in the Hampshire and London Basins (Aldiss, 2014), with calculated unit area for lithological groups, NHMUK otolith abundance and species richness counts. Whilst the Thanet Formation's surface outcrop could be distinguished as a single unit, the formations within the Lambeth and Thames Groups could not be differentiated in Edina Digimap (2022), therefore calculated volumes are given at the group level only.

	Group	Formation	Surface outcrop (km²)		Min unit thickness (m)	Max unit thickness (m)	Mean unit thickness (m)	Unit volume (km³)	Known otolith abundance	Otolith species richness	Otoliths/m	Otolith species/m
			London Basin	Hampshire Basin								
Eocene	Thames	London Clay	5930.55	590.17	4.6	150	77.3	588821.02	7702	128	99.64	1.66
		Harwich			2	24	13.00		452	21	34.77	1.62
	Lambeth	Woolwich	1179.28	244.78	11	14.5	12.75	66574.81	24	3	1.88	0.24
		Reading			12	39	25.50		0	0	0	0
Palaeocene		Upnor			2	15	8.50		0	0	0	0
	Montrose	Thanet	419.52	0	10	37	23.50	869.50	24	6	1.02	0.26

Lithology and depositional setting of the units does not vary significantly enough to account for the difference in otolith abundance and diversity, while environmental energy levels have a negative correlation. For example, the Blackheath and Oldhaven Members were higher energy shallow marine compared to the Woolwich Formation, yet preserve greater otolith abundance, thus there are clearly other factors affecting otolith abundance than purely palaeoenvironment.

3.4.2.2. Biases from sampling localities

Sampling sites with easier accessibility can concentrate collection efforts in particular areas, disregarding others that could yield abundant or unique species. Otoliths are reported from 50 different sample localities (to town level) within the London Basin, yielding 7,611 specimens and 137 species, compared to 12 localities within the Hampshire Basin hosting 569 specimens across 54 species (Figure 3.6), consistent with smaller surface outcrop area in the latter. Similarly, the majority of localities (47) are from the London Clay Formation, coincident with it having the highest mapped surface outcrop (Table 3.1, Figure 3.6), though a number of coastal and inland locations are attributed to cliff sections, road cuttings or boreholes. Noticeably, there is a distinct lack of sampling from the northeast of the London Basin, where the London Clay Formation outcrops on the surface, perhaps a result of more comparatively inaccessible rural locations. There are 35 species shared between the two basins, while 102 are unique to the London Basin and 19 unique to the Hampshire Basin, at least within the NHMUK otolith collection. In the Hampshire Basin, Bognor Regis is an outlier from the trend of reduced otolith abundances and

species richness, having 377 specimens across 37 species, readily obtained from cliff sections.

Species distribution is uneven across the basins and between towns, with two locations (Tolworth and Barrow Brook; Figure 3.6) providing over 500 otoliths individually, four sites have yielded 300 to 500 otoliths to the NHM collection (Bognor Regis, Heathrow Airport, Isleworth and Warden Point), whilst 18 sites have fewer than 50 otoliths and the majority of sites (29) have produced less than 10.

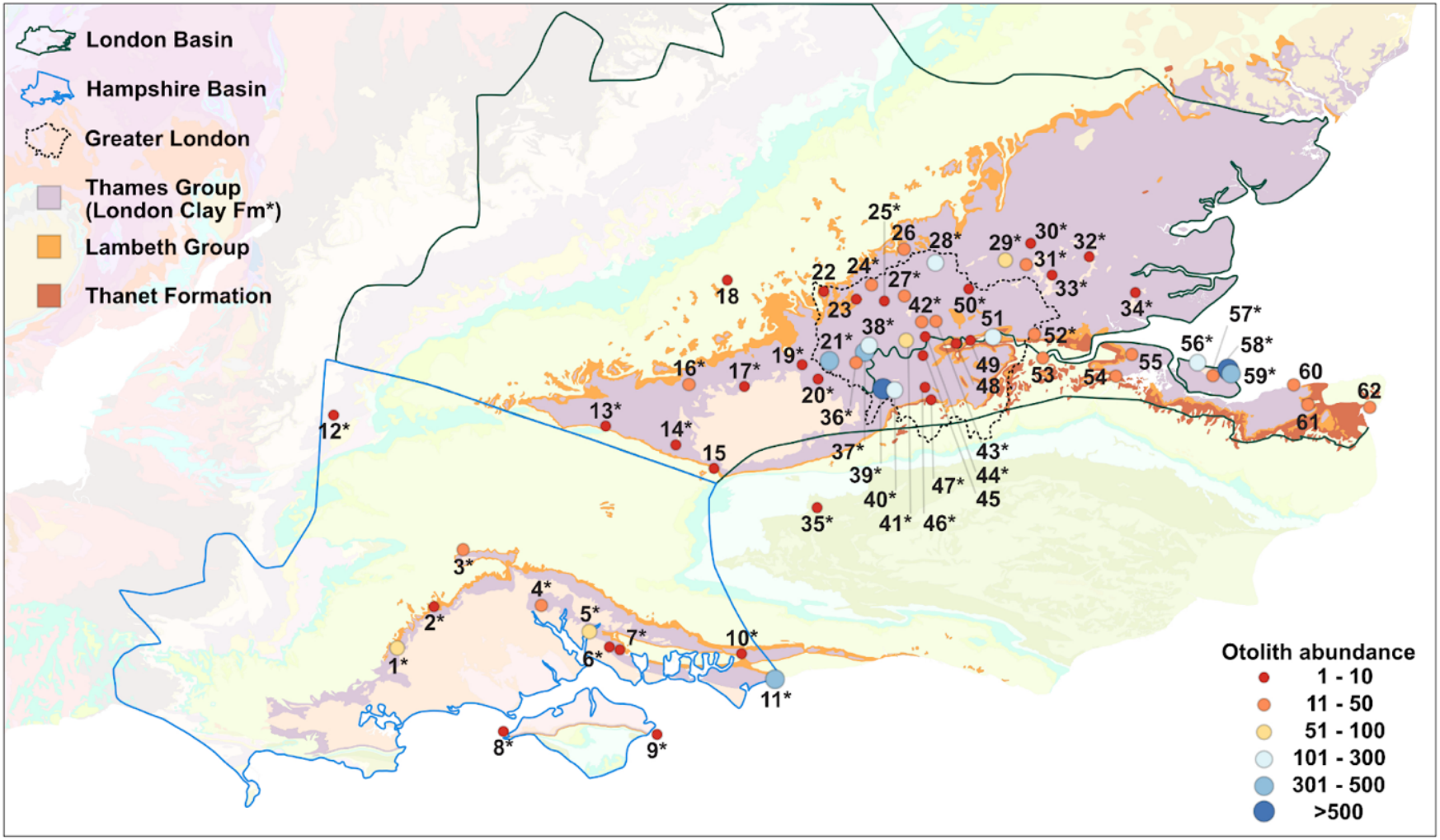
London Basin
Hampshire Basin
Greater London
Thames Group
(London Clay Fm*)
Lambeth Group
Thanet Formation
Otolith abundance
1 - 10
11 - 50
51 - 100
101 - 300
301 - 500
>500
Scale 1:1250000
0 10 20 30 40 50 60 70 80 90 100 km
Projection: British National Grid

Figure 3.6. *(Previous page)* Surface outcrop map of the UK, with three key early Paleogene units highlighted by darker shading (Thanet Formation, Lambeth Group (comprising Upnor, Reading and Woolwich Formations) and Thames Group (Harwich and London Clay Formations)) within the delineations of the London and Hampshire Basins. Otolith abundance is indicated for each sample location using a modified log scale. Geological base map data modified from the British Geological Survey (2022). Key to place names: Holt Wood (1), Sandleheath (2), Clarendon (3), Nursling (4), Lower Swanwick (5), Tichfield (6), Fareham (7), Alum Bay (8), Whitecliffe Bay (9), Chichester (10), Bognor Regis (11), Whaddon (12), Kingsclere (13), Newnham (14), Crondall (15), Shinfield (16), Bracknell (17), Wycombe (18), Wraysbury (19), Staines (20), Heathrow Airport (21), Harefield (22), North Harrow (23), Stanmore (24), Kingsbury (25), Potters Bar (26), Finchley (27), Enfield (28), M25 cutting (29), Ongar (30), Navestock (31), Stock (32), Shenfield (33), Rayleigh (34), Elmbridge (35), Whitton (36), Isleworth (37), Brentford (38), Tolworth (39), Worcester Park (40), Cromwell Road (41), Camden (42), Islington (43), Westminster (44), Clapham (45), Mitcham Common (46), Waddon (47), Greenwich (48), Maryon Park (49), Woodford (50), Abbey Wood (51), Thurrock (52), Swanscombe (53), Upnor (54), High Halstow (55), Minster on Isle of Sheppey (56), Eastchurch on Isle of Sheppey (57), Barrow Brook on Isle of Sheppey (58), Warden Point on Isle of Sheppey (59), Herne Bay (60), Chislet (61), Pegwell Bay (62). Asterisks on the map denote the presence of London Clay Formation at those sites.

3.4.2.3. Biases from collectors and donators

Of the 8,202 specimens in the collection, 4,343 (53%) have the contributor and/or acquisition date noted and are discussed here. The oldest specimens in the collection date from 1833, and were donated by Nathaniel T. Wetherell, with 260 additional specimens donated to the NHMUK by multiple individuals prior to a significant increase in collection and acquisitions from the 1930s onwards (Figure 3.7 a). Two distinct step-wise increases in the number of specimens in the collection (and species richness) occurred in 1930 to 1936 (primarily from William H. Webster, Arthur Wrigley and Alan G. Davis), and 1959 to 1961 (collectors Philip R. Gurr, S.H. Beatson, Alan G. Davis, Fred C. Stinton and Dennis Curry). There is a third much smaller step from 1973 onwards, largely attributed to Stinton, who donated multiple single specimens representing new species, these being holotypes (Figures 3.7 a, b). It is unclear if these steps represent augmented periods of sampling effort or bulk donations to the NHMUK. No early Paleogene samples have been catalogued (or acquired) by the museum since 1983.

Overall, there is a modest positive correlation between otolith abundance and species richness within the NHMUK collection (Figure 3.7 b). The majority of otolith donors to the museum contributed few specimens and thus relatively few species (under 100 otoliths and less than 10 species each). However, Davis was prolific, donating 1,483 individual specimens assigned to 44 species and he made repeated deposits of the same species (for example, *Selachophidum splendens*, *Gnathophis circularis*, *Ampheristus toliapicus* and *Neobythites obtusus*, ~19% of otoliths donated 1930 to 1936 and ~25% from 1959 to 1961), which introduces bias in the internal consistency of taxonomic designations. Also, of note is the high species richness (57)

of the otoliths donated by Stinton compared to the relatively low otolith abundance (198 specimens) due to a large number of single holotype specimens represented by an individual specimen, thus impacting diversity analyses (Stinton 1975-1983).

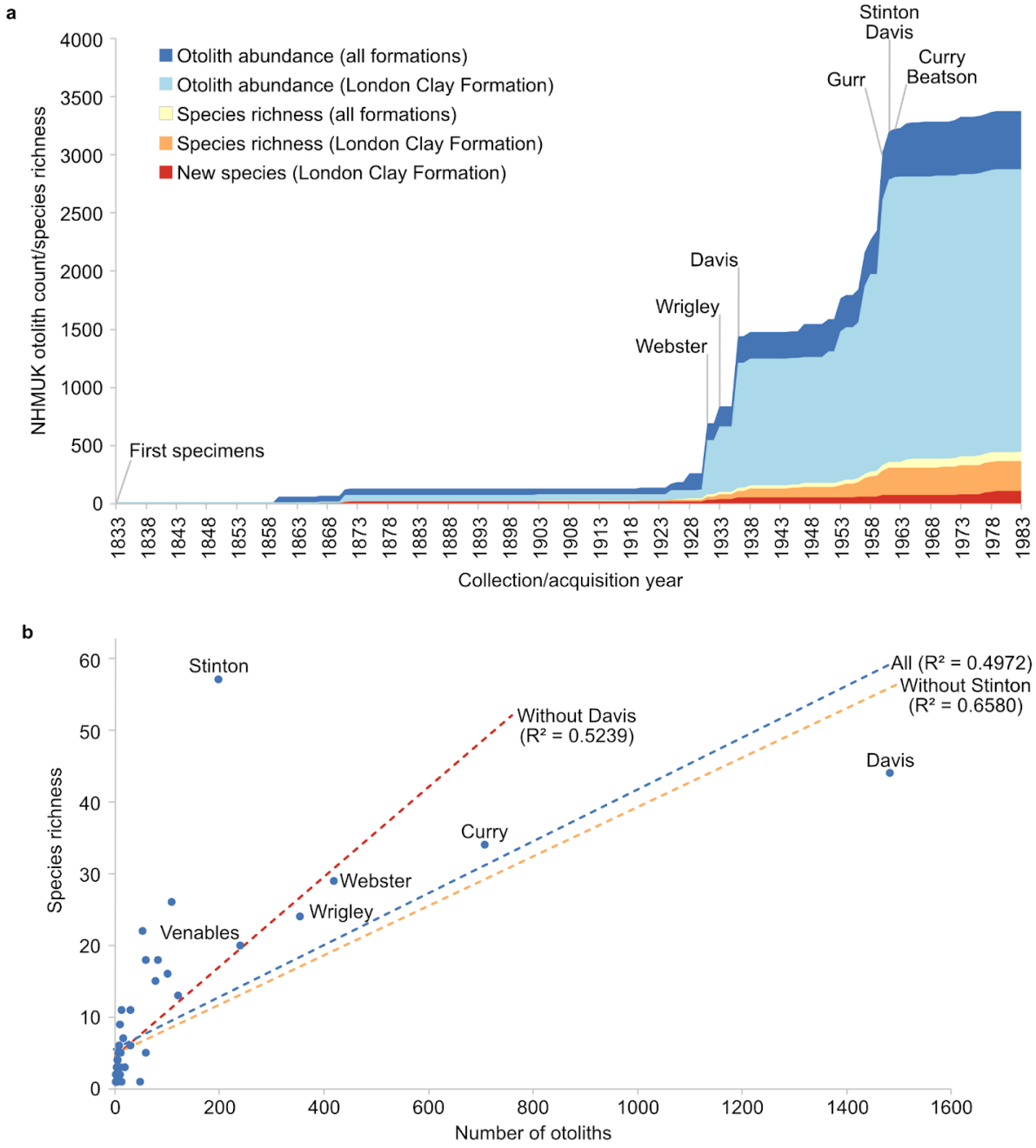

Figure 3.7. *(Continues overleaf)* NHMUK cumulative otolith counts and species richness throughout the acquisition period of 1833 to 1983 (**a**), plotted with the incidence of new otolith species occurring in all early Paleogene units (which

matches that of the London Clay Formation). Note only 3,368 otoliths were curated with date information and are included here. Multiple collectors contribute the same species and so it is counted each time, not purely for unique species. Prominent contributors are indicated. NHMUK early Paleogene otolith counts and species richness according to sample collector and/or contributor (**b**), with linear trendlines ('All' where all contributors are included, and 'Minus Stinton' and 'Minus Davis' where each of these two prolific contributors are removed due to elevated richness counts). Note the samples with an unknown collector/contributor are not included here.

3.5. Discussion

3.5.1. Early Eocene radiation or collection bias?

The NHMUK otolith collection provides a window into the diverse early Eocene actinopterygian palaeocommunity inhabiting UK waters. Though Ophidiiformes (cusk-eels) comprise almost half of the otolith population, 20 of the 64 families are rarer taxa, highlighting significant diversity, even if less dominant in ecospace. This includes genera expanding their known extant latitudinal ranges, such as *Mene*, today a tropical and sub-tropical Indo-Pacific taxa also found in PETM deposits in Denmark (Bonde, 1997) and South America (Friedman and Johnson, 2005).

Whilst there does superficially appear to be a radiation of taxa between the UK-based Palaeocene and early Eocene units (Figure 3.3), coinciding with the hypothesis of increased diversity in response to warmer oceans with poleward migration of tropical species (Bonde, 1997; Friedman and Johnson, 2005; El-Sayed *et al*., 2021), it is difficult to discern if this is a true evolutionary change or merely an artefact of sampling bias given the relative paucity of otoliths obtained from the

preceding strata. Records of Osteichthyes (bony fish) within the PBDB (2024) reveal two UK Palaeocene occurrences and 348 for the Ypresian (early Eocene), globally this rises to 23,935 occurrences across both the Palaeocene and Ypresian. Of these, only two otolith species (*Apogon glaber* and *Ampheristus toliapicus*) appear alongside the PBDB (2024) teeth and skeletal records. Though there is high diversity at species level, and inclusion of some rarer taxa in the NHMUK dataset, patterns of teleost diversity suggested by Schwarzhans *et al.* (2018) contest this warmer ocean diversification paradigm and do not indicate a significant radiation in the early Eocene, moreso a progressive increase in the emergence of Recent taxa from the Cretaceous-Paleogene boundary. This concurs with work by Sibert *et al.* (2018) that suggests open ocean radiation in bony fish subsided by the early Eocene, hence the NHMUK collection is likely highly impacted by sampling bias rather than a true reflection of radiation.

Not all fish present during the early Eocene will be preserved and collected, so the NHMUK collection (as with any collection) offers only a snapshot of the total taxonomic diversity present at the time. Additionally, there are considerable discrepancies between the otolith and skeletal faunas of the London Clay Formation, with few taxa clearly shared between them (only *Ampheristus toliapicus* is a common species between the NHMUK otoliths and body fossil record; Friedman *et al*., 2015). The most abundant skeletal fossil groups in the London Clay Formation, mackerels and their relatives, have very small, delicate otoliths that have low taphonomic potential (Friedman, 2022), hence the two palaeontological records must be used collaboratively in order to generate holistic palaeocommunity reconstructions, rather than relying on one fossil type alone. Otoliths are particularly valuable as they

provide a higher resolution record of community dynamics than comparatively rarer skeletal remains. Whilst biases are evident within the NHMUK database, it does still both confirm and supplement previous palaeocommunity reconstructions of the early Paleogene actinopterygians in the UK.

3.5.2. Challenges with the NHMUK collection

The paucity of information (particularly high-resolution lithostratigraphic information on beds and divisions) available for many of the donated specimens presents clear challenges when trying to reconstruct the evolution of communities through time. This highlights the need for more rigorous sampling and collection processes, and emphasises collecting as much information as possible upon sample acquisition.

3.5.2.1. Geological bias

The amount of rock available for sampling, including unit thickness, outcrop and exposure area, can impact otolith abundance in collections. Unit thickness can vary across the length of strata, with thicker areas providing a greater volume of material from which fossils can be sampled, linking to basin structure and sedimentation rates (the longer the deposition interval, the greater the recorded diversity; Smith and McGowan, 2011). In this dataset, there initially seems an obvious link between unit thickness and otolith abundance (Table 3.1) with the Harwich Formation having six times smaller unit thickness than the London Clay Formation and approximately the same degree fewer otoliths. However, the Harwich and Woolwich Formations have comparatively similar unit thickness but vastly different otolith abundances and

species richness, so clearly there are other factors at play, such as the exposure in cross-section or outcrops from which sampling can occur.

Rock outcrop refers to the material exposed at the surface according to mapping, whereas exposure area is the actual surface material available for sampling. Outcrop exposure is affected by proximity to the coast, elevation, bedrock age, lithology and land use (including urbanisation; Dunhill, 2012). The synclinal structure of the London and Hampshire Basins means the dip of the strata has impacted outcrop, particularly resulting from erosion coincident with the Mid-Lambeth Group Hiatus. The London Basin has lower dip with erosion of overlying younger Tertiary deposits exposing a greater area of London Clay Formation at the surface, whilst the Hampshire Basin strata have steeper dip and the London Clay Formation is expressed across a much narrower area, typically less than 3 km wide (Figure 3.6; King, 1981). Oftentimes, stratigraphic sequences may only be exposed through transient means, such as boreholes, road and railway cuttings, or eroding cliff sections. Many of the NHMUK otoliths can be traced to one of these scenarios, and much of the collection follows road infrastructure in Greater London and Isle of Sheppey cliffs, which is not optimal for diverse geological sampling.

3.5.2.2. Taphonomic bias

Rock preservation potential affects whether an organism will be available for sampling, impacted by the rate of burial, early diagenetic mineralisation and subsequent erosion or deformation processes. Smaller grain size, such as the clay-silts of the London Clay Formation, are conducive to high-level preservation and indeed the unit is considered a Konservat Lagerstätte with three-dimensional

preservation of skeletal remains and microfossils (Friedman *et al.*, 2015). The different preservation potentials of microfossils and skeletons captures a more comprehensive palaeocommunity when combined, but leads to underestimates if each is taken individually.

An additional consideration when interpreting diversity is that bioturbation can impact the stratigraphic resolution by mixing between units, and the excreta or gut contents from these burrowing organisms could create 'false' taphocoenoses (assemblages of dead organisms). Bioturbation, especially *Chondrites* burrows, is common within the London Clay Formation, homogenising the divisions (King, 1981). However, given the burrows have millimetre to centimetre scales and individual division thicknesses are greater than 20 m (Table 3.1) it is unlikely to have a significant impact on sampling within the NHMUK dataset. Furthermore, chemical erosion of delicate carbonate otoliths within clay-rich sediments up to a depth of 3 m could affect the yield from London Clay divisions (King, 1981).

3.5.2.3. Anthropogenic bias

Rock outcrop is a primary driver for sampling effort, as collectors gravitate towards more accessible areas, with a preference for urban locations where road and rail cuttings or boreholes predominate, as well as cliff exposures as they are eroded, compared to rural locations. This may also be linked to the "Bonanza Effect" (Dunhill *et al.*, 2012) in which scientists naturally gravitate towards localities which are known to be fossil-bearing, such as Lagerstätten, rather than seeking new locations that are unknown or not well-studied. For the NHMUK collection, Davis' prolific contribution of London Clay Formation material was sampled from Greater London and the Isle of

Sheppey, coinciding with significant skeletal material finds (Friedman *et al*., 2015). Both of these locations are in the London Basin, but there is outcrop further to the northeast and southwest of the study region which remains largely unsampled and could be affected by accessibility constraints (Figure 3.6).

A collector's preferred area of study can bias which fossils pique interest whilst out in the field, and those which are better preserved are likely to be kept in preference to more fragmentary or deformed material; indeed, most of the NHMUK otoliths are complete. Additionally, there may be enhanced research effort linked to novelty bias (Close *et al.*, 2018) in which the discovery and publication of new taxa is prioritised over those existing, such as Stinton predominantly donating singular occurrences of holotypes to the NHMUK. In this regard, museums may only keep the most interesting fossils that are donated to them due to collection space constraints. Consequently, community ecology metrics such as dominance and evenness are not appropriate to use on NHMUK otoliths as they cannot be a true reflection of diversity on a biased dataset.

Otoliths are susceptible to erosion (they are not commonly found in sediments from very deep water for instance, and certainly not below the calcium carbonate compensation depth; Gauldie *et al.*, 1991) and many previously described otolith-based species have been subsequently rejected due to the waterworn nature of key taxonomic structures (Nolf, 1985, 2013; Schwarzhans, 1993). Juvenile otoliths also have less prominent characteristics to aid taxonomic identification, whilst in older fish growth rates of annuli (annual concentric growth rings of calcium carbonate and organic matter) decline and ornamentation is less prominent. Moreover, intraspecific

variability between otoliths due to genetics, growth rate, feeding history and habitat can lead to generating new species designations based upon slight differences that causes oversplitting of the taxonomy. Historically, naming new species was encouraged to enhance prominence of researchers in the field of vertebrate palaeontology too. Illustrations of otoliths provided in earlier literature (such as Frost, 1925, 1933, 1934; Stinton 1975-1983) often lack sufficient detail to support taxonomic verifications of primary data, especially when significant portions of the holotypes or reference material are not available. Therefore, the challenge of the historical age of the NHMUK collection is clear with previously less robust cataloguing of otolith data and no new additions to the collection since 1983, posing issues for updating taxonomic and stratigraphic information to a modern standard.

3.5.3. Bias mitigation strategies

Natural history collections are clearly a valuable but underutilised resource for evolutionary biological and ecological research. For instance, Marshall *et al.* (2018) investigated fossil marine invertebrate collections in museums from three American states (California, Oregon and Washington) compared to their counterparts in published literature and the PBDB, finding 23 times more spatial data in the collections than is available in online repositories for the benefit of other scientists to use. Though a small study, it highlights a much wider and well-known issue regarding the dearth of museum collection data that is openly accessible. Even in the UK's largest public natural history collection at the NHMUK, less than 1% of their 80 million total specimens are on public display and only ~4.9 million have been digitised (approximately 6% of the total) and are searchable online (Popov *et al.*, 2021).

Providing specimens are archived to museums with sufficient associated data, they can act as custodians of bulk samples for biological diversity, though there are of course inherent spatial and economic restrictions. Maintaining diligent records of curated material, rather than ‘cherry-picking’ the best due to storage constraints helps alleviate some of the ‘novelty bias’ that is already present in the initial collection of samples. Whilst geological and taphonomic factors do impact otolith preservation and sampling unit availability, this dataset is an exemplar of how the biases resulting from anthropogenic sampling efforts and curation decisions can impede palaeocommunity reconstructions, thus a summary of biases to consider when archiving metadata and using museum collections is outlined in Figure 3.8. Many of these suggestions are primarily useful for new samples rather than retrospectively altering museum collections, but current curatorial decisions may benefit.

Ideally, when objects are accessioned, all metadata related to the specimen should be transcribed on specimen labels to avoid dissociation (such as taxonomic designations with citations of where names have originated so changes can be traced through time, georeferencing information that permits supplementary site visits, stratigraphic details to the highest resolution and literature citations). Two-dimensional or three-dimensional images and scans should be associated with records to enable workers from around the world to test taxonomic and/or biometric concepts without visiting the museum. Additionally, where possible, bulk samples including matrix should be taken and archived along with the specimens to allow for true community ecological reconstructions that are not biased by the ‘cherry-picking’ effects of taxonomists looking for the next new species. Any microscopy or computed tomography, geochemical and/or molecular analyses that are conducted on

specimens should also be included in the records associated with the original object, catalogued and accessible as open data (Popov *et al.*, 2021). Further to this, while producing digital databases is resource intensive, collaborating with other museums to create national and global databases, such as Scientific Collections International (www.scicoll.org), can lead to prosperous knowledge sharing and scientific rigour.

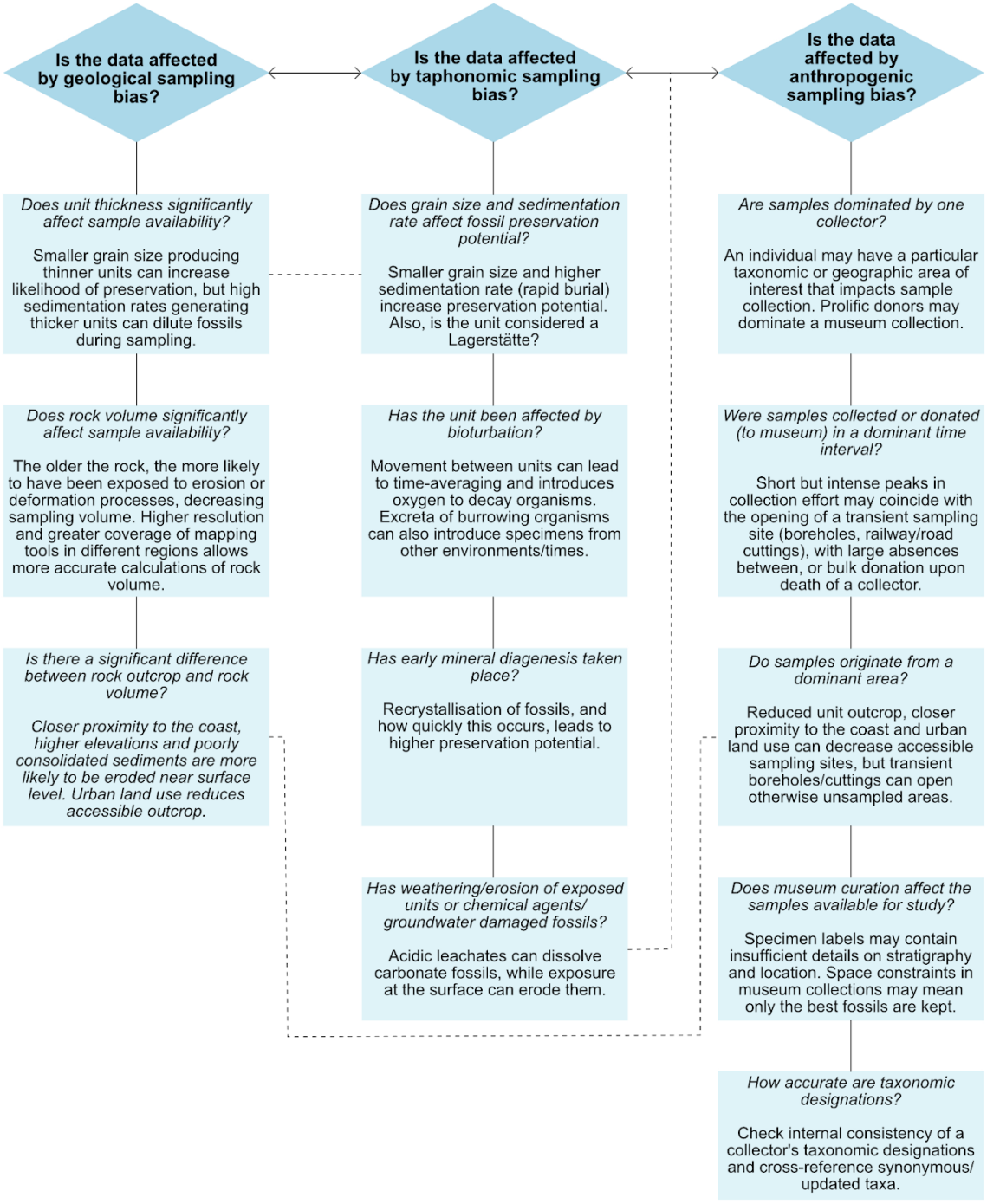

Figure 3.8. *(Previous page)* Flowchart indicating geologic, taphonomic and anthropogenic factors biasing sample collection and acquisition into museums, highlighting potential impacts of recording insufficient data for natural history collections. Solid lines indicate linked concepts within each geological, taphonomic and anthropogenic grouping, whilst dashed lines link sampling considerations across groupings to highlight their interconnected nature.

3.6. Chapter conclusions

Museum collections are a valuable resource for understanding past life. Here, an attempt has been made to establish changes in an early Paleogene actinopterygian palaeocommunity solely from the NHMUK otolith archives, finding that the nature of the collection provides a number of significant barriers to accurate reconstruction of the palaeocommunity despite the large number of specimens (over 8,200). However, when considering the sampling and acquisition period (1833 to 1983), prominent donators of early Paleogene otoliths (from the 43 collectors) and sampling localities for surface outcrop across the south of England (dominantly Greater London and the Isle of Sheppey), it is possible to assess the patterns within the context of the collection. Superficially there appears to be a distinct radiation of actinopterygians across the Palaeocene-Eocene boundary, with just six species in the late Palaeocene and 158 species in the early Eocene. Yet, this research highlights how geological, taphonomic and anthropogenic biases significantly impact the NHMUK collection and therefore palaeocommunity and macroevolutionary reconstructions to suggest that this is a true post-Palaeocene diversification of fish.

Whilst a workflow practice for assessing biases has been suggested for use in future collection practices, further work on the Palaeocene units of the UK in particular is necessary to verify if there is a true radiation into the Eocene or not. This requires additional sampling of Palaeocene units within the UK, concentrating on the southeast of the London Basin. Additionally, whilst a time-intensive process, compilation of a single updated synonymised taxonomy for all known otoliths as a complete reference for future fieldwork sampling would be invaluable to cross-reference globally between historical and modern specimens.

Museum collections must be made more readily accessible for wider study, such as via contribution to online databases to enable their preservation with less handling and avoid the necessity for individual research visits to institutions and replicated synthetic work. Though a daunting task to enable open collection availability, the potential to understand Earth's past, particularly responses to periods of climate change, make it a worthwhile endeavour.

CHAPTER FOUR

Actinopterygian and chondrichthyan productivity, community structure and evolutionary patterns across the early Cenozoic of the Mentelle Basin, Australia (IODP Site U1514)

4.1. Chapter introduction

With fish (ray-finned actinopterygians) forming approximately half of modern vertebrate diversity and being a major component of complex food chains throughout the water column, they are considered an indicator of overall ocean health with enhanced productivity encouraging marine life to proliferate (Maureaud *et al.*, 2017). Fish are also a significant protein source for the world's population (Boyd *et al.*, 2022), making investigating the impact of climate change on their communities an important issue now and in the future. Ecosystem modelling suggests modern fish and shark (cartilaginous chondrichthyans) productivity will significantly shift in decades to come as climate changes, though there is considerable uncertainty in projections with suggestions of both increases and decreases in fish abundance (for example, Heneghan *et al.*, 2021; Tittensor *et al*., 2021). Given this unpredictability, studying fish and shark community turnover and productivity during climate warming in the geological past may help to inform their future responses under similar conditions.

The early Cenozoic offers a particularly important window to explore fish and shark palaeocommunities at carbon dioxide levels and temperatures akin to modern and future predictions. Early Paleogene (~48 to 66 Ma) atmospheric carbon dioxide (pCO_2) reached ~1,500 parts per million (ppm; Rae *et al.*, 2021) and an average

temperature increase of 3.1 to 4.5 °C per doubling of CO_2. This is approximate to 2100 CO_2 worst-case unmitigated emissions projections for Representative Concentration Pathway 8.5 of over 1,000 ppm and 1.5 to 4.5 °C temperature rise per doubling of CO_2 (IPCC, 2022; Inglis *et al.*, 2020). The period was punctuated by a series of global warming events of differing durations, rates and magnitudes of environmental change known as hyperthermals; these are generally defined by a duration of 100 kyr to 2 Myr, a carbon isotope excursion of less than 4 ‰, a doubling of pCO_2 levels, depleted ocean oxygenation, increased ocean acidification of 0.3 to 0.4 pH units, plus intensified hydrological cycles and continental weathering (Foster *et al.*, 2018). The environmental change during the early Paleogene was driven by enhanced North Atlantic igneous province volcanism, silicate weathering (Scheibner and Speijer, 2008; Gutjahr *et al.*, 2017; Jones *et al.*, 2019; van der Boon *et al.*, 2021) and/or 100-kyr and 405-kyr eccentricity cycles triggering release of isotopically light carbon from readily replenished surface reservoirs of the atmosphere, oceans and biosphere (for example, Cramer *et al.*, 2003; Westerhold and Röhl, 2013; Kirtland Turner *et al.*, 2014; Westerhold *et al.*, 2018). Notable warming events include the Palaeocene-Eocene Thermal Maximum (PETM, ~56 Ma, lasting ~200 kyr; Aziz *et al.*, 2008; Murphy *et al.*, 2010), Early Eocene Climatic Optimum (EECO, ~49 to 53 Ma; Vahlenkamp *et al.*, 2020) and Middle Eocene Climatic Optimum (MECO, ~40 Ma, lasting ~400 to 700 kyr; Bohaty *et al.*, 2009). The EECO extended period of global warming was interspersed by a number of short-lived (shorter than 200 kyr) hyperthermal episodes attributed to longer-term eccentricity cycles (Westerhold *et al.*, 2020).

The Palaeocene-Eocene boundary is marked by a negative carbon isotope excursion of 2 to 4 ‰ (McInerney and Wing, 2011) with the injection of isotopically light carbon into the atmosphere and oceans and widespread dissolution of calcium carbonate sediments. The absence of continental-scale ice sheets at the poles created a prominent sustained pole to equator thermal gradient of 13.3 °C (Eichenseer and Jones, 2024), experiencing sea surface temperatures 3 to 8 °C above modern in the tropics (Evans *et al.*, 2018) and 10 to 23 °C greater at high latitudes (Cramwinckel *et al.*, 2018), with bottom water temperatures of 14 °C, ~10 °C higher than mean modern deep ocean (Zachos *et al.*, 2001). Through the EECO, global mean surface and bottom water ocean temperatures were ~4 to 5 °C cooler than the PETM and there was an overall positive carbon isotope excursion of ~0.75 ‰ across the EECO, punctuated by a series of negative excursions at ~0.25 to 0.5 ‰ (Inglis *et al.*, 2020; Vahlenkamp *et al.*, 2020). The latitudinal temperature gradient was smaller during the EECO at ~9 °C (Eichenseer and Jones, 2024). Temperature decline following the EECO was disturbed by the ~500-kyr MECO event, when a characteristic negative carbon isotope excursion of ~0.5 to 1 ‰ (Bohaty *et al.*, 2009) coincides with bottom water temperature increases of 3 to 6 °C (Bijl *et al.*, 2010). Post-MECO cooling through the remainder of the Eocene led into the icehouse world of the Oligocene from ~34 Ma (Westerhold *et al.*, 2020).

Environmental change during the Eocene warming events, particularly the PETM, EECO and MECO for which most data are available as the largest of the events, had a profound impact on marine biota. This included diversification in planktonic microorganisms versus up to 50% extinction of benthic counterparts, notably foraminifera (Speijer *et al.*, 2012; Arreguín-Rodríguez *et al.*, 2022), and a ‘reef gap’

where architectural corals and their vertebrate communities were replaced by algal blooms (Norris *et al.*, 2013). Consequently, there were important implications for lower levels of the trophic system, ultimately feeding into 'pelagification' of the wider marine food web productivity (such as increased abundance of pelagic fish and reduction in demersal bottom-dwelling fish; Petrik *et al.*, 2020). The effect of temperature on primary productivity is widely debated, with some proponents for warmer surface oceans enhancing primary productivity (Savian *et al.*, 2014), leading to greater export and more efficient recycling of nutrients through the stratified ocean for consumers, such as fish and sharks (John *et al.*, 2013). However, cooler temperatures have also been found to have a net positive impact on primary productivity, particularly regions associated with monsoon seasons driven by nutrient upwelling (Dalpadado *et al.*, 2021), whilst others suggest enhanced ocean stratification may prevent loss of surface nutrients to subsurface layers and encourage algal blooms (Roxy *et al.*, 2015). The uniformity of these patterns from the surface to seafloor, as well as spatially within and across ocean basins, is less well-constrained.

In terms of marine vertebrates, open ocean fish and shark abundance and diversity increased steadily through the early Paleogene, with diversity peaking before the EECO and abundance during the EECO in both groups (Sibert and Norris, 2015; Sibert *et al.*, 2018; Britten and Sibert, 2020). Of current known deep sea ichthyolith (calcium phosphate bony fish teeth and shark denticles shed by organisms or delivered to the seafloor via faecal matter) community structure studies of the Palaeocene to middle Eocene (Sibert *et al.*, 2014; Sibert and Norris, 2015; Sibert *et al.*, 2016; Sibert *et al.*, 2018; Britten and Sibert, 2020), peak tooth accumulation

occurred during the EECO of the South Pacific Ocean, with over five times more than in the Palaeocene (Sibert *et al.*, 2018). Rapid diversification in the Palaeocene has been linked to the radiation of species into newly-formed ecological niches following the end-Cretaceous mass extinction (Sibert, 2016; Sibert *et al.*, 2018; Britten and Sibert, 2020). Indeed, for the Pacific Ocean, Sibert *et al.* (2018) identified a ten-fold increase in subtropical ichthyolith abundance from the Palaeocene to the early Eocene, but little tooth morphotype diversification that may indicate species diversity increasing beyond the Palaeocene. This may be a case of reduced tooth morphotype diversity, and therefore fish species, origination as a result of ecological niche saturation in the 'immediate' aftermath of the end-Cretaceous mass extinction.

Investigation of fish and shark productivity and diversity through geological history is facilitated by isolating ichthyoliths from deep sea sediments, generating a high-resolution, dissolution-resistant proxy for population change across a breadth of environments (and sediment types), preserving in greater frequency, abundance (tens to hundreds in a few grams of sediment) and completeness than body fossils (Friedman, 2022b). Further, key changes in distinctive ichthyolith features allows designation of morphogroups, whose composition can be indicative of taxonomic shifts in the marine vertebrate community.

In this study, I investigate bony fish and shark abundance and biodiversity dynamics in the context of oceanographic and climate changes during hyperthermal and longer-term warming events across the Palaeocene to middle Eocene (39.12 to 61.80 Ma). This is based upon ichthyolith abundance and morphotype composition, reconstructed from samples obtained from the Indian Ocean, generating the first

tooth morphotype record from this ocean basin. Ichthyoliths were isolated from sediment cores obtained from International Ocean Discovery Programme (IODP) Site U1514 in the Mentelle Basin, offshore western Australia. This is an oceanographically sensitive site that was situated at a high palaeolatitude of ~60 °S during the early Eocene (Huber *et al.*, 2019), with the Indian Ocean facing a pronounced temperature increase of ~4 to 5 °C at all water depths across the early Paleogene (Barnet *et al.*, 2020). The carbonate-rich (mean 63.8%; Huber *et al.*, 2019) Mentelle Basin is important for early Cenozoic studies, and thus for ichthyolith research, given widespread shallowing of the carbonate compensation depth (CCD; Pälike *et al.*, 2012), as it allows co-production of high-resolution records of environment, sediment and biology. Furthermore, Earth was undergoing a shift in global and Southern Ocean circulation patterns as India rifted from Australia and the initial stages of Tasman Gateway opening began ~48 to 49 Ma, permitting the throughflow of surface waters from the Pacific to Indian Oceans (Bijl *et al.*, 2013; Huber *et al.*, 2019). As such, the movement of warm surface currents, changes in deep water formation and upwelling of nutrient-rich masses are important considerations affecting the local marine climate of the Mentelle Basin during the early Cenozoic.

4.2. Methods

4.2.1. Sampling site

Site U1514 (33°7.2327’S, 113°5.4672’E; Huber *et al.*, 2019; Figure 4.1) is the northernmost of five sites across the Mentelle Basin and Great Australian Bight (modern maximum water depth of 3,850 m) cored during IODP Expedition 369 in the

southeast Indian Ocean in 2017 (Hobbs *et al.*, 2019). The Mentelle Basin forms part of a succession of en echelon basins off the west coast of Australia, between the mainland and Naturaliste Plateau, produced through the rifting of India from Australia during the breakup of the supercontinent Gondwana. With a palaeolatitude of ~60 °S at 50 Ma (Huber *et al*., 2019), Site U1514 provides an opportunity to study large-scale ocean circulation patterns stemming from the initial phases of Tasman Gateway opening through the Late Cretaceous and Cenozoic and associated biotic changes.

Site U1514 yielded three lithological units spanning ~515 m, aged from Pleistocene to Albian (Cretaceous; Huber *et al*., 2019). This included ~81 m of nannofossil and foraminiferal ooze forming sequences dated Pleistocene to Eocene, ~308 m of interbedded nannofossil oozes, clays, clayey chalks and claystones with occasional chert nodules through the Eocene and Palaeocene, and ~126 m of claystones from the Palaeocene through to Albian, with an overall core recovery of 87.5% (Huber *et al*., 2019). Two cored holes, A and C, overlap during the Eocene, creating a ~50 m continuous sedimentary record.

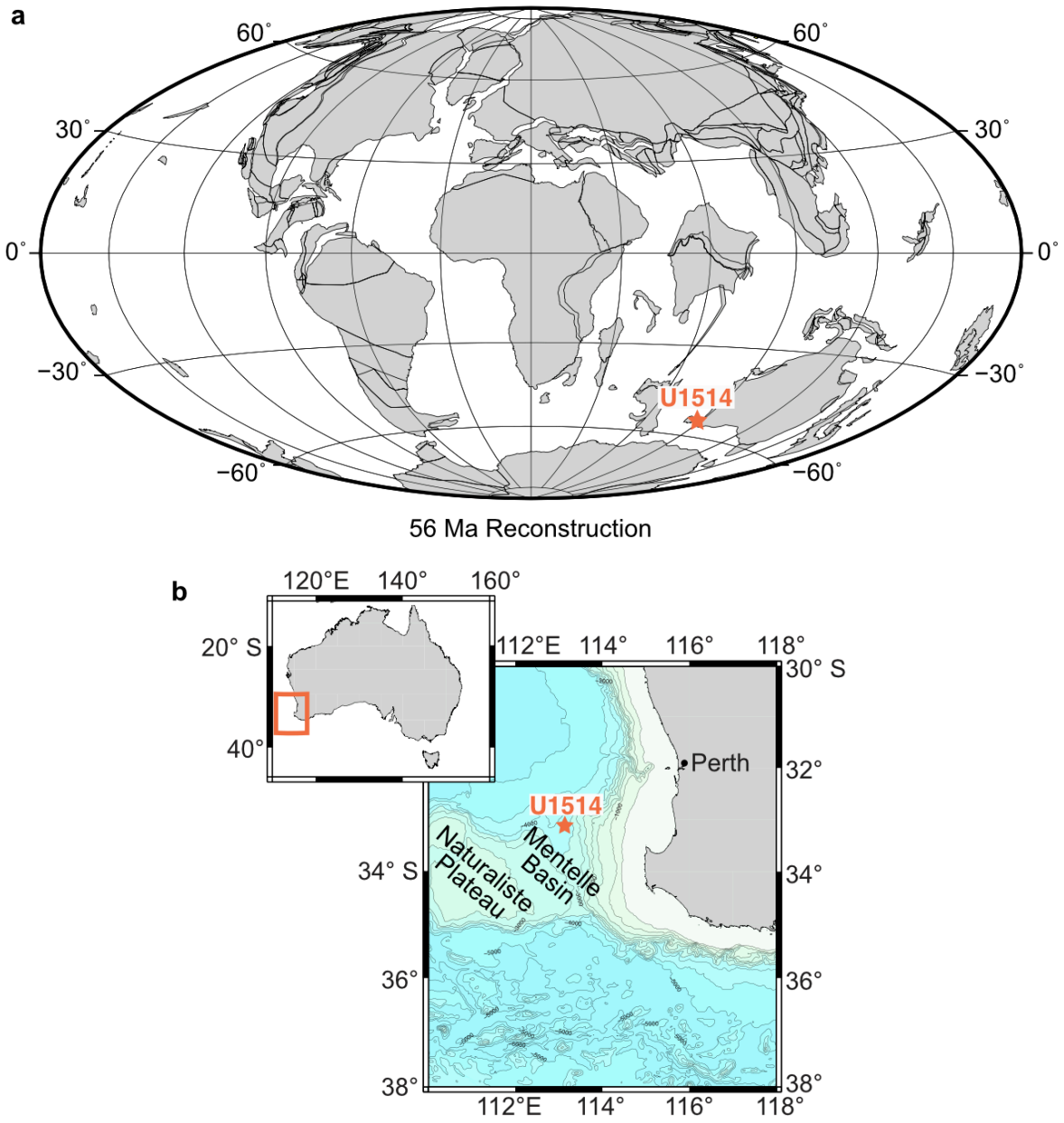

Figure 4.1. Palaeogeographic reconstruction of the Palaeocene-Eocene boundary at 56 Ma (**a**) from the Ocean Drilling Stratigraphic Network (www.odsn.de; Hay *et al.*, 1999) with the orange star marking the location of the study site, U1514. Modern map of Australia and the location of Site U1514 within the Mentelle Basin (**b**; modified from Huber *et al.*, 2019).

4.2.2. Age model

The Site U1514 age model (Figure 4.2, Appendix Table 4.1) uses tie points across holes A and C, with core depth below sea floor (CSF-A) converted to core composite depth below seafloor (CCSF) according to Vahlenkamp *et al*. (2020). The age model was built primarily using astrochronology from shipboard splice refinement in Vahlenkamp *et al*. (2020) covering 142.21 m to 284.21 m CCSF (corresponding to 39.433 to 56.231 Ma), with magnetostratigraphy providing age control either side of this interval to 0.781 Ma (7.99 m CCSF) and 62.221 Ma (368.03 m CCSF; Huber *et al.*, 2019). Across the PETM (278.98 to 280.36 m CCSF), key tie points from the benthic foraminifera carbon isotope data (Boggust, 2022) were used instead of the astronomically-tuned calcium-iron ratios of Vahlenkamp *et al*. (2020) as the latter are offset from the carbon isotope ($\delta^{13}C$) minimum used to identify the PETM. Therefore, the PETM onset and peak through recovery are defined as 55.829 to 55.996 Ma (Röhl *et al.*, 2007; Boggust, 2022).

Hyperthermal events follow the alphabetic system in Hollis *et al.* (2019), and the EECO is defined as beginning at the J event (Chron C24n.2rH1) and ending with the carbon isotope excursion at Chron C22nH5. Site-specific event ages define the PETM at U1514 as 55.87 ± 0.06 Ma, whilst the EECO begins at 53.22 Ma (Vahlenkamp *et al*., 2020). The end of the EECO is not well-constrained at U1514 (Vahlenkamp *et al*., 2020) but is taken to be 49.14 Ma, based upon the beginning of a cooling trend observed in composite carbon and oxygen stable isotope records from Ocean Drilling Project (ODP) Sites 1209, 1258, 1262 and 1263 (Hollis *et al.*, 2019), meaning the warming event lasted 4.12 million years. Site-specific tuning of the MECO was not possible due to the incompleteness of the biostratigraphic and

magnetostratigraphic frameworks covering the interval at this site (Vahlenkamp *et al.*, 2020) and inconsistencies with the precise dating of the MECO globally (Westerhold *et al.*, 2013, 2015; Boulila *et al.*, 2018). However, comparison of the U1514 calcium-iron records with those of ODP Site 1260 (Vahlenkamp *et al.*, 2020) permits pattern correlation that defines the MECO as 40.06 to 40.52 Ma.

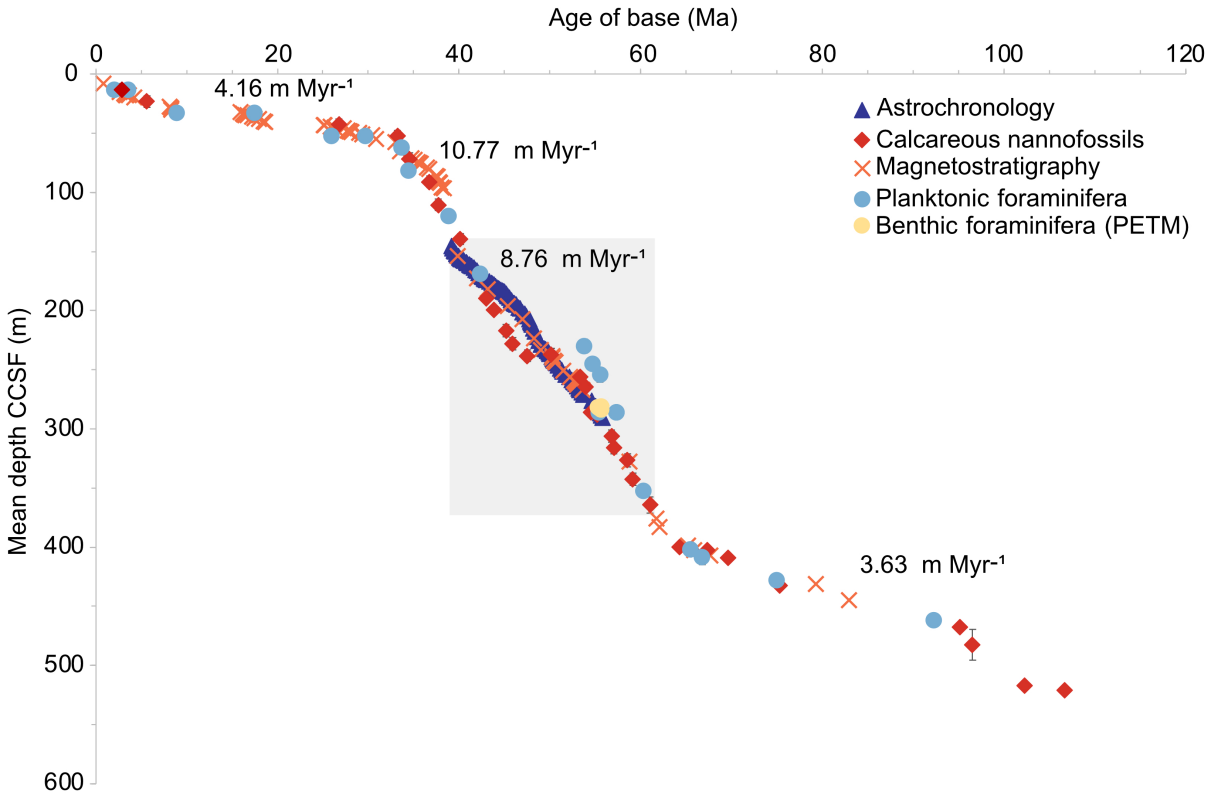

Figure 4.2. Age-depth model and sedimentation rates for Site U1514 based upon astrochronology, magnetostratigraphy, calcareous nannofossils and planktonic foraminifera datums (Huber *et al.*, 2019; Vahlenkamp *et al.*, 2020) correlated to the Geologic Time Scale 2012 (Gradstein *et al.*, 2012). Note that only astrochronology and magnetostratigraphy are employed in this study. Grey shaded box indicates the time and depth interval of this study.

4.2.3. Sample selection and preparation

Post-expedition, 28 ~10 to 20 cc samples were taken at ~7 m (equating to 500 kyrs) intervals spanning the middle Palaeocene to middle Eocene (39.12 to 61.80 Ma). All samples were processed in the sediment preparation lab at the School of Geography, Earth and Environmental Sciences at the University of Birmingham, UK. Ichthyoliths were isolated from bulk sediment samples via dissolution of carbonate components in 10% acetic acid solution (following Sibert *et al.*, 2017), and Calgon (sodium hexametaphosphate) detergent solution where appropriate, and thoroughly washed with deionised water (full methods in section 2.2.1). Subsequently, the residue was treated with LST FastFloat heavy liquid (sodium heteropolytungstates dissolved in water, with a density of 2.80 g mL^{-1}) to separate the ichthyoliths from the remaining siliceous sediment residue based upon density differences (bioapatite ichthyoliths having a density of ~3.1 g cm^{-3}, compared to siliceous material having a density of 2.3 to 2.6 g cm^{-3}), and then dried at 30 °C overnight before being transferred to glass vials. Ichthyolith residues were picked under a stereolight microscope in two sieve size fractions (38 to 63 μm and 63 to 250 μm) and mounted on slides using water soluble Pritt glue for imaging via Leica M205 C microscope with Image-Pro Premier software Version 9.3.1. Ichthyolith images are available via the University of Birmingham's eData repository *titled "Bird, Hannah (2024) Research data supporting PhD thesis 'Actinopterygian and chondrichthyan palaeocommunity responses to early Cenozoic global warming'"* (DOI: 10.25500/edata.bham.00001169). Subsequently, the number of teeth and denticles present in each sample and size fraction were recorded (Appendix Table 4.2).

For comparison with the response to the longer-term EECO warming event, additional high-resolution ichthyolith data was included from three undergraduate student dissertations spanning early Paleogene hyperthermal events at Site U1514 to assess the impact of relatively more rapid global warming on communities (~100 to 200 kyrs versus ~4 Myrs). These data are included here, without further independent verification by the author; PETM data was combined for Haf Nawsath and Lily Goddard, whilst the R and S events data that fall within the EECO was supplied by Zulaikha Sukerdi (Appendix Table 4.3). It is noteworthy that these hyperthermal samples used pre-existing material that had been processed for foraminiferal work and only ichthyoliths from the greater than 63 μm size fraction were available for study. Consequently, they are not included in all of the subsequent analyses as they are not fully comparable when the long-term dataset includes all ichthyoliths over 38 μm, and some processing data was missing (such as bulk density data for the R and S events samples, which prevents assessment of ichthyolith accumulation rates).

4.2.4. Stable carbon and oxygen isotopes

To place ichthyolith abundance and diversity in context of global climate patterns, marine isotopic data was used to infer changes in temperature. Global stable carbon and oxygen isotope data from benthic foraminifera were obtained from the composite record of Westerhold *et al.* (2020) for the Palaeocene to middle Eocene record (herein referred to as the “long-term dataset”), whilst low resolution (~25 to 30 kyrs resolution) site-specific isotopes from bulk carbonates were sourced from Edgar *et al.* (2022). PETM benthic foraminifera carbon and oxygen isotopes were supplied by Boggust (2022) as measured on Site U1514 samples.

4.2.5. X-ray fluorescence data

X-ray fluorescence (XRF) scanning of cores provides a continuous and non-destructive record of sediment chemistry that can be used as palaeoenvironmental proxies for the entire study interval. Whilst a suite of elements were measured, this study focuses on calcium (Ca), barium (Ba) and silica (Si) as known proxies for marine dissolution events and terrigenous versus biological productivity. Site U1514 XRF information was sourced from the IODP LIMS database (IODP Joides Resolution Science Operator, 2018; Hobbs *et al*., 2019) as provided by the Expedition 369 Science Party, using the 50 kV dataset for elemental intensities of barium and calcium and 10 kV for silica. Scanning was conducted on two instruments, necessitating calibration of the records to correct for any offset to ensure consistency of elemental concentrations. Barium, calcium, silica and iron (Fe) measurements were adjusted using site-specific XRF calibrations that convert counts to concentrations as per Figure 2.2 of Kirby (2022), though for Ca/Fe and Si/Fe this only changes axis magnitude not overall data pattern as there was no instrumental offset.

4.2.6. Ichthyolith accumulation rate

Ichthyolith accumulation rate (IAR; Sibert, 2016) is considered a measure of fish and shark productivity, representing productivity changes over a specified time period and/or preservation potential. It is calculated based upon the total abundance of teeth and denticles per gram of sediment in each sample as an indicator of flux to the seafloor, normalised to sediment dry bulk density and sedimentation rate.

$$\text{IAR} = \text{ichthyolith abundance} * \text{dry bulk density} * \text{sedimentation rate}$$

$$\frac{\text{ichthyoliths}}{\text{cm}^2\ \text{kyr}^{-1}} = \frac{\text{ichthyoliths}}{\text{g}} * \frac{\text{g}}{\text{cm}^3} * \frac{\text{cm}^3}{\text{kyr}}$$

Ichthyolith abundance was derived from counting whole and fragmented teeth and denticles from weighed samples, dry bulk density measurements came from the IODP LIMS database (IODP Joides Resolution Science Operator, 2018; Hobbs *et al*., 2019) and the sedimentation rate (0.876 cm kyr^{-1} for ~39 to 62 Ma interval) was determined from the site-specific age model (Section 4.2.2). Using a fixed versus moving average dry bulk density in the IAR equation (above) made no distinct difference with a variation of 1.27 g cm^{-3} between minimum and maximum values (Appendix Figure 4.1), hence the moving average was used for all subsequent analyses.

An important component of IAR is sedimentation rate, which is impacted by the resolution of the age model, but the high resolution astrochronology record for Site U1514 (average 150 kyrs between tie points) during the early Cenozoic helps alleviate this. IAR also helps to mitigate the effects of dissolution, which disproportionately removes carbonate material leaving the phosphatic ichthyoliths behind, often observed as spikes in ichthyolith count data. These dissolution events can be identified through changes in Ca/Fe ratios in XRF data.

4.2.7. Ichthyolith morphotypes

The shape and internal structure of teeth alludes to fish taxonomy and diet to inform ecological, productivity and community reconstructions. Tooth morphotypes were identified from images using a character-based coding system documenting size in

three dimensions and overall shape; surface texture; curvature; symmetry, size, length and location of blades and barbs; pulp cavity shape and size; base shape; tip shape and material (updated from Sibert (2016) and Sibert *et al.* (2018); Figure 2.1, Figure 4.3).

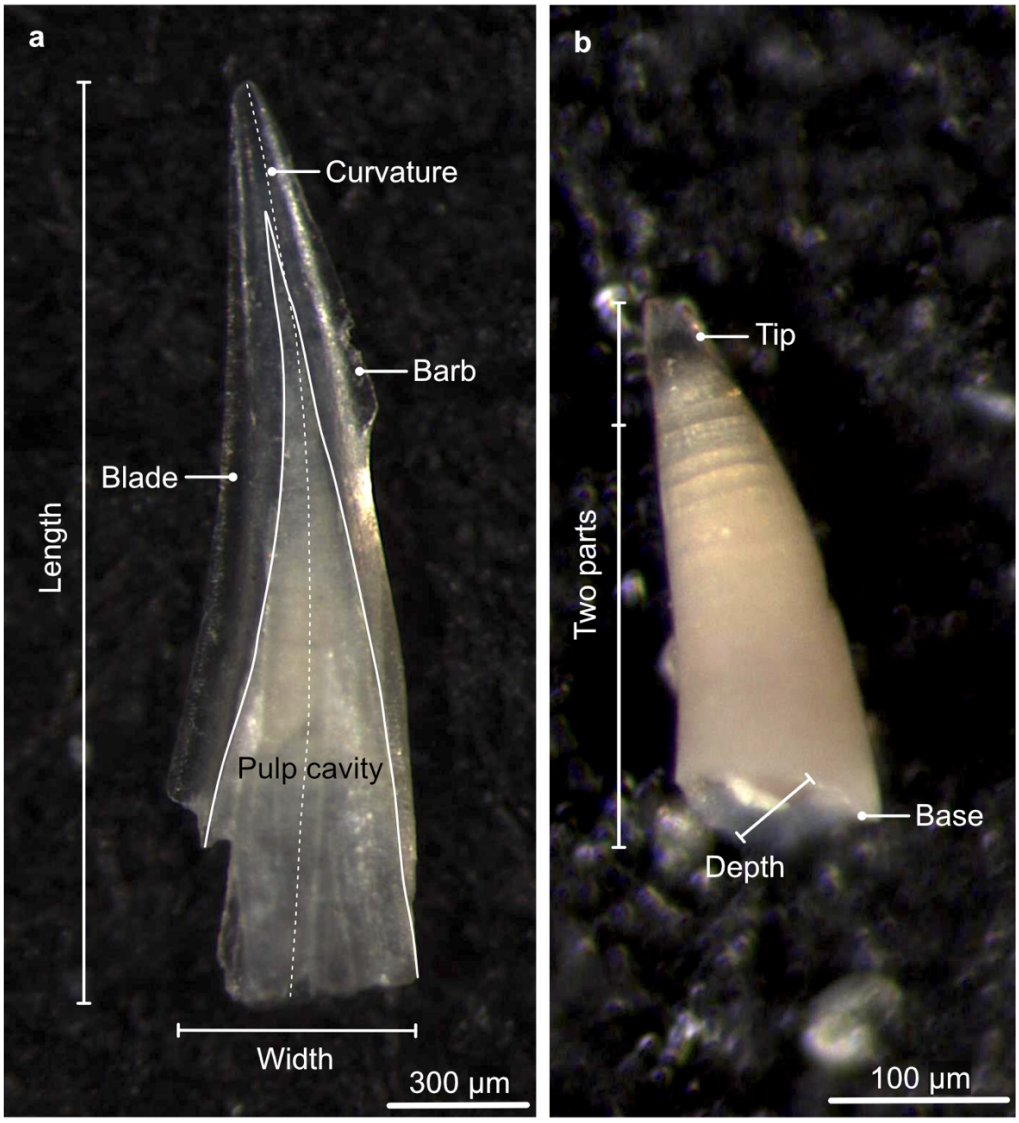

Figure 4.3. Example triangle (**a**; curved 1/4 barb morphotype, specimen ID: 369 U1514C 7R 6W 0-2 cm #4, 51.6 Ma) and cone (**b**; medium curved two-part straight tip morphotype, specimen ID: 369 U1514A 22F 1W 110-112 cm #3, 46.2 Ma) teeth from Site U1514 labelled with broad categories of characteristics investigated through the coding system of Sibert (2016) and Sibert *et al.* (2018).

The codes assigned to each tooth were then compared to a live database of known tooth morphotypes (created and maintained by Sibert, 2024) to compare teeth to descriptions and images of pre-existing morphotype aliases or designate new morphotypes with a unique combination of character traits as appropriate for addition to the database, alongside example images.

Furthermore, whilst denticles were picked from the samples, and a similar denticle morphotype database exists, their abundance in the U1514 dataset was too low for sufficient community analyses, hence they were not coded beyond generic shape.

4.2.8. R scripts

Exploration of the character-based coding system was conducted in R Studio (version 4.3.2; R Core Team, 2023) using the *ichthyoliths* packages developed by Dr Elizabeth Sibert (available from: https://github.com/esibert/ichthyoliths). This included modification of scripts to visualise morphospecies range charts, origination and extinction rates (based upon Foote, 2000) and non-metric multi-dimensional scaling (NMDS) ordination using the *vegan* package (Oksanen *et al.*, 2022) to determine morphospecies diversity clustering.

4.3. Results

4.3.1. Ichthyolith abundance through time

Fish tooth counts for this study of Site U1514 span 39.12 to 61.80 Ma over the late Palaeocene to middle Eocene including the EECO and multiple hyperthermal events. The total number of ichthyoliths (teeth and denticles) larger than 38 μm varied from one to 88 per sample in the low-resolution record with an overall inconsistent pattern

of peaks and troughs throughout the study interval (Figure 4.4 a, b). An apparent decline at the PETM is a factor of low sampling intensity and core availability, and is supplemented by the higher-resolution ichthyolith data from undergraduate student projects. In the more heavily sampled hyperthermal intervals, total ichthyolith abundance increased considerably in the peak of the hyperthermals, despite missing the 38 to 63 μm sieve size fraction where teeth are generally most abundant. In the peak of the PETM, total ichthyoliths reached 252 teeth and denticles, and 116 during the R and S hyperthermal events. No studied samples fall within the MECO, the closest is just after the event at 39.95 Ma. While teeth were relatively abundant at Site U1514, denticles (shark scales) were less so as most samples had fewer than four denticles, and the highest abundance observed was 10 denticles in a sample. Thus, the denticle dataset is too small for evolutionary studies, so further analyses are limited to tooth morphotype diversity.

To enable comparison and account for differentiation in the volume of bulk sample material processed and thus residue available for picking (for example, more bulk sediment increases the possibility of greater ichthyolith extraction), abundances (ichthyoliths per gram) were calculated. Abundance varies throughout the study interval (0.13 to 4.87 ichthyoliths g^{-1}), peaking just prior to the early EECO (at 4.87 ichthyoliths g^{-1}) and then declining, with sporadic smaller increases (2.19, 1.73 and 1.35 ichthyoliths g^{-1}), through the remainder of the EECO. This pattern of peaks and troughs in abundance continues through to the MECO, fluctuating 0.23 to 1.75 ichthyoliths g^{-1} but with no clear trend.

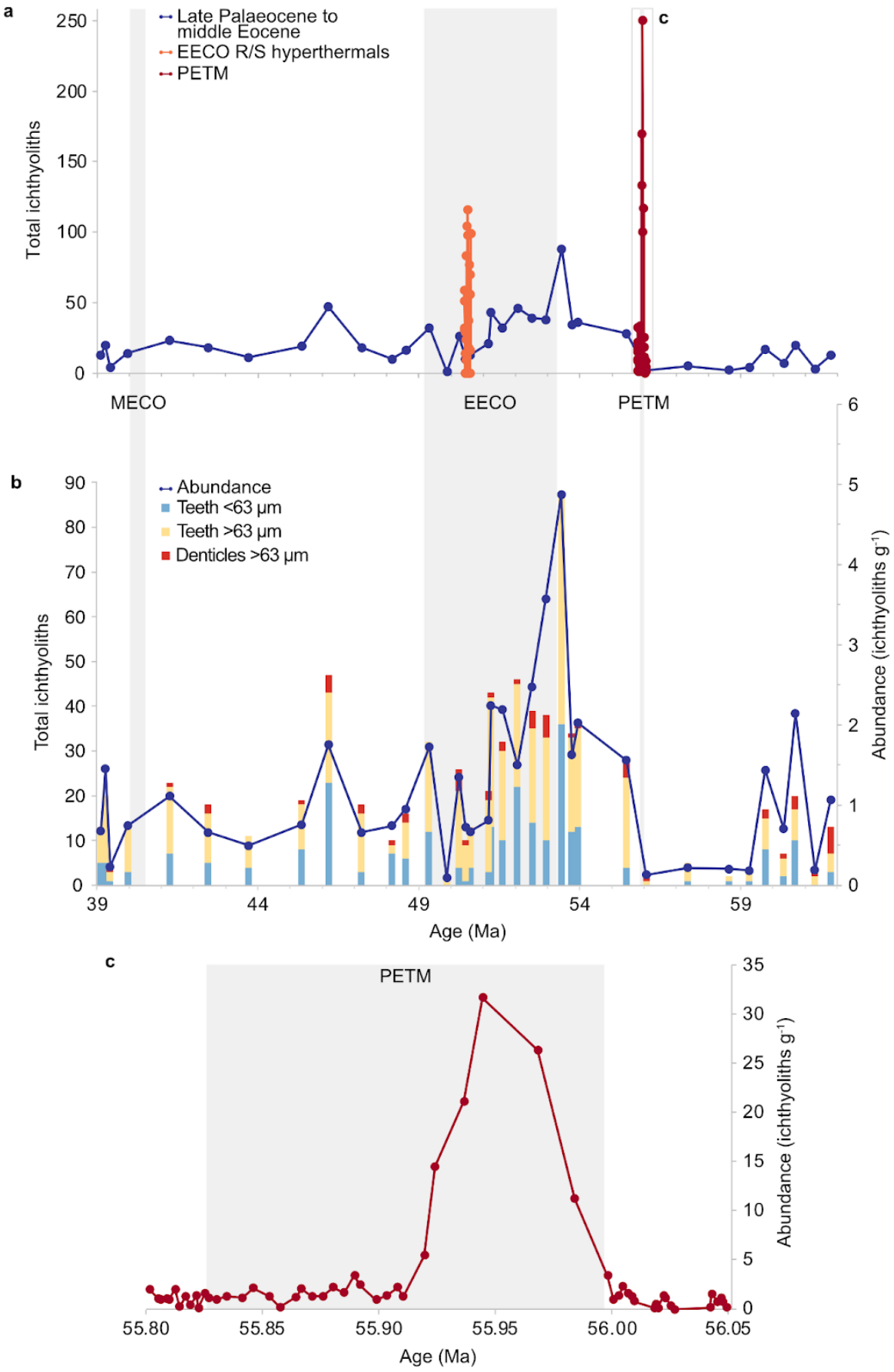
a
Late Palaeocene to middle Eocene
EECO R/S hyperthermals
PETM
Total ichthyoliths
MECO
EECO
PETM
c
b
Abundance
Teeth <63 µm
Teeth >63 µm
Denticles >63 µm
Total ichthyoliths
Abundance (ichthyoliths g-1)
Age (Ma)
c
PETM
Abundance (ichthyoliths g-1)
Age (Ma)

Figure 4.4. *(Previous page)* Total ichthyolith (teeth and denticles of all size fractions) counts spanning the late Palaeocene to middle Eocene (**a**), supplemented by data from three undergraduate students studying hyperthermal events at the site. The PETM data is combined for two students (Haf Nawsath and Lily Goddard), whilst the third dataset covering the ECCO R and S events is by Zulaikha Sukerdi. Ichthyolith counts by component (**b**; teeth and denticles) and size fraction (less than 63 μm and over 63 μm) for the author's dataset only through the study interval, plotted against abundance (ichthyoliths g^{-1}). Combined ichthyolith abundance (**c**) for the two undergraduate PETM datasets. Abundance for the EECO R and S events could not be calculated due to the absence of dry bulk sample weights.

The high resolution PETM data has an ichthyolith abundance spike (31.84 ichthyoliths g^{-1}) during the peak of the event (55.964 to 55.933 Ma; Boggust, 2022) followed by a rapid decline down to background levels of less than 5 ichthyoliths g^{-1} (Figure 4.4 c), with both student datasets independently verifying each other with elevated abundances in sync during this window (Appendix Figure 4.2). The benefit of using abundance instead of raw tooth and denticle counts is apparent for the samples at 51.60 Ma and 52.07 Ma where the abundance is lower for the latter despite overall having more ichthyoliths, a consequence of having twice the bulk dry sample weight during processing (Appendix Figure 4.3).

4.3.2. IAR in context of climate patterns and productivity

4.3.2.1. IAR and isotopic climate patterns

The global curve for carbon ($\delta^{13}C$) and oxygen ($\delta^{18}O$) isotopes from benthic foraminifera (Westerhold *et al.*, 2020) broadly matches U1514 site-specific carbon and oxygen isotopes from bulk carbonates in terms of trend, albeit values are generally ~1 to 1.5 ‰ higher, consistent with the deep sea versus surface water signals they record (Edgar *et al.*, 2022; Figure 4.5 a, b). Across the study interval $\delta^{13}C$ varies considerably, peaking at 3.74 ‰ at 57.7 Ma and troughing at 1.03 ‰ at 52.9 Ma for the U1514-specific isotopes. A clear negative spike in $\delta^{13}C$ occurs at the PETM, displaying the characteristic decline of the hyperthermal, being ~3.5 ‰ in the global dataset and ~2 ‰ for the U1514 isotopes. This is superimposed on a general decreasing $\delta^{13}C$ trend leading into the EECO, when U1514 benthic carbon increases 1.06 ‰ in line with a known augmentation in pCO_2. Thereafter, $\delta^{13}C$ plateaus until a smaller magnitude increase for the MECO ~40 Ma, which is apparent in the global curve but not prominent in the U1514 isotopes.

Similarly, $\delta^{18}O$ varies considerably across the 39 to 62 Ma study interval, from -1.59 to 0.21 ‰ in the U1514 isotopes (Edgar *et al.*, 2022). Whilst the site-specific and global $\delta^{18}O$ display a ~1.5 ‰ divergence either side of the EECO, they coalesce to overall similar values during this extended warming period, having a minima of -0.99 ‰ in the middle of the event. Once more there is a prominent characteristic negative $\delta^{18}O$ spike at the PETM in the global dataset, but this is entirely absent from the site-specific isotopic measurements. The MECO $\delta^{18}O$ stabilises after an initial small increase in the U1514 data compared to a prominent rise in the global curve. Overall, there is a weak positive trend between U1514 $\delta^{13}C$ and $\delta^{18}O$ for the Palaeocene to

middle Eocene (Edgar *et al.*, 2022), with a linear regression value of 0.0068 (Appendix Figure 4.4), and only a slightly stronger positive trend for the PETM isotopes with a regression of 0.1302 (Boggust, 2022).

Within the EECO are a number of hyperthermal events, identified at Site U1514 based upon low Ca/Fe ratios that imply calcium carbonate dissolution events (Vahlenkamp *et al.*, 2020) rather than isotopic changes, which are too low resolution. Site U1514 IAR data does not show a sustained high through the EECO but instead a number of peaks and troughs, the former of which occur associated with hyperthermals (Figure 4.5 c, Appendix Figures 4.5 and 4.6). Studied samples approximately correspond to seven hyperthermal events (R at exactly 56 Ma, and the remainder within 10 to 200 kyrs being H1, H2, I2, K, L and S; Vahlenkamp *et al.*, 2020). However, despite sampling around hyperthermals, not all of these are expressed as peaks in IAR. The maximum IAR of 8.9 ichthyoliths cm^{-1} kyr^{-1} corresponds to hyperthermal I2, with IAR generally declining through the EECO as $\delta^{13}C$ increases. The second largest peak at 7.5 ichthyoliths cm^{-1} kyr^{-1} occurs post-MECO.

Focusing on the PETM IAR (Figure 4.6), there is a somewhat clearer pattern matching the evolution of the hyperthermal, with variable values (0 to 3 ichthyoliths cm^{-1} kyr^{-1}) before the event, reaching a distinct peak of ~6 ichthyoliths cm^{-1} kyr^{-1} through the peak of the PETM before declining during the recovery and post-PETM (0.2 to 3.4 ichthyoliths cm^{-1} kyr^{-1}).

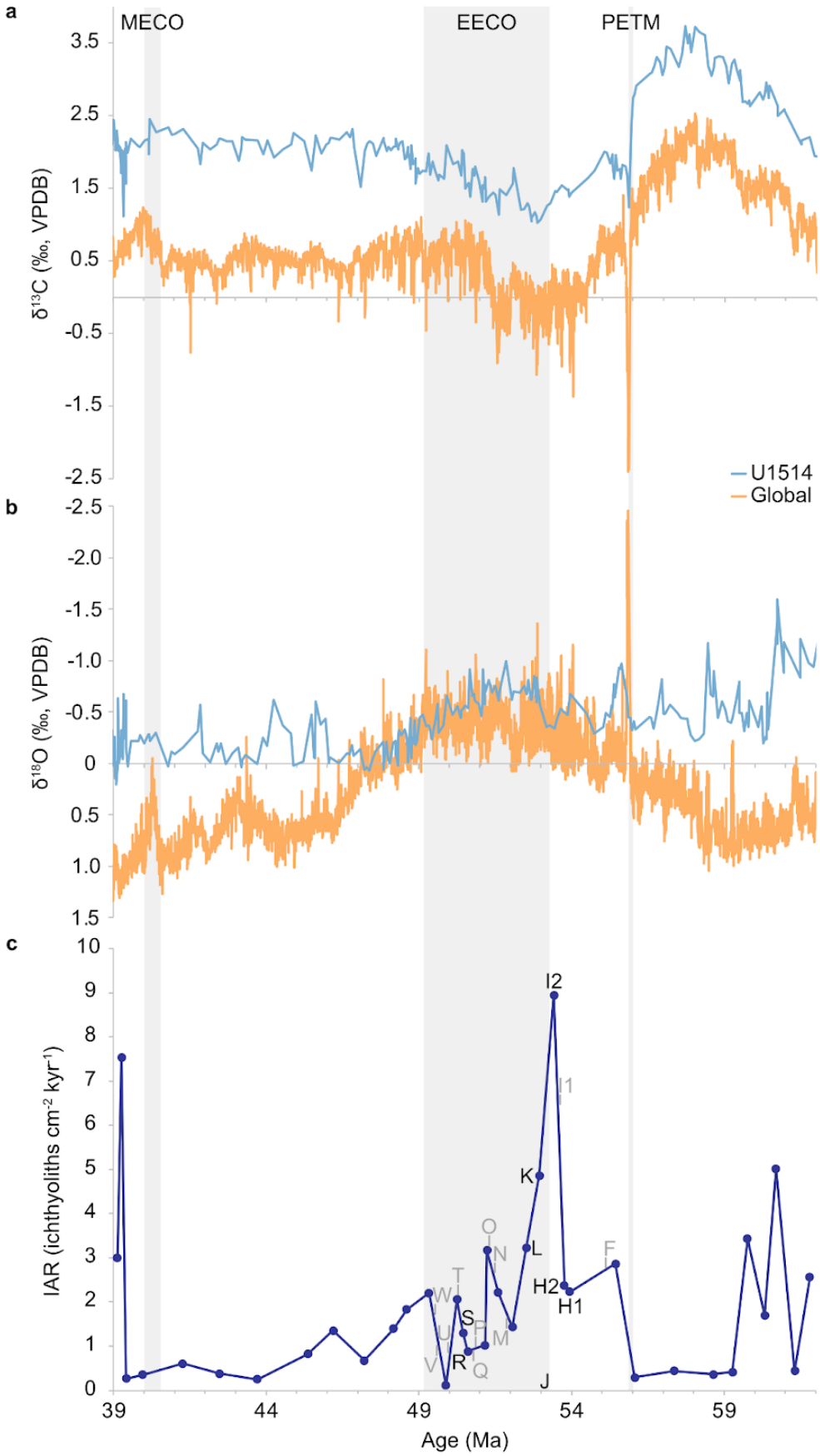
a
MECO
EECO
PETM
3.5
2.5
1.5
0.5
-0.5
-1.5
-2.5
δ13C (‰, VPDB)
U1514
Global
b
-2.5
-2.0
-1.5
-1.0
-0.5
0
0.5
1.0
1.5
δ18O (‰, VPDB)
c
10
9
8
7
6
5
4
3
2
1
0
IAR (ichthyoliths cm-2 kyr-1)
I2
I1
K
L
O
N
T
W
S
U
P
M
V
R
Q
J
H2
H1
F
39
44
49
54
59
Age (Ma)

Figure 4.5. *(Previous page)* Carbon isotope curves for Site U1514 (**a**; based on bulk carbonates, Edgar *et al.*, 2022) and the global composite (from benthic foraminifera, Westerhold *et al.*, 2020). Oxygen isotopes (**b**) from aforementioned sources**.** Ichthyolith accumulation rate (**c**), with samples corresponding to hyperthermal events (denoted in black for approximately matching samples and grey for non-sampled hyperthermals, per the alphanumeric system outlined in Vahlenkamp *et al.*, 2020). The J event marks the beginning of the EECO.

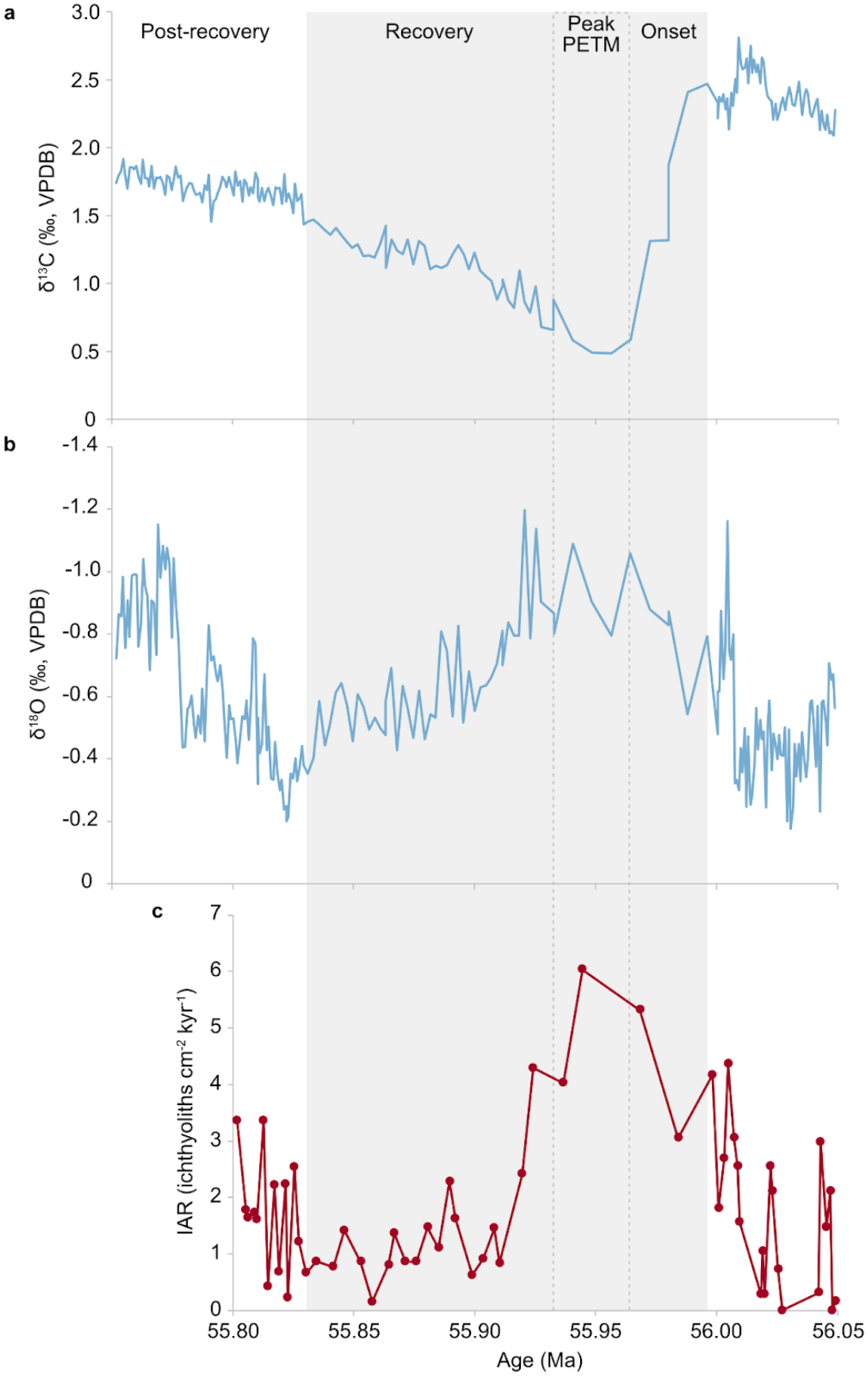
a
Post-recovery
Recovery
Peak PETM
Onset
δ13C (‰, VPDB)
3.0
2.5
2.0
1.5
1.0
0.5
0
b
δ18O (‰, VPDB)
-1.4
-1.2
-1.0
-0.8
-0.6
-0.4
-0.2
0
c
IAR (ichthyoliths cm-2 kyr-1)
7
6
5
4
3
2
1
0
55.80
55.85
55.90
55.95
56.00
56.05
Age (Ma)

Figure 4.6. *(Previous page)* Stable carbon and oxygen isotope and IAR changes across the PETM. High resolution $\delta^{13}C$ isotopes (**a**) from benthic foraminifera (Boggust, 2022). Benthic foraminiferal $\delta^{18}O$ (**b**) from aforementioned source. Combined IAR data (**c**) from two undergraduate students matched to peak PETM (defined based on Boggust, 2022). Grey shaded box defines the PETM from onset to recovery, with dashed box highlighting peak.

The relationship between ichthyolith abundance and climate is further explored by testing for trends between IAR and stable isotope values (Figure 4.7), which display weak but statistically significant negative and positive correlation between IAR and $\delta^{13}C$ and $\delta^{18}O$ isotopes respectively. For $\delta^{13}C$ and IAR correlation, p values are 0.03 for the long-term data, 4.3×10^{-8} for the PETM data and 9.8×10^{-6} for all datasets combined, and for $\delta^{18}O$ and IAR correlation, 0.2, 3.6×10^{-4}, 0.01 respectively. Comparatively, the PETM data displays a slightly stronger correlation between palaeoenvironmental proxies and IAR than the longer-term dataset.

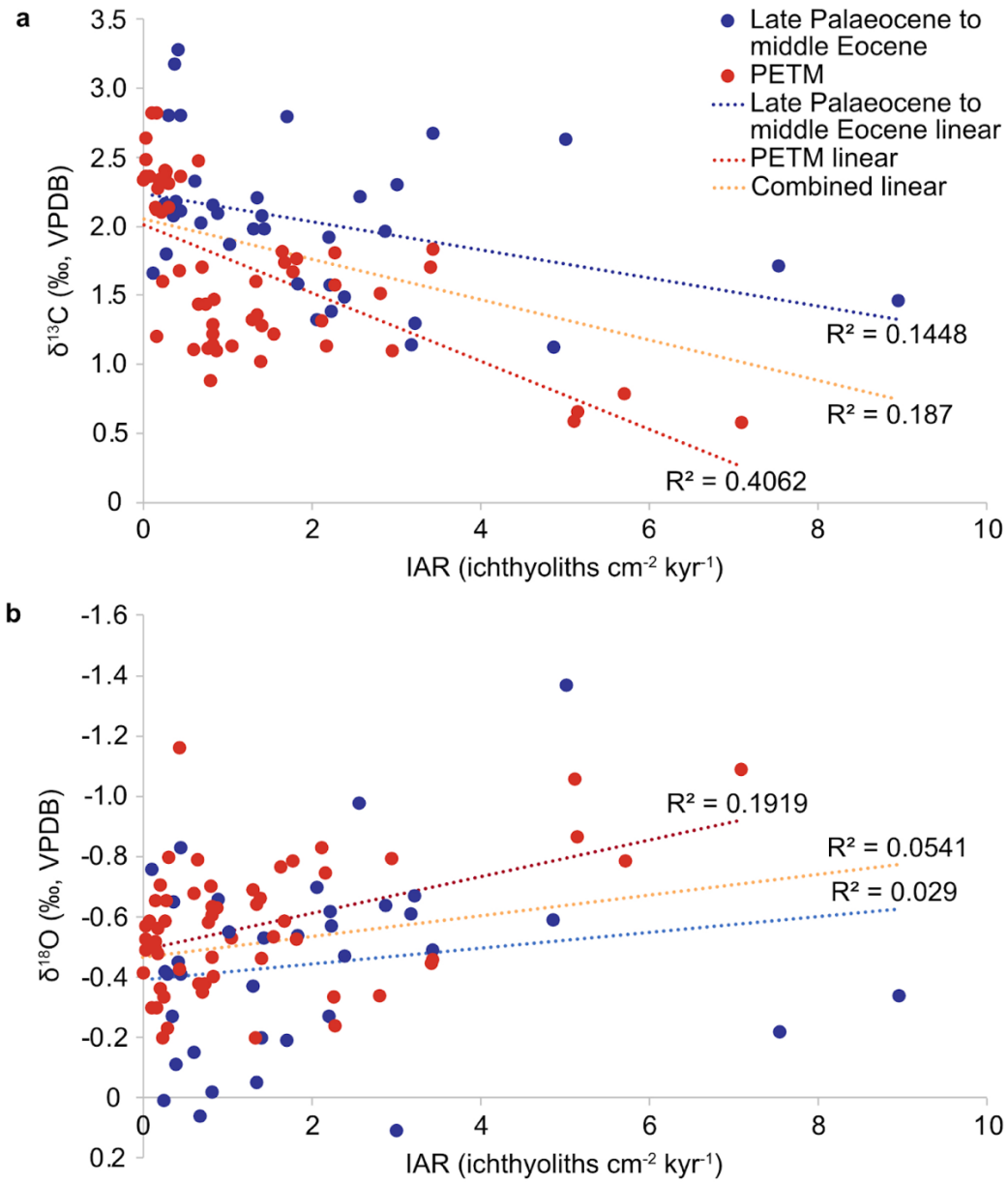

Figure 4.7. Crossplots of IAR against carbon (**a**) and oxygen (**b**) isotope values in the same sample for both the lower resolution long-term dataset across the late Palaeocene and middle Eocene, and the high resolution PETM data. Individual regression lines for each dataset are presented alongside a combined linear trend for the entire available data. Isotopes for late Palaeocene to middle Eocene data from Edgar *et al.* (2022; blue dots) and PETM from Boggust (2022; red dots).

4.3.2.2. IAR and geochemical productivity proxies

Marine productivity can be estimated based upon sediment elemental proxies obtained via x-ray fluorescence (XRF) analyses. Calcium-iron (Ca/Fe) ratios are key indicators of hyperthermals as they mark dissolution of calcium carbonate sediments as the calcium compensation depth shoals in response to warmer and more acidic oceans in a high pCO_2 world, though recent studies have suggested a potential decoupling of this trend during the early Cenozoic (Greene *et al.*, 2019). The data shows highly variable Ca/Fe ratios throughout the study interval (10.26 to 24.30; Figure 4.8 b) with no overarching trend. There is a rapid decline in Ca/Fe at the PETM to 11.44 and transient decreases corresponding to hyperthermal events in the EECO, though at a smaller magnitude of change, reaching a low of 14.87 (apart from one outlier towards the end of the EECO where Ca/Fe ratio is comparable to the PETM at 11.60). These decreases are superimposed on the overall EECO pattern of a small increase in Ca/Fe through the interval before a more prominent decrease towards the end of the EECO. Post-EECO there is a general increasing trend, which continues through the MECO but is highly variable.

Sampling during hyperthermal dissolution events can lead to a bias in ichthyolith accumulation, hence the use of IAR helps to alleviate this by accounting for variations in sedimentation rate. At site U1514, Ca/Fe ratios do show a notable trough matching to hyperthermal I2, but otherwise there is no clear pattern between calcium dissolution and IAR in the records, meaning increases in ichthyolith abundance are true reflectors of fish productivity rather than impacted by concentration bias.

Silica-iron (Si/Fe) ratios explore productivity when differentiating between biological and terrigenous sources. Peaks in biological silica in sediments imply enhanced productivity of siliceous microorganisms in the surface ocean. Si/Fe is generally low through the study interval (0.002 to 0.015; Figure 4.8 c), with notable elevations in the late Palaeocene (maximum 0.06) and during the EECO (maximum 0.04), with only a small increase around the end of the MECO (maximum ~0.01). The peaks and troughs cannot be reliably determined as biological or terrigenous in origin via U1514 smear slide data, which indicate a relatively small contribution of silica to sediment composition overall (2% siliciclastic and 5% biosiliceous; Huber *et al.*, 2019). Preceding the EECO, terrigenous silica was rarely present (1 to 5%), and it decreased during the EECO (under 1%, trace), before returning to rare levels thereafter. For biological silica, diatoms disappear from the smear slide record prior to the start of the EECO, radiolarians decline in abundance from common (5 to 15%) to rare and trace amounts, whilst sponge spicule fragments continue being common through to the middle of the EECO before reducing to rare and trace amounts and disappearing from the smear slide record by the end of the event. Therefore, smear slide data does not suggest a notable increase in biological silica abundance during the EECO. Whilst this shows an opposing trend to the general increase in Si/Fe in the XRF data, this could be a factor of smear slide samples being taken at low temporal resolution (up to 3 m between), thus missing transient changes in silica.

Barite accumulates on the seafloor due to the sinking and decomposition of organic matter, having a high preservation rate and being less affected by diagenesis compared to carbonates (Hull and Norris, 2011). Determining the biogenic component against non-biogenic barium is conducted through comparison to a

terrestrial tracer, such as iron. Therefore, barium-iron (Ba/Fe) ratios are a useful indicator of open ocean export productivity from epipelagic (up to 200 m water depth) to benthic realms. The calibrated Ba/Fe record for Site U1514 displays high variation throughout the study interval (523.59 to 4555.67) but again with prominent increases in the late Palaeocene (peaking at 3813.77 during the PETM; Figure 4.8 d, Appendix Figure 4.7) and EECO (904.01 to 4555.67). Once more, the Ba/Fe record is particularly varied through the EECO but remains at a higher frequency throughout, whilst the MECO is expressed as a consistent plateau after an initial rapid peak and trough at the beginning of the event.

Cross-plotting IAR against Ca/Fe, Si/Fe and Ba/Fe ratios (Figure 4.9), the PETM record shows an opposing linear trend to the longer-term late Palaeocene to middle Eocene data. As Ca/Fe and Ba/Fe increases, IAR weakly decreases for the longer-term dataset, whilst it increases for the PETM samples. This same trend is also observed in the Si/Fe crossplots, though linear regression values are very low.

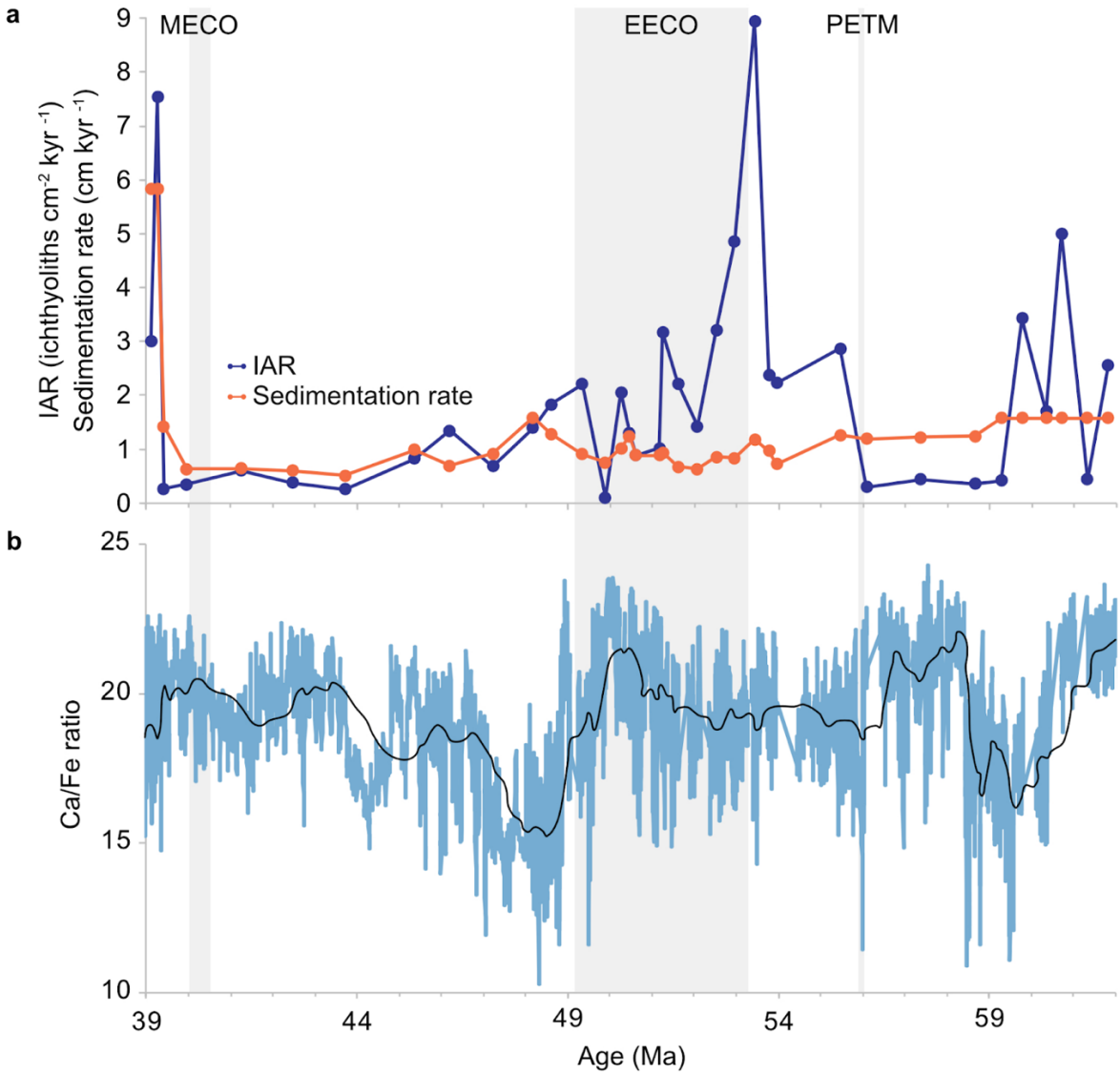

Figure 4.8. Ichthyolith accumulation rate and sedimentation rate (**a**) alongside palaeoenvironmental proxies for the PETM and EECO. Ca/Fe (**b**), Si/Fe (**c**) and Ba/Fe (**d**) ratios have been calibrated according to Kirby (2022) to account for differences in XRF instrumentation, with a moving average also applied (black line). Parts **c** and **d** continue overleaf.

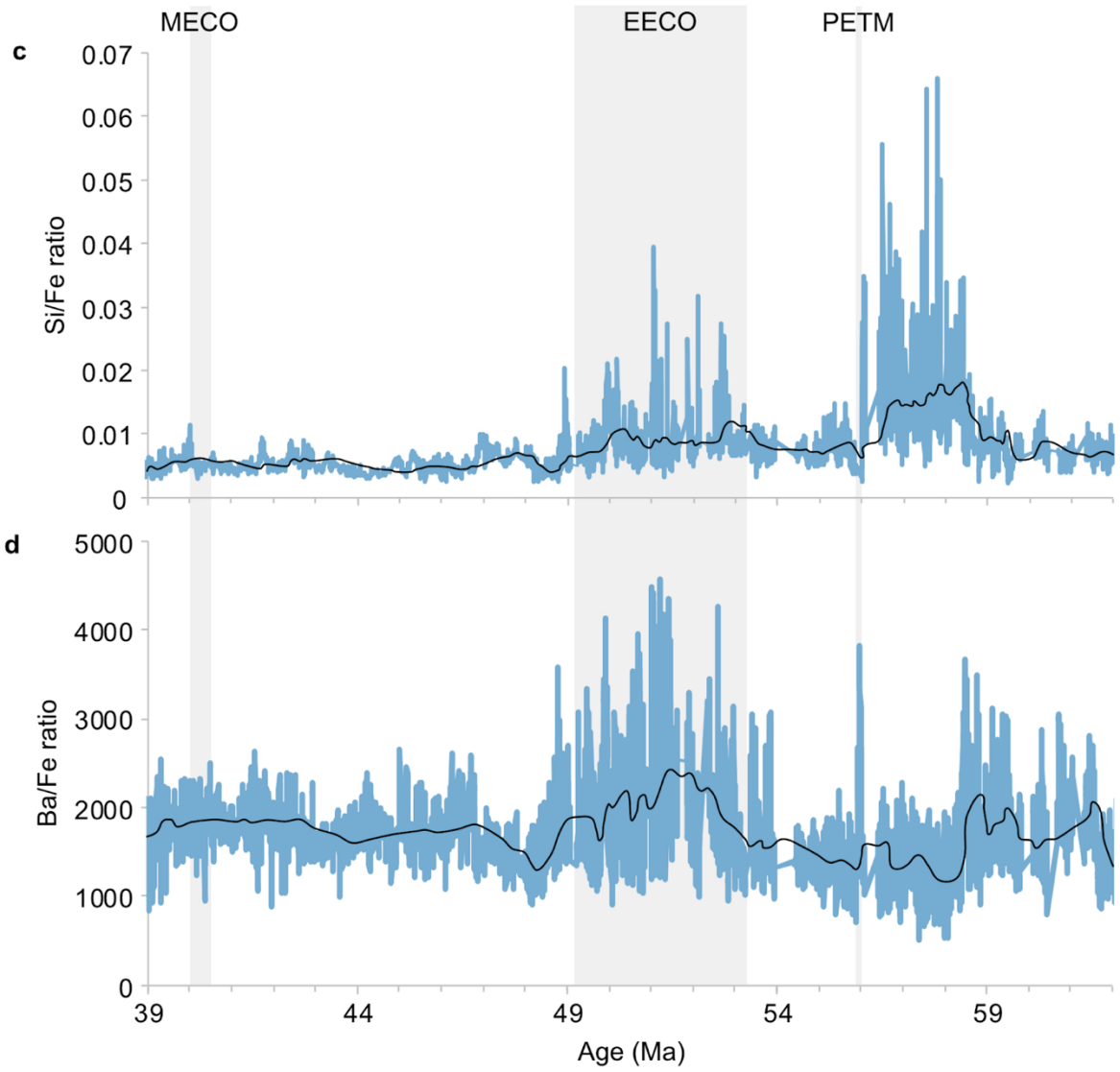
MECO
EECO
PETM
c
Si/Fe ratio
0.07
0.06
0.05
0.04
0.03
0.02
0.01
0
d
Ba/Fe ratio
5000
4000
3000
2000
1000
0
39
44
49
54
59
Age (Ma)

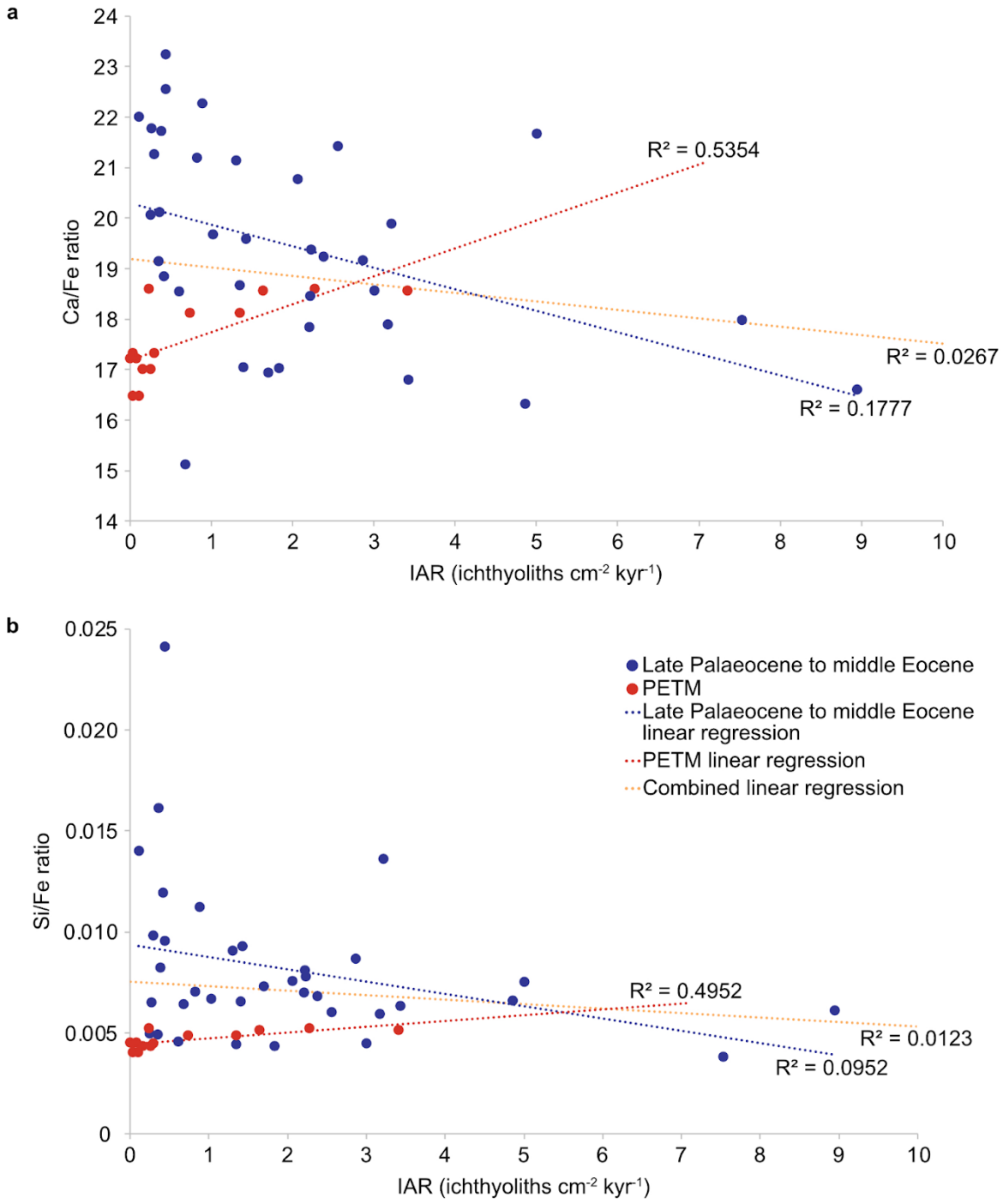

Figure 4.9. Palaeoenvironmental proxies of Ca/Fe (**a**), Si/Fe (**b**) and Ba/Fe (**c**) ratios as a function of IAR, with minimum and maximum ratio deviations for each core. Linear regressions for the late Palaeocene to middle Eocene and PETM datasets are presented separately, as well as a combined trend for all available data. Part **c** continues overleaf.

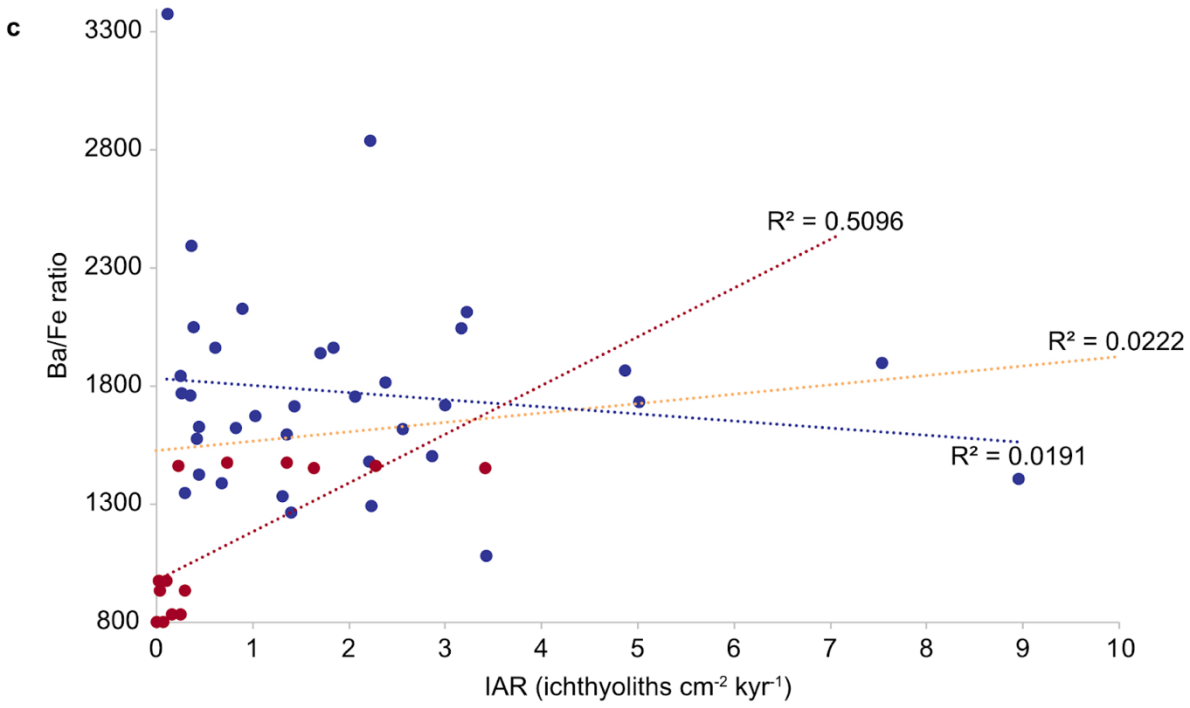

4.3.3. Community composition metrics

Relative tooth size and shape can be indicative of fish body size and function, though there can be considerable variation in this relationship between species and its association with trophic levels (Keppeler *et al.*, 2020). The tooth character coding system used for morphotyping (Sibert, 2016) divides teeth into four overall shape categories (squat, medium, long and extra-long; Figure 4.10) based upon the ratio of length and width of the tooth. For the longer-term dataset (Figure 4.11 a), values for all tooth shapes are low throughout the interval (zero to nine ichthyoliths within a particular shape category), except for the EECO when there is a peak of 30 ichthyoliths in the medium shape category. Immediately preceding the EECO there is an even larger peak in medium (37) and long (43) teeth which falls close to the timing of hyperthermal I2. Overall, the end-member sizes of squat and extra-long teeth are less abundant than medium and long teeth, but all generally track the same pattern

of increases and decreases. A distinct change in tooth shape is also apparent for the PETM data (Figure 4.11 b), with over five times more teeth of medium and long sizes found during the peak of the event than immediately prior, whilst squat and extra-long forms remain low in abundance throughout. Though the PETM does show a clear shift in tooth community composition, the R and S events (Figure 4.11 c) do not, with peaks, predominantly for medium teeth, instead occurring either side of the events. However, this pattern is inconsistent across the rest of the EECO hyperthermals.

The relative abundance of smaller size fractions (less than 63 μm) to larger (greater than 63 μm), which incorporates all shapes squat to extra-long (Figure 4.12 a), shows the larger size fraction to dominate the assemblage; one may tentatively suggest the over 63 μm fraction dominates during the warming events, but the distinct shift at the PETM is affected by the low number of samples available in the long-term dataset. The same comparison was not possible for the high resolution PETM and R and S events as no data is available on ichthyoliths smaller than 63 μm. In addition to the aspect ratio shape character, it is also possible to compare data across the dominant shapes of teeth, broadly falling into cones (circular base in cross-section) and triangles (flat base in cross-section; Figure 4.12 b, c, d) which may be indicative of feeding function. Across the longer-term data and short-lived hyperthermals, there is not a clear pattern in the abundance of cones versus triangles to environmental change, or through time more broadly, as there is high variance of generally 20 to 70% cones (correspondingly 30 to 80% triangles). Meanwhile, the PETM and R and S events data do not show trends in shape, varying 0 to 67% and 0 to 55% (with a singular peak at 100%) cones respectively.

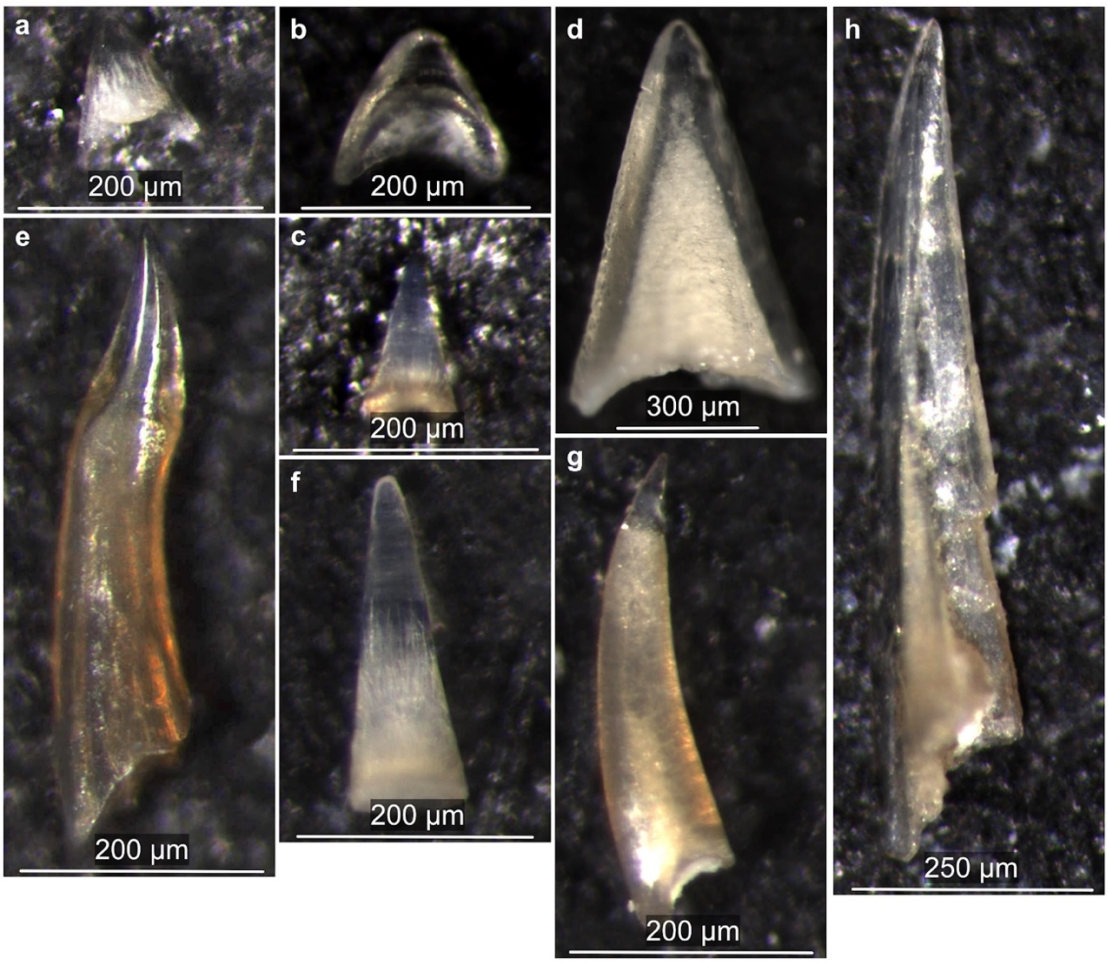

Figure 4.10. Examples of teeth picked from the longer-term dataset, with representative triangles and cones for squat (**a**, **b**), medium (**c**, **d**), long (**e**, **f**) and extra-long (**g**, **h**) teeth, respectively.

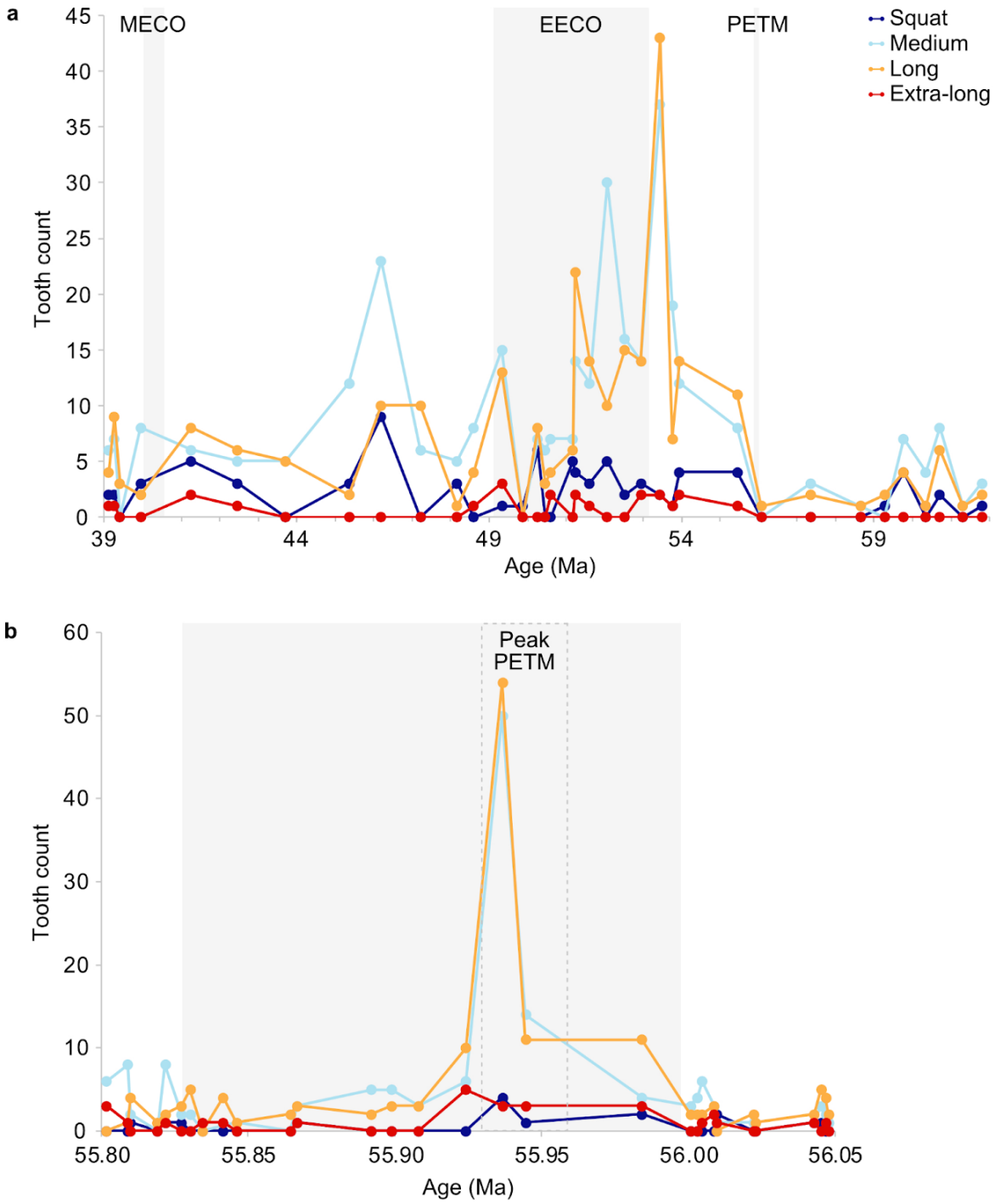

Figure 4.11. Late Palaeocene to middle Eocene tooth shape abundances (**a**) by relative size fraction (squat, medium, long, extra-long). PETM data (**b**) for tooth shape categories. EECO tooth shape data (**c**) covering R and S events (dated based upon Vahlenkamp *et al.*, 2020) continues overleaf.

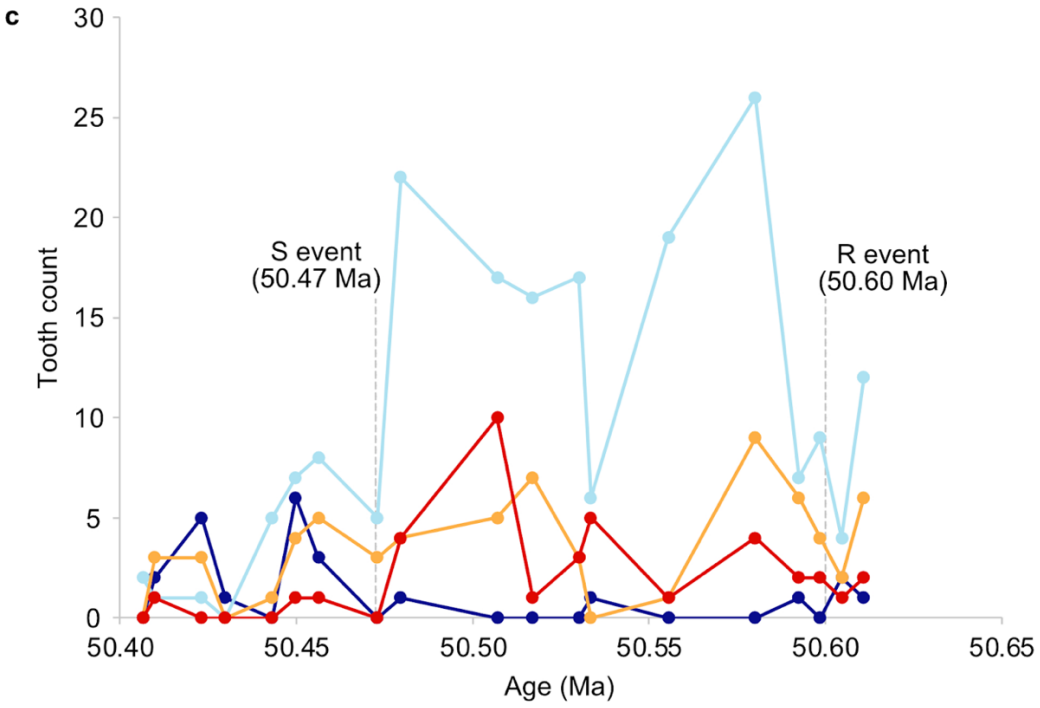
c
30
25
20
15
10
5
0
Tooth count
S event
(50.47 Ma)
R event
(50.60 Ma)
50.40
50.45
50.50
50.55
50.60
50.65
Age (Ma)

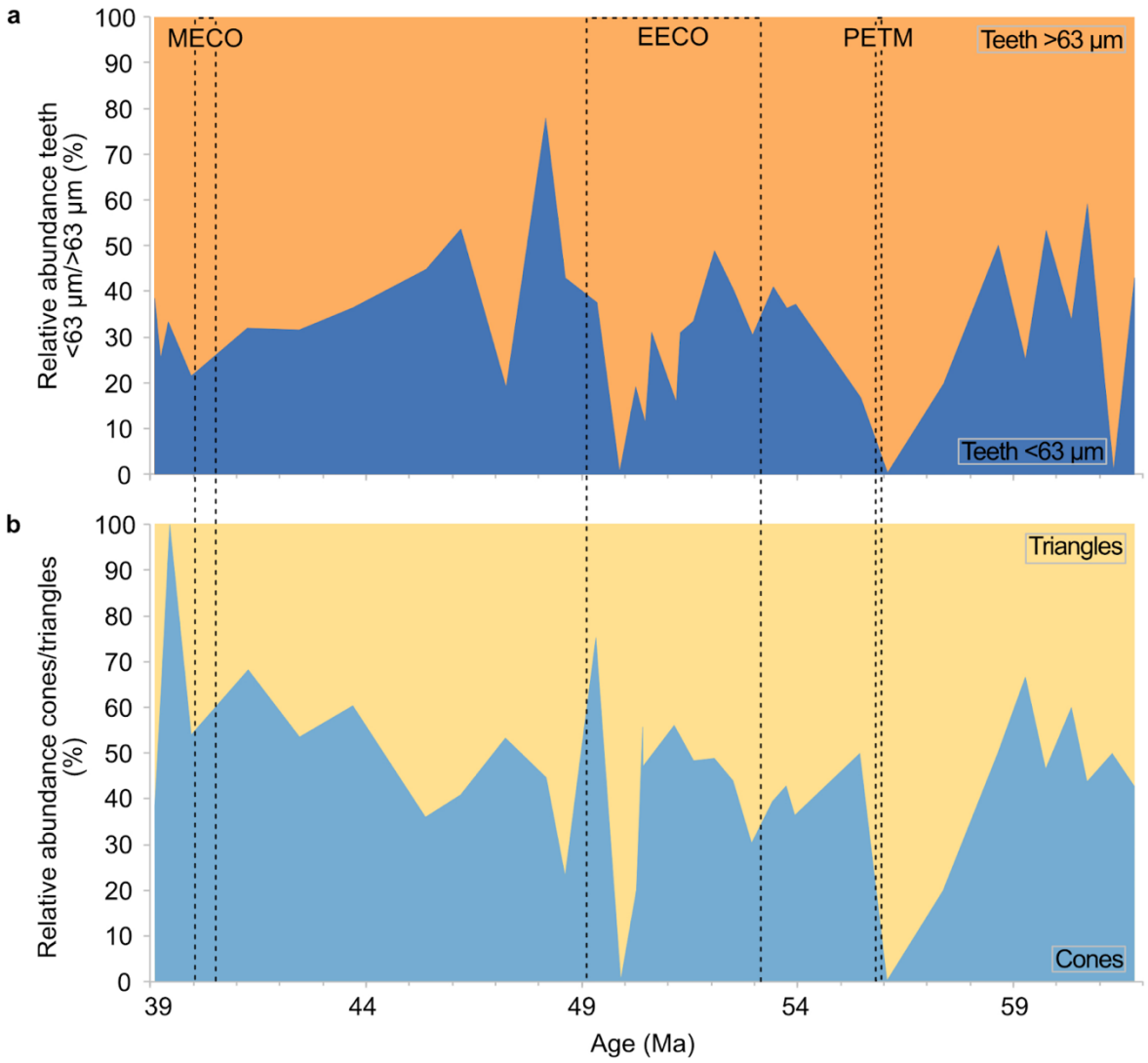

Figure 4.12. Relative abundance of teeth smaller than 63 µm to larger than 63 µm (**a**) and cones to triangles for the longer-term dataset (**b**), for the PETM (**c**) and the R and S events (**d**). Parts **c** and **d** continue overleaf.

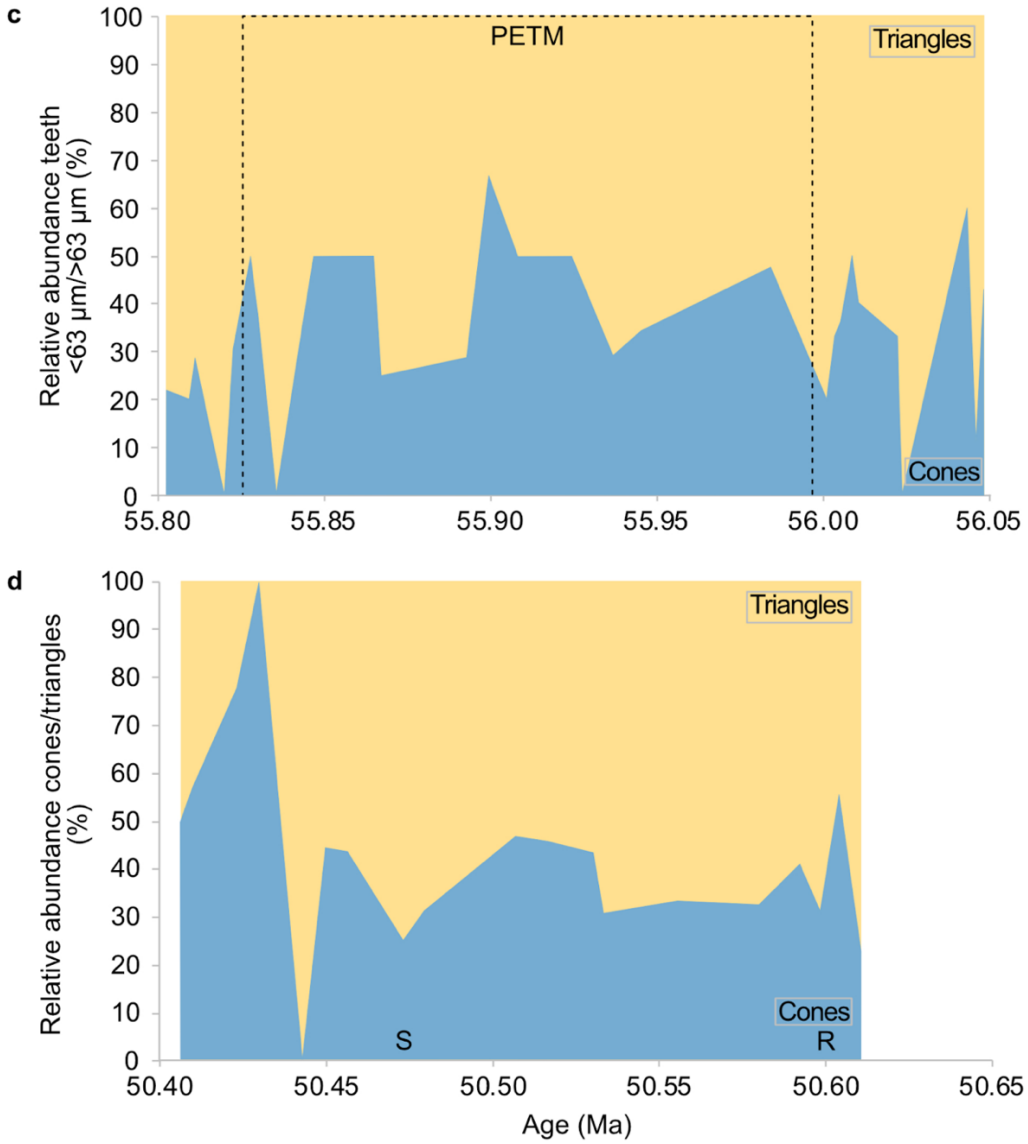

4.3.4. Morphotype occurrences through time

Across the entire dataset, 182 unique tooth morphotypes were identified (Figure 4.13), although this is likely an undercount as there were a number of teeth which were too broken to code or assign to a morphotype. Of these, 34 occur in the late Palaeocene prior to the PETM, 100 occur in the PETM (73 new morphotypes and removing seven morphotypes which are not present in the PETM but do range through from pre-PETM to the EECO and beyond), nine new morphotypes occur

between the PETM and EECO, 57 originate during the EECO and an additional nine post-EECO (though none correspond to the MECO). Therefore, within a given time slice, morphotype richness is one to 73, with the highest numbers associated with the most intense sampling. It should be noted that the spike in morphotypes during the PETM is heavily influenced by the concentrated sampling, thus complicating interpretation of true morphotype abundance and diversity patterns.

There are two distinct increases in morphotype origination in the record, corresponding to the high intensity sampling at the PETM and EECO R and S events, when placed in context of the comparatively lower 'origination' occurring either side based upon lower-intensity sampling of the long-term dataset. This being said, 64% (116) of the morphotypes existed prior to the EECO, with less origination seemingly initiated by the longer warming event. As might be expected, there is a significant positive correlation between increasing ichthyolith count and morphotype richness (Appendix Figure 4.8) and rarefaction curves begin to plateau after sampling ~100 to 250 ichthyoliths (Appendix Figure 4.9).

The most abundant morphotype in the dataset (more than 11 occurrences in a time slice) is "elongated 1/2 straight root" during the PETM, with "generic triangles" and "generic cones" (where the tooth could not be assigned a morphotype beyond generally triangular or conical in shape) being prominent at the EECO onset and during the R and S events respectively. Eight morphotypes have six to 10 occurrences in a particular time slice, these being "1/4 dome root cone", "generic cone", "generic triangle", "1/2 straight root", "medium 3/4 straight root", "long 3/4 straight root straight blades" and "extra-long straight cone" (Figure 4.14). Two of

these morphotypes occur six to 10 times at numerous points through the range chart (“1/4 dome root cone” immediately preceding the EECO, approaching the middle EECO and the end of the MECO; “generic cone” at the PETM boundary and middle EECO). Of these morphotypes, there is no universal consistent characteristic that may account for the reason for their abundance, though half do have straight roots. There are 13 morphotypes occurring four to five times in a single time slice, almost half of these being at the EECO onset, and 58 morphotypes present two to three times, predominantly throughout the EECO. Only two morphotypes range through the entire dataset, these being “generic cone” and “long 3/4 straight root”.

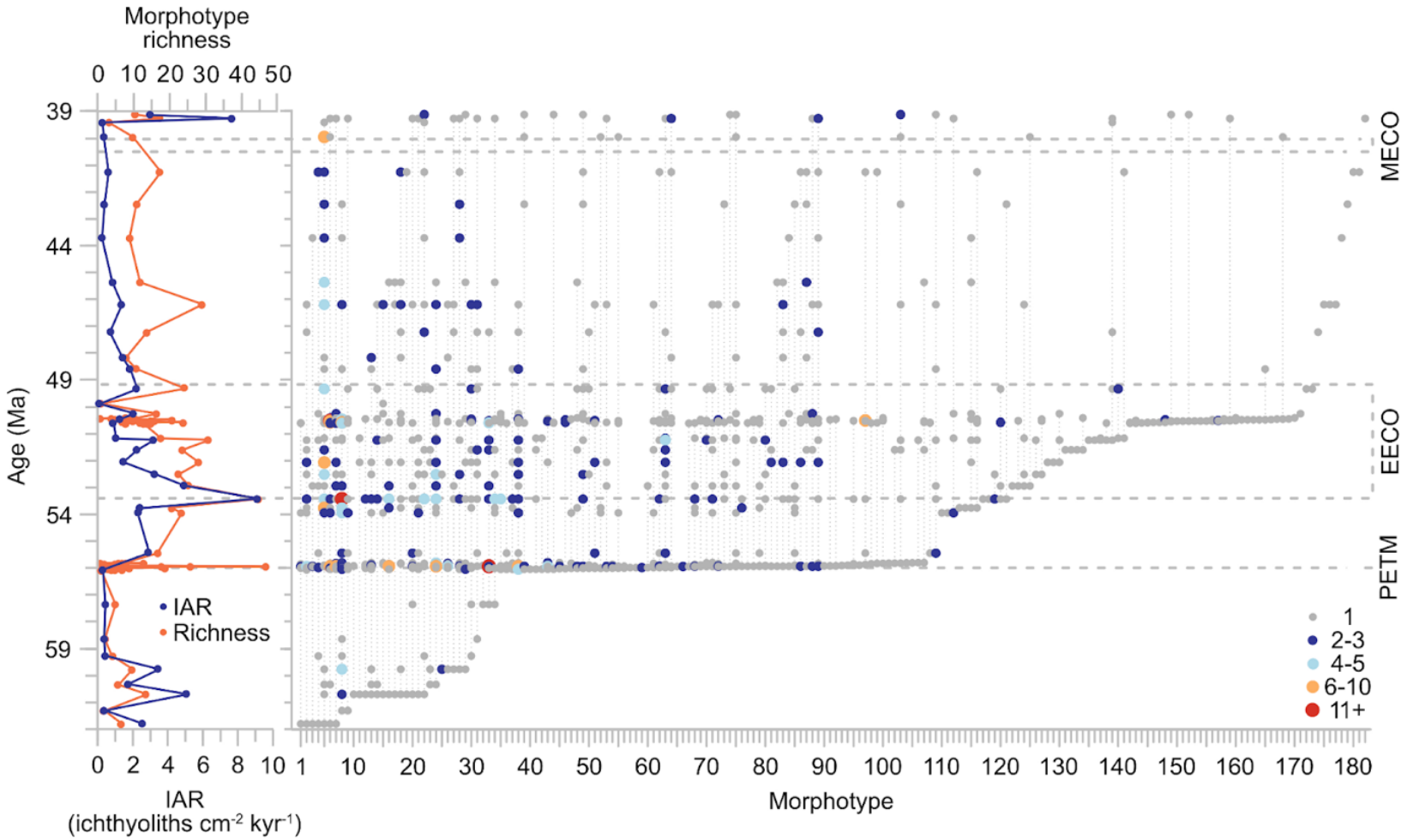

Figure 4.13. Morphotype range chart for Site U1514, plotted against morphotype richness for the entire dataset and IAR for the late Palaeocene to middle Eocene dataset. Dot colour and size represents morphotype abundance within a time slice, whilst the morphotype key can be found in Appendix Table 4.4.

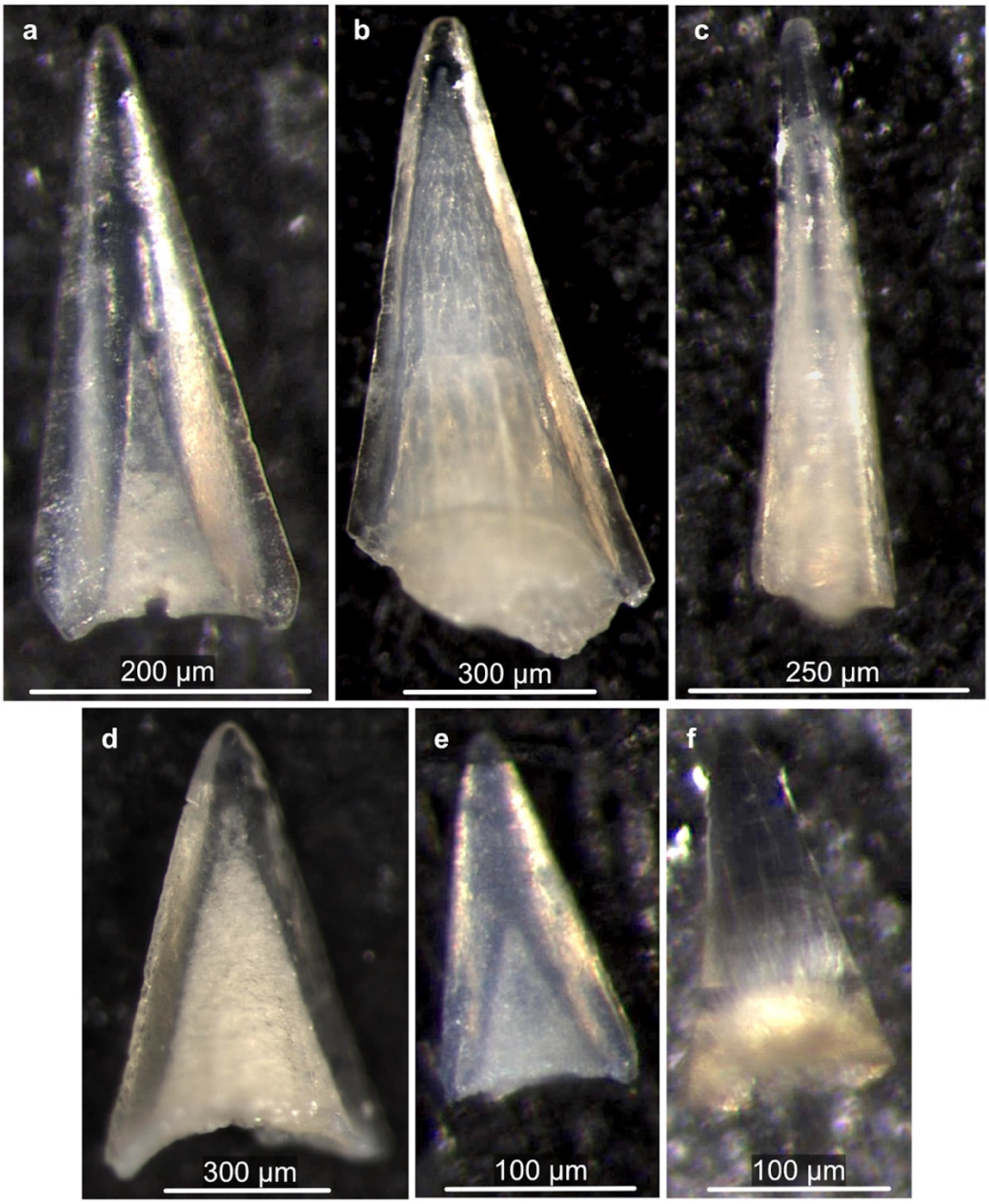

Figure 4.14. Examples of abundant tooth morphotypes at Site U1514: elongated 1/2 straight root (**a**), long 3/4 straight root straight blades (**b**), extra-long straight cone (**c**), medium 3/4 straight root (**d**), 1/2 straight root (**e**) and 1/4 dome root cone (**f**).

4.3.5. Morphotype origination and extinction

Morphotype origination and extinction can be estimated based upon the number of new morphotypes appearing or disappearing as a percentage of what was present in

the previous time slice (Foote, 2000). For the collective dataset, the mean origination and extinction rates are both 0.22 morphotypes per lineage million years (morph. Lmy^{-1}) with morphotype origination spiking during the PETM at ~1 capita per lineage million years (capita Lmy^{-1}; Figure 4.15 a) but remaining at zero through the EECO and beyond. Extinction rate is consistently zero throughout the study interval, barring a marginal increase at the PETM to ~0.4 capita Lmy^{-1} and another less than 0.1 capita Lmy^{-1} around the end of the MECO. The mean origination and extinction rates are broken down into 0.25 morph. Lmy^{-1} and 0.35 morph. Lmy^{-1} respectively for the late Palaeocene to middle Eocene dataset, 0.25 morph. Lmy^{-1} and 0.062 morph. Lmy^{-1} respectively for the PETM, and 0.14 morph. Lmy^{-1} and 0.22 morph. Lmy^{-1} respectively for the EECO R and S events. The estimated richness fluctuates in line with this, increasing rapidly at the PETM from ~35 to ~95 morphotypes, peaking in the EECO at ~100 morphotypes, then gradually declining through the rest of the early to middle Eocene towards pre-PETM/Palaeocene values of fewer than 35 morphotypes.

To test the influence of including the high resolution hyperthermal datasets, when only the late Palaeocene to middle Eocene data is used a more variable origination and extinction pattern is observed, whereby origination dominates through to the middle EECO and extinction thereafter (Figure 4.15 b). Here the mean origination and extinction rates both change to 0.39 morph. Lmy^{-1}. This also highlights the edge effect (Foote, 2000), where there is an anomalous elevated origination rate at the oldest point of the plot and extinction at the youngest point, purely due to the absence of bounding data.

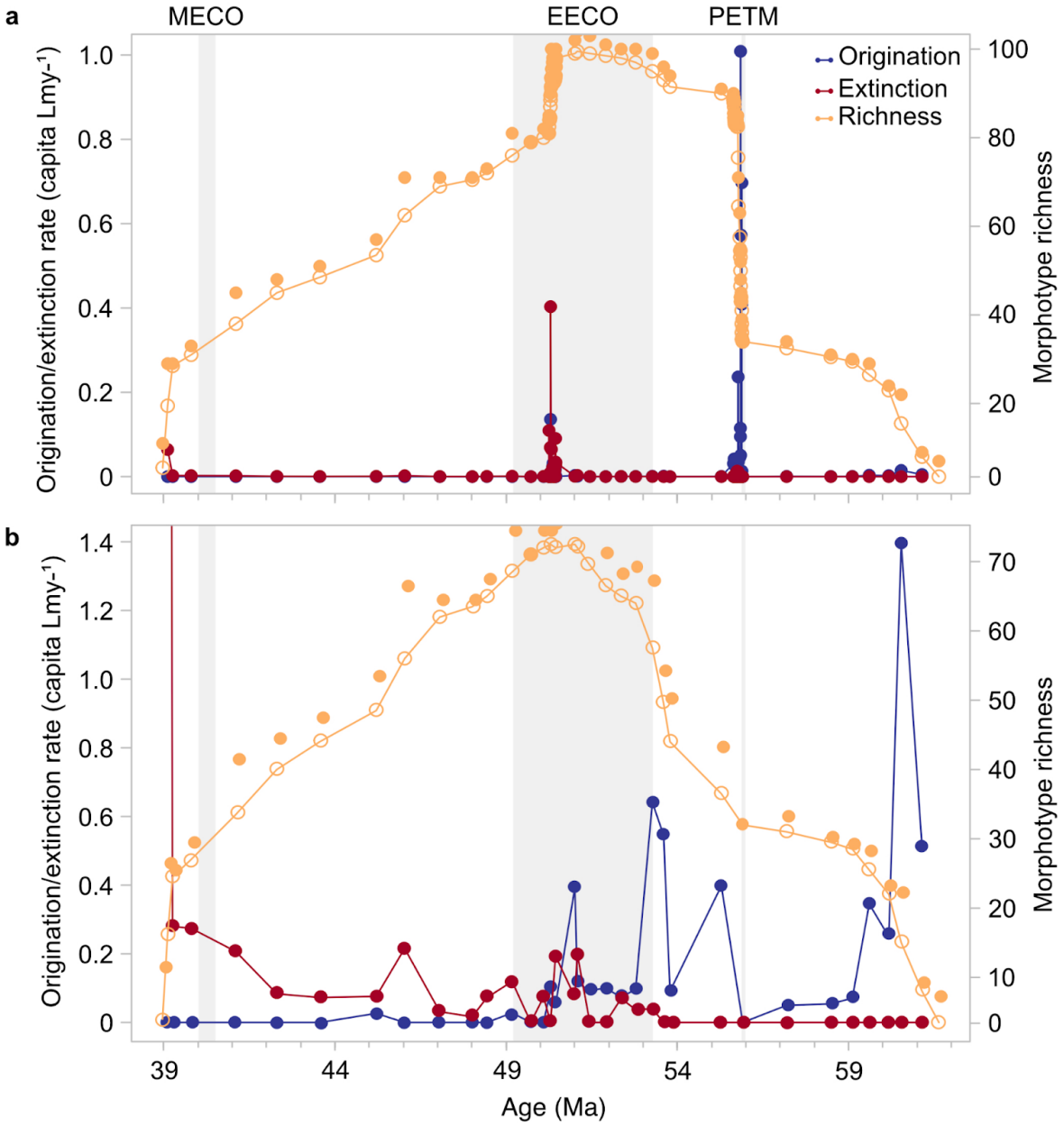

Figure 4.15. Per capita origination and extinction rates per lineage million years (Foote, 2000), alongside morphotype richness (filled circles are total observed richness and hollow circles estimated richness for when species are missing between samples but presence is assumed) for the entire U1514 dataset (**a**) and for the longer-term dataset only (**b**) to test the influence of hyperthermal data.

4.3.6. Morphospace occupation

Morphospace occupation analyses permit determination of similarity between fish communities preceding, during and following the EECO based upon a singular coded characteristic or morphotype, whereby greater overlap indicates community stability through a time period and outliers imply diversification. This was conducted through non-metric multidimensional scaling (NMDS) ordination via a custom R function (Sibert *et al.*, 2018). Generally, the teeth cluster into two groups of cones and triangles (Figure 4.16) with most of the tooth morphotypes overlapping in all three time bins defined (pre-EECO older than 53.22 Ma, EECO 49.14 to 53.22 Ma, post-EECO younger than 49.14 Ma) suggesting community stability. Beyond this, each time bin has only a small number of morphotypes unique to it, the most being in the EECO.

Further manipulation of the NMDS code permits exploration of a plethora of character states in the dataset such as curved versus straight shape, one or multiple parts (for example, a distinct tip as in Figure 4.3 b), and the presence or absence of blades and barbs (Figure 4.17, Appendix Figures 4.10 to 4.13). Most teeth are uncurved with minor curve, major curve and recurved teeth plotting together separately in morphospace as expected. The number of tooth parts overlaps considerably between one and two parts, with the former dominating the assemblage, and three-part teeth plotting entirely separately in alternative ordination views. The absence of blades plots separately to teeth with symmetrical, asymmetrical and single blades. Most teeth have no barbs and there are only singular occurrences of 1/3 and 3/4 barbs, with the remainder being 1/4 barbs and mostly overlapping the barbless community.

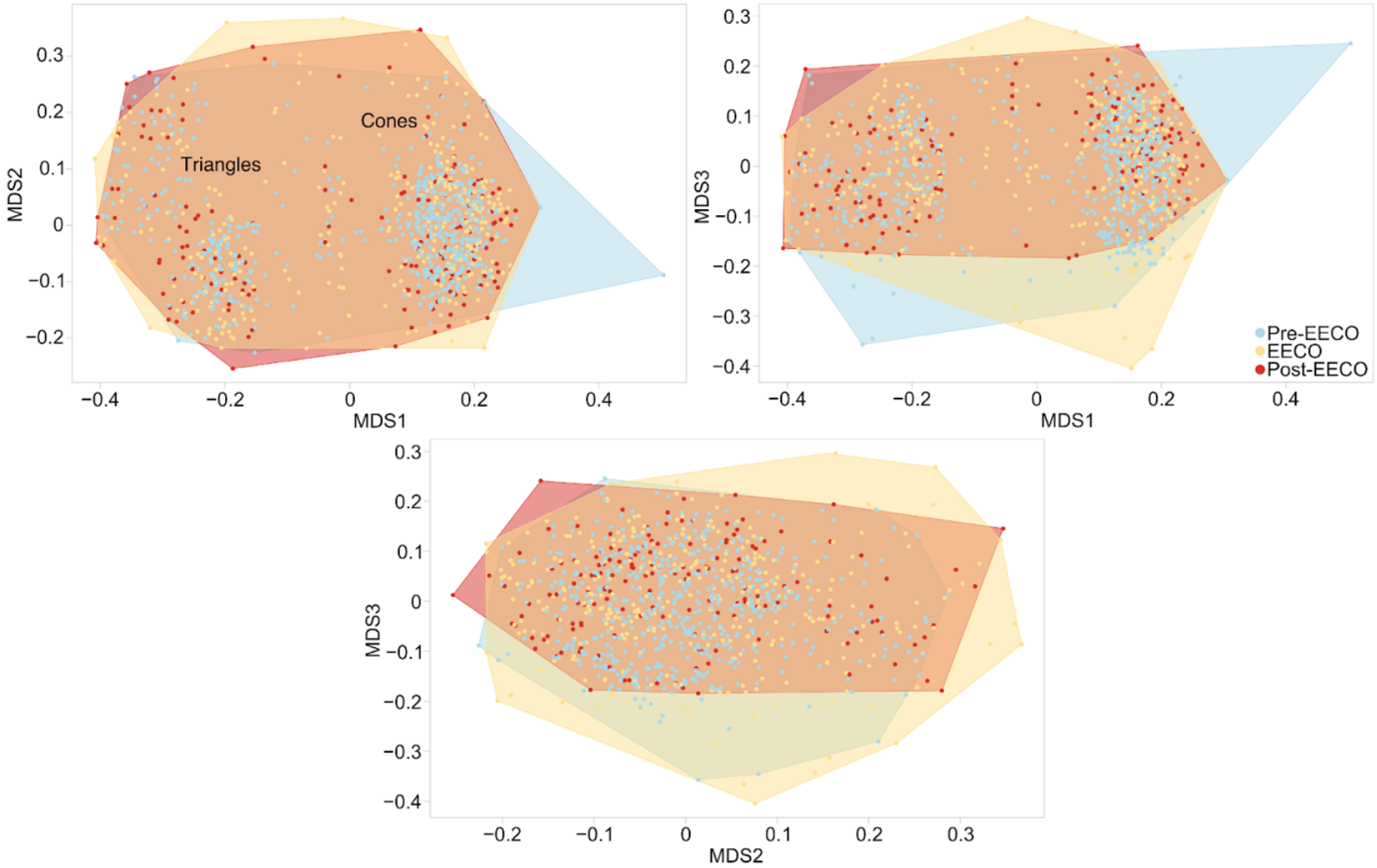

Figure 4.16. Morphotype morphospace occupation for the collective dataset across three time bins (pre-EECO, EECO and post-EECO) to determine community similarity through the study interval.

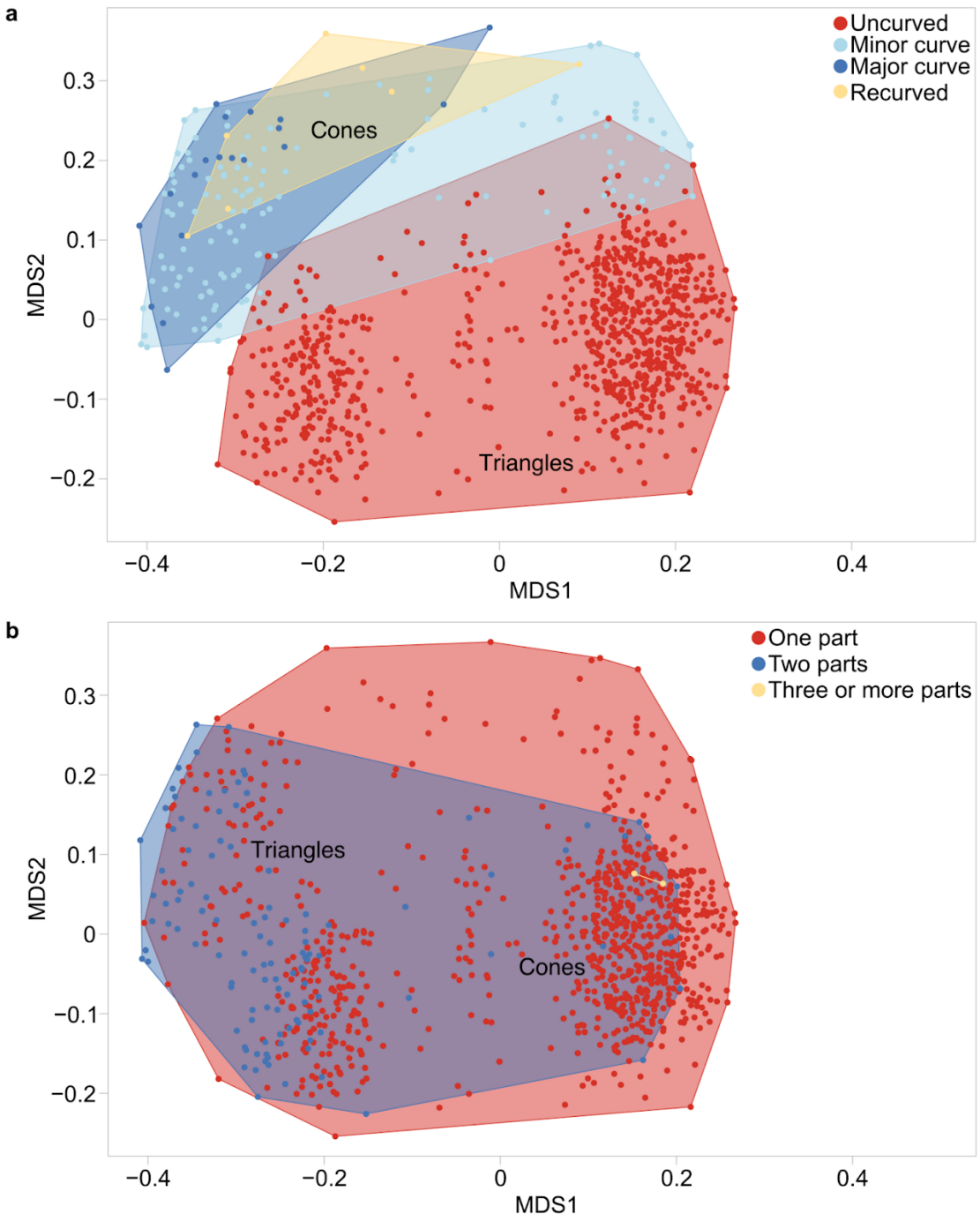

Figure 4.17. Morphotype morphospace occupation for characteristics of the tooth coding system, including curvature (**a**), number of parts (**b**), as well as the presence of blades (**c**) and barbs (**d**). Parts **c** and **d** continue overleaf. MDS1 and 2 for x-y coordinates presented here and full x-y, x-z, y-z variations in Appendix Figures 4.10 to 4.13.

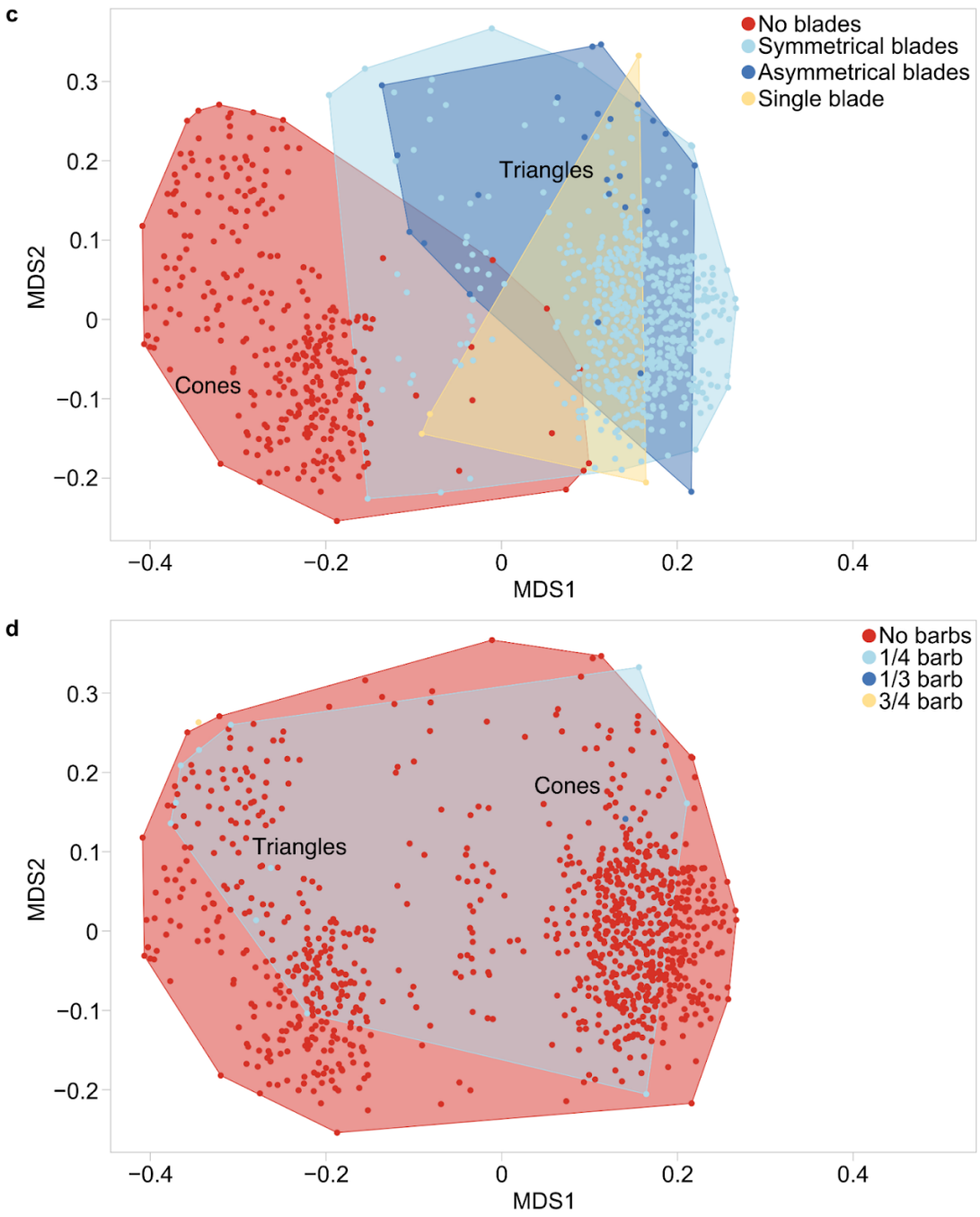

4.4. Discussion

4.4.1. Productivity at Site U1514

Site U1514 productivity is inferred from palaeoproxies of increased Ca/Fe, Si/Fe and Ba/Fe, as well as spikes in IAR (dominantly reflecting fish as sharks are only a small contribution) through the longer-term EECO record and the hyperthermals (PETM

and R and S events). IAR is a metric of productivity integrated over time, and can be a reflection of a small standing stock of fish and sharks but with high turnover or an abundant population with low rates of mortality and reproduction; in both cases IAR would be elevated. Whilst additional sampling throughout the study interval would certainly be beneficial to further validate the robustness of IAR increases, especially through the lesser-sampled EECO, the low sedimentation rate at Site U1514 means IAR represents a real signal of increasing fish abundance over concentration bias due to dissolution of carbonate sediments (except for the PETM where this is a key diagnostic characteristic).

Overall, there is generally higher Ca/Fe in the EECO than immediately preceding or following it, equating to less dissolution or a change in the balance of inputs to the site in a warmer world that would otherwise concentrate ichthyoliths. Benthic foraminiferal $\delta^{18}O$ values reveal deep ocean temperatures of 12.5 to 17.5 °C at Site U1514 (Kirby, 2022) and the site is consistently above the local CCD, ~4 to 4.5 km and shoaling to ~3 to 3.25 km in the EECO; Slotnick *et al*., 2015), except for the hyperthermal punctuations which correspond to rapid declines in weight percentage of calcium carbonate (Vahlenkamp *et al.*, 2020), like the PETM. This change in carbonate is also linked to the site's sedimentation rate reducing from ~1 cm kyr^{-1} to ~0.7 cm ky^{-1} from 49 Ma (Vahlenkamp *et al.*, 2020) and could be a decline in carbonate-producing organisms or transient shoaling of the CCD and associated carbonate burndown, referencing chemical erosion of carbonate below the seafloor in the uppermost few centimetres of sediment (Bralower *et al.*, 2014). However, given the CCD is known to have deepened over the course of the early to middle Eocene (outside of warming events) and the suggestion that carbonate compensation depths

decoupled from climate change during the early Cenozoic (Greene *et al.*, 2019) it is unlikely to be a primary driver of the carbonate changes observed at the site, therefore may correspond to real shifts in primary productivity of carbonate producers.

Furthermore, sustained elevated Ba/Fe through the EECO alludes to enhanced export productivity of organic matter from the surface layer to ocean depths and more efficient carbon and nutrient recycling at this time. It is worth noting recent modelling research into early Eocene twilight zones (200 m to 1,000 m; Crichton *et al.*, 2023) suggests that organic matter may not have reached deeper parts of the ocean as surface productivity would have been metabolised by bacteria faster in a warmer environment in the upper water layers, perhaps even twice as fast as modern marine bacterial respiration (John *et al.*, 2013). This is supported by a known organic matter deficit in Eocene sediments (Olivarez Lyle and Lyle, 2006). John *et al.* (2013) further suggest that in the modern day this could track to a 20% reduction in twilight zone food supply under current low emissions scenarios, potentially reaching over 50% by 2100. As such, whilst surface productivity may have increased, the net effect of export productivity at depth may have made trophic webs through the ocean layers more complex, thus could impact the flux of biological matter to the seafloor and therefore IAR.

Peaks in Si/Fe are offset to the IAR record and some of the hyperthermals, which suggests there could have been delayed responses in increased primary productivity and/or enhanced continental weathering transporting silica to the oceans during the EECO. The latter scenario is supported by the XRF data being mostly lithogenic

inputs derived from chemical and physical weathering of Australia due to elevated temperatures and annual precipitation (for example, Elliot Smith *et al*., 2008; Broz *et al.*, 2024). Such conditions have been modelled for the Eocene of Australia through seasonal monsoons (Carmichael *et al*., 2016; 2017). Kirby (2022) suggests the influx of Si to Site U1514 is likely the result of clay deposition from weathering runoff, as there is a coincident increase in potassium derived from metamorphosed granitic bedrock. Hence, the changes in Si/Fe are likely due to terrigenous rather than biological origin and thus are not easily linked to surface primary productivity.

Yet, this intensified terrestrial hydrological cycle would have delivered more nutrients to the southern Indian Ocean through riverine input, being locally sourced more than transported across ocean basins as the gateway between Australia and Antarctica was not fully open yet (Siesser, 1995). Directly following the EECO at ~48 to 49 Ma, the Tasman Gateway began to open (Bijl *et al.*, 2013), with the XRF data displaying an immediate spike in Ca, Ba and Si, suggesting transient increased productivity, but this is not expressed as changes in IAR in the studied dataset.

Additionally, the matching pattern of the U1514 benthic foraminiferal carbon and oxygen isotopes (Edgar *et al.*, 2022) and the global isotopes (Westerhold *et al.*, 2020) lends support to the interconnected nature of the ocean basins at depth during this time, displaying similar temperature patterns and the potential extrapolation of productivity and diversity analyses to global scale. A coincident rapid negative spike in $\delta^{13}C$ and $\delta^{18}O$ at the PETM are indicative of this hyperthermal, but the relationship is less pronounced for the EECO and MECO. Overall, the EECO has an increasing trend in $\delta^{13}C$, with the warmest part at the onset and punctuated by small decreases

corresponding to hyperthermals. This more prominent decrease at the start of the warming event does indeed match the highest IAR value in the long-term dataset, which otherwise shows a declining trend through the climate perturbation.

Whilst there is some variation, overall XRF palaeoproductivity proxies and IAR data do support increased primary and export productivity during a warmer world.

4.4.2. Open ocean fish diversity at Site U1514

Site U1514 data suggests decoupling of open ocean shallow to mid-water fish diversity and productivity, with relative stability in the fish community diversity across the EECO, despite elevated productivity, and following on from apparent intense origination at the PETM. Exploration of individual coded tooth characteristics through morphospace occupation shows similarity across all time slices (pre-EECO, EECO, post-EECO), thus suggesting assemblage stability. This concurs with previous Paleogene research (Sibert and Norris, 2015; Sibert *et al*., 2016; Sibert *et al.*, 2018) finding overall stability and ecological dominance of pelagic fish communities, with potential equilibrium migration of open ocean species both into and out of the area to find suitable ambient conditions for survival.

Temperature has been proposed as a key contributory factor to fish survival and diversification, with the metabolic theory of ecology based upon the principle that warmer ambient conditions drive increased ectotherm metabolism, which is ultimately less efficient and therefore leads to decreasing body size (Brown *et al.*, 2004). This is also consistent with work finding that the increased oxygen requirement under warmer conditions would cause downsizing of more active predatory (usually larger)

fish (van Rijn *et al.*, 2017). Whilst there does seem to be a general abundance of medium and long teeth compared to end-members of squat and extra-long during the hyperthermals (especially in the PETM), the variety of these tooth shapes occur within both the under 63 μm and over 63 μm size fractions and there is insufficient evidence to suggest a correlation between warming and changes in fish body size at Site U1514 in the studied record. Indeed, some previous research shows different results on body size during warming conditions, with one study finding a compounding effect of smaller fish becoming smaller whilst larger fish grow even larger (Audzijonyte *et al.*, 2020), and another suggesting tooth size and shape linking to body size and trophic level is only possible for carnivorous fish (Keppeler *et al.*, 2020). Given the longer-term dataset and higher-resolution EECO R and S event datasets do not show a distinct change in community composition in terms of size, this could lend support to some level of stability in the fish community post-Palaeocene and that elevated ocean temperatures may not have been significant for fish turnover, but may have contributed towards productivity.

Moreover, there is no clear preference towards cone-shaped teeth (for piercing and holding prey) or triangle-shaped teeth (for slicing) throughout the study interval. These tooth shapes are linked to feeding function of carnivorous predatory fish and thus there is no support for a change in fish form for feeding during the late Palaeocene through middle Eocene. Similarly, many of the other specific coding features (such as blades, barbs and number of parts) do not stand out in morphospace occupation analyses to individually correlate with diversity changes.

Instead, morphotype classification is the main indicator of community diversity across the study interval, though the range chart clearly shows the effect of sampling intensity on morphotype richness and how this may bias the interpretation of the PETM as a major origination event, artificially driving down pre-EECO diversity measurements. Having said this, if the PETM and EECO R and S events morphotype occurrences are removed from the range chart, the lower-intensity long-term dataset still shows an increase in morphotype occurrence at the EECO onset and declining post-event.

Overall, the apparent stasis in fish community turnover across the early Paleogene is not indicative of significant change in response to the ambient environmental patterns of elevated ocean temperatures and nutrient enrichment of surface waters, as might be expected. The reasons for this are further explored in the context of global environmental patterns in Section 4.4.3.

Whilst denticles were rare at Site U1514 and thus the dataset too small for in-depth time series or statistical analyses of open ocean shark communities, denticles can be split into two major groups: linear, which have straight ridges and are found on most modern sharks to assist fluid dynamics for long-distance swimming, and geometric, intricate patterns that are mostly found on their ambush predator counterparts (Sibert and Rubin, 2021). The relative abundance of these in the longer-term dataset favours linear denticles at 64% compared to 36% geometric forms, which matches ratios from the South Pacific Ocean for the late Eocene, but little denticle form data is available for the Palaeocene and early Eocene (Sibert and Rubin, 2021). This may suggest a prevalence of migratory sharks within and across ocean basins to encourage

intermixing of taxa (which could either increase diversity or reduce it due to cosmopolitan species), but the U1514 dataset is too small to further explore this pattern.

4.4.3. Site U1514 productivity and diversity in context of global patterns

Surface waters of the Pacific, Atlantic and Indian ocean sectors of the Southern Ocean were not connected during the early Eocene, hindering dispersal and mixing of water masses. Shallow throughflow from the Pacific to southern Indian Ocean only occurred as the Tasman Gateway opened ~48 to 49 Ma (Bijl *et al.*, 2013), so one might expect open ocean marine community composition and trends to be distinct in each ocean basin. Despite this limited connection between ocean basins during the late Palaeocene and early Eocene, similar patterns of increasing productivity but relative stasis in diversity are also observed at Deep Sea Drilling Project (DSDP) Site 596 in the South Pacific gyre (Sibert *et al.*, 2018; Britten and Sibert, 2020) and Site U1553, Campbell Plateau off the coast of New Zealand (Bissell *et al.*, 2024), suggesting bony fish communities, at least in the Southern Hemisphere, remained stable after the Palaeocene and through the Eocene.

In the South Pacific Ocean there is a noticeable increase in IAR, interpreted as fish productivity during the early Eocene greenhouse, most prominently a ten-fold augmentation across the early Eocene at Site 596, with IAR peaking at ~300 ichthyoliths cm^{-2} Myr^{-1} (Sibert *et al.*, 2018) and ~21,600 ichthyoliths cm^{-2} Myr^{-1} for Site U1553 (Bissell *et al.*, 2024), compared to ~9,000 ichthyoliths cm^{-2} Myr^{-1} for U1514. Yet, origination rates do not keep pace, going from an average ~0.3 capita Lmy^{-1} in the early Palaeocene to ~0.1 capita Lmy^{-1} approaching the PETM and declining

further still to 0.05 capita Lmy^{-1} in the EECO at Site 596 (Sibert *et al.*, 2018) and similarly changing from ~0.3 capita Lmy^{-1} at the PETM to 0.15 capita Lmy^{-1} during the EECO at Site U1553 (Bissell *et al.*, 2024). Whilst PETM origination rates at these two sites are lower than at Site U1514, they are marginally higher for the EECO.

However, caution is warranted in comparing IAR across sites due to a number of factors that may lead to underrepresentation, such as the fact some fish species resorb their teeth during tooth replacement (Sibert and Norris, 2015), incomplete core recovery at drilling sites and the methodologies undertaken. The latter includes ichthyoliths being trapped on filter papers and static energy preventing complete removal from vials for picking, as well as size fractions picked (as 50 to 80% of ichthyoliths occur in the smallest 38 to 63 μm size fraction; Sibert *et al.*, 2017) and the orientation of teeth under reflected light microscopy to accurately morphotype. The smaller IAR reported for Site 596 is likely mostly a factor of methodology, as only ichthyoliths larger than 106 μm were counted compared to 38 to 150 μm for U1553 and 38 to 250 μm for U1514. As the vast majority of teeth (over 80%) are found in the 38 to 106 μm size fraction, the methodological differences may have a significant impact on total IAR calculations. This also factors into the undergraduate PETM and EECO R and S events data at Site U1514, where only ichthyoliths in the 63 to 250 μm size fraction were picked and identified to morphotype. Additionally, estimates of modern productivity at Site U1553 are 100 times higher than for Site 596 (Bissell *et al.*, 2024), thus a similar difference in the Eocene may also have factored into the disparate IAR values. Interestingly, the three sites have an order of magnitude difference between them, with Site 596 known to be highly oligotrophic (nutrient deficient) open ocean with very low productivity, whilst Site U1553 is coastal and

nutrient-rich with high primary productivity; Site U1514 is an open ocean site but with some terrestrial influence and therefore perhaps also benefits from nutrient runoff to support a thriving marine community.

After increasing diversity through the late Paleocene into early Eocene, with a prominent increase in origination around the PETM, there are few additions of novel morphotypes leading into the EECO peak diversity, after which fish communities remain relatively stable. This is particularly noticeable at Site U1553, compared to the gyre location, and closely matches that of Site U1514, which is understandable given their geographical proximity (~5,000 km distance). Here, 136 morphotypes were identified in the Site 596 dataset, but these cannot be correlated to the current morphotype database which has since been updated, and 178 morphotypes at Site U1553, thus relatively similar to the 182 morphotypes observed at Site U1514. Of these, for the latter two sites, 43 are novel to U1553. Sampling through the earlier Palaeocene at Site 596 reveals a less prominent increase in origination at the PETM (18 new morphotypes) and similarly for Site U1553 (31 new morphotypes), compared to the high apparent origination at Site U1514 (73 morphotypes), which is likely purely a result of sampling intensity bias, as individual samples at the PETM have an order of magnitude more teeth than all the pre-PETM samples combined.

Therefore, during the EECO, the fish community was likely responding as a collective, with total abundance increasing and decreasing with the hyperthermals, rather than particular morphotypes, and therefore fish species, taking over as an extremophile community. This pattern of increasing diversity in the Palaeocene but relative stability through the Eocene has also been observed in phylogenetic

analyses of spiny-rayed fishes (Ghezelayagh *et al.*, 2022), carangarian fishes (such as flatfishes and archerfishes; Ribeiro *et al.*, 2018) and carcharhiniform sharks (Brée *et al.*, 2022).

The observed changes have been linked to deep ocean temperatures, with a strong positive correlation between warming and ichthyolith abundance due to warmer bottom waters and thermal destratification (Britten and Sibert, 2020; Marinov *et al.*, 2006; Schmidt *et al.*, 2004). Subsequently, there is a coincident decline in productivity post-EECO as climate cooled into the Eocene-Oligocene transition and Antarctic glaciation. Site U1514 deep ocean temperatures for the EECO (12.5 to 17.5 °C; Kirby, 2022) are in the same range as other ocean basins, such as Site 1262 in the South Atlantic Ocean being ~12 to 16 °C (Barnet *et al.*, 2019) and ~12 to 20 °C at Site 1172 in the South Pacific Ocean (Hollis *et al.*, 2012). Therefore, the interconnectivity of oceans at depth may have played a key role in regulating global ocean temperatures, maintaining warmer water masses towards the poles and preventing glaciation in a greenhouse world, thus proliferating ambient conditions to support elevated fish productivity.

This is coupled with nutrient supply changes, as elevated surface productivity from nutrient input feeds through trophic systems to support elevated export and fish productivity. As a whole, Site U1514 has sustained elevated Ba/Fe across the EECO in line with enhanced export productivity from the surface to deep ocean, which matches that found at ODP Site 738 (Kerguelen Plateau), which has higher measurements of biological barium through the EECO, further evidencing elevated export of organic matter around the Australian continent (Diester-Hass and Faul,

2019). Furthermore, localised currents around the continent may have played a role in encouraging the upwelling of nutrient-rich waters, alike the eastern boundary current 50 to 100 km off the coast of Australia today (Talley *et al.*, 2011), which would have led to warm water incursions via a proto-Leeuwin Current (Vahlenkamp *et al.*, 2020).

4.5. Chapter conclusions

Whilst overall fish abundance increased through the warming events of the early Paleogene in line with elevated temperatures and nutrient influxes from enhanced continental hydrological cycles, standing diversity peaked prior to the EECO and then stabilised with little turnover during the interval of extreme warmth (evidenced by community similarity via tooth morphotype analyses across time slices studied).

Being the first ichthyolith morphotype record from the Indian Ocean, sampling just one site for an entire basin has inherent bias in terms of local effects on fish communities. However, similar patterns are observed across other sites in the open and coastal South Pacific Ocean, with varying environmental settings and sedimentary facies. Ultimately, this is strongly suggestive of a positive relationship between global fish productivity and elevated temperatures.

Though current ichthyolith morphotype records from different ocean basins (Pacific and Indian Oceans) show increased diversity at the PETM and relative stasis through the early to middle Eocene, the robustness of these conclusions would benefit further from additional sampling of the Indian Ocean, as well as venturing into the currently poorly explored (in terms of ichthyoliths) Atlantic Ocean. Importantly, sampling cores

with higher intensity is paramount to achieve sufficient temporal resolution and ichthyolith abundances for morphotyping during both short-lived hyperthermals and extended periods of warming, such as the EECO. To extend the record into the MECO, further work is required to generate robust high-resolution stable isotope stratigraphy to define the event at Site U1514 and precisely date ichthyoliths. Additional sampling may also permit expansion of the denticle dataset within the Indian Ocean in order to conduct analyses on shark population dynamics through the warming interval.

Whilst at different temporal scales, the conclusions of enhanced ichthyolith (and therefore fish) diversity and productivity during short-lived warming events (PETM), but stability in diversity across protracted warming (EECO) is an important insight for the future of our ocean ecosystems. Given the acceleration of modern global warming, the scenario of enhanced productivity and diversity of the PETM may be applicable, but it remains to be seen whether fish communities can keep pace with the rapidity of current climate change. Looking to the past is an important way to inform models for future scenarios of climate change and how Earth's interconnected systems may respond, beyond solely extrapolating from modern carbon dioxide emissions and global temperatures. Therefore, the Mentelle Basin ichthyolith community is important as it highlights how current and future global warming may positively impact fish productivity and diversity, therefore securing a food and income source for the populations who rely on them.

CHAPTER FIVE

Actinopterygian productivity, community structure and evolutionary patterns in the South Atlantic Ocean during the Middle Eocene Climate Optimum

5.1. Chapter introduction

The Eocene epoch is a tale of two halves, experiencing greenhouse climate conditions from the PETM through to the EECO (Vahlenkamp *et al*., 2020), followed by a distinct cooling trend through to the Oligocene transition (~34 Ma) when ice sheets formed on Antarctica (Zachos *et al*., 1992; Liu *et al*., 2009). However, this descent into an icehouse world was punctuated by a short-lived warming event at ~40 to 40.5 Ma, the Middle Eocene Climate Optimum (MECO). The event lasted ~400 to 700 kyr and is characterised by gradual warming (over ~400 to 500 kyr) through to the peak (lasting less than 100 kyr) at 40 Ma, followed by rapid cooling over the following ~50 to 100 kyr (Bohaty *et al.*, 2009; Moebius *et al.*, 2015; Rivero-Cuesta *et al.*, 2019).

The MECO is identified based upon a distinct negative oxygen isotope ($\delta^{18}O$) excursion of ~0.5 to 1.0 ‰ from foraminiferal and bulk sediment records recorded globally (including Bohaty *et al.*, 2009; Boscolo-Galazzo *et al.*, 2014; Edgar *et al.*, 2020), whilst a smaller negative carbon isotope ($\delta^{13}C$) excursion of less than 0.5 ‰ can be observed at some but not all sites during the $\delta^{18}O$ minimum (Giorgioni *et al.*, 2019), superimposed on an increasing $\delta^{13}C$ trend that peaks post-MECO (Bohaty and Zachos, 2003). Such a small $\delta^{13}C$ change is unusual for warming events and has proven challenging to recreate through modelling and for determining the driving mechanism(s), particularly as it is not geographically ubiquitous (Sluijs *et al.*, 2013).

Atmospheric carbon dioxide (pCO_2) levels rose by ~320 parts per million (ppm; Heneghan *et al.*, 2020), from ~550 ppm to 870 ppm, during the event, though some estimates predict much larger change with increases in pCO_2 of 2,000 to 3,000 parts per million by volume (ppmv; Bijl *et al*., 2010). Associated warming through the MECO produced a pole to equator thermal gradient of ~14 °C (Inglis *et al*., 2015), though across the entire Eocene this gradient was 19 to 26 °C (Cramwinckel *et al.*, 2018) compared to ~30 °C today (Gaskell *et al.*, 2022; Eichenseer and Jones, 2024). Kirby (2022) identified a ~1 to 3 °C increase in latitudinal gradient compared to pre-MECO. Surface and bottom waters warmed ~3 to 6 °C (Bijl *et al.*, 2010; Boscolo-Galazzo *et al.*, 2014) and became more acidic as the carbonate compensation depth (CCD) shoaled by ~500 to 1,500 m globally, leading to a decrease in carbonate mass accumulation rates (Bohaty *et al.*, 2009).

Given the smaller increase in pCO_2 (~320 ppm) compared to the preceding warming events of the PETM (a wide range from 200 to 2,800 ppm but average ~1,500 ppm; McInerney and Wing, 2011) and EECO (~1,400 ppm; Anagnostou *et al.*, 2016), the release of isotopically light carbon from methane hydrates, peatland, permafrost and heating of organic carbon from intrusions, as have been invoked for causing the earlier Eocene warming events, are not considered the main drivers of the MECO warming (for example, Svensen *et al.*, 2004; Bohaty *et al.*, 2009; Lunt *et al.*, 2011; DeConto *et al.*, 2012). Instead, there is a potential link to increased volcanic activity of the Iranian Azerbaijan–Bazman Arc occurring in the Neotethys subduction zone, but this requires further work to precisely date and confidently associate these events (van der Boon *et al*., 2021). Recent work has further suggested 1.5 Myr-long (~40.5 to 42 Ma) ridge/arc volcanism and hydrothermal activity along Broken Ridge and the

Kerguelan Plateau, south Indian Ocean, could have led to prolonged carbon dioxide release as Australia rifted away from Antarctica (Lim *et al.*, 2024). Besides volcanism, the temperature rise has also been linked to the 2.4 Myr eccentricity cycle (Westerhold and Röhl, 2013) and may have been sustained by increased clay formation retaining carbonate-forming cations on land, disrupting the carbonate-silicate cycle and leading to an accumulation of CO_2 in the atmosphere (Krause *et al.*, 2023).

Furthermore, Bohaty *et al.* (2009) suggest that the CCD remained above pre-event depths of ~3,000 m for 100 to 250 kyr and link this to CO_2 increasing incrementally through the MECO, meaning the source of atmospheric CO_2 couldn't have been initiated by a single mass release event and could support the aforementioned prolonged volcanism. Arimoto *et al.* (2020) further suggest these changes in carbonate chemistry may be linked to eccentricity-scale influences on seasonality, weakening continental weathering and nutrient supply to the oceans, as well as seasonal development of the thermocline. This reduced continental silicate weathering also means an alternative mechanism behind the rapidity of the cooling (by ~6 °C; Bohaty *et al.*, 2009) at the MECO's termination is needed, which is postulated to be a result of a significant increase in organic carbon burial, based upon positive shifts in bulk carbonate and foraminiferal $\delta^{13}C$ values.

The effect of this MECO warming and reduced upper ocean stratification (Arimoto *et al.*, 2020) on marine life is most notably seen in a decline in planktic foraminifera mass accumulation rates, indicating a reduction in primary and export productivity (Boscolo-Galazzo *et al.*, 2014; Lowery *et al.*, 2020). For example, Edgar *et al.* (2013)

identified temporary mass ‘bleaching’ of planktic foraminifera hosting photosymbionts, with reduced test sizes and overall abundance, primarily linked to ocean temperature increases, but also acidification and nutrient supply changes. Additionally, pelagic siliceous phytoplankton responded differently across the globe, with reduced accumulation during the MECO peak and termination in the North Atlantic (Witkowski *et al.*, 2014) but an increase in the Southern Ocean (Witkowski *et al.*, 2012), which could be a reflection of nutrient input to the respective basins. Conversely, benthic foraminiferal assemblage composition remained stable across the MECO, suggesting the warming was gradual enough for them to adapt (Moebius *et al*., 2015).

For marine vertebrates, Sibert *et al.* (2018) identified pelagic fish origination pulses in the early Paleogene based upon ichthyolith morphotypes, following the end-Cretaceous mass extinction opening ecological niche space in the Pacific Ocean to enable speciation. Further ichthyolith work across global basins, including the Atlantic Ocean, has also identified increases in marine vertebrates post-Cretaceous, specifically a proliferation of fish over sharks (Sibert and Norris, 2015). However, little is known of fish and shark responses to the MECO specifically, with few records and none at high resolution. Although, Adnet *et al.* (2020) did identify changes in large predatory shark populations with Carcharhiniformes (ground sharks) replacing Lamniformes (mackerel sharks) in nearshore palaeoenvironments of the Tethys seaway during the MECO, with the decline of Lamniformes being global and continuing through to their present day diversity (Condamine *et al.*, 2019).

Following on from early Paleogene productivity increases alongside rapid bony fish diversification across the PETM (~200 kyr-long hyperthermal, Chapter Four; McInerney and Wing, 2011) and subsequent stasis over the extended EECO warming (~4.12 Myr interval), the MECO provides an interesting opportunity to explore fish and shark abundance and diversity patterns during an intermediate duration warming event (~500 kyrs), characterised by a different magnitude and pattern of warming: gradual warming and rapid cooling versus rapid warming and gradual cooling of the PETM or gradual warming and cooling of the EECO.

To explore fish and shark palaeocommunity response to the MECO, ichthyoliths (bony fish teeth and shark denticles composed of calcium phosphate) were isolated from two ocean drilling sites in the South Atlantic Ocean (Ocean Drilling Project (ODP) Site 702, Islas Orcadas Rise, and ODP Site 1263, Walvis Ridge) to generate a high-resolution proxy for population dynamics. These two locations permit comparison of abundance and diversity of ichthyoliths, and therefore fish and sharks, between sites to validate patterns identified in the ocean basin, as well as wider comparison to other early Paleogene warming events.

5.2. Methods

5.2.1. Sampling sites

ODP Site 702 (50°56.760′S, 26°22.122′W; Ciesielski *et al.*, 1988; Figure 5.1) was cored across Holes A and B in 1987 as part of Expedition 114, on the Islas Orcadas Rise, a 500 km-long and 180 km-wide north-northwest trending ridge in the South Atlantic Ocean that is the eastern boundary of the Georgia Basin and formed due to

rifting in the early Paleogene (Rivero-Cuesta *et al.*, 2019). This rifting created a passageway between the adjacent Meteor Rise that permitted throughflow of waters from the South Atlantic northwards. Palaeogeographic reconstructions place the site at a palaeolatitude of ~53.5 °S at 40 Ma (Müller *et al.*, 2018) and palaeodepth of 2,000 to 2,200 m during the Eocene (Heneghan *et al.*, 2020). Cored sediments cover the late Palaeocene to Quaternary, with 100% and 66% recovery in Holes A and B respectively (Ciesielski *et al.*, 1988). Linear sedimentation rates were ~10 m Myr^{-1} for the late Palaeocene to early middle Eocene, increasing to ~14 m Myr^{-1} through the remainder of the Eocene (Ciesielski *et al.*, 1988). For this study, cored early to late Eocene sediments occur in lithologic subunit IIB (~170 m thick), predominantly comprised of nannofossil chalks and oozes, with high (up to 95%) carbonate content (Raymond *et al.*, 1991).

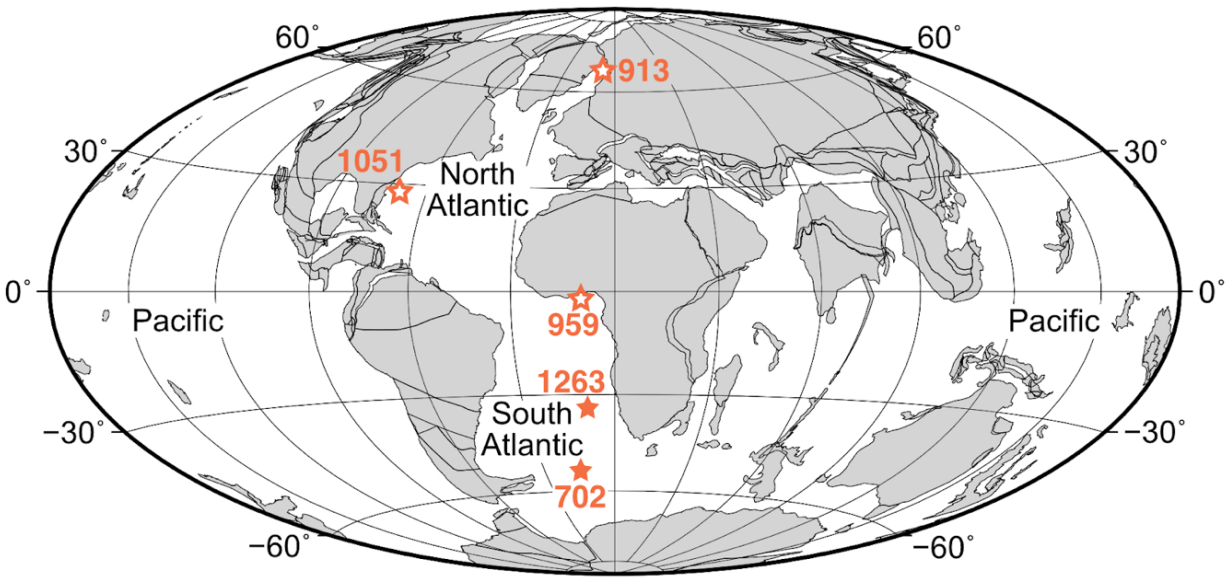

40 Ma Reconstruction
★ Studied MECO sites
☆ MECO ichthyoliths not available for study

Figure 5.1. *(Previous page)* Palaeogeographic reconstruction of the middle Eocene at 40 Ma from the Ocean Drilling Stratigraphic Network (www.odsn.de; Hay *et al.*, 1999) with filled orange stars marking the location of the study sites in the South Atlantic Ocean, 702 and 1263, at 40 Ma (Müller *et al.*, 2018). Hollow orange stars denote Sites 913, 959 and 1051 that were initially considered for study but could not be included here for ichthyolith analyses.

ODP Site 1263 (28°32′S, 2°47′E; Zachos *et al*., 2004) was cored across four holes (A to D) in 2003 during Expedition 208 on the north-facing flank of Walvis Ridge, also in the South Atlantic section of the Southern Ocean. During the Eocene, the site was located at a palaeolatitude of ~34.5 °S (Müller *et al.*, 2018) and a palaeodepth of ~2,000 m (Zachos *et al*., 2004). The expedition cored sediments across the late Palaeocene to Pleistocene to capture Cenozoic climate events, with 100% recovery across the four holes (Zachos *et al*., 2004). Linear sedimentation rates peaked at ~23 m Myr^{-1} in the late Palaeocene, dropping to ~8 m Myr^{-1} through the early Eocene and declining further still to ~2 m Myr^{-1} in the middle Eocene (Zachos *et al*., 2004). Lithologic subunit IB (~187 m thick in Hole B; Zachos *et al*., 2004) covers the early to late Eocene at the site, with nannofossil oozes dominating the sedimentary succession.

Whilst ODP Sites 913 (Greenland Basin, North Atlantic), 959 (Cote d'Ivoire-Ghana Marginal Ridge, eastern equatorial Atlantic) and 1051 (Blake Nose Plateau, western North Atlantic) were originally intended for study to produce a transect through the Atlantic Ocean, limited core availability for the first two (~32% and ~58% respectively; Myhre *et al.*, 1995; Mascle *et al.*, 1996) meant there were fewer samples for

processing that covered the interval of study. Those that were available were subjected to the same lab procedure to attempt ichthyolith extraction, but would not break down due to their lithologies (siltstone and claystone), and ichthyoliths were unable to be extracted, hence could not be included in this research. Although ODP Site 1051 could be fully processed, the samples were comparatively unfossiliferous with too few ichthyoliths for robust analyses.

5.2.2. Age model

Here, the published age model of Heneghan *et al.* (2020; Figure 5.2) was used, which correlates Sites 702 and 1263 to the Geologic Timescale 2012 (GTS2012; Gradstein *et al*., 2012) based upon a composite of $\delta^{18}O$ and $\delta^{13}C$ isotopes, and magnetostratigraphy. Within this, the MECO duration is identified between 40.110 to 40.516 Ma based upon the initial decrease and the most negative $\delta^{18}O$ values, but here the end is extended to 40.096 Ma to encompass the carbon isotope excursion of Bohaty *et al.* (2009), meaning the event lasted ~400 kyrs.

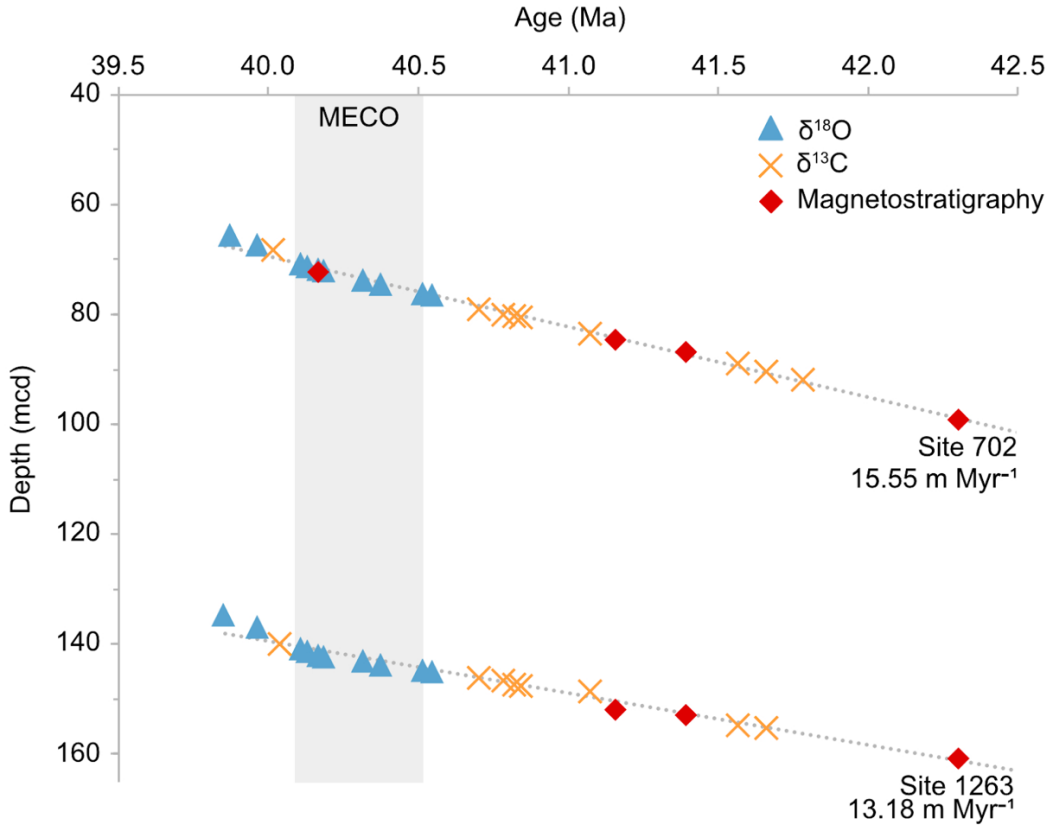

Figure 5.2. Age-depth model and average sedimentation rates for Sites 702 and 1263 from Heneghan *et al.* (2020) correlated to GTS2012 (Gradstein *et al*., 2012). Grey shaded box defines MECO according to $\delta^{18}O$ changes.

This age range for the MECO falls closely in line with that calculated individually for Site 702 based upon bulk isotope data from Bohaty *et al.* (2009), defined as 40.096 to 40.512 Ma, with the peak occurring at 40.096 to 40.194 Ma and lasting 98 kyrs. Additionally, it aligns with ODP Site 1263 bulk isotope data from Bohaty *et al.* (2009) and benthic isotopes from Boscolo-Galazzo *et al*. (2014). Overlaying both datasets reveals a very similar pattern in oxygen isotopes to define the MECO at Site 1263 as 40.100 to 40.495 Ma, with the peak for the former defined as 40.100 to 40.165 Ma (lasting 65 kyrs), and the latter as 40.118 to 40.191 Ma (lasting 73 kyrs).

5.2.3. Sample selection and preparation

For Site 702, 15 samples were obtained from the International Ocean Discovery Program Bremen Core Repository, Germany, taken at ~30 cm (=25 kyr) intervals from Hole B cores, with five samples pre-MECO (older than 40.516 Ma), five samples during the warming event including at least one within the peak (40.110 to 40.516 Ma), and five samples post-MECO (younger than 40.110 Ma). These time bins are defined based upon the age model (Heneghan *et al.*, 2020). For Site 1263, the same spatial and temporal interval over the three MECO phases were requested, though only four samples were available for the pre- and mid-MECO due to core availability. All samples were processed to separate the over 38 μm sieve size fraction from which the ichthyoliths were picked, as in Chapter 4 section 4.2.3 and section 2.2.1, at the School of Geography, Earth and Environmental Sciences at the University of Birmingham, UK. Ichthyolith images are available via the University of Birmingham's eData repository *titled "Bird, Hannah (2024) Research data supporting PhD thesis 'Actinopterygian and chondrichthyan palaeocommunity responses to early Cenozoic global warming'"* (DOI: 10.25500/edata.bham.00001169).

5.2.4. Stable carbon and oxygen isotopes

Isotopic data was used to identify patterns of climate change across the MECO, particularly $\delta^{18}O$ as an indicator of temperature change as the $\delta^{13}C$ excursion was not characteristic of the event. For both Sites 702 and 1263, bulk sediment isotopes originated from Bohaty *et al.* (2009), as later isotopic studies (Rivero-Cuesta *et al.*, 2019; Boscolo-Galazzo *et al.*, 2014) are based upon this earlier dataset. Westerhold *et al.* (2020)'s composite record of benthic foraminiferal global stable carbon and

oxygen isotope data was used to compare site-specific with worldwide climate patterns, though the two are offset due to the nature of the latter record being matched across multiple sites.

5.2.5. X-ray fluorescence data

X-ray fluorescence (XRF) data is limited for Sites 702 and 1263, but one record does exist for the former (Rivero-Cuesta *et al.*, 2019). The published ages were correlated to the age model used here (Heneghan *et al.*, 2020) for plotting across the MECO peak.

5.2.6. Ichthyolith accumulation rate

Fish and shark productivity can be quantitatively measured via ichthyolith accumulation rate (IAR), which is a function of ichthyolith abundance, sedimentation rate and dry bulk density (ich cm^{-2} kyr^{-1}; Sibert, 2016; see section 4.2.6 of Chapter Four for an explanation of the calculation). Site 702 dry bulk density was derived from the shipboard report (Ciesielski *et al*., 1988), though only one or two dry bulk density measurements were available per core section so a single or average of two was used, where applicable.

Dry bulk density data is not available for Hole B of Site 1263, from which the studied samples are derived (cores 8H and 9H), hence the relevant data was obtained from Hole A (cores 14H and 15H; Zachos *et al.*, 2004), with matching nannofossil ooze lithologies. An average of the available six dry bulk density values in the corresponding lithology were therefore used in the IAR calculation at 1.2712 g cm^{-3}, which has a maximum and minimum standard deviation of 0.0488 g cm^{-3} and 0.0362

g cm^{-3} respectively. Sibert *et al*. (2014) notes that small changes in dry bulk density do not have significant impacts on the IAR calculation.

5.2.7. Ichthyolith morphotypes

An ichthyolith tooth character coding system (updated from Sibert (2016) and Sibert *et al.* (2018); Figure 2.1) was employed to identify the internal and external shape and structure of fish teeth and assign to morphotype, as a method of observing change in morphotype diversity, and therefore feeding function, through time. Refer to sections 2.2.2 and 4.2.7 for detailed explanation of the coding technique and resources used, as well as Appendix Table 5.1 for morphotype coding of the studied teeth. Due to the limited number of denticles within the dataset, these were not studied further beyond initial count.

5.2.8. R scripts

The *ichthyoliths* R packages developed by Dr Elizabeth Sibert (available from: https://github.com/esibert/ichthyoliths) were used to analyse the tooth morphotypes in R Studio (version 4.3.2; R Core Team, 2023) in terms of range charts, origination and extinction rates (Foote, 2000) and non-metric multi-dimensional scaling ordination for diversity clustering using the R package *vegan* (Oksanen *et al.*, 2022).

5.3. Results

5.3.1. Ichthyolith abundance and accumulation in the South Atlantic Ocean

Ichthyoliths from Sites 702 and 1263 span 39.6 to 41.1 Ma, including pre-MECO, the onset and peak of the event and post-MECO. The total number of ichthyoliths (teeth

and denticles) across both sites is 1,096 (574 and 522 from Sites 702 and 1263 respectively), composed of 999 teeth and 97 denticles, with an average of 36 ichthyoliths per sample. As for Chapter Four, the denticle dataset is relatively small for evolutionary studies, with a maximum of nine in any individual sample, thus is not considered in further detail here.

Individual sample ichthyolith counts follow a similar pattern of change and absolute values across the study interval. Ichthyolith counts vary from 11 to 82 across the dataset (Figure 5.3), with ~30 to 50 ichthyoliths pre-MECO, increasing to a maximum at both sites at the end of peak MECO (69 and 82 ichthyoliths respectively for Sites 702 and 1263), before rapidly declining to pre-MECO counts after the event. To more robustly compare the changes in ichthyoliths between the two sites, abundance takes into consideration both changes in sedimentation rate and the effect of dry bulk sample weight to standardise the number of ichthyoliths present in a unit of sediment. Abundance is moderately more varied for Site 702 pre-MECO, from ~1 to 2.5 ichthyoliths g^{-1}, but higher at Site 1263 at 1.5 to 2.5 ichthyoliths g^{-1}, with the caveat of the gap in sample availability between 40.4 to 40.7 Ma at the latter site making the pattern slightly less clear. At both locations there is a sharp increase in abundance at the end of the MECO peak, reaching a maximum of 3.6 and 3.4 ichthyoliths g^{-1} at Sites 702 and 1263 respectively. The post-MECO recovery is less steep at Site 702, gradually declining back to pre-MECO levels, whilst at Site 1263 the decline in abundance is abrupt and reduced compared to pre-MECO (~0.75 to 1.5 ichthyoliths g^{-1}).

To further place this abundance in the context of ichthyolith accumulation per unit of time, IAR corrects for the effect of sedimentation rate by calculating ichthyolith flux to the seafloor. At Site 702, IAR is generally decoupled from the plateaued sedimentation rate (Figure 5.4, Appendix Figure 5.1), varying ~30 to 80 ichthyoliths cm^{-2} kyr^{-1} pre-MECO and into the MECO onset, increasing to ~210 ichthyoliths cm^{-2} kyr^{-1} at the end of peak MECO coincident with a doubling of the sedimentation rate by more than 1 cm kyr^{-1}. IAR decouples from sedimentation rate post-MECO, as the former declines to a low of 30 ichthyoliths cm^{-2} kyr^{-1} and the latter remains elevated. A similar pattern is observed at Site 1263, though an increase in sedimentation rate of 1.63 cm kyr^{-1} occurs during the MECO onset at 40.36 Ma and coincides with a near ten-fold increase in IAR to a maximum of 156 ichthyoliths cm^{-2} kyr^{--1}. IAR then remains elevated through the rest of the MECO, until a rapid decline to 78 ichthyoliths cm^{-2} kyr^{-1} at the end of the peak and a more gradual decline thereafter. Between the two locations, Site 702 consistently has higher IAR than Site 1263 when comparing across the same time slice.

IAR values at Sites 702 and 1263 are two to three orders of magnitude higher than for Site U1514 in Chapter Four and highlights the significant role of sedimentation rate in ichthyolith accumulation. For example, if the Site U1514 sedimentation rate was doubled to be akin to those at Sites 702 and 1263, then the former's IAR would be two orders of magnitude greater too.

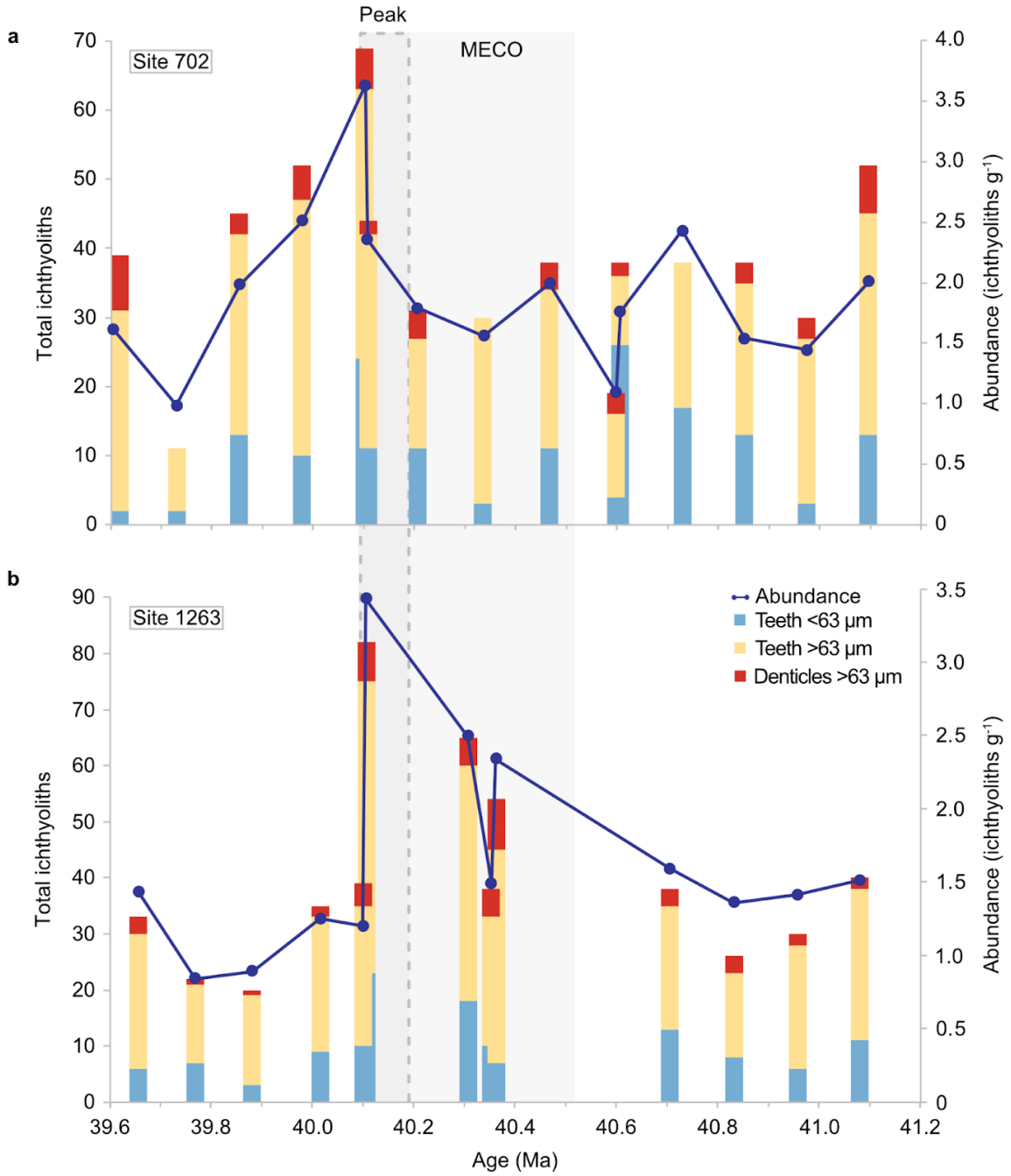

Figure 5.3. Total ichthyolith counts across the MECO for Sites 702 (**a**) and 1263 (**b**) differentiated by ichthyolith component (teeth and denticles) and size fraction (38 to 63 µm and over 63 µm), plotted against abundance to standardise for dry bulk sample weight. In all figures, the lighter grey shaded box denotes the MECO onset, whilst the darker box with dashed boundary outlines the peak defined by the interval of $\delta^{18}O$ minima.

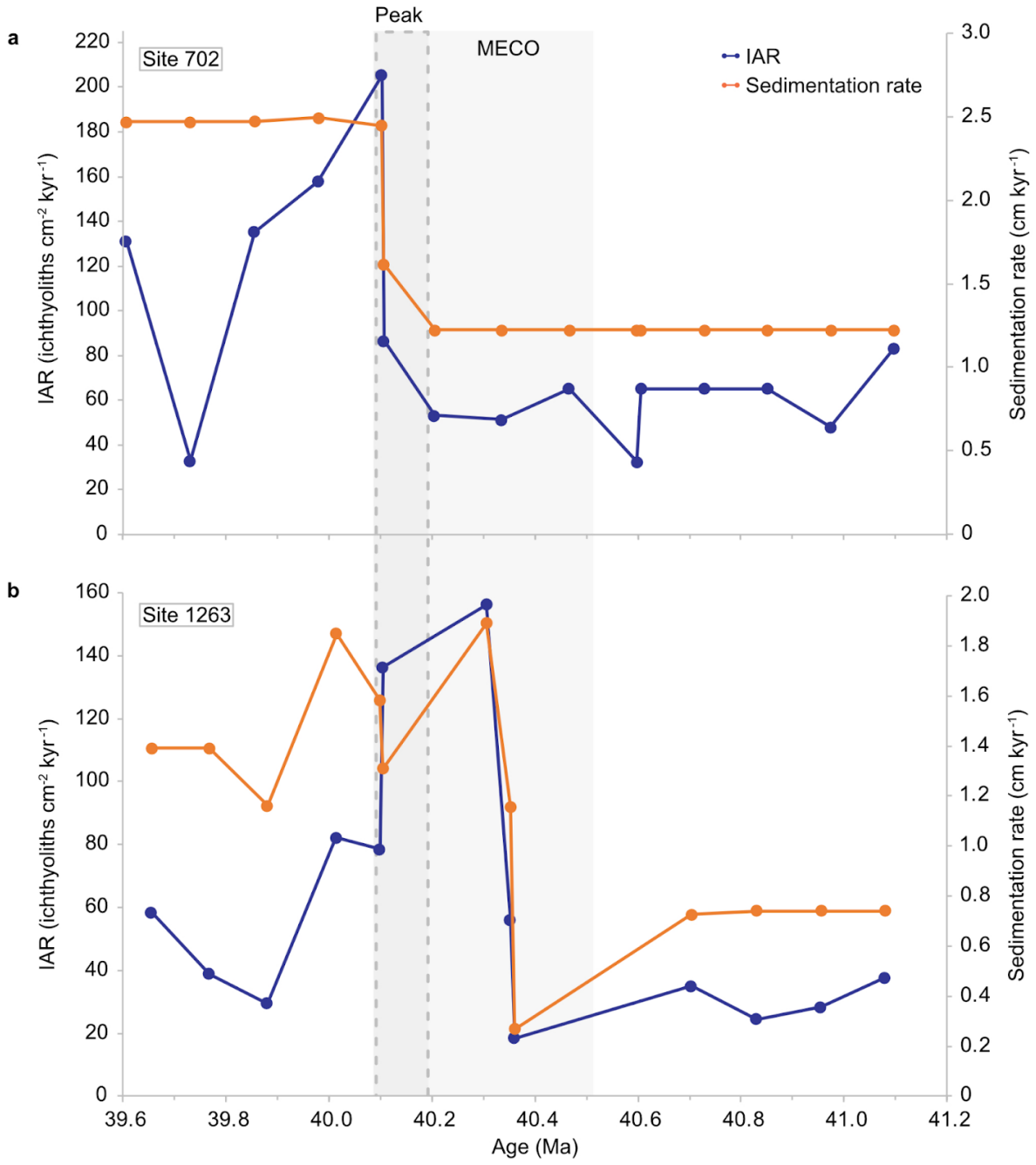

Figure 5.4. Ichthyolith accumulation rate and sedimentation rate across the MECO for Sites 702 (**a**) and 1263 (**b**).

5.3.2. Climate patterns

5.3.2.1. Carbon and oxygen isotopes

Correlation of the global (Westerhold *et al.*, 2020) and site-specific (Bohaty *et al.*, 2009) benthic carbon and oxygen isotopes overall display matching patterns of change across the study interval, though with some temporal offset (Figure 5.5). This offset is attributed to using different timescales, as well as the former being a composite from multiple sites, with high influence from the Southern Ocean and a degree of compression and lengthening of the global stack at various points. As such, the MECO is here defined based upon the site-specific oxygen isotopes.

Both Sites 702 and 1263 display highly fluctuating $\delta^{18}O$ values prior to the MECO, varying 0.3 to 0.9 ‰ for the site-specific isotopes, with a gradual decrease through to peak MECO. The lowest $\delta^{18}O$ values occur at ~40 Ma across numerous Southern Ocean sites (Bohaty *et al.*, 2009), with a decrease observed beginning ~100 kyr beforehand and marking the start of the peak event, as seen in Figure 5.5. During the peak, Site 702 experienced a lower $\delta^{18}O$ of approximately -0.5 ‰ compared to approximately -0.2 ‰ for Site 1263, before an abrupt increase marking the end of the event. Whilst $\delta^{18}O$ returned to pre-MECO values at Site 702, at Site 1263 they increased beyond previous levels to ~1.2 ‰.

The change in $\delta^{13}C$ is less clear, being highly variable preceding and during the MECO (including the peak), though the end of the event is marked by a positive carbon shift, with Site 702 experiencing a ~0.3 ‰ increase and Site 1263 a ~0.5 ‰ rise. $\delta^{13}C$ values remain elevated compared to pre-MECO levels thereafter across the study interval. Overall, there is a weak positive correlation between $\delta^{18}O$ and

$\delta^{13}C$ with a combined linear regression of 0.0169, though it is slightly stronger for Site 1263 (Appendix Figure 5.2).

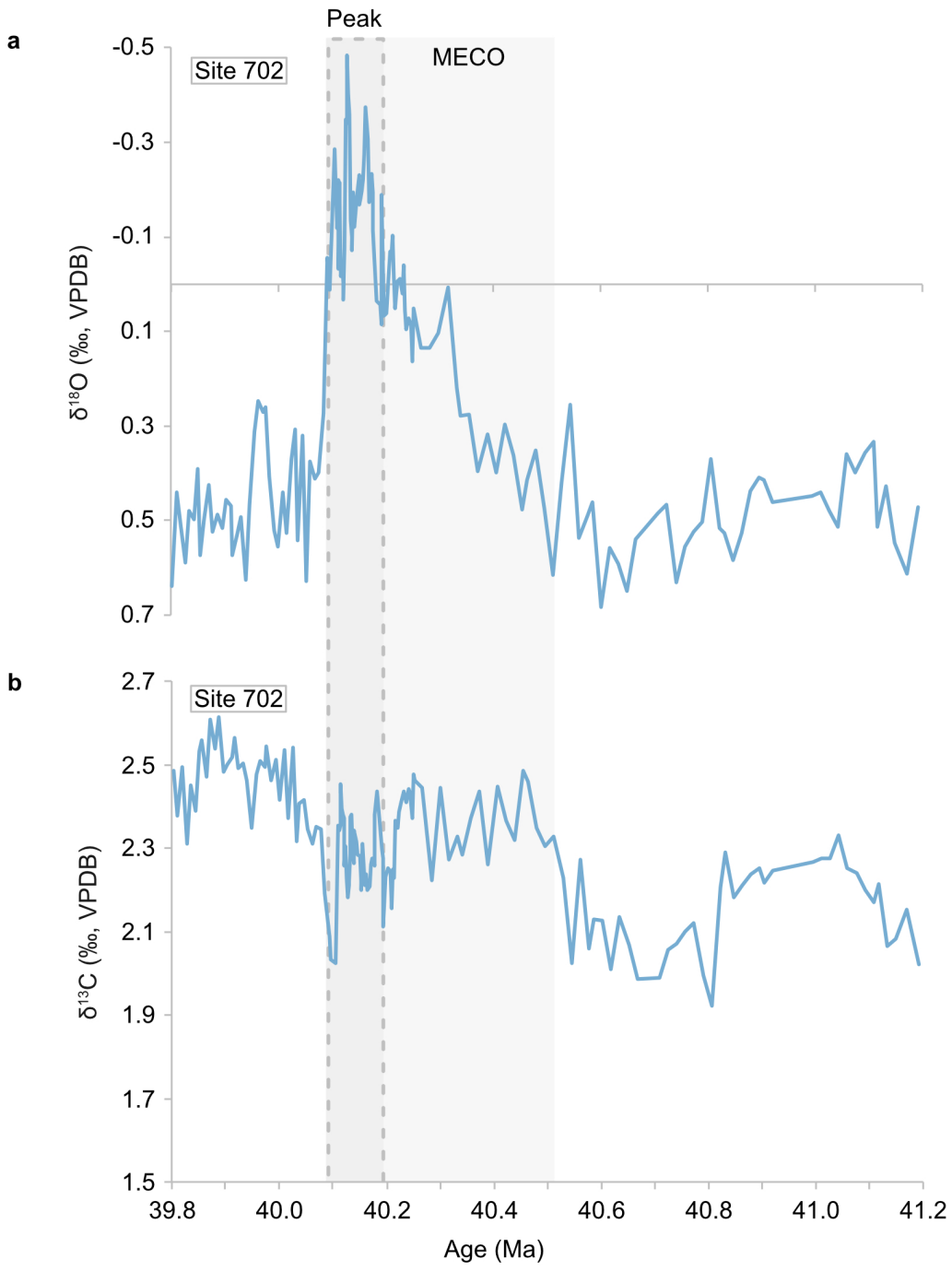

Figure 5.5. Bulk carbon and oxygen isotopes for Sites 702 (**a**, **b**) and 1263 (**c**, **d**; Bohaty *et al.*, 2009). Parts **c** and **d** continue overleaf.

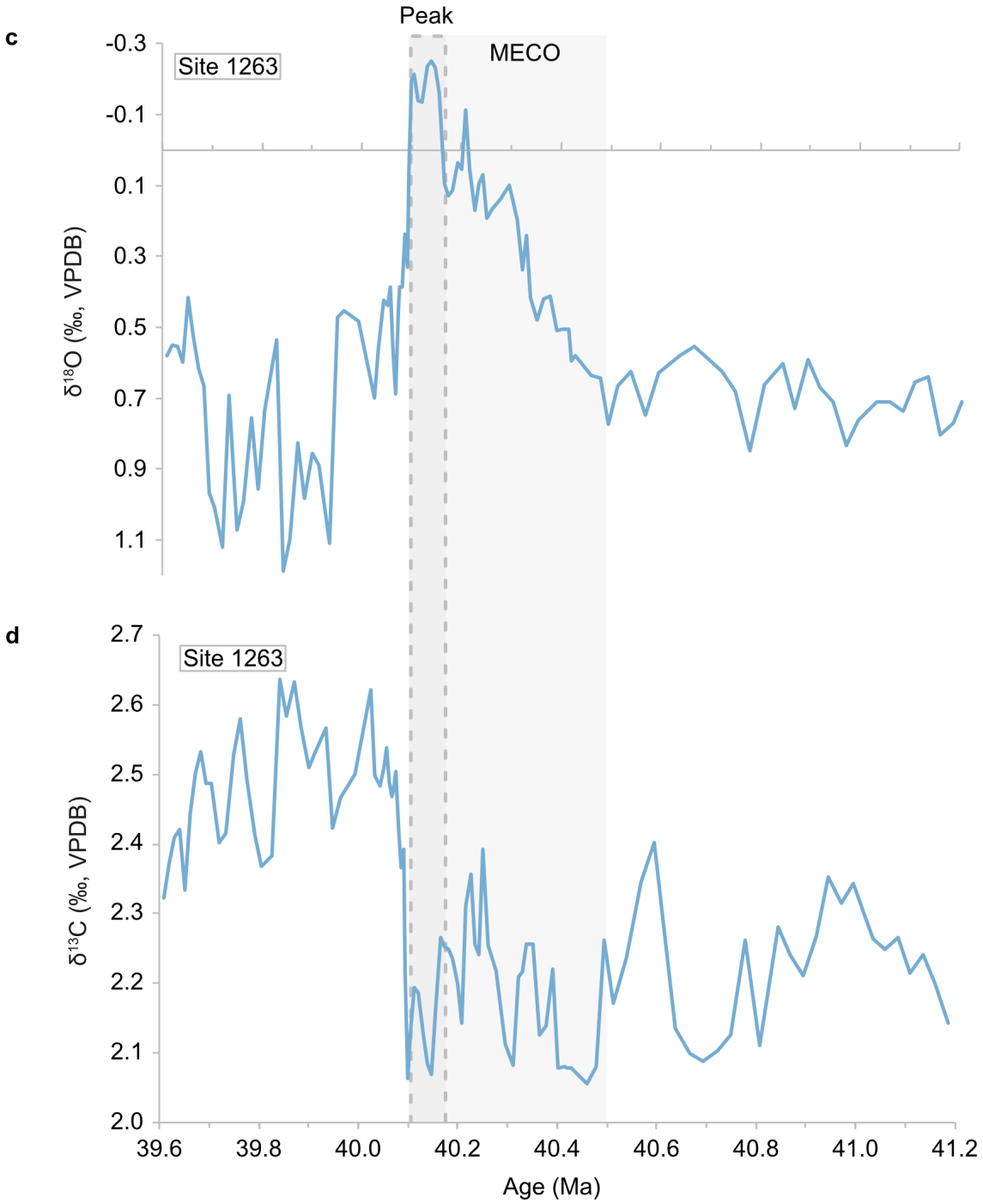

5.3.2.2. Environmental proxy data

Sediment geochemistry can be used to infer ocean productivity, especially calcium values as this can link to the primary and export productivity of organisms such as planktic and benthic foraminifera and calcareous nannofossils. It may also link to

ocean acidification, a common signal of hyperthermal events, as for the PETM (Foster *et al.*, 2018). There are few x-ray fluorescence (XRF) analyses for Sites 702 and 1263, but one record of calcium-iron (Ca/Fe) ratios does exist for Site 702 (Figure 5.6; Rivero-Cuesta *et al.*, 2019). This Ca/Fe record spans peak and post-MECO and is highly variable (38.6 to 242.4) throughout, but the lowest Ca/Fe values occur in the peak of the MECO at 40.16 Ma.

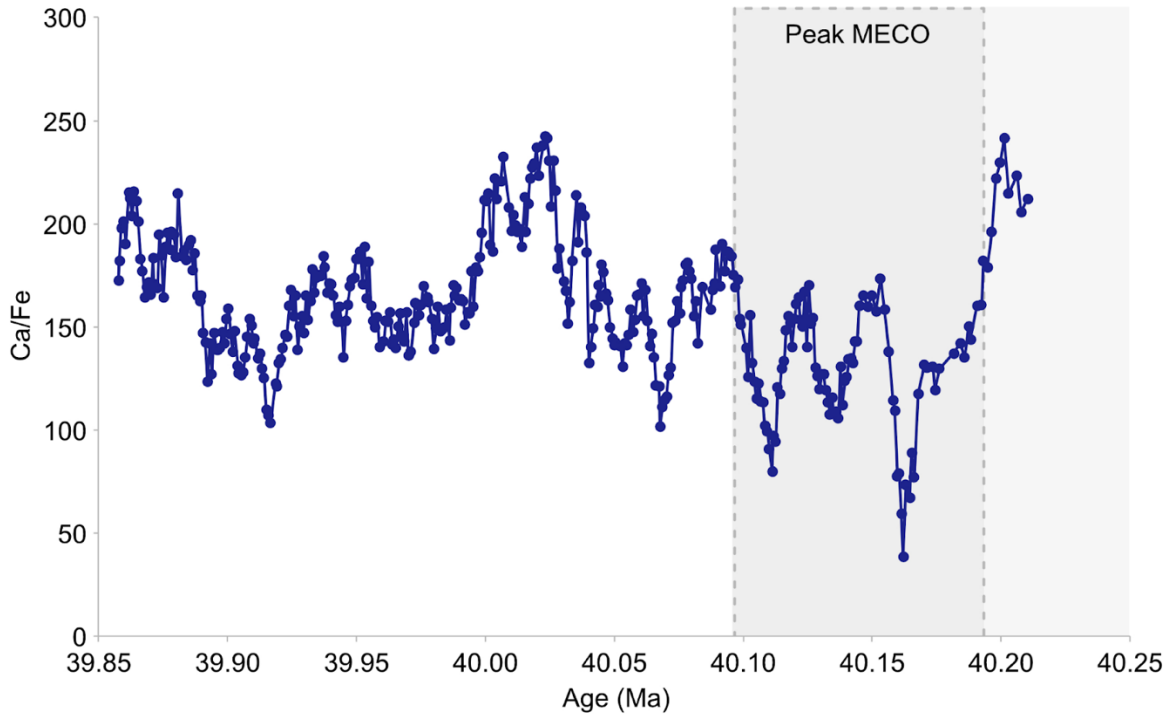

Figure 5.6. Ca/Fe ratios across the MECO interval (Rivero-Cuesta *et al.*, 2019). Note the full extent of the MECO onset (lighter grey shaded box) is not covered by the data and is off the scale of the figure.

This reduction in carbonate matches records of lower foraminifera abundance and accumulation (Figure 5.7), which is calculated similar to IAR in the number of foraminifera per unit of sediment in a particular time slice. Whilst there are no records of planktic foraminifera accumulation rate (PFAR; an estimate of primary productivity)

for Sites 702 and 1263, benthic foraminifera accumulation rates (BFAR) can be used to infer export productivity. Coarse fraction accumulation rates (CFAR) are the combined carbonate input from planktic and benthic foraminifera (as well as all coarse sediment grains over 63 μm), so can semi-quantitatively represent both types of productivity. At both locations, BFAR increases into the MECO, with values for Site 702 tripling from 510 to 1,625 foraminifera cm^{-2} ky^{-1}, whilst for Site 1263 there was a five-fold increase from 56 to 284 foraminifera cm^{-2} ky^{-1}. During the MECO onset, however, BFAR then starts to decline through to the peak of the event reaching a low of 191 and 82 foraminifera cm^{-2} ky^{-1} for Sites 702 and 1263 respectively. This shift is more rapid at Site 702, with an abrupt reduction occurring over ~100 kyr and a more gradual decrease over the next ~300 kyr.

CFAR displays a similar pattern to BFAR for Site 1263, increasing through to the early MECO and decreasing during the remainder of the onset and peak, declining from 0.05 to 0.01 coarse grains cm^{-2} ky^{-1}, finishing with lower values post- than pre-MECO. However, the pattern at Site 702 is less clear, being highly variable within an order of magnitude (0.01 to 0.10 coarse grains cm^{-2} ky^{-1}) across the pre-MECO and event onset, reaching a low (0.02 coarse grains cm^{-2} ky^{-1}) at the start of the peak. There is then a rapid increase over the next ~100 kyr to a maximum of 0.12 coarse grains cm^{-2} ky^{-1} at the end of the peak and a return to pre-event levels thereafter.

Beyond carbonate, silica-iron (Si/Fe) ratios can be an indicator of primary productivity from siliceous microorganisms and/or terrigenous input from continental weathering. No Si/Fe data is available for the two sites but smear slides (Ciesielski *et al.*, 1988)

reveal the dominant lithology in each core is composed of 94 to 95% nannofossils with only trace amounts of siliceous microfossils such as diatoms and radiolarians.

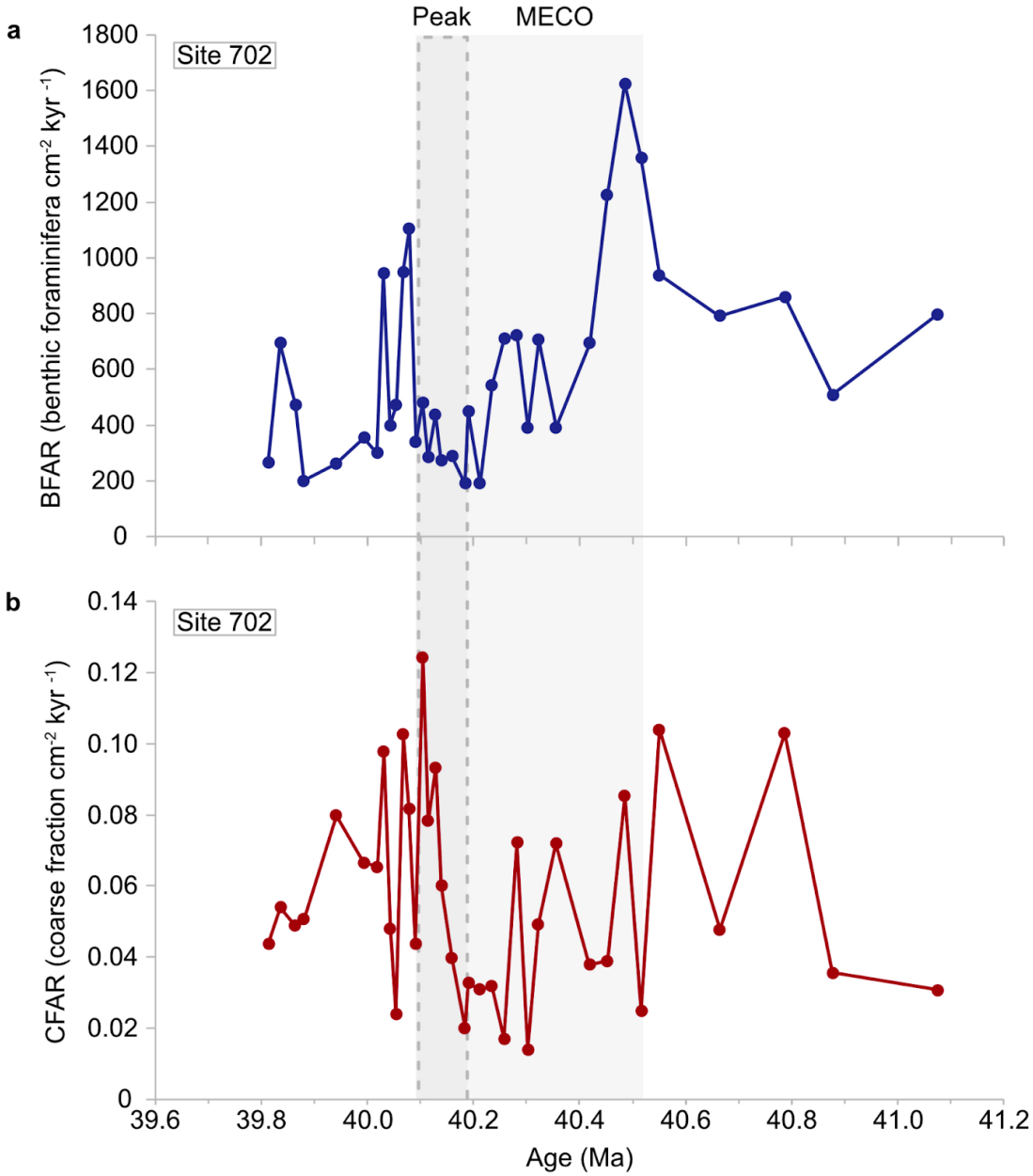

Figure 5.7. Benthic foraminifera (BFAR; blue) and coarse fraction (CFAR; red) accumulation rates for Sites 702 (**a, b**; Rivero-Cuesta *et al.*, 2019) and 1263 (**c, d**; Boscolo-Galazzo *et al.*, 2014) across the MECO. Parts **c** and **d** continue overleaf.

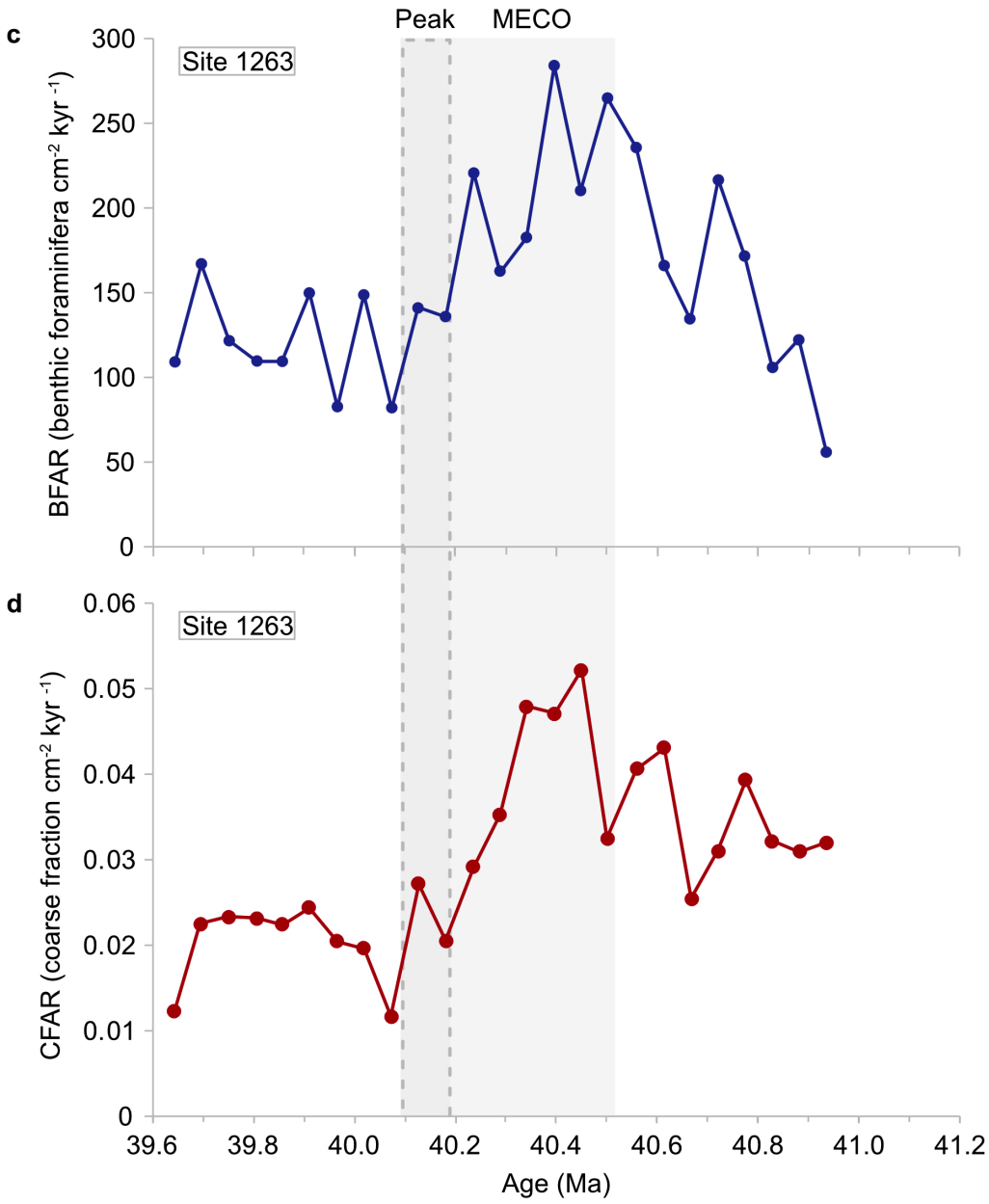

5.3.3. Community composition

Whilst there is some suggestion the size and shape of fish teeth can be linked to body size and feeding type, the pattern is not ubiquitous and can vary depending upon trophic level (Keppeler *et al.*, 2020). This being said, it is notable that at both sites the end member tooth shape categories (exemplified in Figure 4.10) of squat and extra-long are consistently less abundant than medium and long teeth, with the

latter two being tightly coupled in terms of pattern of change (Figure 5.8). At Site 702, medium teeth dominate the assemblage throughout, except for peak MECO when long teeth rise slightly higher to an abundance of 29 over medium teeth at 26, though this is within sampling error. Whilst the numbers of medium and long teeth are highly variable leading into the MECO, there is a distinct increase of ~10 teeth in both shape categories during the peak, before a decline to pre-event levels. Conversely, at Site 1263 long teeth predominate the assemblage throughout. Both shape categories vary within ~10 to 25 teeth prior to the peak, as for Site 702, but are comparatively slightly elevated during the peak with medium teeth reaching a count of 36.

Actual tooth sizes show that the ichthyolith assemblage is dominated by the large (63 to 250 μm) size fraction at both sites (Figure 5.9 a, c) with no clear shifts across the MECO. Instead, there is one anomalous peak at ~40.6 Ma when there is a ~30% increase in the smaller size fraction (38 to 63 μm) at Site 702.

Additionally, the overall shape of the teeth generally falls into two broad categories of cones (circular base in cross section) and triangles (flat cross section), but a third is present at one site - rectangles (regular polygonal base in cross section; Figure 5.9 b, d). Overall, cones are most common across the study interval at both locations with only Site 1263 showing a change in the peak MECO. Here, there is a ~17% reduction in cones compared to triangles, but also isolated and short-lived occurrences of rectangular teeth (four in total).

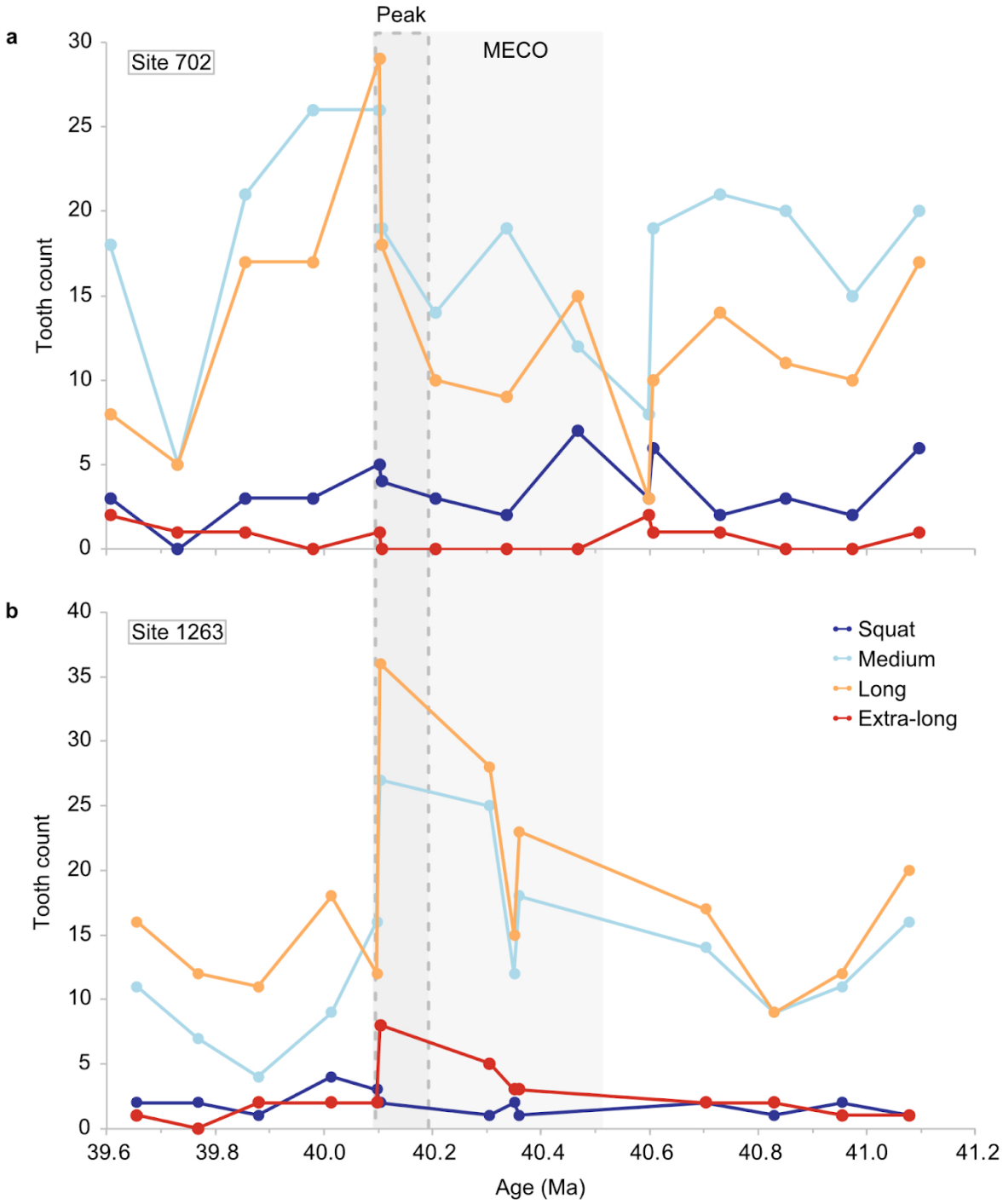

Figure 5.8. Abundances of the four tooth shape categories (squat, medium, long and extra-long) across the MECO at Sites 702 (**a**) and 1263 (**b**).

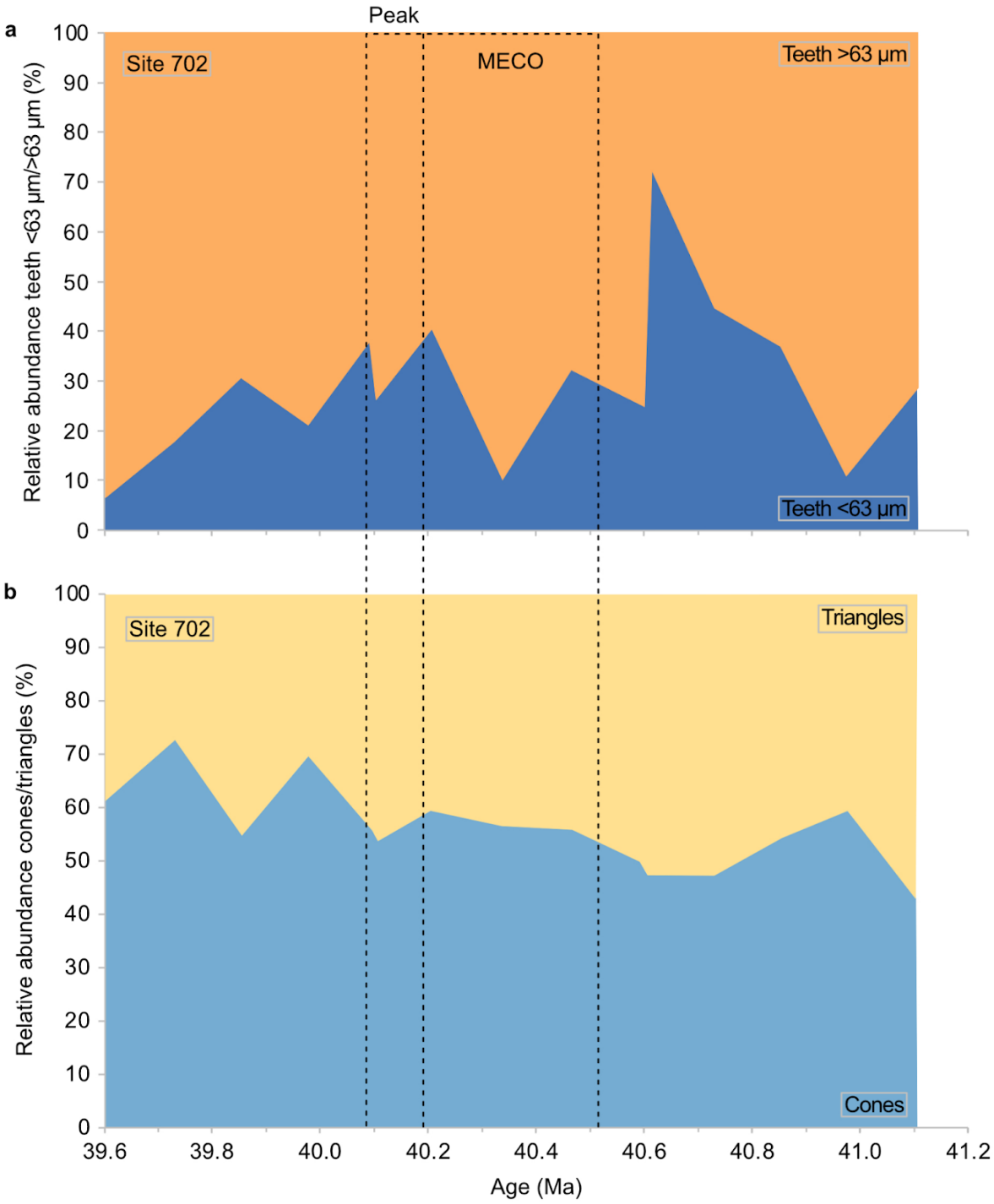

Figure 5.9. Relative abundance of teeth 38 to 63 µm and 63 to 250 µm and cones to triangles and rectangles for Sites 702 (**a**, **b**) and 1263 (**c**, **d**). Parts **c** and **d** continue overleaf.

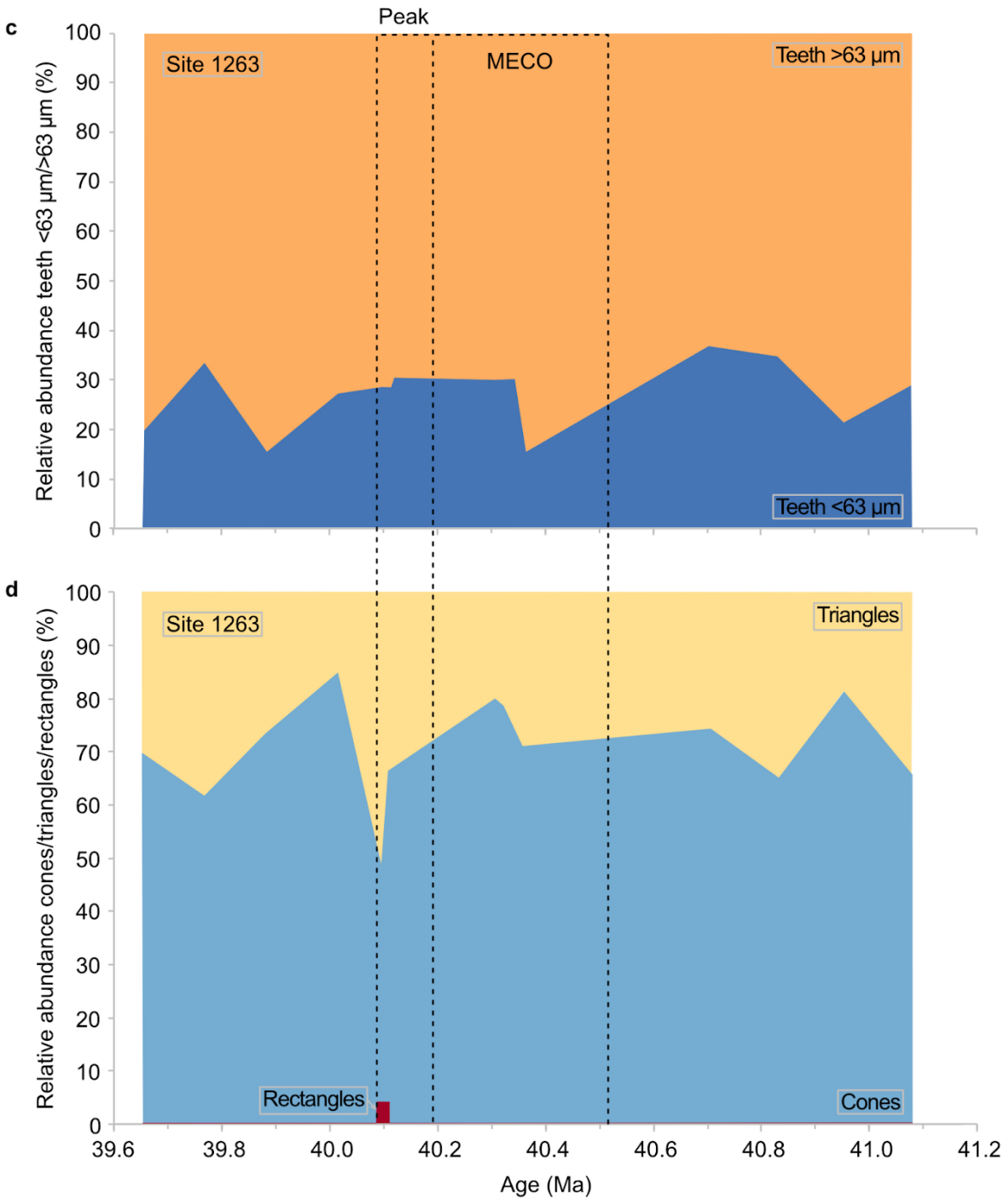

5.3.4. Morphotype occurrences through time

Across the study interval, there are 120 tooth morphotypes, with 61 common to both sites. Prior to the MECO, 83 morphotypes are identified, with an additional 27 originating during the event (10 in the peak alone) and 10 in the recovery phase

(Figure 5.10, Appendix Figures 5.3 and 5.4). Most of the morphotypes (20) “originating” in the MECO are seemingly short-lived as they also disappear by the end of the event peak. Morphotype richness is closely coupled with IAR, both reaching maxima at the end of the MECO peak with a richness of 25 and 37 for Sites 702 and 1263 respectively. This relationship has a strong positive correlation, particularly for Site 1263 which has a linear trend regression of 0.6415 and p value of 6.1×10^{-5} (Appendix Figure 5.5).

The most abundant morphotype (83 occurrences) is “1/4 dome root cone”, closely followed by “1/4 dome root cone no cap” (73 occurrences; Figure 5.11). “Generic triangle” and “generic cone”, where the tooth could not be identified to a specific morphotype beyond base cross section shape, comprise the next two most prominent morphotypes (75 and 67 occurrences respectively), with abundance of a particular morphotype then halving for “long 3/4 straight root straight blades” (32 occurrences) and “straight dome root” (30 occurrences). All of these morphotypes range through the entire dataset, as do the less abundant "convex 1/2 dome root", "long straight striated cone", "medium 3/4 straight root", "medium rootless cone" and "squat rootless cone". There are an additional 14 morphotypes with over 11 occurrences in a single time slice, therefore deemed comparatively abundant, 26 with six to 10 occurrences, 11 with four to five appearances and the most occurrences (28 and 35 respectively) for morphotypes that are only present two to three times or once. Within the latter are some of the more unusual morphotypes that required new designations through this study, such as “extra-long middle barb cone” and “bumpy bladed triangle”, whose broken segments are referred to as rectangles (Figure 5.9) and coded as “straight many cusps” (Figure 5.11).

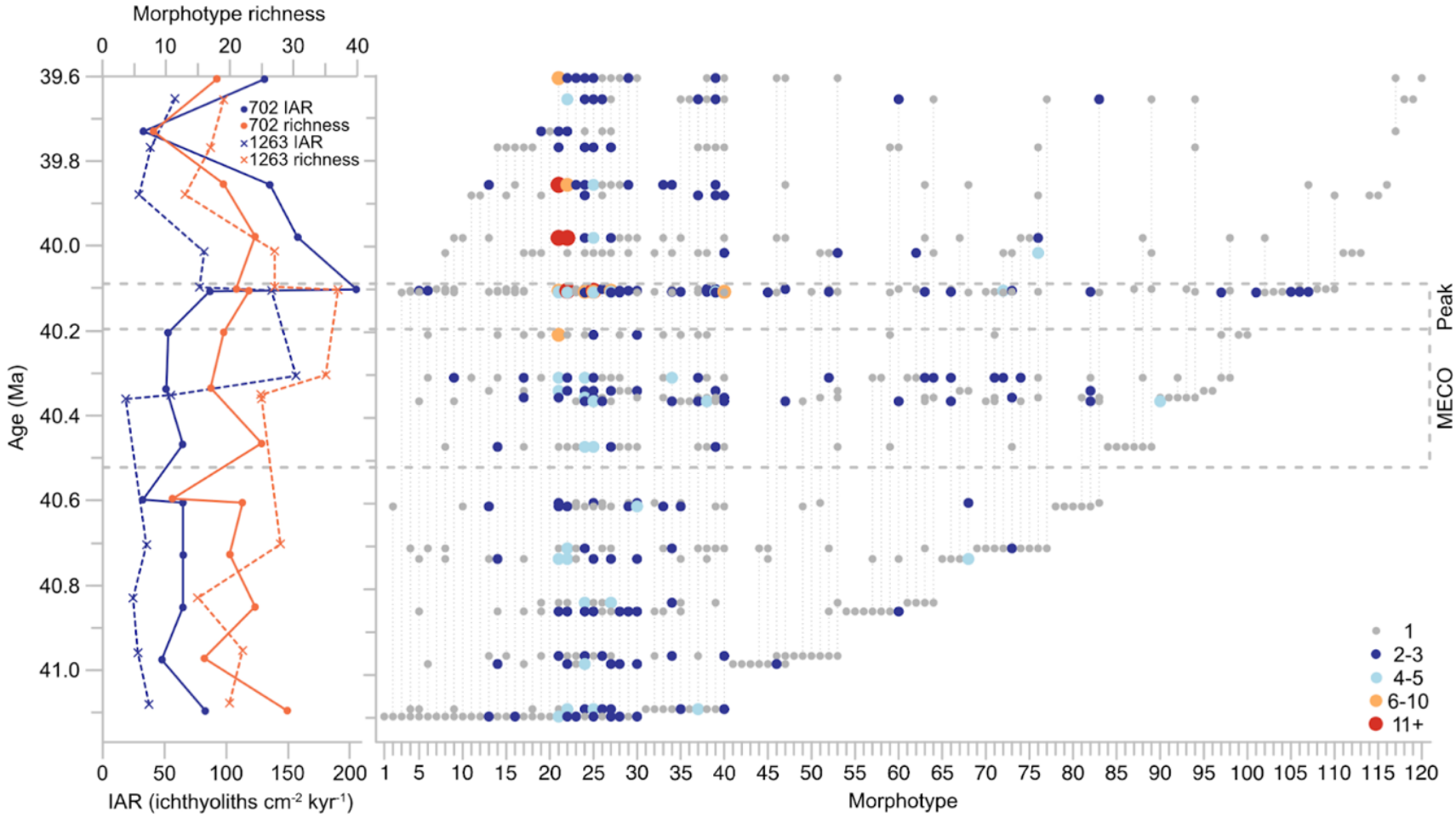

Figure 5.10. Combined morphotype range chart for Sites 702 and 1263 ordered by first appearance to highlight origination, alongside ichthyolith accumulation rate (IAR) and richness for both locations. Dot colour and size indicates morphotype abundance within a time slice and the morphotype key is available in Appendix Table 5.2.

When the range chart is ordered according to last appearance (Figure 5.12, Appendix Figures 5.6 and 5.7), through the MECO there is a loss of 36 morphotypes, approximately half of which are longer-ranging taxa from pre-MECO. 21 of these extinctions occur at the end of the MECO peak, twice the number happening at any other time through the study interval (excluding morphotypes 103 to 120 which are biased by the effect of the end of sampling at ~39.6 Ma in this study).

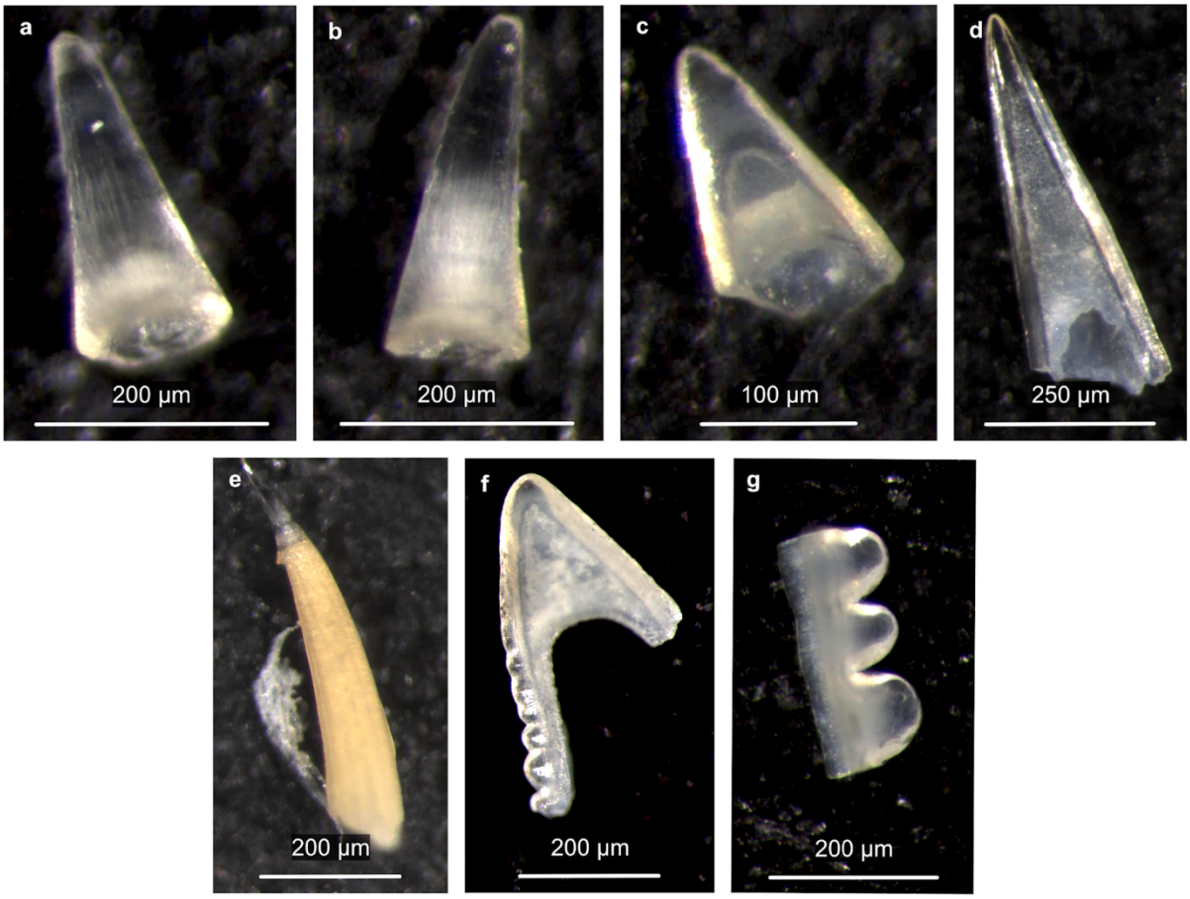

Figure 5.11. Examples of abundant teeth (**a** to **d**) and new morphotypes (**e** to **g**) at Sites 702 and 1263: 1/4 dome root cone (**a**), 1/4 dome root cone no cap (**b**), straight dome root (**c**), long 3/4 straight root straight blades (**d**), extra-long curved middle barb cone (**e**), bumpy bladed triangle (**f**) and straight many cusps (**g**).

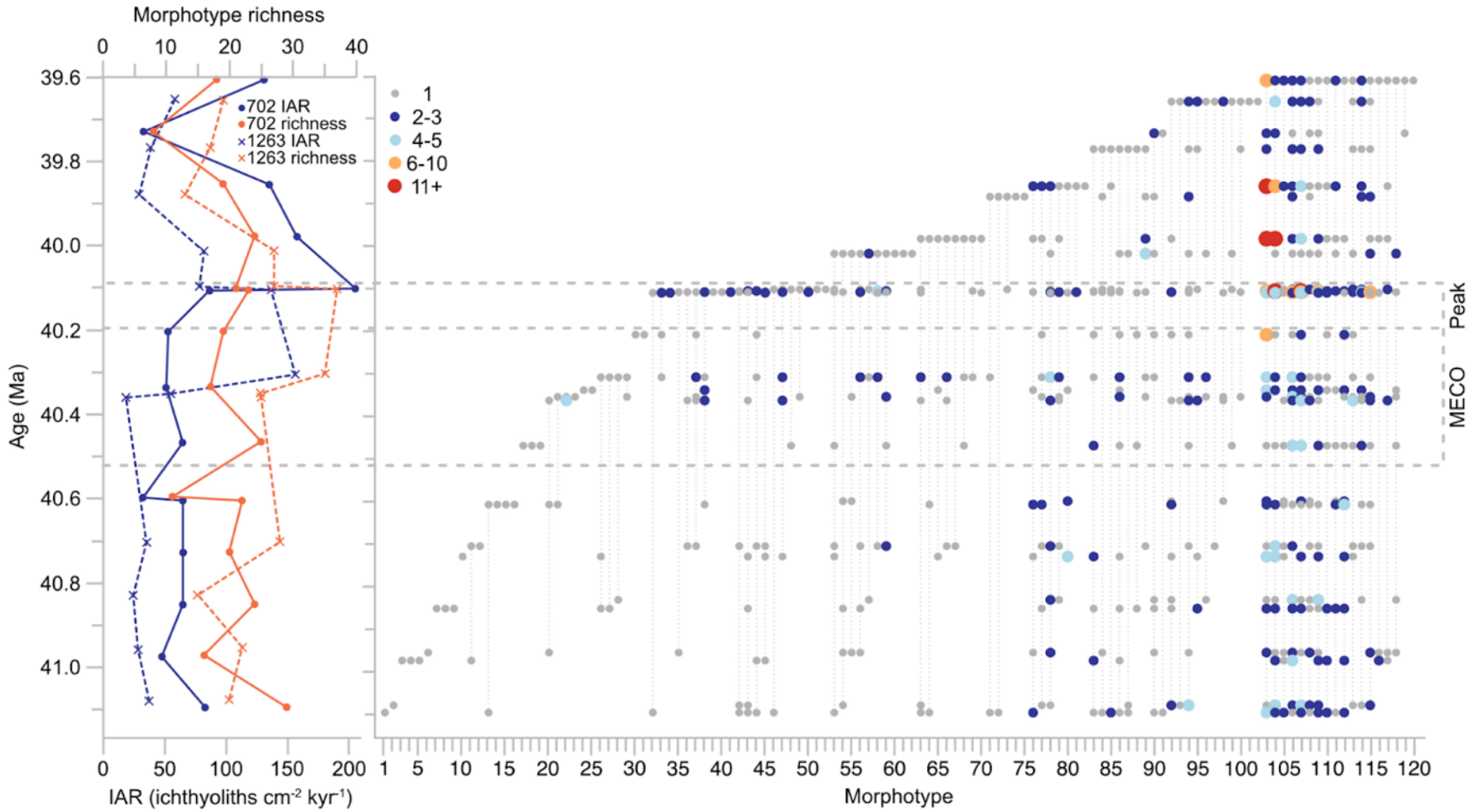

Figure 5.12. Combined morphotype range chart for Sites 702 and 1263 ordered by last appearance to highlight extinction, alongside IAR and richness for both locations. Dot colour and size indicates morphotype abundance within a time slice and the morphotype key is available in Appendix Table 5.3.

5.3.5. Morphotype origination and extinction

Origination and extinction rates of morphotypes can be estimated by assessing their appearance and disappearance relative to what was present in the immediately preceding time slice (Foote, 2000). Combining the data for both sites permits a holistic overview of morphotype occurrence and diversity in the South Atlantic Ocean across the MECO, rather than simply a local origination or extinction metric. The average origination and extinction rates across the study interval are 0.26 morphotypes per lineage million years (morph. Lmy^{-1}) and 0.36 morph. Lmy^{-1} respectively (Figure 5.13, Appendix Figure 5.8). Overall, there is a pattern of higher origination preceding the event peak up to 0.59 morph. Lmy^{-1} (discounting the edge effect of the spike at ~41.1 Ma), with a prominent increase to 0.20 morph. Lmy^{-1} towards the end of the peak at ~40.1 Ma, before declining to mostly zero origination thereafter. Conversely, extinction rates are mostly zero prior to the event, but this spikes higher than origination to 2.35 morph. Lmy^{-1} at the end of the peak before declining to low but persistent extinction rates up to 0.62 morph. Lmy^{-1} post-MECO (again accounting for the edge effect on the last datum at ~39.6 Ma). Cumulative morphotype richness increases gradually through the study interval, and is highest mid-MECO, declining marginally into the peak with a distinct reduction at the end of the MECO, before continued richness loss through the remainder of the recovery phase.

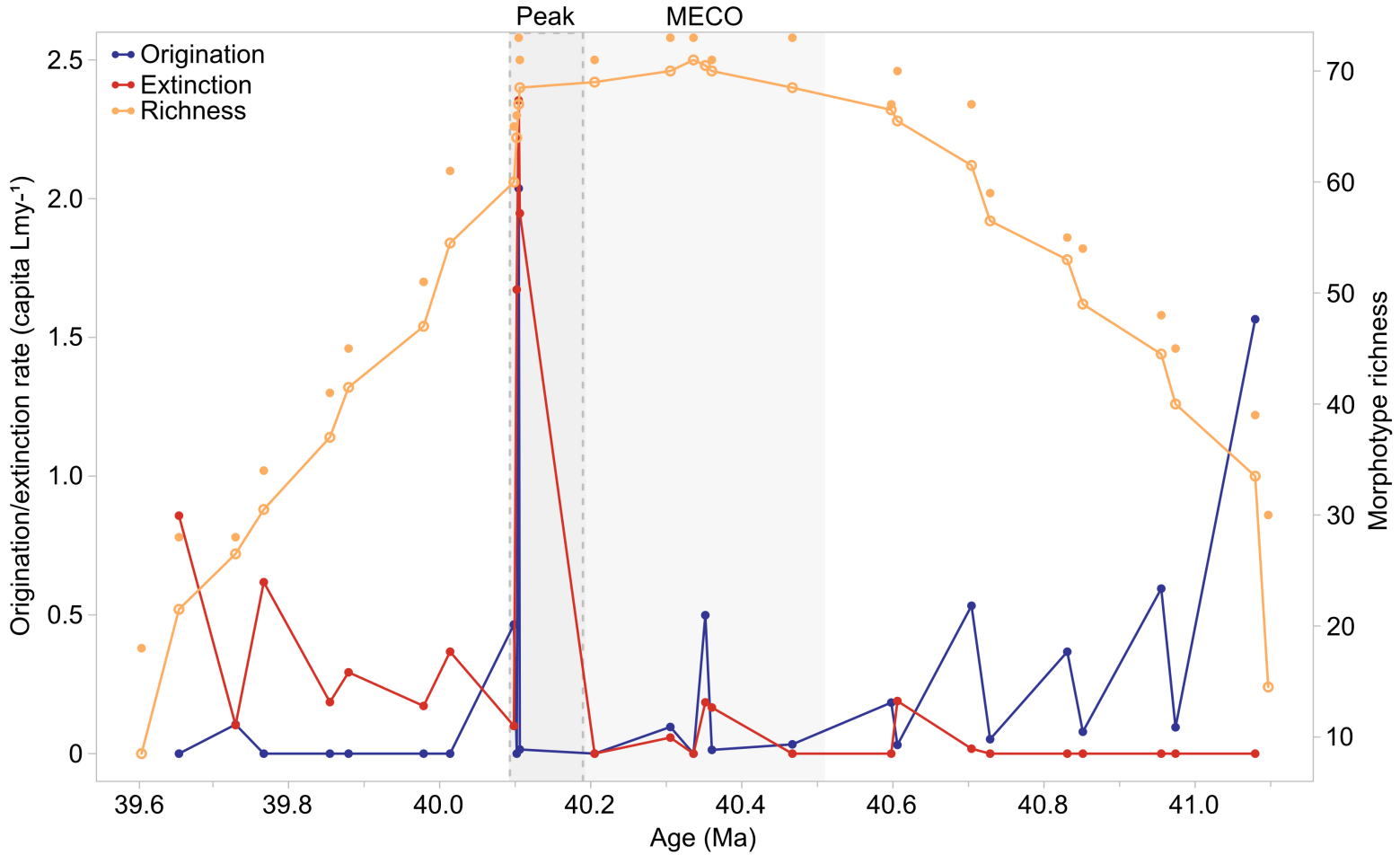

Figure 5.13. Per capita origination and extinction rates per lineage million years (Foote, 2000) combined for Sites 702 and 1263, alongside morphotype richness (hollow circles represent estimated richness which accounts for the range of morphotypes being absent from a sample but present at a later point, whilst filled circles are total observed richness).

5.3.6. Morphospace occupation

Non-metric multidimensional scaling (NMDS) via the *vegan* R package using a disparity matrix calculated with a custom R package (Sibert *et al.*, 2018) can be used to visualise morphospace occupation preceding, during and after the MECO (pre-MECO after 40.516 Ma, MECO 40.110 to 40.516 Ma and post-MECO before 40.110 Ma) and thus see patterns of community change. Based purely upon morphotype occurrence, the teeth cluster into two main groupings of triangles and cones, with a small number of rectangles in between (Figure 5.14), and show considerable overlap across the study interval. At Site 702, MECO morphospace occupation is smaller than before and after the event, plus one tooth seemingly biases the position of the post-MECO convex hull. Site 1263 presents a clearer picture with an increase in morphotypes across the event and reduction afterwards, in line with the patterns of origination and extinction. However, when the two sites are combined, morphospace occupation shows relative stability in morphotype diversity across the entire study interval, rather than contraction of the convex hulls and extinction.

Additional exploration of particular coded characteristics through NMDS generally highlights the groupings of triangles and cones (Figure 5.15). Curvature is dominantly seen in cones with the three character states of minor, major and recurved plotting separately to the uncurved triangles. Similarly, the bladed triangles plot separately to non-bladed codes, whilst barbs are restricted to cones.

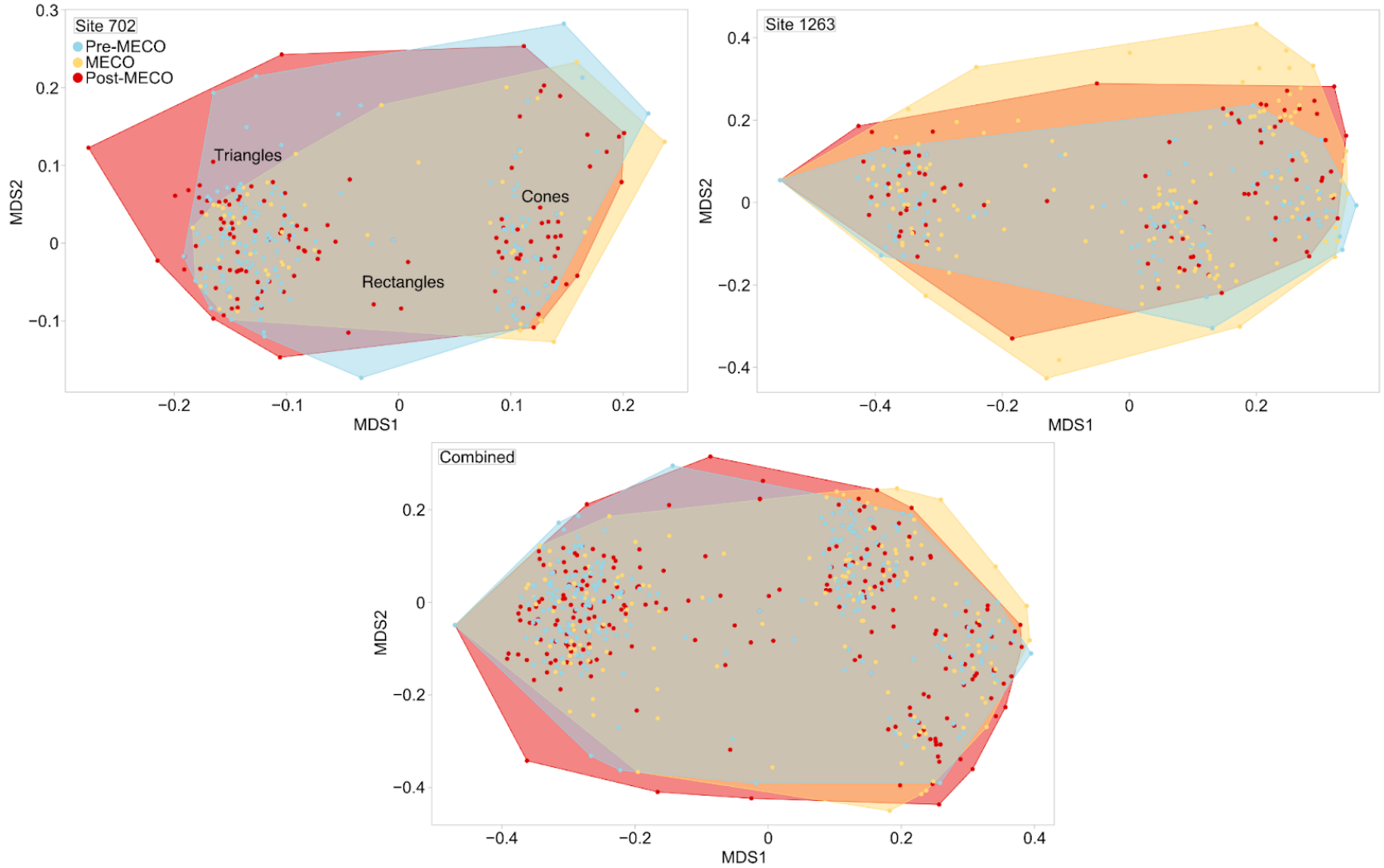

Figure 5.14. Morphospace occupation according to morphotype for Sites 702 and 1263, as well as both locations combined, across pre-MECO, MECO and post-MECO time bins to assess community diversity.

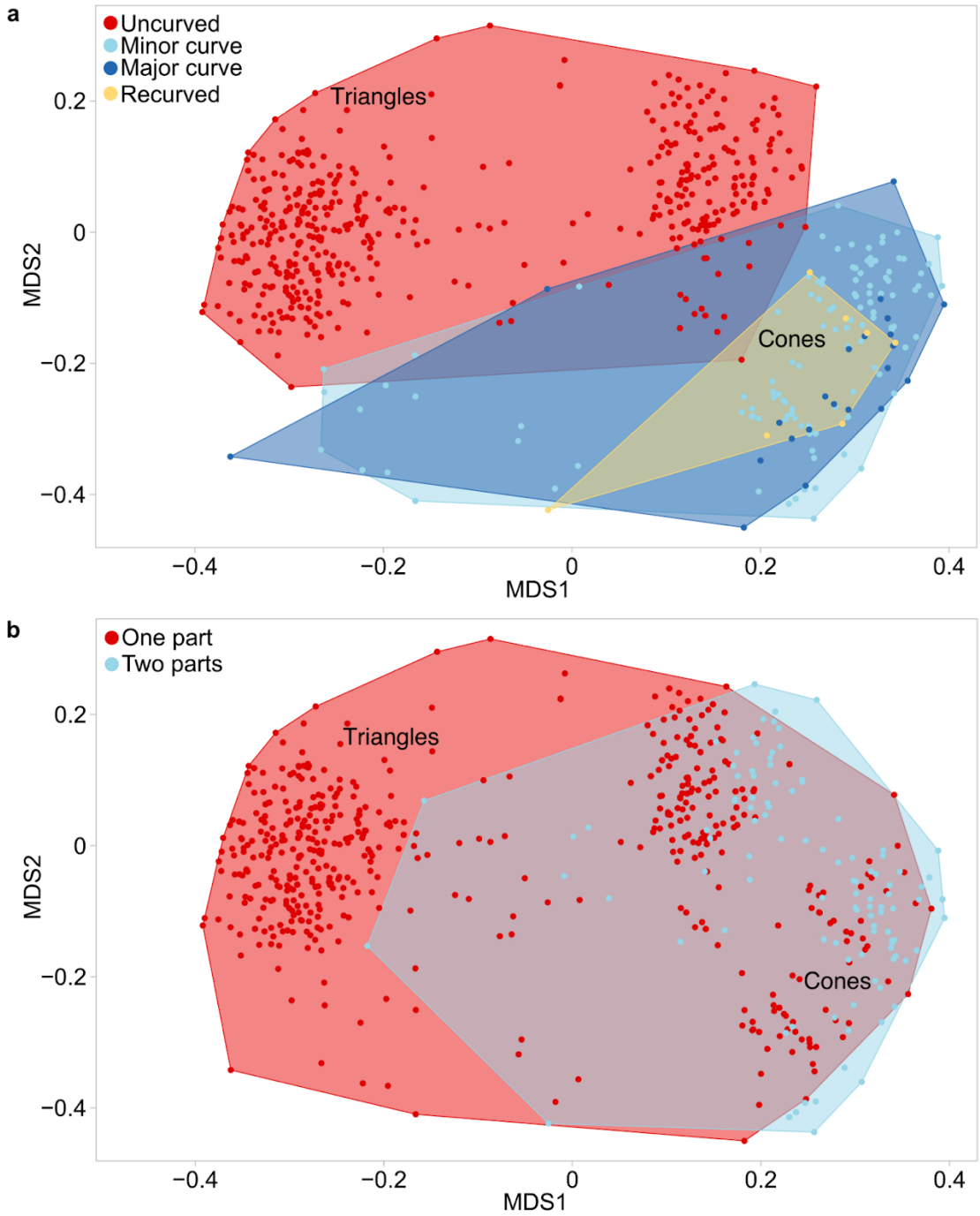

Figure 5.15. Morphospace occupation for four characteristics of the tooth coding system combined for both sites: curvature (**a**), number of parts (**b**), blades (**c**) and barbs (**d**). Parts **c** and **d** continue overleaf.

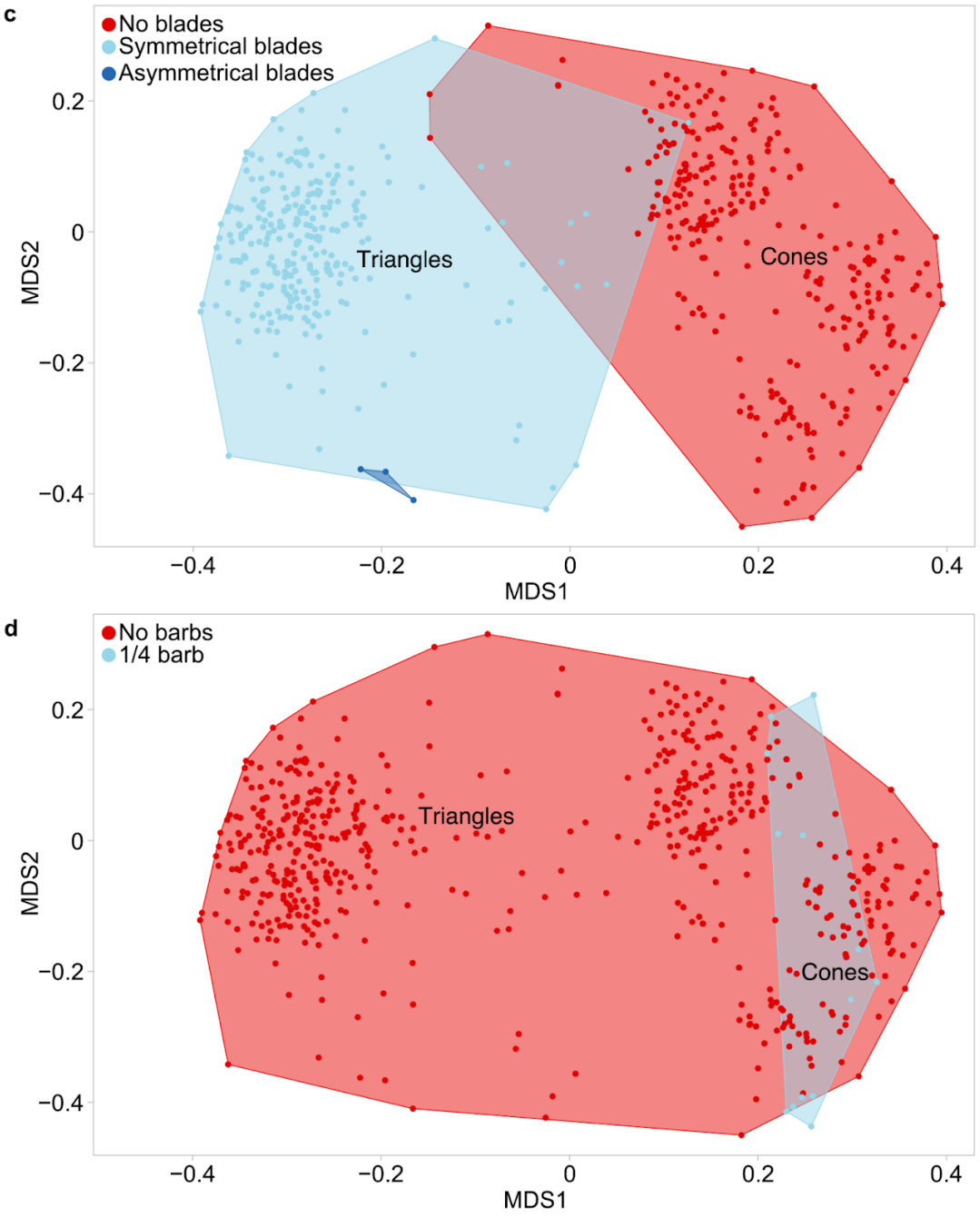

5.4. Discussion

5.4.1. Productivity in the South Atlantic Ocean

Sites 702 and 1263, from the relatively high and mid-southern latitudes respectively, overall share similar patterns of elevated fish productivity during peak MECO, suggesting a common response to the MECO in the South Atlantic. Both locations

experienced elevated ichthyolith accumulation during the event, most notably with maximum IARs during peak MECO, implying enhanced deep-sea (bony) fish production, associated with maximum sea surface temperatures of ~11 °C and ~16 °C at Sites 702 and 1263 respectively (reaching up to ~17 °C and ~21 °C respectively calculated with the Bayfox 95% confidence interval; Kirby, 2022). The IAR values here fall in line with those displayed in a composite of known IAR from global oceans (Sibert *et al.*, 2020), with all South Atlantic values occurring during relatively high productivity conditions.

Whilst there appears to have been elevated productivity pertaining to bony fish during the MECO, other organisms do not support this as a universal occurrence in the marine realm. Reductions in Ca/Fe, BFAR and CFAR records at the sites signal a decline in calcium export to the seafloor from calcareous primary producers and/or enhanced dissolution. The latter is in line with other hyperthermal events such as the PETM, as both study sites were susceptible to the ~1,500 m shoaling of the CCD that occurred during the MECO (Bohaty *et al.*, 2009). Borelli *et al.* (2021) suggest a combination of reduced calcium carbonate production and ocean ventilation at the surface as major factors in decreasing transport and burial of carbon to the seafloor at this time. As such, diminished surface ocean productivity and export productivity through the water column is inferred for the MECO. This indicates inefficiency of the carbon cycle, with less carbon reaching the seafloor for burial, therefore accumulating in the ambient marine environment and reducing ocean-atmosphere interactions to draw down carbon dioxide, thus exacerbating climate warming (Rivero-Cuesta *et al.*, 2019). Furthermore, the lack of biogenic silica in smear slide data at both sites is indicative of a reduced input from both the primary productivity of

siliceous microorganisms, as well as terrigenous silica output from continental weathering in the southern mid to high latitudes during the Eocene.

Arimoto *et al.* (2020) suggest this carbonate productivity conundrum is linked to eccentricity cycles, particularly the 2.4 Myr minima, causing reduced seasonality and weathering rates. Such a change in continental weathering is supported by osmium isotopes from Site 1263, as well as equatorial Atlantic Site 959 and equatorial Pacific Site U1333, which see negative shifts across the MECO, which indicate a reduction in weathering of felsic silicate rocks (van der Ploeg *et al.*, 2018). The driver of this feedback cycle currently remains elusive despite modelling efforts (Sluijs *et al.*, 2013). Consequently, this would have decreased nutrient input to the oceans and available supply for the metabolic process of primary producers. Additionally, this may have been exacerbated during summer months by a reduced mixed layer leading to a weaker thermocline and upper ocean stratification (Arimoto *et al.*, 2020).

Elevated surface ocean temperatures likely also played a significant role in export productivity, as a 10 °C rise in the ambient water temperature is believed to double metabolic rates (Dillon *et al.*, 2010; Boscolo-Galazzo *et al.*, 2018; Chrichton *et al.*, 2023). Surface and deep waters warmed by similar amounts during the MECO (~4 °C; Boscolo-Galazzo *et al.*, 2014) meaning metabolic rates may have been elevated throughout the water column. Subsequently, this would mean organic matter from primary producers floating through the upper layers of the water column would be metabolised faster by bacteria, reducing that reaching lower depths, therefore impacting food supply through complex trophic webs. Hence, a combination of high

sea temperatures and reduced nutrient supply may have contributed to minimising primary and export productivity through the MECO.

Yet, IAR taken at face value suggests the productivity of fish increased during the warming event, which means another factor must be at play. This could be sedimentation rate, as at both sites this doubles coincident with the IAR peaks (Figure 5.4) and may be a factor of concentration bias due to carbonate dissolution.

5.4.2. Marine fish diversity in the South Atlantic Ocean

Like the PETM and EECO studied in Chapter Four, Sites 702 and 1263 show a decoupling of productivity and diversity during warming. Whilst there appear to be both considerable originations and extinctions of morphotypes during the peak of the event, overall extinction is slightly elevated at 0.1 morph. Lmy^{-1} more than origination (Figures 5.10, 5.12, 5.13 and 5.14). Considering the MECO is marked by carbonate dissolution, ichthyoliths are concentrated in the sediment samples, so there is an increase in tooth abundance and therefore higher likelihood of observing additional morphotypes, which would translate to an increase in diversity; however, that is not the case in this study with the elevated extinction rates being a real signal of diversity decline.

Such turnover could relate to the aforementioned reduced productivity impacting marine food webs, thus necessitating alterations of feeding function to enable consumers to seek alternative food sources. For example, during the peak, a particularly novel tooth “bumpy bladed triangle” and its broken segments of “straight many cusps” occurs. Whilst these morphotypes have been found infrequently at

other sites of different ages (Sibert, 2024), they comprise only four specimens found throughout the ~3,400 teeth studied across Sites U1514, 702 and 1263. This suggests it could have been a localised short-lived boom of a particular fish species occurring in response to changing diet or ecological range. As such, only during the event termination is there a clear change in diversity, with increased extinction of shallow to mid-water fish. This is likely a result of reduced primary productivity as a food source, destabilising marine trophic webs across a breadth of lower and higher order predators.

In addition to diet, the effect of temperature on metabolism is complex, with constraints surrounding the metabolic theory of ecology (Brown *et al.*, 2004) discussed in Chapter 4 also applicable here. The ratio of tooth size across both size fractions (38 to 63 μm and 63 to 250 μm) is relatively stable through the study interval, thus there is no indication of downsizing of fish body sizes in response to a warmer world to conserve energy. Similarly, across the four categories of tooth shapes, the most dominant of medium and long teeth are tightly coupled, suggesting that the more energy is input into the system then the pelagic community reacts as a collective rather than particular outliers becoming more prevalent and preferentially thriving in a warmer world.

5.4.3. South Atlantic Ocean productivity and diversity compared to global patterns

The South Atlantic is characterised by reduced primary productivity, as is the southern high latitude Site 1172, but this pattern does not appear to have been universal, with locations in the North Atlantic (Site 1051), Kerguelan Plateau (Site

738), Southern Ocean (Site 748) and Indian Ocean (Site 749) all experiencing the opposite trend (Witkowski *et al.*, 2012; Witkowski *et al.*, 2014; Moebius *et al.*, 2014). Indeed, this contrast in productivity was not solely for calcareous microorganisms either, as tropical Site 1260, Demerera Rise, and subtropical Sites 1250 and 1251, North Atlantic, saw increases in siliceous productivity from diatoms and silicoflagellates compared to the absence of abundant silica at the locations studied here (Renaudie *et al.*, 2009; Witkowski *et al.*, 2020).

Borelli *et al.* (2021) identified primary productivity, ocean circulation (including the effect of stronger currents on the biological pump) and weathering rate changes as the main causes of heterogeneity in carbonate and silica accumulation across global ocean basins at different depths. Douglas *et al.* (2014) further noted a ~5 to 15 °C difference in sea surface temperature between the Pacific and Atlantic Oceans may have influenced metabolic processes, whilst Savian *et al*. (2014) suggest aeolian-derived dust may have increased nutrient supply to some basins after correlating iron fertilisation with a switch from oligotrophic to eutrophic conditions. The MECO is part of a time of oceanographic complexity with the continued opening and expansion of multiple seaways, including the Tasman Gateway (Bijl *et al.*, 2013) and Drake Passage (Scher and Martin, 2006), allowing for the circulation of cooler polar Antarctic Bottom Waters into global ocean basins, plus narrowing of the Tethys Gateway affecting throughflow between northerly Atlantic and Pacific Oceans (Allen and Armstrong, 2008). For example, in the Neo-Tethys and expanding across the North Atlantic, the MECO peak is associated with reduced oxygen supply, eutrophication from continental runoff and acidification of carbonates (Witkowski *et al.*, 2014; D'Onofrio *et al.*, 2021). The Indian and South Atlantic sections of the

Southern Ocean were also sources of deep water formation in the early Cenozoic (Moebius *et al.*, 2014). As such, these variations in primary and export productivity likely expand to affecting the productivity and diversity of consumers through the rest of the marine trophic webs.

Ecological change is strongly linked with macroevolutionary speciation and extinction (Ezard *et al.*, 2011) and the fact that the MECO, alike the PETM and EECO, all show some level of change in either productivity or diversity, highlights the role of the ambient environment in marine community response.

5.4.4. Early Paleogene climate event comparisons

Whilst the PETM and EECO are characterised by prominent $\delta^{13}C$ excursions, this is less evident for the MECO (Giorgioni *et al.*, 2019), suggesting differing driving mechanisms for the warming events. Whilst the PETM and EECO hyperthermals are thought to have been caused by sudden release of isotopically light carbon from volcanism and/or changes in silicate weathering (for example, Scheibner and Speijer, 2008; van der Boon *et al.*, 2021), mechanisms working on the scale of hundreds of thousands of years as per the MECO calls for a source other than abrupt carbon release and tectonic or palaeogeographic reconfigurations. Giorgioni *et al.* (2019) and Westerhold and Röhl (2013) suggest that the MECO occurs within close proximity of 400 kyr and 2.4 Myr eccentricity cycles and that this could have reduced seasonality and the drawdown of CO_2 via weathering, accounting for some of the observed nutrient deficiencies and sea temperature rise.

Another major difference between the studied hyperthermal events is the abrupt termination of the MECO, which has been variably attributed to an increase in

continental silicate weathering reducing pCO_2 to initiate cooling and/or increased sequestration of marine carbon creating a negative feedback (D'Onofrio *et al.*, 2021). Elsworth *et al.* (2017) and Langton *et al.* (2016) suggest that a change from the relatively homogeneous water column of the South Atlantic in the MECO to stratification of the ocean at its termination influenced Atlantic Meridional Overturning Circulation, thus resulting in enhancement of seasonality and precipitation over the continents which exacerbated weathering and post-event recovery.

The biological effects of these differing environmental conditions over varying timescales are also apparent in the productivity and diversity of tooth morphotypes. Whilst the rapidity of warming and cooling across the PETM seemingly encouraged high productivity and fish turnover, the more gradual warming of the MECO may have enabled time for species to adapt, thus there is no significant origination through the event, only elevated extinction coinciding with the abrupt termination. The elevated extinction rate compared to previous hyperthermals studied here may be a consequence of this being part of the step down in baseline climate, closing in on the tipping point from greenhouse to icehouse conditions.

5.5. Chapter conclusions

Unlike other early Cenozoic warming events, the MECO of the South Atlantic did not experience enhanced productivity in terms of primary producers, but did see an elevation in fish and shark IAR coincident with possible concentration bias of calcium carbonate dissolution. The rate of climate change across the MECO onset may have been steady enough to enable marine communities to progressively adapt to the

changing environmental conditions, thus did not experience significant shifts in productivity. Additionally, diversity across the MECO is more akin to the relative stasis of the extended warming across the EECO, except for the termination of the event which coincides with slightly elevated extinction and could be attributable to the rapidity of the climate reversal. Consequently, the timescale of the climate perturbation seems to be a major factor in fish productivity and diversity.

Whilst the relative proximity of Sites 702 and 1263 allow validation of similar patterns across the South Atlantic, the known differences in primary productivity globally could mean that there are also differing responses to the warming event by other marine communities, such as fish. Given this is currently the only known IAR record covering the MECO, further work is required to explore this at more sites; initially this project intended to analyse a transect of sites from North to South Atlantic, but issues with sample availability in the core repository and lithology for sample processing meant that Sites 913 and 1051 (North Atlantic) and 959 (equatorial Atlantic) could not be studied in sufficient detail. Therefore, it is imperative to identify sites with good MECO recovery and sediments that may be readily broken down for ichthyolith extraction, including ODP Site 865 (equatorial Pacific nannofossil oozes and foraminiferal sands) and ODP Site 748 (Southern Ocean nannofossil oozes and chalks) to expand previous work on the Pacific Ocean transect, as well as IODP Site U1408 (North Atlantic nannofossil ooze and clay) and ODP Site 647 (North Atlantic) if techniques for extracting ichthyoliths more effectively from claystones can be developed to work towards an Atlantic Ocean transect of ichthyolith data.

Moreover, definitively constraining the mechanism behind the gradual warming and rapid cooling of the MECO is necessary to understand how modern interventions to ultimately draw down greenhouse gas emissions could eventually impact the planet, if a negative feedback loop is initiated. Nevertheless, whether the climate perturbation is short, like the PETM, or longer, like the MECO, actinopterygians seemingly adapt to maintain a thriving marine community.

CHAPTER SIX

Conclusions

6.1. Summary of research findings

Given the ever-pressing concern over modern climate change and implications for the future, this thesis aimed to use intervals of climate change in geological history to assess biotic responses to global warming and associated environmental change. The early Paleogene encompasses the warmest interval within the last 66 million years of the Cenozoic, and is punctuated by numerous warming events of different rates, magnitudes and timescales (Westerhold *et al*., 2020). The impact of these events on marine vertebrates was chosen as a specific focus given that they are a significant component of the fauna in the marine realm, and have been subject to little research to date, creating large uncertainty over how marine ecosystems will react to anthropogenic-induced changes in the ocean. Fish, in particular, are the most abundant group of vertebrates in the ocean, and a critical proxy for overall ocean ecosystem health because of their role in marine trophic systems, as well as being a valuable protein source for humans globally. Here, relatively new methodologies harnessing ichthyoliths from deep-sea sediments are used to generate high resolution palaeocommunity reconstructions of bony fish (with limited analysis of sharks) in order to assess productivity and diversity responses.

Chapter Three reconstructs shallow water (less than 200 m; King, 1981) fish communities from a subtropical sea, based upon the NHMUK otolith collection across the late Palaeocene and early Eocene, spanning ~50 to 59 Ma. Ultimately, whilst few samples were available for the Palaeocene (Thanetian), a detailed understanding of

the earliest Eocene (Ypresian) fauna of southern England was possible, with the bulk of sampling coming from the well-known and highly fossiliferous London Clay Formation. Superficially, both productivity (in terms of abundance) and otolith species diversity do increase from the late Palaeocene and through the early Eocene warming period, peaking within units B and C of the London Clay Formation. However, the paucity of Palaeocene specimens means it is not possible to directly link this to PETM radiation, though the overall high abundance and diversity of fish through the Eocene concurs with records from elsewhere globally, such as Bolca, Italy (Friedman and Carnevale, 2018), that suggest Eocene fish diversity was generally high. The challenges of relying upon museum collections to reconstruct the palaeocommunity are that multiple geological (such as stratigraphy, taphonomy and outcrop availability) and anthropogenic (including collector interest, otolith taxonomy inconsistencies and museum storage constraints) biases impinge upon conclusions. Therefore, the chapter concludes with recommendations for reducing the biasing effect of these factors from sampling in the field through to museum acquisitions processes.

In **Chapter Four**, the response of bony fish and sharks to longer term warming over millions of years of the early Paleogene (~48 to 66 Ma) was conducted through novel analyses of ichthyoliths from IODP Site U1514, the first record of its kind from the Indian Ocean. Whilst shark denticles were limited for robust analyses, fish teeth were abundant for morphotyping and palaeocommunity assessment. Low resolution sampling (~500 kyr spacing) across the study interval identified increased fish productivity during the EECO but relative stasis in the overall palaeocommunity diversity, with comparatively few originations and extinctions. However, when the

higher resolution (~2 to 10 kyrs spacing) data is considered, there is significant origination of deep sea fish during the PETM itself (preceding the EECO by ~3 Myrs). Though this abrupt increase in diversity may be a factor of sampling intensity, many of these tooth morphotypes do continue to range through the Eocene and this does concur with prior studies on fish and sharks (such as Sibert *et al.*, 2016; Sibert *et al.*, 2018) suggesting that they began to thrive and diversify in the newly-opened niche spaces following the end-Cretaceous mass extinction. With volcanic degassing contributing significant amounts of carbon dioxide to the atmosphere and an intensified hydrological cycle conducive to enhanced rates of terrestrial weathering, an increased nutrient supply to the oceans would have supported primary productivity, which filtered through the trophic system to fish, encouraging their population growth and diversity.

Finally, in **Chapter Five,** the intermediate warming of the MECO, ~40 Ma, in the South Atlantic Ocean was explored; this research is the first deep sea Atlantic Ocean ichthyolith data from the Cenozoic, as studies were previously predominantly restricted to the Pacific Ocean. Comparison between two locations (ODP Sites 702 and 1263) found very similar patterns of productivity and diversity across the MECO, with elevated fish abundance during the peak of the event at ~ 40.2 Ma for ~100 kyrs, but slightly reduced diversity, with the latter being unique to the MECO compared to the prior studied climate events. Unfortunately, the denticle dataset here was too small to enable further analyses of shark productivity and diversity changes across the early Paleogene. Whilst geochemical data suggest reduced nutrient supply in the Southern Ocean coinciding with a decline in primary and export productivity, the response of fish seems to be decoupled from this somewhat during

the MECO as their abundance unusually increased during more eutrophic conditions and their diversity decreased, perhaps in response to the rapid rate of climate change, or as a result of concentration bias from carbonate sediment dissolution due to shoaling of the CCD. These patterns are not ubiquitous across the planet, though, as sites in the North Atlantic (Site 1051), Kerguelan Plateau (Site 738), Southern Ocean (Site 748) and Indian Ocean (Site 749) experienced the opposite trend (Witkowski *et al.*, 2012; Witkowski *et al.*, 2014; Moebius *et al.*, 2014). Therefore, the role of oceanographic circulation in the Southern Ocean could be a major factor in the differences between northern and southern hemispheres, with continued opening of the Tasman Gateway and Drake Passage further complicating the marine response to climate change.

The results of this thesis highlight how the pattern and temporal scale of warming and post-event cooling are crucial to atmospheric, oceanic and biospheric responses. When timescales of environmental change are shorter, meaning the onset and/or termination of the warming event are rapid, organisms are not able to adapt, leading to higher rates of turnover. In this research, this is evidenced by the high rates of fish origination and extinction across the entirety of the PETM (relative to the EECO or long-term Palaeocene-Eocene change), and elevated extinction at the end of the MECO. As such, the rapidity of global warming and cooling is linked to the driving mechanisms of the climate perturbations, be that comparatively rapid input of carbon to the atmosphere from volcanic degassing, silicate weathering or the longer-term effect of changing eccentricity cycles.

Therefore, considering which scenario is most, although not completely, analogous for current and future climate change, the rapidity of the PETM in terms of carbon input to the atmosphere is similar to the enhanced rate of greenhouse gas release in the modern day (~1,500 ppm in the PETM compared to over 1,000 ppm by 2100 for Representative Concentration Pathway 8.5; Rae *et al.*, 2021; IPCC, 2022; Inglis *et al.*, 2020). Consequently, the elevated productivity and turnover of fish during this time may hold true for communities in the oceans today. In this sense, we may expect deep sea fish to withstand the tests of modern climate change and help to support an overall successful marine community, despite short-term challenges.

6.2. Future Paleogene research

Palaeoclimate studies into the early Paleogene are by no means complete, and indeed this research highlights areas where additional exploration is vital to further answer knowledge gaps. Whilst this research has emphasised the power of historical museum collections for palaeocommunity analyses, more work is required to improve the rigour and accessibility of this data. This includes investing time and resources into digitising collections catalogued in museums, with transcription of data and visualisation of specimens (as a minimum two-dimensional images, but preferentially three-dimensional scans) to make them publicly and globally available for further study. Continued addition to biodiversity databases (such as PBDB) is also paramount to this process, with a particular focus on smaller fossil material (including otoliths, teeth and denticles) compared to body fossils, and indeed there is a wealth of material which is published but not yet widely accessible in online databases (such as the holotypes described in Stinton (1975-1983) and housed in the NHMUK).

Ichthyoliths can be used to assess the overarching response of the marine community to warming, thus advantage must be taken of this currently underutilised resource in palaeoclimate research. This includes dedicating time and resources to extracting ichthyoliths from currently available cores (particularly ichthyolith-rich carbonate lithologies) and finding new techniques to tackle problematic lithologies that do not readily break down to yield them (such as freeze-thaw and electric pulse fragmentation; Kennedy and Coe, 2014; Beasley *et al*., 2020). Additionally, this encompasses identifying more sites with suitable lithologies from the early Paleogene across all ocean basins to extract ichthyoliths from and ideally sample at thousands to tens of thousands of years resolution to fully capture patterns of productivity and diversity during warming events. This consequently provides more robust datasets with ample ichthyoliths for palaeocommunity analyses compared to lower resolution long-term datasets. Therefore, this could include sampling across the other EECO hyperthermal events to supplement the R and S events considered in this thesis and validate these patterns during short-lived climate perturbations. Moreover, the North Atlantic and Southern Oceans could benefit from further ichthyolith sampling as the Pacific Ocean has been comparatively well-studied, as well as additional transects from polar to tropical regions in order to continue exploring the differing effects of geographical distribution (as seen in the case of productivity and diversity patterns across global MECO sites in Chapter Five). Sampling in this manner must also be mindful of methodologies detailed in this thesis for mitigating against geologic and anthropogenic biases when handling data and generating new datasets to support the robustness of research into a key window of Earth's history.

Beyond continued research into the driving mechanisms of the three overarching warming events investigated (PETM, EECO and MECO), expansion of palaeoproxy records, such as XRF data, is vital to understand both changing environmental conditions and primary producer productivity, as they are linked to overall ocean health. For example, high resolution silica records across the various warming intervals can allude to terrigenous (from weathering) or biological input (from primary productivity), whilst additional barium data can support conclusions over export productivity. This is especially evident when studying older core sites where XRF data was not historically routinely obtained, but is now vital to bridging the gap between geochemical, ecological and biological responses to climate change.

LIST OF REFERENCES

Adnet, S., Marivaux, L., Cappetta, H. *et al*. 2020. Diversity and renewal of tropical elasmobranchs around the Middle Eocene Climatic Optimum (MECO) in North Africa: New data from the lagoonal deposits of Djebel el Kébar, Central Tunisia. *Palaeontologia Electronica*, 23, a38.

Aldiss, D.T. 2014. The stratigraphical framework for the Palaeogene successions of the London Basin, UK. *British Geological Survey Open Report*, OR/14/008. 95pp.

Aldiss, D.T. 2021. Personal communication via email, 12 October.

Alfaro, M.E., Faircloth, B.C., Harrington, R.C. *et al.* 2018. Explosive diversification of marine fishes at the Cretaceous–Palaeogene boundary. *Nature Ecology and Evolution*, 2, 688-696.

Allen, M.B. and Armstrong, H.A. 2008. Arabia–Eurasia collision and the forcing of mid-Cenozoic global cooling. *Palaeogeography, Palaeoclimatology, Palaeoecology*, 265, 52-58.

Anagnostou, E., John, E.H., Edgar, K.M. *et al.* 2016. Changing atmospheric CO_2 concentration was the primary driver of early Cenozoic climate. *Nature*, 533, 380-384.

Arimoto, J., Nishi, H., Kuroyanagi, A. *et al.* 2020. Changes in upper ocean hydrography and productivity across the Middle Eocene Climatic Optimum: Local insights and global implications from the Northwest Atlantic. *Global and Planetary Change*, 193, 103258.

Arreguín-Rodríguez, G.J., Thomas, E. and Alegret, L. 2022. Some like it cool: Benthic foraminiferal response to Paleogene warming events, *Palaeogeography, Palaeoclimatology, Palaeoecology*, 593, 110925.

Arroyo-Zúñiga, K.I., Pacheco-Ovando, R., Granados-Amores, E. *et al.* 2022. Lapillus otolith shape, a useful taxonomic feature for the identification of sea catfishes (Ariidae: Siluriformes) from the north-eastern Pacific. *Journal of Fish Biology*, 101, 1262-1269.

Auderset, A., Moretti, S., Taphorn, B. *et al.* 2022. Enhanced ocean oxygenation during Cenozoic warm periods. *Nature*, 609, 77-82.

Audzijonyte, A., Richards, S.A., Stuart-Smith, R.D. *et al.* 2020. Fish body sizes change with temperature but not all species shrink with warming. *Nature, Ecology and Evolution*, 4, 809-814.

Aziz, H.A., Hilgen, F.J., van Luijk, G.M. *et al*. 2008. Astronomical climate control on paleosol stacking patterns in the upper Paleocene-lower Eocene Willwood Formation, Bighorn Basin, Wyoming. *Geology*, 36, 531-34.

Barnet, J.S.K., Littler, K., Westerhold, T. *et al*. 2019. A high-fidelity benthic stable isotope record of Late Cretaceous–Early Eocene climate change and carbon-cycling. *Paleoceanography and Paleoclimatology*, 34, 672-691.

Barnet, J.S.K., Harper, D.T., LeVay, L.J. *et al.* 2020. Coupled evolution of temperature and carbonate chemistry during the Paleocene-Eocene; new trace element records from the low latitude Indian Ocean. *Earth and Planetary Science Letters*, 545, 116414.

Beasley, C., Parvaz, D.B., Cotton, L. and Littler, K. 2020. Liberating microfossils from indurated carbonates: comparison of three disaggregation methods. *Journal of Micropalaeontology*, 39, 169-181.

Bernard, E. 2022. Personal communication during visit to Natural History Museum, 9 February.

Bijl, P.K., Houben, A.J.P., Schouten, S. *et al.* 2010. Transient Middle Eocene atmospheric CO_2 and temperature variations. *Science*, 330, 819-821.

Bijl, P.K., Bendle, J.A.P., Bohaty, S.M. *et al.* 2013. Eocene cooling linked to early flow across the Tasmanian Gateway. *Proceedings of the National Academy of Sciences*, 110, 9645-9650.

Bissell, I.C., Hull, P. M. and Sibert, E.C. 2024. [In preparation] Five degrees of global warming increases fish biomass but not extinction in the Early Eocene.

Boggust, I.G. 2022. A reconstruction of the palaeoenvironment at Hole U1514C, south-eastern Indian Ocean, across the Paleocene-Eocene Thermal Maximum. Masters thesis, University of Birmingham.

Bohaty, S.M. and Zachos, J.C. 2003. Significant Southern Ocean warming event in the late middle Eocene. *Geology*, 31, 1017-1020.

Bohaty, S.M., Zachos, J.C., Florindo, F. and Delaney, M.L. 2009. Coupled greenhouse warming and deep-sea acidification in the middle Eocene. *Paleoceanography*, 24, PA2207.

Bonde, N. 1997. ‘A distinct fish fauna in the basal ash series of the Fur/Ølst Formation (Upper Paleocene, Denmark)’. *In* Thomasen, E and Pedersen, S.A.S. (eds.) *Geology and Palaeontology of the Mo-clay*. Denmark: Aarhus Geoscience, 6, 33-48.

Borrelli, C., Katz, M.E. and Toggweiler, J.R. 2021. Middle to Late Eocene changes of the ocean carbonate cycle. *Paleoceanography and Paleoclimatology*, 36, e2020PA004168.

Boscolo-Galazzo, F.E., Thomas, M., Pagani, C. *et al.* 2014. The middle Eocene climatic optimum (MECO): A multiproxy record of paleoceanographic changes in the southeast Atlantic (ODP Site 1263, Walvis Ridge). *Paleoceanography*, 29, 1143-1161.

Boscolo-Galazzo, F., Crichton, K.A., Barker, S. and Pearson, P.N. 2018. Temperature dependency of metabolic rates in the upper ocean: A positive feedback to global climate change? *Global and Planetary Change*, 170, 201-212.

Boulila, S., Vahlenkamp, M., De Vleeschouwer, D. *et al.* 2018. Towards a robust and consistent middle Eocene astronomical timescale. *Earth and Planetary Science Letters*, 486, 94-107.

Boyd, C.E., McNevin, A.A. and Davis R.P. 2022. The contribution of fisheries and aquaculture to the global protein supply. *Food Security*, 14, 805-827.

Bralower, T.J., Kelly, D.C., Gibbs, S. *et al.* 2014. Impact of dissolution on the sedimentary record of the Paleocene–Eocene thermal maximum. *Earth and Planetary Science Letters*, 401, 70-82.

Brée, B., Condamine, F.L. and Guinot, G. 2022. Combining palaeontological and neontological data shows a delayed diversification burst of carcharhiniform sharks likely mediated by environmental change. *Science Reports*, 12, 21906.

British Geological Survey (2020) *The BGS Lexicon of Named Rock Units* [online]. Keyworth, Nottingham. Available from https://www.bgs.ac.uk/technologies/the-bgs-lexicon-of-named-rock-units/. Accessed: 2022.

Britten, G.L. and Sibert, E.C. 2020. Enhanced fish production during a period of extreme global warmth. *Nature Communications*, 11, 5636.

Brown, J.H., Gillooly, J.F., Allen, A.P. *et al.* 2004. Toward a metabolic theory of ecology. *Ecology*, 85, 1771-1789.

Broz, A.P., Prtichard-Peterson, D. Spinola, D. *et al.* 2024. Eocene (50–55 Ma) greenhouse climate recorded in nonmarine rocks of San Diego, CA, USA. *Scientific Reports*, 14, 2613.

Carmichael, M.J., Lunt, D.J., Huber, M. *et al*. 2016. A model–model and data–model comparison for the early Eocene hydrological cycle. *Climate of the Past*, 12, 455-481.

Carmichael, M.J., Inglis, G.N., Badger, M.P.S. *et al.* 2017. Hydrological and associated biogeochemical consequences of rapid global warming during the Paleocene-Eocene Thermal Maximum. *Global and Planetary Change*, 157, 114-138.

Casier, E. 1966. *Faune Ichthyologique du London Clay.* London: British Museum (Natural History). 496pp.

Chang, M-Y. and Geffen, A.J. 2012. Taxonomic and geographic influences on fish otolith microchemistry. *Fish and Fisheries*, 14, 458-492.

Ciesielski, P.F., Kristoffersen, Y., Shipboard Scientific Party *et al.* 1988. Site 702. *Proceedings of the Ocean Drilling Program Initial Reports*, 114, 483-548.

Close, R.A., Evers, S.W., Alroy, J. and Butler, R.J. 2018. How should we estimate diversity in the fossil record? Testing richness estimators using sampling-standardised discovery curves. *Methods in Ecology and Evolution*, 9, 1386-1400.

Collinson, M.E. 2000. Fruit and seed floras from the Palaeocene/Eocene transition and subsequent Eocene in southern England: Comparison and palaeoenvironmental implications, *GFF*, 122, 36-37.

Collinson, M.E., Hooker, J.J. and Gröcke, D.R. 2003. 'Cobham Lignite Bed and penecontemporaneous macrofloras of southern England: A record of vegetation and fire across the Paleocene-Eocene Thermal Maximum.' *In* Wing, S.L., Gingerich, P.D., Schmitz, B. and Thomas, E. (eds.) *Causes and consequences of globally warm climates in the Early Paleogene*. Boulder, Colorado: Geological Society of America Special Paper, 369, 333-349.

Condamine, F.L., Romieu, J. and Guinot, G. 2019. Climate cooling and clade competition likely drove the decline of lamniform sharks. *Proceedings of the National Academy of Sciences*, 116, 20584-20590.

Cramer, B.S., Wright, J.D., Kent, D.V. and Aubry, M-P. 2003. Orbital climate forcing of $\delta^{13}C$ excursions in the late Paleocene–early Eocene (chrons C24n–C25n). *Palaeoceanography*, 18, 1097.

Cramwinckel, M.J., Huber, M., Kocken, I.J. *et al.* 2018. Synchronous tropical and polar temperature evolution in the Eocene. *Nature*, 559, 382-366.

Crichton, K.A., Wilson, J.D., Ridgwell, A. *et al.* 2023. What the geological past can tell us about the future of the ocean's twilight zone. *Nature Communications*, 14, 2376.

Dalpadado, P., Arrigo, K.R., van Dijken, G.L. *et al.* 2021. Warming of the Indian Ocean and its impacts on temporal and spatial dynamics of primary production. *Progress in Oceanography*, 198, 102688.

DeConto, R.M., Galeotti, S., Pagani, M. *et al.* 2012. Past extreme warming events linked to massive carbon release from thawing permafrost. *Nature*, 484, 87-91.

Diester-Haass, L. and Faul, K. 2019. Paleoproductivity reconstructions for the Paleogene Southern Ocean: A direct comparison of geochemical and micropaleontological proxies. *Paleoceanography and Paleoclimatology*, 34, 79-97.

Dillon, M.E., Wang, G. and Huey, R.B. 2010. Global metabolic impacts of recent climate warming. *Nature*, 467, 704-706.

D'Onofrio, R., Zaky, A.S., Frontalini, F. *et al.* 2021. Impact of the Middle Eocene Climatic Optimum (MECO) on foraminiferal and calcareous nannofossil assemblages in the Neo-Tethyan Baskil Section (Eastern Turkey): Paleoenvironmental and paleoclimatic reconstructions. *Applied Sciences*, 11, 11339.

Douglas, P.M.J., Affek, H.P., Ivany, L.C. *et al.* 2014. Pronounced zonal heterogeneity in Eocene southern high-latitude sea surface temperatures. *Proceedings of the National Academy of Sciences*, 111, 6582-6587.

Doyle, P.S. and Riedel, W.R. 1979. *Ichthyoliths: Present status of taxonomy and stratigraphy of microscopic fish skeletal debris.* Scripps Institute of Oceanography Report 197926, 235pp.

Dunhill, A.M. 2012. Problems with using rock outcrop area as a paleontological sampling proxy: rock outcrop and exposure area compared with coastal proximity, topography, land use and lithology. *Paleobiology*, 38, 126-143.

Dunhill, A.M., Benton, M.J., Twitchett, R.J. and Newell, A.J. 2012. Completeness of the fossil record and the validity of sampling proxies at outcrop level. *Palaeontology*, 55, 1155-1175.

Echreshavi, S., Esmaeili, H.R., Teimori, A. and Safaie, M. 2021. Otolith morphology: A hidden tool in the taxonomic study of goatfishes (Teleostei: Perciformes: Mullidae). *Zoological Studies*, 60, e36.

Edgar, K.M., Bohaty, S.M., Gibbs, S.J. *et al.* 2013. Symbiont 'bleaching' in planktic foraminifera during the Middle Eocene Climatic Optimum. *Geology*, 41, 15-18.

Edgar, K.M., Bohaty, S.M., Coxall, H.K. *et al.* 2020. New composite bio- and isotope stratigraphies spanning the Middle Eocene Climatic Optimum at tropical ODP Site 865 in the Pacific Ocean. *Journal of Micropalaeontology*, 39, 117-138.

Edgar, K.M., MacLeod, K.G., Hasegawa, T. *et al.* 2022. Data report: Cenozoic and Upper Cretaceous bulk carbonate stable carbon and oxygen isotopes from IODP Expedition 369 Sites U1513, U1514, and U1516 in the southeast Indian Ocean. *Proceedings of the International Ocean Discovery Program* 369. Available at: http://publications.iodp.org/proceedings/369/206/369_206.html [Accessed May 2023].

Edina Digimap. 2022. *Geology* [online]. Available from: https://digimap.edina.ac.uk/geology. Accessed: 2022.

Eichenseer, K. and Jones, L.A. 2024. Bayesian multi-proxy reconstruction of early Eocene latitudinal temperature gradients. *Climate of the Past*, 20, 349-362.

Elliot Smith, M., Carroll, A.R. and Mueller, E.R. 2008. Elevated weathering rates in the Rocky Mountains during the Early Eocene Climatic Optimum. *Nature Geoscience*, 1, 370-374.

Ellison, R.A., Knox, R.W.O., Jolley, D.W. and King, C. 1994. A revision of the lithostratigraphical classification of the early Palaeogene strata of the London Basin and East Anglia. *Proceedings of the Geologists' Association*, 105, 187-197.

Ellison, R.A., Woods, M.A., Allen, D.J., *et al*. 2004. *Geology of London: special memoir for 1: 50000 geological sheets 256 (north London), 257 (Romford), 270 (south London), and 271 (Dartford)(England and Wales)*. British Geological Survey.

El-Sayed, S., Friedman, M., Anan, T. *et al*. 2021. Diverse marine fish assemblages inhabited the paleotropics during the Paleocene-Eocene thermal maximum. *Geology*, 49, 993-998.

Elsworth, G., Galbraith, E., Halverson, G. and Yang, S. 2017. Enhanced weathering and CO_2 drawdown caused by latest Eocene strengthening of the Atlantic meridional overturning circulation. *Nature Geoscience*, 10, 213-216.

Evans, D., Wade, B.S., Henehan, M. *et al*. 2018. Revisiting carbonate chemistry controls on planktic foraminifera Mg/Ca: Implications for sea surface temperature and

hydrology shifts over the Paleocene–Eocene Thermal Maximum and Eocene–Oligocene transition, *Climates of the Past*, 12, 819-835.

Ezard, T.H.G., Aze, T., Pearson, P.N. and Purvis, A. 2011. Interplay between changing climate and species' ecology drives macroevolutionary dynamics. *Science*, 332, 349-351.

Foote, M. 2000. Origination and extinction components of taxonomic diversity: general problems. *Paleobiology*, 26, 74-102.

Foster, G.L., Hull, P., Lunt, D.J. and Zachos, J.C. 2018. Placing our current 'hyperthermal' in the context of rapid climate change in our geological past, *Philosophical Transactions of the Royal Society A*, 376, 20170086.

Friedman, M. and Johnson, G.D. 2005. A new species of Mene (Perciformes: Menidae) from the Paleocene of South America, with notes on paleoenvironment and a brief review of menid fishes. *Journal of Vertebrate Paleontology*, 25, 770-783.

Friedman, M. 2010. Explosive morphological diversification of spiny-finned teleost fishes in the aftermath of the end-Cretaceous extinction. *Proceedings of the Royal Society B: Biological Sciences*, 277, 1675-1683.

Friedman, M., Beckett, H.T., Close, R.A and Johanson, Z. 2015. 'The English Chalk and London Clay: two remarkable British bony fish Lagerstätten'. *In* Johanson, Z., Barrett, P.M, Richter, M and Smith, M (eds.) *Arthur Smith Woodward: His life and influence on modern vertebrate palaeontology*. London: Geological Society Special Publications 430, 165-200.

Friedman, M. and Carnevale, G. 2018. The Bolca Lagerstätten: shallow marine life in the Eocene. *Journal of the Geological Society*, 175, 569-579.

Friedman, M. 2022. Personal communication via email, 8 February.

Friedman, M. 2022b. The macroevolutionary history of bony fishes: A paleontological view. *Annual Review of Ecology, Evolution, and Systematics*, 53, 353–77.

Frost, G.A. 1925. Eocene fish otoliths from the London District and the Isle of Wight. *Annals and Magazine of Natural History*, 9, 160-165.

Frost, G.A. 1933. Otoliths of fishes from the Lower Tertiary formations of Southern England - Isospondyli, Apodes, Berycomorphi. *Annals and Magazine of Natural History*, 12, 387-396.

Frost, G.A. 1934. Otoliths of fishes from the lower tertiary formations of Southern England - Percomorphi. *Annals and Magazine of Natural History*, 13, 380-386.

Gaskell, D.E., Huber, M., O'Brien, C.L. *et al.* 2022. The latitudinal temperature gradient and its climate dependence as inferred from foraminiferal $\delta^{18}O$ over the past 95 million years. *Earth, Atmospheric, and Planetary Sciences*, 119, e2111332119.

Gauldie, R.W., Coote, G., Mulligan, K.P. *et al.* 1991. Otoliths of deep water fishes: structure, chemistry and chemically-coded life histories. *Comparative Biochemistry and Physiology Part A: Physiology*, 100, 1-31.

Ghezelayagh, A., Harrington, R.C., Burress, E.D. *et al.* 2022. Prolonged morphological expansion of spiny-rayed fishes following the end-Cretaceous. *Nature, Ecology and Evolution*, 6, 1211-1220.

Giorgioni, M., Jovane, L., Rego, E.S. *et al.* 2019. Carbon cycle instability and orbital forcing during the Middle eocene Climatic optimum. *Scientific Reports*, 9, 9357.

Gradstein, F.M., Ogg, J.G., Schmitz, M.D. and Ogg, G.M. 2012. *The geologic time scale 2012*. Elsevier. 250pp.

Greene, S.E., Ridgwell, A., Kirtland Turner, S. *et al.* 2019. Early Cenozoic decoupling of climate and carbonate compensation depth trends. *Paleoceanography and Paleoclimatology*, 34, 930-945.

Gutjahr, M., Ridgwell, A., Sexton, P.F. *et al.* 2017. Very large release of mostly volcanic carbon during the Palaeocene-Eocene Thermal Maximum. *Nature*, 548, 573-577.

Hammer, Ø., Harper, D.A.T. and Ryan, P.D. 2001. Past: Paleontological Statistics software package for education and data analysis. *Palaeontologia Electronica*, 4, 1-9. https://www.nhm.uio.no/english/research/resources/past/.

Hastings, P.A., Walker, H.J. and Galland, G.R. 2014. *Fishes: A guide to their diversity*. University of California Press, USA.

Hay, W.W., DeConto, R., Wold, C.N. *et al.* 1999. Alternative global Cretaceous paleogeography. *In* Barrera, E. and Johnson, C. (eds.). The Evolution of Cretaceous Ocean/Climate Systems. *Geological Society of America Special Paper 332*, 1-47.

Heneghan, M.J., Edgar, K.M., Foster, G.L. *et al*. 2020. Revisiting the Middle Eocene Climatic Optimum “Carbon Cycle Conundrum” with new estimates of atmospheric pCO_2 from boron isotopes. *Paleoceanography and Paleoclimatology*, 35, e2019PA003713.

Heneghan, R.F., Galbraith, E., Blanchard, J.L. *et al.* 2021. Disentangling diverse responses to climate change among global marine ecosystem models. *Progress in Oceanography*, 198, 102659.

Hobbs, R.W., Huber, B.T., Bogus, K. A. and the Expedition 369 Scientists. 2019. *Australia Cretaceous climate and tectonics*. *In* Proceedings of the International Ocean Discovery Program, 369: College Station, TX.

Hollis, C.J., Taylor K.W., Handley, L. *et al.* 2012. Early Paleogene temperature history of the Southwest Pacific Ocean: Reconciling proxies and models. *Earth and Planetary Science Letters*, 349-350, 53-66.

Hollis, C.J., Dunkley Jones, T., Anagnostou, E. *et al*. 2019. The DeepMIP contribution to PMIP4: methodologies for selection, compilation and analysis of latest Paleocene and early Eocene climate proxy data, incorporating version 0.1 of the DeepMIP database. *Geoscientific Model Development*, 12, 3149-3206.

Huber, B.T., Hobbs, R.W., Bogus, K.A. *et al*. 2019. Site U1514. *In* Hobbs, R.W., Huber, B.T., Bogus, K.A. and the Expedition 369 Scientists, *Australia Cretaceous Climate and Tectonics*. Proceedings of the International Ocean Discovery Program, 369: College Station, Texas.

Huck, C.E., van de Flierdt, T., Jiménez-Espejo, F.J. *et al.* 2016. Robustness of fossil fish teeth for seawater neodymium isotope reconstructions under variable redox conditions in an ancient shallow marine setting. *Geochemistry, Geophysics, Geosystems*, 17, 679-698.

Hull, P.M. and Norris, R.D. 2011. Diverse patterns of ocean export productivity change across the Cretaceous-Paleogene boundary: New insights from biogenic barium. *Paleoceanography and Paleoclimatology*, 26, PA3205.

Inglis, G.N., Farnsworth, A., Lunt, D. *et al.* 2015. Descent toward the icehouse: Eocene sea surface cooling inferred from GDGT distributions. *Paleoceanography and Paleoclimatology*, 30, 1000-1020.

Inglis, G.N., Bragg, F., Burls, N.J. *et al*. 2020. Global mean surface temperature and climate sensitivity of the early Eocene Climatic Optimum (EECO), Paleocene–Eocene Thermal Maximum (PETM), and latest Paleocene. *Climate of the Past*, 16, 1953-1968.

Intergovernmental Panel on Climate Change (IPCC). 2022. *Climate Change 2022: Impacts, Adaptation and Vulnerability. Contribution of Working Group II to the Sixth Assessment Report of the Intergovernmental Panel on Climate Change*. Cambridge University Press, Cambridge, UK and New York, USA.

IODP LIMS Online Report Portal. 2018. International Ocean Discovery Program JOIDES Resolution Science Operator. Available online: http://web.iodp.tamu.edu/LORE [Accessed: June 2023, Version 18.1].

John, E.H., Pearson, P.N., Coxall, H.K. *et al*. 2013. Warm ocean processes and carbon cycling in the Eocene. *Philosophical Transactions of the Royal Society A,* 371, 20130099.

Johns, M.J., Barnes, C.R. and Narayan, Y.R. 2005. Cenozoic and Cretaceous Ichthyoliths from the Tofino Basin and Western Vancouver Island, British Columbia, Canada. *Palaeontologia Electronica*, 8, 2.29A.

Jones, S.M., Hoggett, M., Greene, S.E. and Dunkley Jones, T. 2019. Large Igneous Province thermogenic greenhouse gas flux could have initiated Paleocene-Eocene Thermal Maximum climate change. *Nature Communications*, 10, 5547.

Kennedy, A.E. and Coe, A.L. 2014. Development of the freeze–thaw processing technique for disaggregation of indurated mudrocks and enhanced recovery of calcareous microfossils. *Journal of Micropalaeontology*, 33, 193-203.

Keppeler, F.W., Montaña, C.G. and Winemiller, K.O. 2020. The relationship between trophic level and body size in fishes depends on functional traits. *Ecological Monographs*, 90, e01415.

King, C. 1981. Stratigraphy of the London Clay and associated deposits. Rotterdam: Backhuys, *Tertiary Research Special Papers*, 6, 158pp.

King, C. 2006. 'Palaeogene and Neogene: uplift and a cooling climate.' *In* Brenchley, P.J. and Rawson, P.F. (eds.) *The geology of England and Wales.* London: The Geological Society, 395-428.

King, C. 2016. 'East Anglia and the London Basin (Paleocene and Eocene)'. *In* Gale. A.A. and Barry, T.L. (eds.) *A revised correlation of Tertiary rocks in the British Isles and adjacent areas of NW Europe*. London: Geological Society Special Reports, 27, 329-375.

Kirby, N.J. 2022. *Climatic, Oceanographic and environmental change in the early to middle Eocene*. PhD thesis, University of Birmingham. Available from: https://core.ac.uk/download/613172352.pdf.

Kirtland Turner, S., Sexton, P.F., Charles, C.D., and Norris, R.D. 2014. Persistence of carbon release events through the peak of early Eocene global warmth. *Nature Geoscience*, 7, 748-751.

Knox, R.W.O. 1996. 'Tectonic controls on sequence development in the Palaeocene and earliest Eocene of southeast England: implications for North Sea stratigraphy'. *In* Hesselbo, S.P. and Parkinson, D.N. (eds.) *Sequence stratigraphy in British Geology*. London: Geological Society Special Publication, 103, 209-230.

Krause, A.J., Sluiks, A., van der Ploeg, R. *et al.* 2023. Enhanced clay formation key in sustaining the Middle Eocene Climatic Optimum. *Nature Geoscience*, 16, 730-738.

Langton, S.J., Rabideaux, N.M., Borrelli, C. and Katz, M.E. 2016. Southeastern Atlantic deep-water evolution during the late-middle Eocene to earliest Oligocene (Ocean Drilling Program Site 1263 and Deep Sea Drilling Project Site 366). *Geosphere*, 12, 1032-1047.

Lim, D., Xu, Z., Kim, J. *et al*. 2024. Enhanced volcanic activity and long-term warmth in the middle Eocene revealed by mercury and osmium isotopes from IODP Expedition 369 Site U1514. *Earth and Planetary Science Letters*, 627, 118565.

Lin, C-H., Girone, A. and Nolf, D. 2016. Fish otolith assemblages from Recent NE Atlantic sea bottoms: A comparative study of palaeoecology. *Palaeogeography, Palaeoclimatology, Palaeoecology*, 446, 98-107.

Liu, Z., Pagani, M., Zinniker, D. *et al*. 2009. Global cooling during the Eocene-Oligocene climate transition. *Science*, 323, 1187-1190.

Lowery, C.M., Bown, P.R., Fraass, A.J. and Hull, P.M. 2020. Ecological response of plankton to environmental change: thresholds for extinction. *Annual Review of Earth and Planetary Sciences*, 48, 402-429.

Lunt, D.J., Ridgwell, A., Sluijs, A. *et al.* 2011. A model for orbital pacing of methane hydrate destabilization during the Palaeogene. *Nature Geoscience*, 4, 775-778.

MacLeod, K.G., Quinton, P.C., Sepúlveda, J. and Negra, M.H. 2018. Post-impact earliest Paleogene warming shown by fish debris oxygen isotopes (El Kef, Tunisia). *Science*, 360, 1467-1469.

Marinov, I., Gnanadesikan, A., Toggweiler, J.R. and Sarmiento, J.L. 2006. The Southern Ocean biogeochemical divide. *Nature*, 441, 964-967.

Marshall, C.R., Finnegan, S., Clites, E.C. *et al*. 2018. Quantifying the dark data in museum fossil collections as palaeontology undergoes a second digital revolution. *Biology Letters*, 14, 20180431.

Mascle, J., Lohmann, G.P., Clift, P.D. *et al.* 1996. Site 959. *Proceedings of the Ocean Drilling Program Initial Reports*, 159, 65-150.

Maureaud, A., Gascuel, D., Colléter, M. *et al.* 2017. Global change in the trophic functioning of marine food webs. *PLOS One*, 12, e0182826.

McInerney, F.A. and Wing, S.L. 2011. The Paleocene-Eocene Thermal Maximum: A perturbation of carbon cycle, climate, and biosphere with implications for the future. *Annual Review of Earth and Planetary Sciences*, 39, 489-516.

Miller, K.G., Browning, J.V., Schmelz, W.J. *et al*. 2020. Cenozoic sea-level and cryospheric evolution from deep-sea geochemical and continental margin records. *Science Advances*, 6, eaaz1346.

Moebius, I., Friedrich, O. and Scher, H.D. 2014. Changes in Southern Ocean bottom water environments associated with the Middle Eocene Climatic Optimum (MECO). *Palaeogeography, Palaeoclimatology, Palaeoecology*, 405, 16-27.

Moebius, I., Friedrich, O., Edgar, K.M. and Sexton, P.F. 2015. Episodes of intensified biological productivity in the Atlantic Ocean during the termination of the Middle Eocene Climatic Optimum (MECO). *Paleoceanography*, 30, 1041-1058.

Müller, R.D., Cannon, J., Qin, X. *et al.* 2018. GPlates: Building a virtual Earth through deep time. *Geochemistry, Geophysics, Geosystems*, 19, 2243-2261.

Murphy, B.H., Farley, K.A. and Zachos, J.C. 2010. An extraterrestrial ^{3}He-based timescale for the Paleocene–Eocene thermal maximum (PETM) from Walvis Ridge, IODP Site 1266. *Geochimica et Cosmochimica Acta*, 74, 5098-5108.

Myhre, A.M., Thiede, J., Firth, J.V. *et al.* 1995. Site 913. *Proceedings of the Ocean Drilling Program Initial Reports*, 151, 345-382.

Nelson, J.S., Grande, T.C. and Wilson, M.V.H. 2016. *Fishes of the World*. Fifth edition. New Jersey: Wiley. 745pp.

Nolf, D. 1985. ‘Otolithi piscium’. *In* Schultze, H-P. (ed.) *Handbook of Paleoichthyology* (10th edition). Stuttgart and New York: Gustav Fischer Verlag. 145pp.

Nolf, D. 2013. *The diversity of fish otoliths past and present*. Brussels: Royal Belgian Institute of Natural Sciences. 222pp.

Norris, R.D., Kirtland Turner, S., Hull, P.M. and Ridgwell, A. 2013. Marine ecosystem responses to Cenozoic global change, *Science*, 341, 492-498.

Oksanen, J., Simpson, G., Blanchet, F. *et al.* 2022. vegan: Community Ecology Package. R package version 2.6-4. https://CRAN.R-project.org/package=vegan.

Olivarez Lyle, A. and Lyle, M.W. 2006. Missing organic carbon in Eocene marine sediments: Is metabolism the biological feedback that maintains end-member climates? *Palaeoceanography and Palaeoclimatology*, 21, PA2007.

Paleobiology Database. 2024. PBDB Navigator [online]. Available from: https://paleobiodb.org/navigator/. Accessed March 2023 to August 2024.

Pälike, H., Lyle, M.W., Nishi, H. *et al.* 2012. A Cenozoic record of the equatorial Pacific carbonate compensation depth. *Nature*, 488, 609-614.

Park, J.M., Kang, M.G., Kim, J.H. *et al.* 2023. Otolith morphology as a tool for stock discrimination of three rockfish species in the East Sea of Korea. *Frontiers in Marine Science*, 10, 1301178.

Paxton, R. 2000. Fish otoliths: do sizes correlate with taxonomic group, habitat and/or luminescence? *Philosophical Transactions of the Royal Society B*, 355,1299-1303.

Petrik, C.M., Stock, C.A., Andersen, K.H. *et al.* 2020. Large pelagic fish are most sensitive to climate change despite pelagification of ocean food webs. *Frontiers in Marine Science*, 7, 588482.

Popov, D., Roychoudhury, P., Hardy, H. *et al*. 2021. The value of digitising natural history collections. *London: Natural History Museum, Research Ideas and Outcomes*, 7, e78844.

Quayle, W.J. 1987. English Eocene Crustacea (lobsters and stomatopod). *Palaeontology*, 3, 581-612.

Rae, J.W.B., Zhang, Y.G., Liu, X. *et al*. 2021. Atmospheric CO_2 over the past 66 million years from marine archives. *Annual Review of Earth and Planetary Sciences*, 49, 609-41.

R Core Team. 2023. R: A language and environment for statistical computing. R Foundation for Statistical Computing, Vienna, Austria. https://www.R-project.org.

Raymond, C.A., LaBrecque, J.L. and Kristoffersen, Y. 1991. Islas Orcadas Rise and Meteor Rise: The tectonic and depositional history of two aseismic plateaus from Sites 702, 703 and 704. *In* Ciesielski, P.F. *et al.* (eds.) *Proceedings of the Ocean Drilling Program 114 Scientific Results.* College Station, Texas, 5-22.

Ribeiro, E., Davis, A.M., Rivero-Vega, R.A. *et al.* 2018. Post-Cretaceous bursts of evolution along the benthic-pelagic axis in marine fishes. *Proceedings of the Royal Society Biological Sciences,* 285, 20182010.

Rivero-Cuesta, L., Westerhold, T., Agnini, C. *et al*. 2019. Palaeoenvironmental changes at ODP Site 702 (South Atlantic): Anatomy of the Middle Eocene Climate Optimum. *Oceanography and Climatology*, 34, 2047-2066.

Röhl, U., Westerhold, T., Bralower, T.J. and Zachos, J.C. 2007. On the duration of the Paleocene–Eocene Thermal Maximum (PETM). *Geochemistry, Geophysics, Geosystems*, 8, Q12002.

Roxy, M.K., Modi, A., Murtugudde, R. *et al.* 2015. A reduction in marine primary productivity driven by rapid warming over the tropical Indian Ocean. *Geophysical Research Letters*, 43, 826-833.

Savian, J.F., Jovane, L., Frontalini, F. *et al.* 2014. Enhanced primary productivity and magnetotactic bacterial production in response to middle Eocene warming in the Neo-Tethys Ocean. *Palaeogeography, Palaeoclimatology, Palaeoecology*, 414, 32-45.

Scheibner, C. and Spiejer, R.P. 2008. Late Paleocene–early Eocene Tethyan carbonate platform evolution - A response to long- and short-term paleoclimatic change. *Earth-Science Reviews*, 90, 71-102.

Scher, H.D. and Martin, E.E. 2004. Circulation in the Southern Ocean during the Paleogene inferred from neodymium isotopes. *Earth and Planetary Science Letters*, 228, 391-405.

Scher, H.D. and Martin, E.E. 2006. Timing and climatic consequences of the opening of Drake Passage. *Science*, 312, 428-430.

Schmidt, D.N., Thierstein, H.R., Bollmann, J. and Schiebel, R. 2004. Abiotic forcing of plankton evolution in the Cenozoic. *Science*, 303, 207-210.

Schubert, R. 1916. Obereocäne otolithen vom Barton Cliff bei Christchurch (Hampshire). *Jahrbuch der Kaiserlich-Königlichen Geologischen Gesellschaft* , 65, 277-288.

Schulz-Mirbach, T., Ladich, F., Plath, M. and Heß, M. 2019. Enigmatic ear stones: what we know about the functional role and evolution of fish otoliths. *Biological Reviews*, 94, 457-482.

Schwarzhans, W. 1993. *Otolithi piscium: a comparative morphological treatise of recent and fossil otoliths of the family Sciaenidae (Perciformes)*. München: Verlag Dr. Friedrich Pfeil. 245pp.

Schwarzhans, W., Beckett, H.T., Schein, J.D. and Friedman, M. 2018. Computed tomography scanning as a tool for linking the skeletal and otolith-based fossil records of teleost fishes. *Palaeontology*, 61, 511-541.

Shannon, C.E. and Weaver, W. 1949. *The mathematical theory of communication*. Urbana: University of Illinois Press. 131pp.

Sibert, E.C., Hull, P.M. and Norris, R.D. 2014. Resilience of Pacific pelagic fish across the Cretaceous/Palaeogene mass extinction. *Nature Geoscience*, 7, 667-670.

Sibert, E.C. and Norris, R.D. 2015. New age of fishes initiated by the Cretaceous-Paleogene mass extinction. *Proceedings of the National Academy of Sciences*, 112, 8537-8542.

Sibert, E.C. 2016. 'A novel coding scheme for quantifying the morphological variation of tooth-type ichthyoliths' *In* Sibert, E.C. *Ichthyoliths as a paleoceanographic and paleoecological proxy and the response of open-ocean fish to Cretaceous and Cenozoic global change*, PhD thesis. University of California, San Diego, 163-175.

Sibert, E., Norris, R., Cuevas, J. and Graves, L. 2016. Eighty-five million years of Pacific Ocean gyre ecosystem structure: long-term stability marked by punctuated change. *Proceedings B*, 283, 20160189.

Sibert, E.C., Cramer, K.L, Hastings, P.A. and Norris, R.D. 2017. Methods for isolation and quantification of microfossil fish teeth and elasmobranch dermal denticles (ichthyoliths) from marine sediments. *Palaeontologia Electronica*, 20.1.2T, 1-14.

Sibert, E., Friedman, M., Hull, P. *et al.* 2018. Two pulses of morphological diversification in Pacific pelagic fishes following the Cretaceous-Palaeogene mass extinction. *Proceedings B*, 285, 20181194.

Sibert, E.C., Zill, M.E., Frigyik, E.T. and Norris, R.D. 2020. No state change in pelagic fish production and biodiversity during the Eocene–Oligocene transition. *Nature Geoscience*, 13, 238-242.

Sibert, E.C. and Rubin, L.D. 2021. An early Miocene extinction in pelagic sharks. *Science*, 372, 1105-1107.

Sibert, E.C. 2023. Personal communication via Zoom and email throughout the year.

Sibert, E.C. 2024. Personal communication via Zoom and email throughout the year, providing access to private coding spreadsheet for ichthyolith researchers.

Siesser, W.G. 1995. Paleoproductivity of the Indian Ocean during the Tertiary Period. *Global and Planetary Change*, 11, 71-88.

Slotnick, B.S., Laurentana, V., Backman, J. *et al.* 2015. Early Paleogene variations in the calcite compensation depth: new constraints using old borehole sediments from across Ninetyeast Ridge, central Indian Ocean. *Climate of the Past*, 11, 473-493.

Sluijs, A., Brinkhuis, H., Crouch, E.M. *et al*. 2008. Eustatic variations during the Paleocene-Eocene greenhouse world. *Paleoceanography*, 23, PA4216.

Sluijs, A., Zeebe, R.E., Bijl, P.K. and Bohaty, S.M. 2013. A middle Eocene carbon cycle conundrum. *Nature Geoscience*, 6, 429-434.

Smith, A.G., Smith, D.G. and Funell, B.M. 1994. *Atlas of Mesozoic and Cenozoic coastlines*. Cambridge: Cambridge University Press. 112pp.

Smith, A.B. and McGowan, A.J. 2011. 'The ties linking rock and fossil records and why they are important for palaeobiodiversity studies'. *In* McGowan, A.J. and Smith, A.B. (eds.) *Comparing the geological and fossil records: implications for biodiversity studies*. London: Geological Society Special Publications, 358, 1-7.

Speijer, R.P., Scheibner, C., Stassen, P. and Morsi, A-M.M. 2012. Response of marine ecosystems to deep-time global warming: A synthesis of biotic patterns across the Paleocene-Eocene thermal maximum (PETM). *Austrian Journal of Earth Sciences*, 105, 6-16.

Stap, L., Lourens, L.J., Thomas, E. *et al.* 2010. High-resolution deep-sea carbon and oxygen isotope records of Eocene Thermal Maximum 2 and H2. *Geology*, 38, 607-610.

Stinton, F.C. 1975. *Fish otoliths from the English Eocene Part 1*. London: The Palaeontographical Society, 1-56.

Stinton, F.C. 1977. *Fish otoliths from the English Eocene Part 2*. London: The Palaeontographical Society, 57-126.

Stinton, F.C. 1978. *Fish otoliths from the English Eocene Part 3*. London: The Palaeontographical Society, 127-189.

Stinton, F.C. 1980. *Fish otoliths from the English Eocene Part 4*. London: The Palaeontographical Society, 191-258.

Stinton, F.C. 1983. *Fish otoliths from the English Eocene Part 5*. London: The Palaeontographical Society, 259-320.

Stock, M., Nguyen, B., Courtens, W. *et al*. 2021. Otolith identification using a deep hierarchical classification model. *Computers and Electronics in Agriculture*, 180, 105883.

Svensen, H., Planke, S., Malthe-Sørenssen, A. *et al.* 2004. Release of methane from a volcanic basin as a mechanism for initial Eocene global warming. *Nature*, 429, 542-545.

Tackett, L.S., Zierer, D. and Clement, A.C. 2022. Actinopterygian and chondrichthyan ichthyoliths reveal enhanced cosmopolitanism in Late Triassic marine ecosystems. *Historical Biology*, 35, 2022-2035.

Talley, L.D., Pickard, G.L. Emery, W.J. and Swift, J.H. 2011. 'Indian Ocean'. *In* Talley, L.D. (ed.) *Descriptive Physical Oceanography*. London: Elsevier, 363-399.

Tanaka, E., Mimura, K., Ohta, J. *et al.* 2024. Composite ages of pelagic clay enriched in rare-earth elements in the Pacific Ocean based on Sr isotope chemostratigraphy and ichthyolith biostratigraphy. *Newsletters on Stratigraphy*, 57, 359-387.

Tittensor, D.P., Novaglio, C., Harrison, C.S. *et al.* 2021. Next-generation ensemble projections reveal higher climate risks for marine ecosystems. *Nature Climate Change*, 11, 973-981.

Tracey, S., Donovan, S.K., Clements, D. *et al*. 2002. Temporary exposures of the Eocene London Clay Formation at Highgate, north London: rediscovery of a fossiliferous horizon 'lost' since the nineteenth century. *Proceedings of the Geologists' Association*, 113, 319-331.

Vahlenkamp, M., De Vleeschouwer, D., Batenburg, S.J. *et al*. 2020. A lower to middle Eocene astrochronology for the Mentelle Basin (Australia) and its implications for the geologic time scale. *Earth and Planetary Science Letters*, 529, 115865.

van der Boon, A., Kuiper, K.F., van der Ploeg, R. *et al.* 2021. Exploring a link between the Middle Eocene Climatic Optimum and Neotethys continental arc flare-up. *Climate of the Past*, 17, 229-239.

van der Ploeg, R., Selby, D., Cramwinckel, M. *et al.* 2018. Middle Eocene greenhouse warming facilitated by diminished weathering feedback. *Nature Communications*, 9, 2877.

van Rijn, I., Buba, Y., DeLong, J. *et al.* 2017. Large but uneven reduction in fish size across species in relation to changing sea temperatures. *Global Change Biology,* 23, 3667-3674.

Ward, D.J. 1978. The *Lower London Tertiary (Palaeocene) succession of Herne Bay, Kent*. Institute of Geological Sciences Report 78/10. Available at: https://pubs.bgs.ac.uk/publications.html?pubID=B01102 (accessed February 2024).

Westerhold, T. and Röhl, U. 2013. Orbital pacing of Eocene climate during the Middle Eocene Climate Optimum and the chron C19r event: Missing link found in the tropical western Atlantic. *Geochemistry, Geophysics, Geosystems*, 14, 4811-4825.

Westerhold, T., Röhl, U., Frederichs, T. *et al.* 2015. Astronomical calibration of the geological timescale: closing the middle Eocene gap. *Climate of the Past*, 11, 1181-1195.

Westerhold, T., Röhl, U., Frederichs, T. *et al*. 2017. Astronomical calibration of the Ypresian timescale: implications for seafloor spreading rates and the chaotic behavior of the solar system? *Climate of the Past*, 13, 1129-1152.

Westerhold, T., Röhl, U., Donner, B. and Zachos, J.C. 2018. Global extent of Early Eocene hyperthermal events: A new Pacific benthic foraminiferal Isotope record from Shatsky Rise (ODP Site 1209). *Paleoceanography and Paleoclimatology*, 33, 626-642.

Westerhold, T., Marwan, N., Drury, A.J. *et al.* 2020. An astronomically dated record of Earth's climate and its predictability over the last 66 million years. *Science*, 369, 1383-1387.

Whitaker, W. 1866. On the "Lower London Tertiaries" of Kent. *Quarterly Journal of the Geological Society*, 22, 404-434.

White, E.I. 1931. *The vertebrate faunas of the English Eocene. Volume I: From the Thanet Sands to the Basement Bed of the London Clay*. London: British Museum (Natural History). 123pp.

Witkowski, J., Bohaty, S.M., McCartney, K. and Harwood, D.M. 2012. Enhanced siliceous plankton productivity in response to middle Eocene warming at Southern Ocean ODP Sites 748 and 749. *Palaeogeography, Palaeoclimatology, Palaeoecology*, 326, 78-94.

Witkowski, J., Bohaty, S.M., Edgar, K.M. and Harwood, D.M. 2014. Rapid fluctuations in mid-latitude siliceous plankton production during the Middle Eocene Climatic Optimum (ODP Site 1051, western North Atlantic). *Marine Micropaleontology*, 106, 110-129.

Wrigley, A. 1924. Faunal divisions of the London Clay illustrated by some exposures near London. *Proceedings of the Geologists' Association*, 35, 245-259.

Zachos, J.C., Breza, J.R. and Wise, S.W. 1992. Early Oligocene ice-sheet expansion on Antarctica: Stable isotope and sedimentological evidence from Kerguelen Plateau, southern Indian Ocean. *Geology*, 20, 569-573.

Zachos, J., Pagani, M.N., Sloan, L. *et al.* 2001. Trends, rhythms, and aberrations in global climate 65 Ma to Present. *Science*, 292, 686-693.

Zachos, J.C., Kroon, D., Blump, P. *et al.* 2004. Site 1263. *Proceedings of the Ocean Drilling Program Initial Reports*, 208, 1-112.

Zhang, L., Hay, W., Wang, C. and Gu, X. 2019. The evolution of latitudinal temperature gradients from the latest Cretaceous through the Present. *Earth-Science Reviews*, 189, 147-158.

Zhuang, L., Ye, Z. and Zhang, C. 2015. Application of otolith shape analysis to species separation in *Sebastes spp*. from the Bohai Sea and the Yellow Sea, northwest Pacific. *Environmental Biology of Fishes*, 98, 547-558.

APPENDICES

Appendix 1: Supplementary material for Chapter Three

Appendix Table 3.1. NHMUK otolith database from this study, documenting information on specimen labels, plus stratigraphic and taxonomic updates where necessary.

Due to the large file size, Appendix Table 3.1 has been deposited online within the University of Birmingham eData Repository, titled "NHMUK Otolith Palaeocene-Ypresian Dataset (Appendix Table 3.1)_HBird2024.xlsx". It is available within the repository titled "Bird, Hannah (2024) Research data supporting PhD thesis 'Actinopterygian and chondrichthyan palaeocommunity responses to early Cenozoic global warming'" (DOI: 10.25500/edata.bham.00001169).

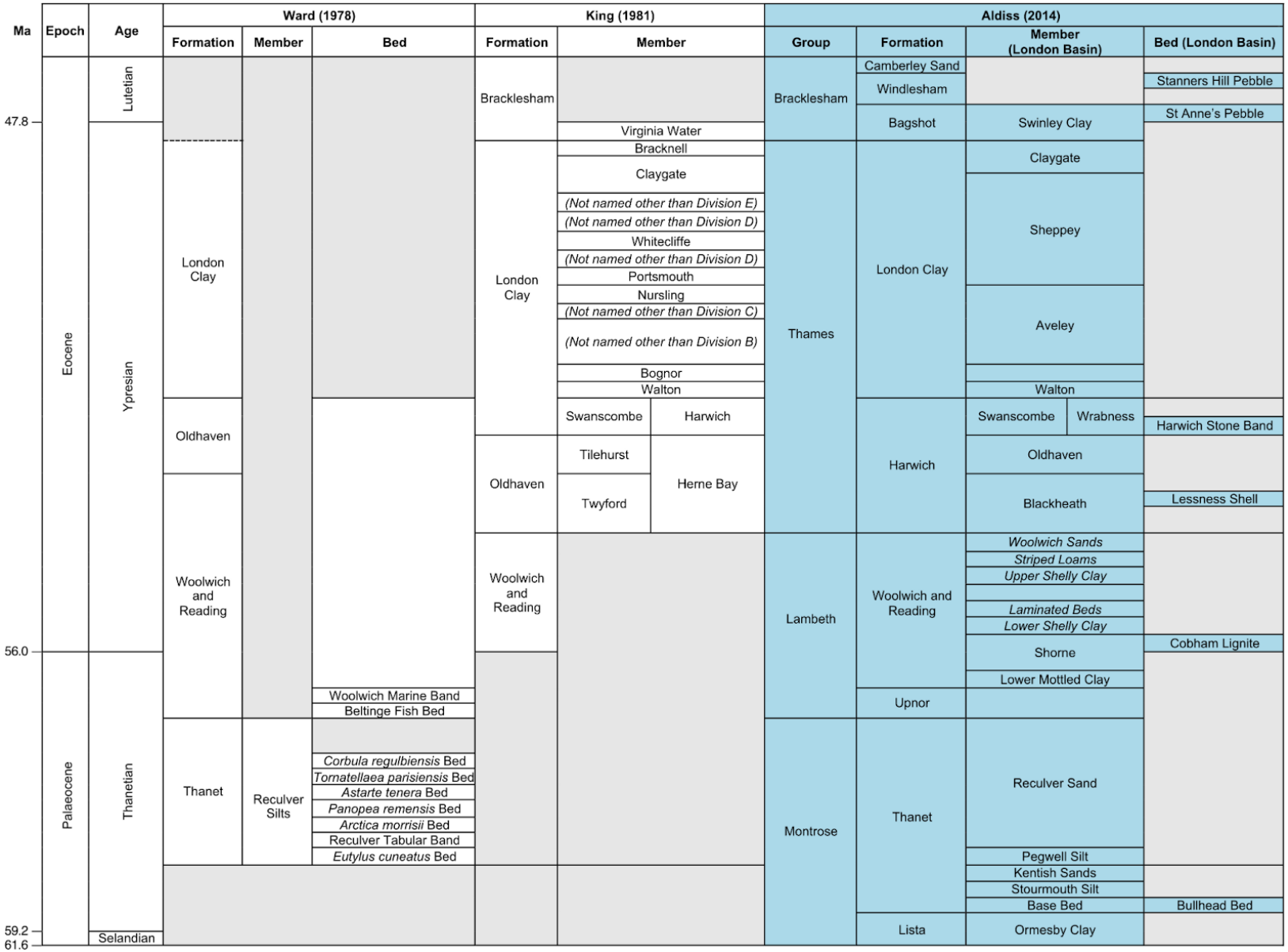
Ma
Epoch
Age
Ward (1978)
Formation
Member
Bed
King (1981)
Formation
Member
Aldiss (2014)
Group
Formation
Member (London Basin)
Bed (London Basin)
47.8
56.0
59.2
61.6
Eocene
Palaeocene
Lutetian
Ypresian
Thanetian
Selandian
London Clay
Oldhaven
Woolwich and Reading
Thanet
Reculver Silts
Woolwich Marine Band
Beltinge Fish Bed
Corbula regulbiensis Bed
Tornatellaea parisiensis Bed
Astarte tenera Bed
Panopea remensis Bed
Arctica morrisii Bed
Reculver Tabular Band
Eutylus cuneatus Bed
Bracklesham
Virginia Water
Bracknell
Claygate
(Not named other than Division E)
(Not named other than Division D)
Whitecliffe
(Not named other than Division D)
Portsmouth
Nursling
(Not named other than Division C)
(Not named other than Division B)
Bognor
Walton
Swanscombe
Harwich
Tilehurst
Twyford
Herne Bay
Camberley Sand
Windlesham
Bagshot
Swinley Clay
Claygate
Sheppey
Aveley
Walton
Swanscombe
Wrabness
Oldhaven
Blackheath
Woolwich Sands
Striped Loams
Upper Shelly Clay
Laminated Beds
Lower Shelly Clay
Shorne
Lower Mottled Clay
Reculver Sand
Pegwell Silt
Kentish Sands
Stourmouth Silt
Base Bed
Ormesby Clay
Stanners Hill Pebble
St Anne's Pebble
Harwich Stone Band
Lessness Shell
Cobham Lignite
Bullhead Bed
Bracklesham
Thames
Lambeth
Montrose
London Clay
Harwich
Woolwich and Reading
Upnor
Thanet
Lista

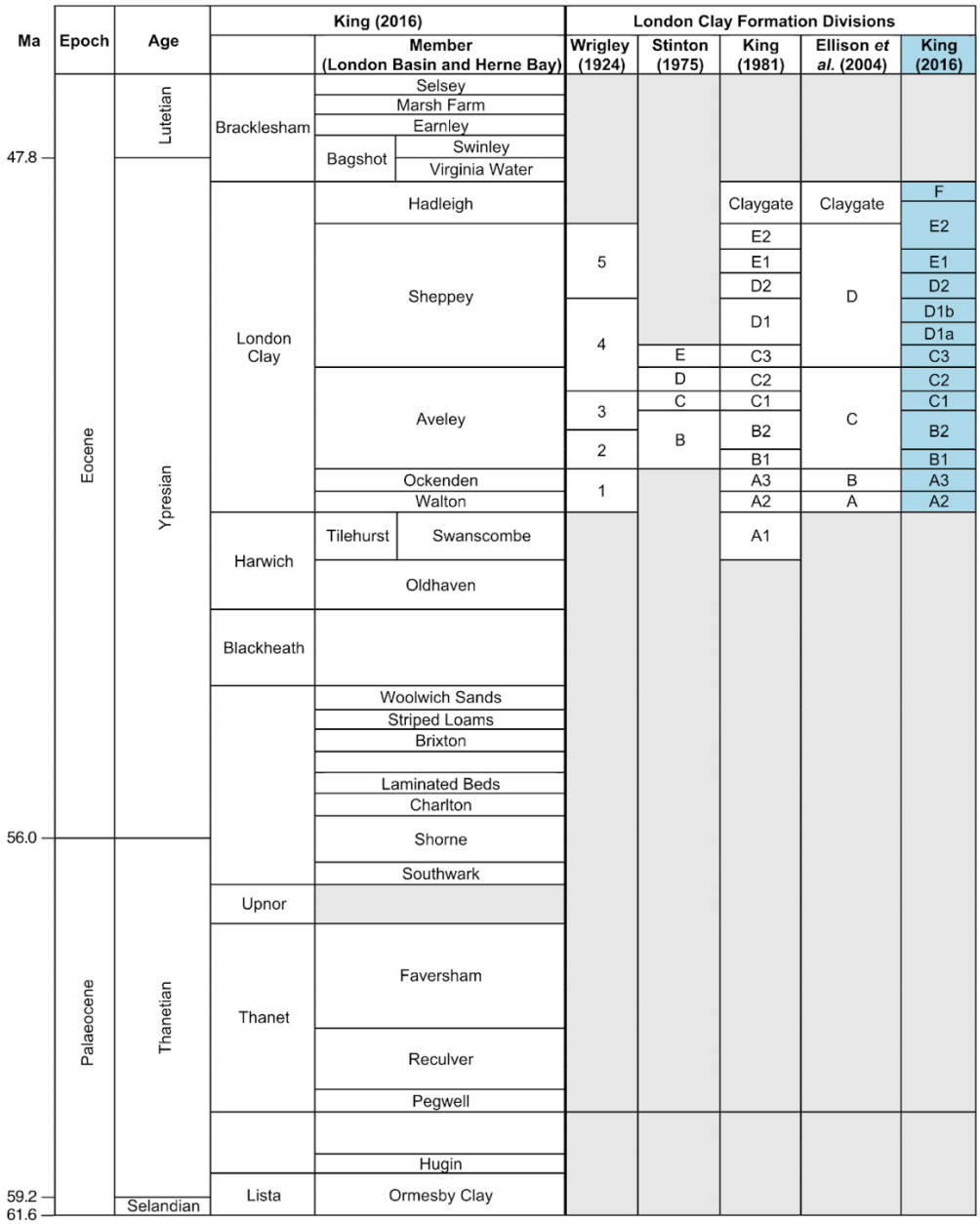

Appendix Figure 3.1. *(Previous page also)* Stratigraphic name and boundary changes through historical publications, correlating to the modern accepted Paleogene succession per the British Geological Society (highlighted blue; Aldiss (2014) for the general Paleogene succession and King (2016) for the London Clay divisions). Unknown stratigraphic information, or that which is not specified as for London Clay divisions columns, is greyed out, whilst dashed lines represent boundaries being unclear. Stratigraphic chart continues across two pages.

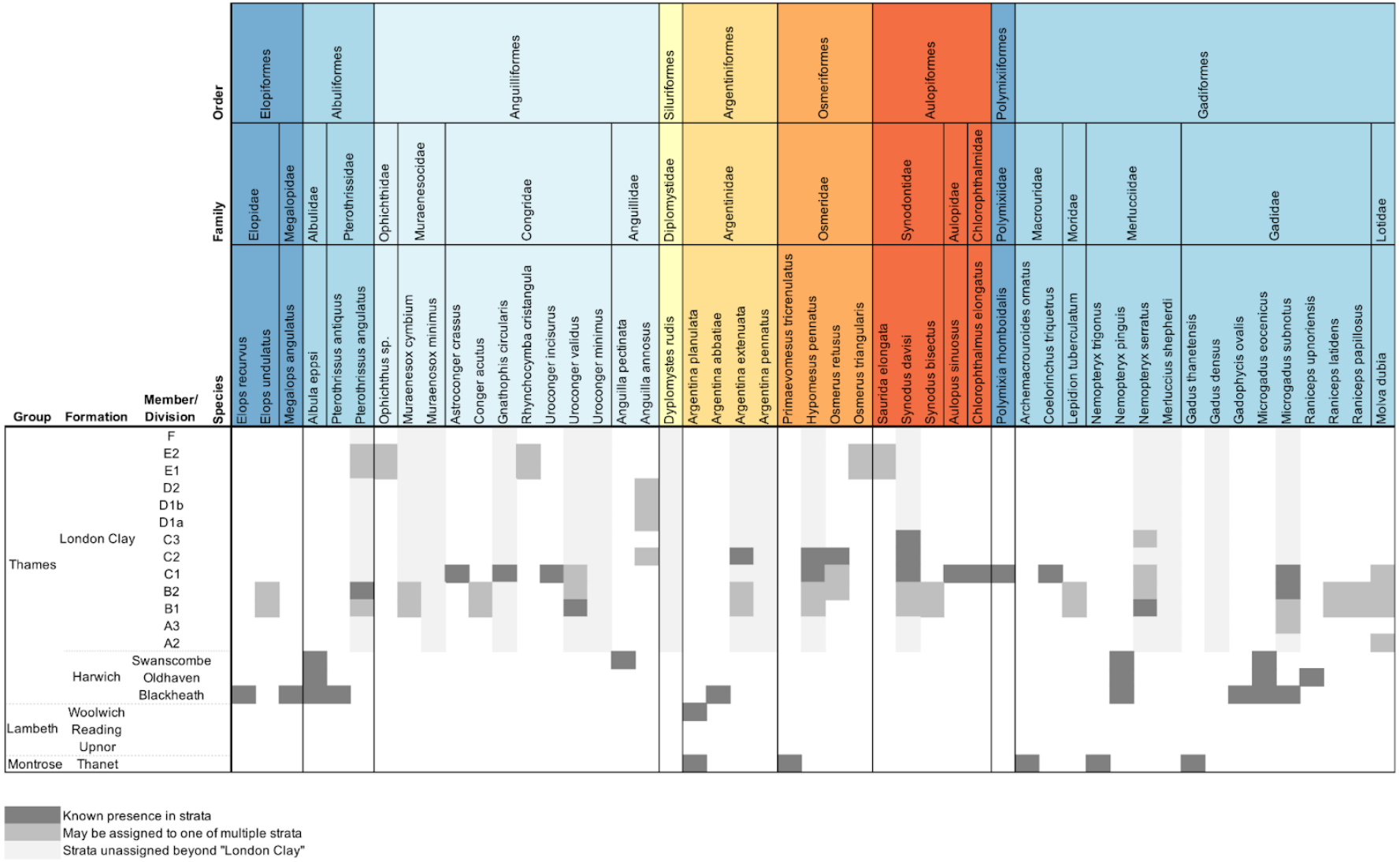
Order
Family
Species
Group
Formation
Member/ Division
Elopiformes
Elopidae
Elops recurvus
Elops undulatus
Megalopidae
Megalops angulatus
Albuliformes
Albulidae
Albula eppsi
Pterothrissidae
Pterothrissus antiquus
Pterothrissus angulatus
Anguilliformes
Ophichthidae
Ophichthus sp.
Muraenesocidae
Muraenesox cymbium
Muraenosox minimus
Congridae
Astroconger crassus
Conger acutus
Gnathophis circularis
Rhynchocymba cristangula
Uroconger incisurus
Uroconger validus
Uroconger minimus
Anguillidae
Anguilla pectinata
Anguilla annosus
Siluriformes
Diplomystidae
Dyplomystes rudis
Argentiniformes
Argentinidae
Argentina planulata
Argentina abbatiae
Argentina extenuata
Argentina pennatus
Osmeriformes
Osmeridae
Primaevomesus tricrenulatus
Hypomesus pennatus
Osmerus retusus
Osmerus triangularis
Aulopiformes
Synodontidae
Saurida elongata
Synodus davisi
Synodus bisectus
Aulopidae
Aulopus sinuosus
Chlorophthalmidae
Chlorophthalmus elongatus
Polymixiiformes
Polymixiidae
Polymixia rhomboidalis
Gadiformes
Macrouridae
Archemacrouroides ornatus
Coelorinchus triquetrus
Moridae
Lepidion tuberculatum
Merlucciidae
Nemopteryx trigonus
Nemopteryx pinguis
Nemopteryx serratus
Merluccius shepherdi
Gadidae
Gadus thanetensis
Gadus densus
Gadophycis ovalis
Microgadus eocenicus
Microgadus subnotus
Raniceps upnoriensis
Raniceps latidens
Raniceps papillosus
Lotidae
Molva dubia
Thames
London Clay
F
E2
E1
D2
D1b
D1a
C3
C2
C1
B2
B1
A3
A2
Harwich
Swanscombe
Oldhaven
Blackheath
Lambeth
Woolwich
Reading
Upnor
Montrose
Thanet
Known presence in strata
May be assigned to one of multiple strata
Strata unassigned beyond "London Clay"

Appendix Figure 3.2. *(Previous page)* Biostratigraphic range chart of NHMUK otolith taxa in the early Paleogene at species level. Dark grey boxes indicate definitive presence of taxa in the lithostratigraphic unit, whilst the lighter grey corresponds to taxa that may be assigned to one of multiple London Clay Formation sub-divisions. The palest grey represents taxa known from the London Clay Formation but for which further stratigraphic detail is uncertain. Colour coding of taxonomic names is for illustrative purposes only. The range chart continues overleaf two pages.

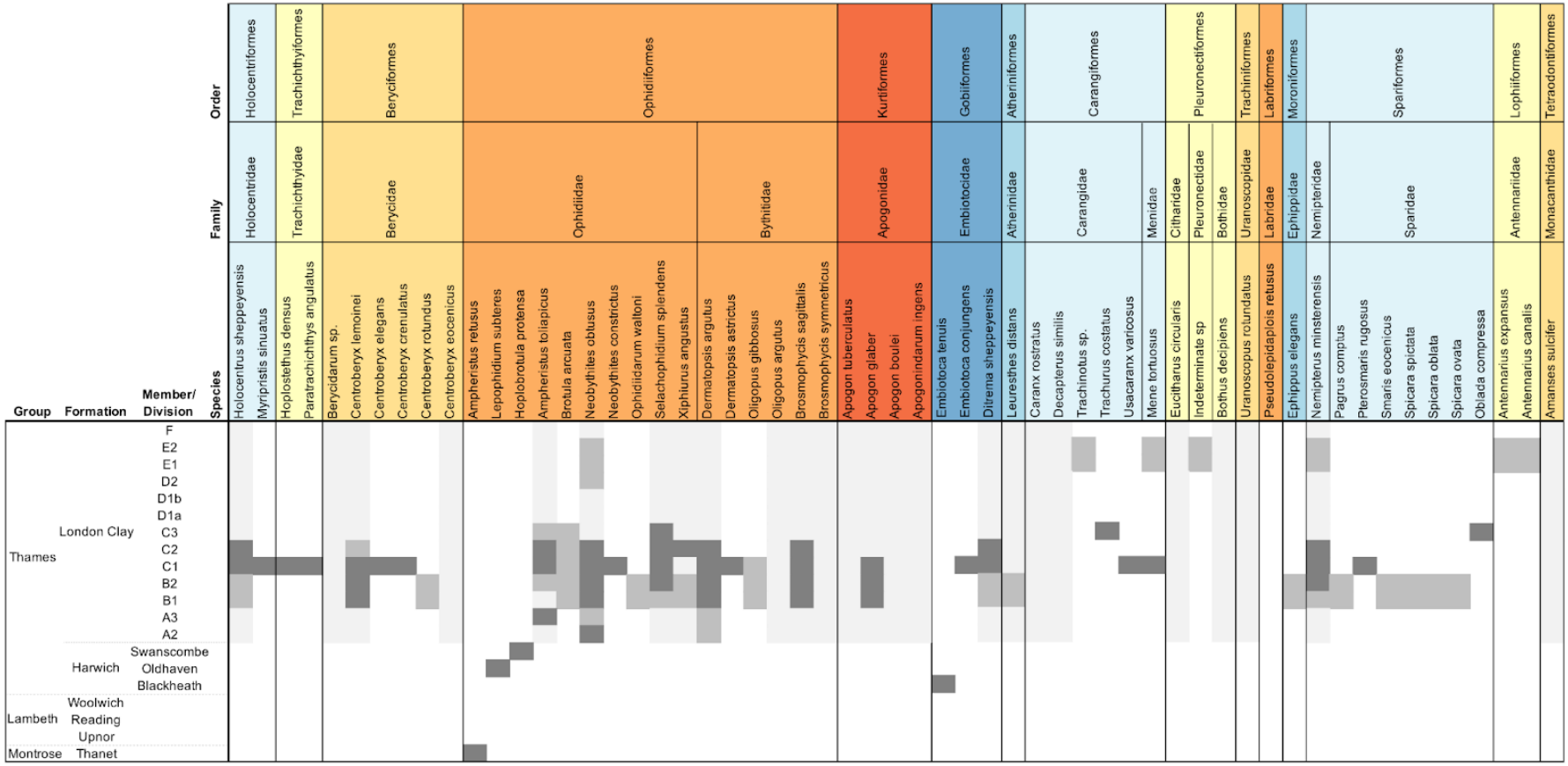
Order
Family
Species
Group
Formation
Member/ Division
Holocentriformes
Trachichthyiformes
Beryciformes
Ophidiiformes
Kurtiformes
Gobiiformes
Atheriniformes
Carangiformes
Pleuronectiformes
Trachiniformes
Labriformes
Moroniformes
Spariformes
Lophiiformes
Tetraodontiformes
Holocentridae
Trachichthyidae
Berycidae
Ophidiidae
Bythitidae
Apogonidae
Embiotocidae
Atherinidae
Carangidae
Menidae
Citharidae
Pleuronectidae
Bothidae
Uranoscopidae
Labridae
Ephippidae
Nemipteridae
Sparidae
Antennariidae
Monacanthidae
Holocentrus sheppeyensis
Myripristis sinuatus
Hoplostethus densus
Paratrachichthys angulatus
Berycidarum sp.
Centroberyx lemoinei
Centroberyx elegans
Centroberyx crenulatus
Centroberyx rotundus
Centroberyx eocenicus
Ampheristus retusus
Lepophidium subteres
Hoplobrotula protensa
Ampheristus toliapicus
Brotula arcuata
Neobythites obtusus
Neobythites constrictus
Ophidiidarum waltoni
Selachophidium splendens
Xiphiurus angustus
Dermatopsis argutus
Dermatopsis astrictus
Oligopus gibbosus
Oligopus argutus
Brosmophycis sagittalis
Brosmophycis symmetricus
Apogon tuberculatus
Apogon glaber
Apogon boulei
Apogonindarum ingens
Embiotoca tenuis
Embiotoca conjungens
Ditrema sheppeyensis
Leuresthes distans
Caranx rostratus
Decapterus similis
Trachinotus sp.
Trachurus costatus
Usacaranx varicosus
Mene tortuosus
Eucitharus circularis
Indeterminate sp
Bothus decipiens
Uranoscopus rotundatus
Pseudolepidaplois retusus
Ephippus elegans
Nemipterus minsterensis
Pagrus comptus
Pterosmaris rugosus
Smaris eocenicus
Spicara spictata
Spicara oblata
Spicara ovata
Oblada compressa
Antennarius expansus
Antennarius canalis
Amanses sulcifer
Thames
Lambeth
Montrose
London Clay
Harwich
Woolwich
Reading
Upnor
Thanet
Swanscombe
Oldhaven
Blackheath
F
E2
E1
D2
D1b
D1a
C3
C2
C1
B2
B1
A3
A2

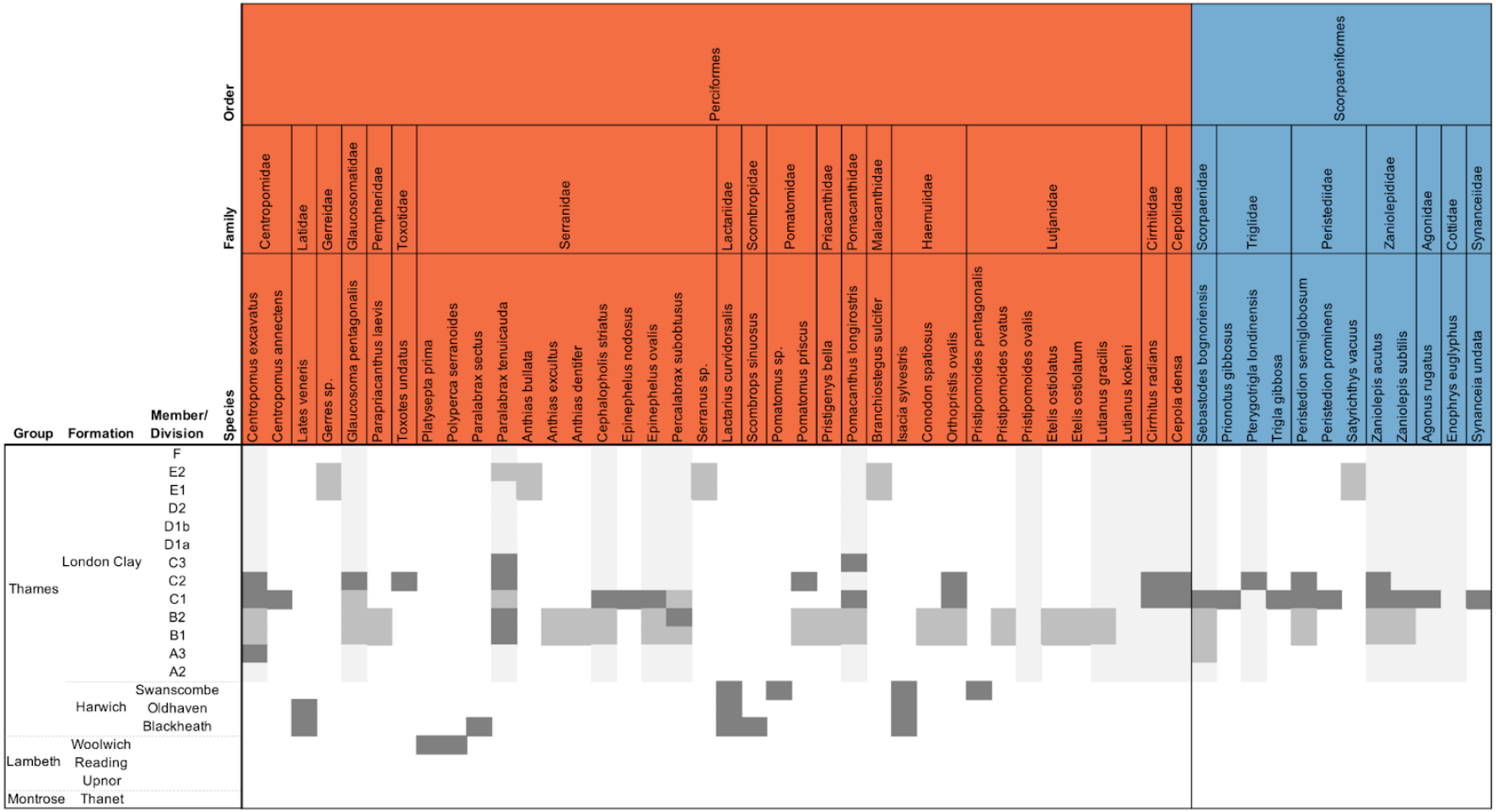
Order
Perciformes
Scorpaeniformes
Family
Centropomidae
Latidae
Gerreidae
Glaucosomatidae
Pempheridae
Toxotidae
Serranidae
Lactariidae
Scombropidae
Pomatomidae
Priacanthidae
Pomacanthidae
Malacanthidae
Haemulidae
Lutjanidae
Cirrhitidae
Cepolidae
Scorpaenidae
Triglidae
Peristediidae
Zaniolepididae
Agonidae
Cottidae
Synanceiidae
Species
Centropomus excavatus
Centropomus annectens
Lates veneris
Gerres sp.
Glaucosoma pentagonalis
Parapriacanthus laevis
Toxotes undatus
Platysepta prima
Polyperca serranoides
Paralabrax sectus
Paralabrax tenuicauda
Anthias bullata
Anthias excultus
Anthias dentifer
Cephalopholis striatus
Epinephelus nodosus
Epinephelus ovalis
Percalabrax subobtusus
Serranus sp.
Lactarius curvidorsalis
Scombrops sinuosus
Pomatomus sp.
Pomatomus priscus
Pristigenys bella
Pomacanthus longirostris
Branchiostegus sulcifer
Isacia sylvestris
Conodon spatiosus
Orthopristis ovalis
Pristipomoides pentagonalis
Pristipomoides ovatus
Pristipomoides ovalis
Etelis ostiolatus
Etelis ostiolatum
Lutianus gracilis
Lutianus kokeni
Cirrhitus radians
Cepola densa
Sebastodes bognoriensis
Prionotus gibbosus
Pterygotrigla londinensis
Trigla gibbosa
Peristedion semiglobosum
Peristedion prominens
Satyrichthys vacuus
Zaniolepis acutus
Zaniolepis subtilis
Agonus rugatus
Enophrys euglyphus
Synanceia undata
Group
Formation
Member/ Division
Thames
London Clay
F
E2
E1
D2
D1b
D1a
C3
C2
C1
B2
B1
A3
A2
Harwich
Swanscombe
Oldhaven
Blackheath
Lambeth
Woolwich
Reading
Upnor
Montrose
Thanet

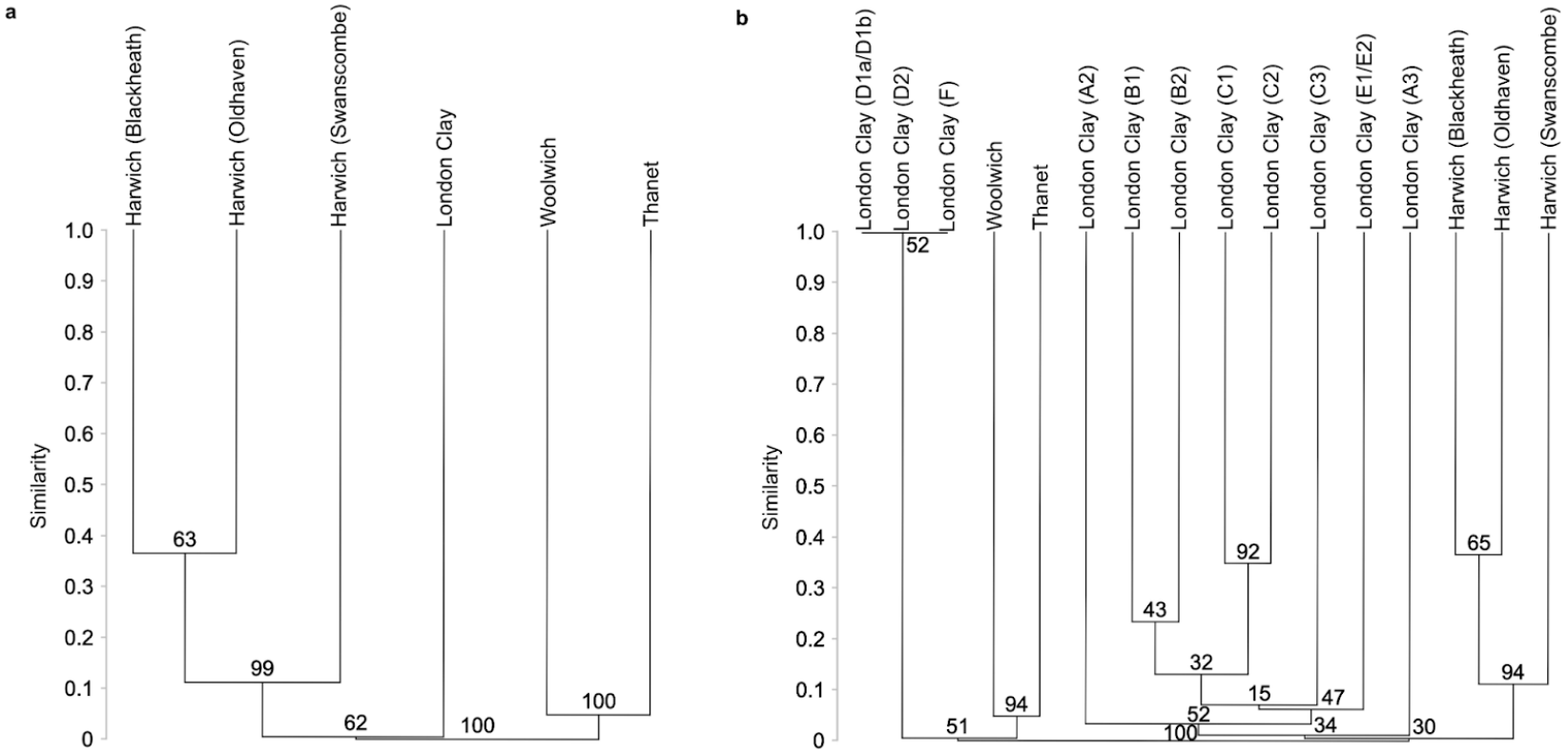

Appendix Figure 3.3. Bray-Curtis dissimilarity (**a**) of NHMUK otoliths from late Palaeocene and early Eocene units, run with bootstrap 1,000. Numbers on nodes indicate the percentage of runs producing those groupings. The analysis was re-run considering only the specimens known from specific London Clay divisions (**b**) and with all possible designations of specimens within the London Clay divisions (**c**). Part **c** continues overleaf.

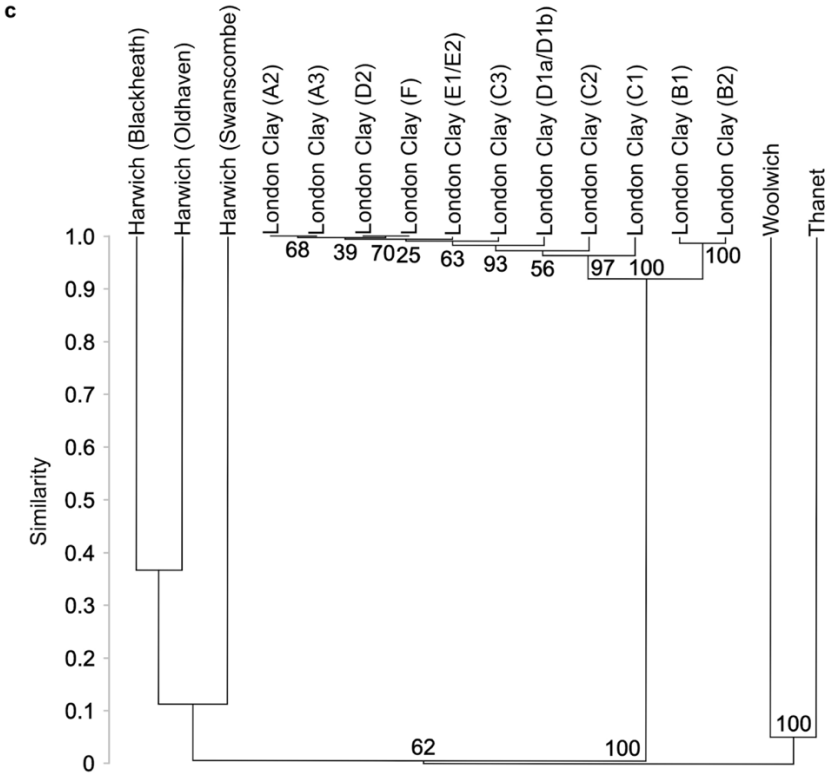
c
Harwich (Blackheath)
Harwich (Oldhaven)
Harwich (Swanscombe)
London Clay (A2)
London Clay (A3)
London Clay (D2)
London Clay (F)
London Clay (E1/E2)
London Clay (C3)
London Clay (D1a/D1b)
London Clay (C2)
London Clay (C1)
London Clay (B1)
London Clay (B2)
Woolwich
Thanet
Similarity
1.0
0.9
0.8
0.7
0.6
0.5
0.4
0.3
0.2
0.1
0
68
39
70
25
63
93
56
97
100
100
62
100
100

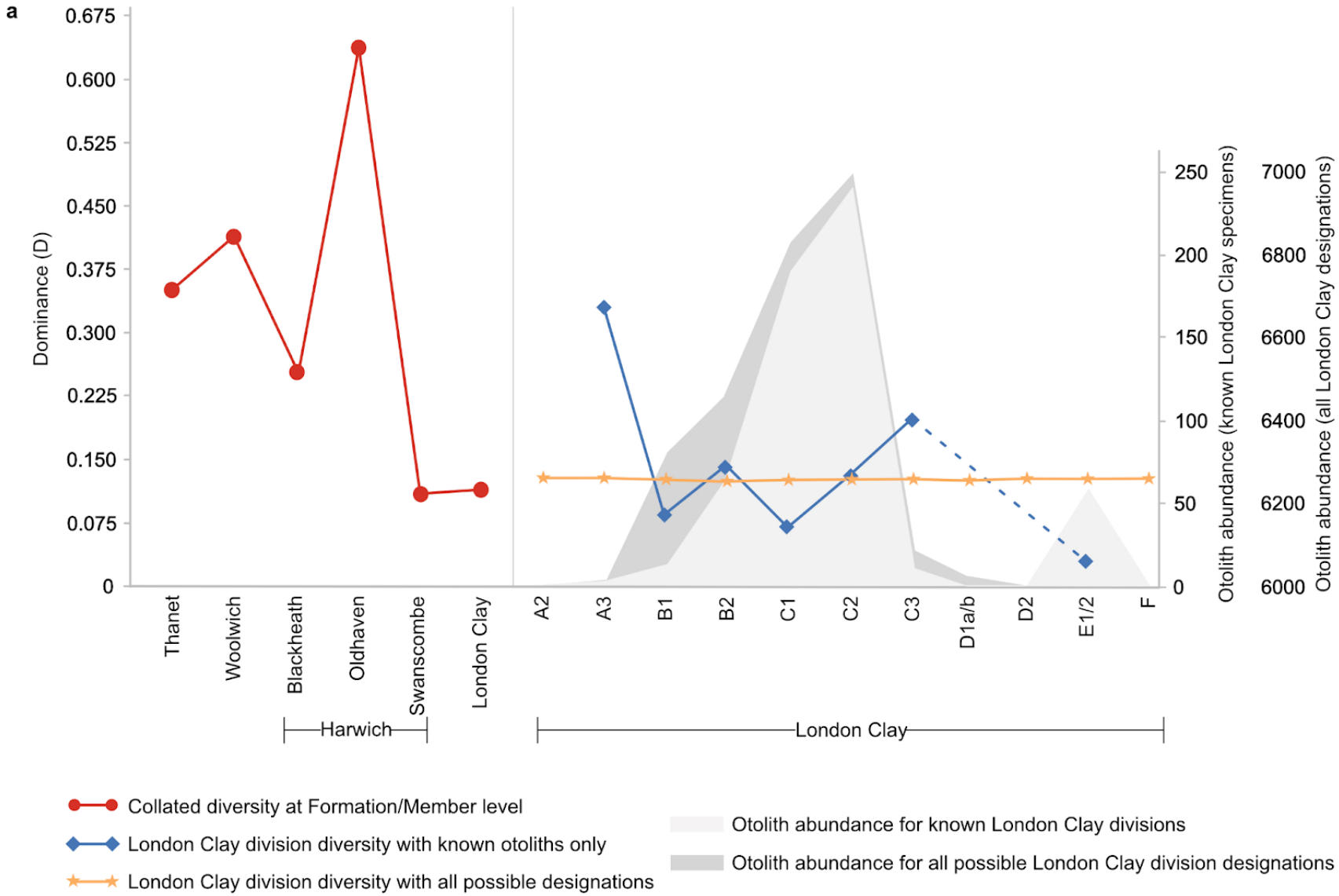
a
Dominance (D)
0.675
0.600
0.525
0.450
0.375
0.300
0.225
0.150
0.075
0
Otolith abundance (known London Clay specimens)
250
200
150
100
50
0
Otolith abundance (all London Clay designations)
7000
6800
6600
6400
6200
6000
Thanet
Woolwich
Blackheath
Oldhaven
Swanscombe
London Clay
A2
A3
B1
B2
C1
C2
C3
D1a/b
D2
E1/2
F
Harwich
London Clay
Collated diversity at Formation/Member level
London Clay division diversity with known otoliths only
London Clay division diversity with all possible designations
Otolith abundance for known London Clay divisions
Otolith abundance for all possible London Clay division designations

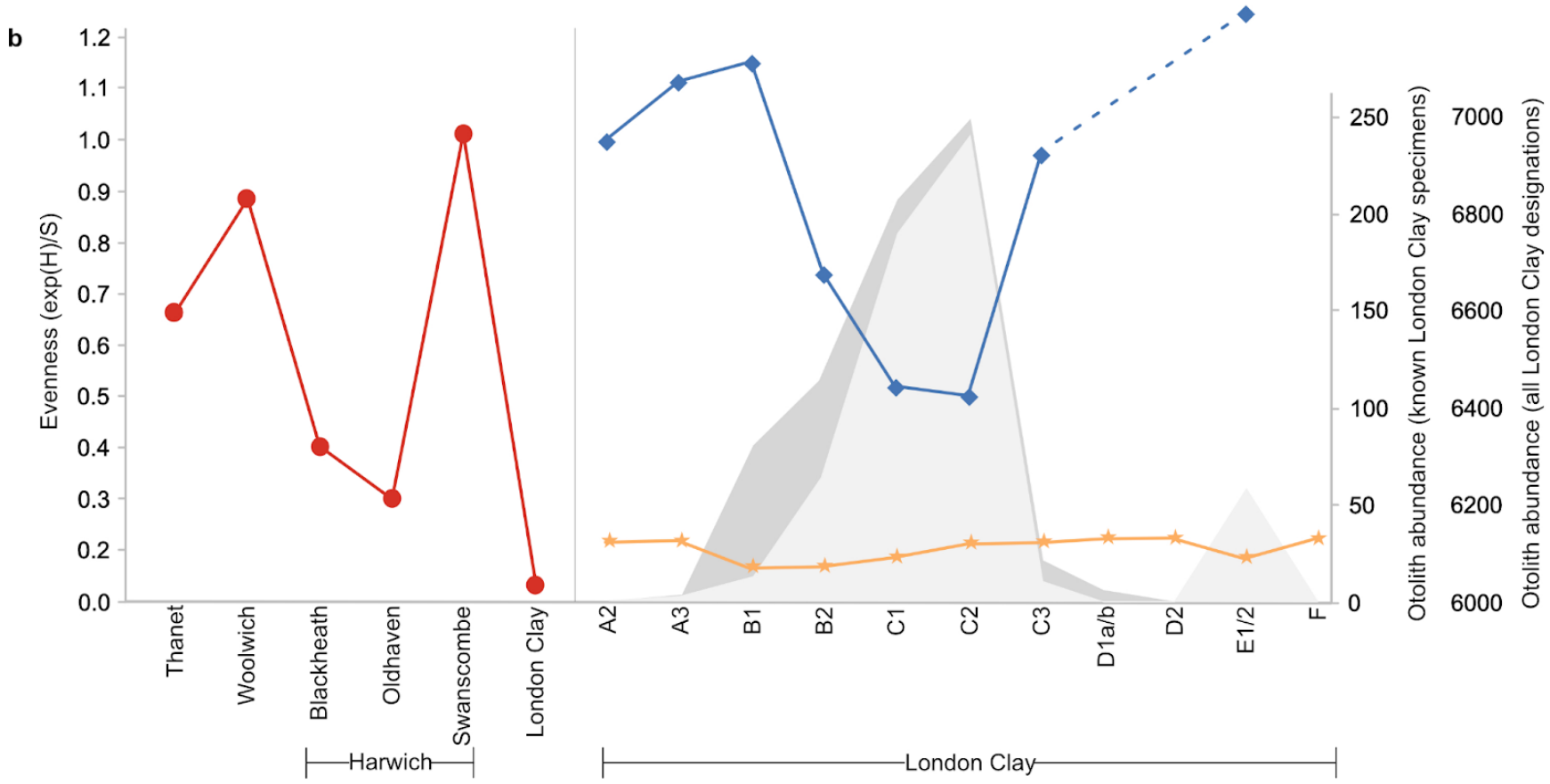

Appendix Figure 3.4. *(Previous page also)* Dominance (**a**) and evenness (**b**) indices for the early Paleogene NHMUK otolith collection, though without standardised sampling the 'cherry-picked' data biases these tests. In each panel, the left side shows diversity indices for all stratigraphic units as a whole (where London Clay Formation divisions are collated) and the right side

has diversity indices calculated where [1] otoliths can be definitively assigned to a division of the London Clay Formation (blue) and [2] assignment of specimens to all possible divisions (orange), with extrapolation across absent data points for units D1a/b, D2 and F. Indeterminate species are removed to avoid skewing data (especially as they dominate divisions E1 and E2). The known and all possible designation otolith abundances for London Clay specimens are also shown.

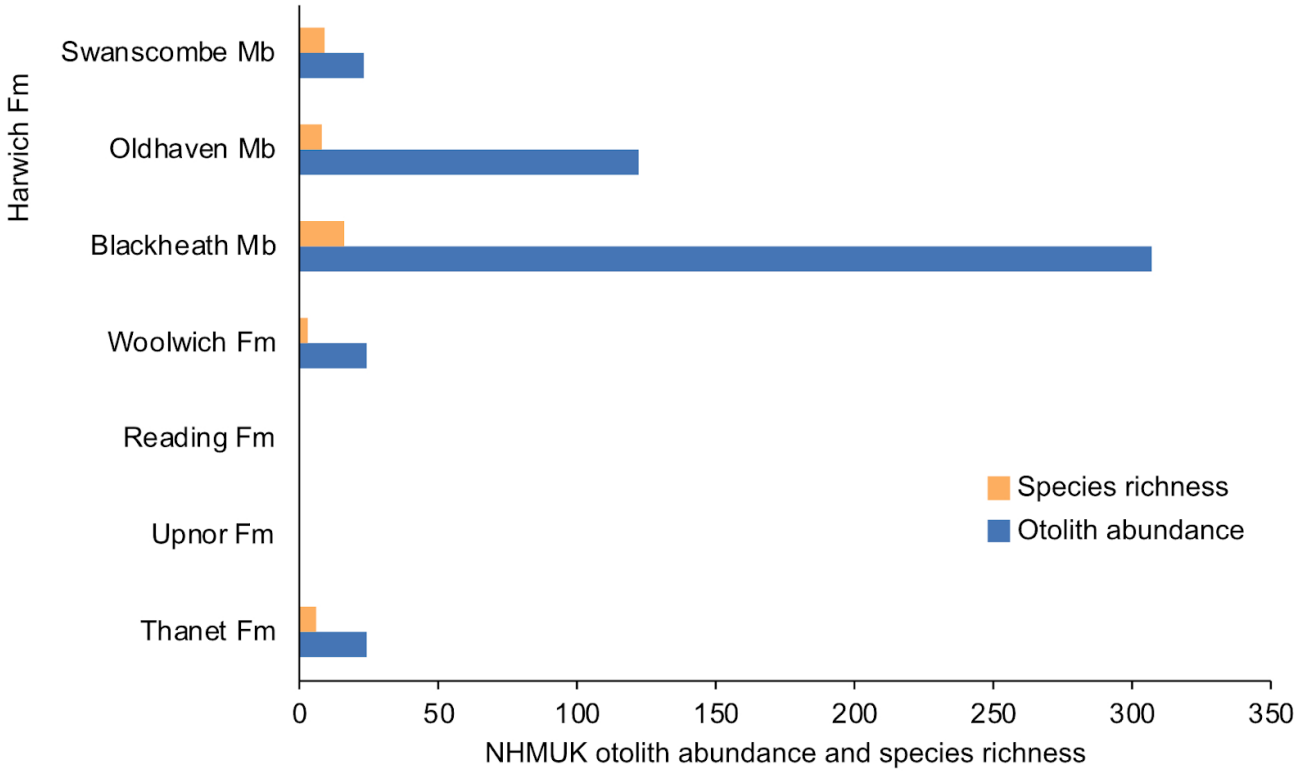

Appendix Figure 3.5. Otolith abundance and species richness of NHMUK specimens in early Paleogene stratigraphic units, excluding the London Clay Formation as this impairs data visualisation due to significantly increased otolith count.

Appendix 2: Supplementary material for Chapter Four

Appendix Table 4.1.* Astrochronologic, magnetostratigraphic and biostratigraphic datums used to generate Site U1514 age model.

Appendix Table 4.2.* Ichthyolith morphotype coding for low resolution late Palaeocene to middle Eocene dataset.

Appendix Table 4.3.* Ichthyolith morphotype coding for high resolution PETM and EECO R and S events provided by undergraduates Haf Nawsath, Lily Goddard and Zulaikha Sukerdi.

***** *Due to large file sizes, Appendix Tables 4.1, 4.2 and 4.3 have been deposited online within the University of Birmingham eData Repository, respectively titled: "Site U1514 age model (Appendix Table 4.1).xlsx", "Site U1514 Palaeocene and Eocene ichthyolith morphotype coding (Appendix Table 4.2).xlsx" and "Site U1514 PETM and EECO hyperthermal ichthyolith morphotype coding (Appendix Table 4.3).xlsx". They are available within the repository titled "Bird, Hannah (2024) Research data supporting PhD thesis 'Actinopterygian and chondrichthyan palaeocommunity responses to early Cenozoic global warming'"* (DOI: 10.25500/edata.bham.00001169).

Appendix Table 4.4. Morphotype key for range chart (Figure 4.13). Continued overleaf.

Range chart key	Morphotype
[1]	Straight triangle 3/4 concave root
[2]	1/4 straight root
[3]	Convex triangle 3/4 funnel root
[4]	Squat rootless cone
[5]	1/4 dome root cone
[6]	Generic cone
[7]	Long 3/4 straight root
[8]	Generic triangle
[9]	Long striated cone curved tip
[10]	Upper 3/4 bladed triangle
[11]	3/4 total root cone
[12]	Too broken to code
[13]	Convex triangle 3/4 dome root
[14]	Elongated straight bladed cone
[15]	Squat convex triangle dome root
[16]	1/2 straight root
[17]	Curved cone 1/4 total root
[18]	1/4 dome root triangle
[19]	Wide base curved triangle
[20]	Medium curved two part straight tip
[21]	Squat dome root cone
[22]	Long minor curved cone
[23]	Curved medium cone dome root
[24]	Medium 3/4 straight root
[25]	Squat convex cone 1/4 total root
[26]	Two part straight squat tip
[27]	Elongated 1/4 straight root cone
[28]	Elongated two part squat tip
[29]	Medium triangle 3/4 concave root
[30]	Medium 3/4 funnel root

Range chart key	Morphotype
[31]	Medium rootless cone
[32]	Horseshoe
[33]	Elongated 1/2 straight root
[34]	Extended straight root
[35]	1/2 funnel root flared blades
[36]	Medium 1/4 dome root
[37]	3/4 funnel root
[38]	Long 3/4 straight root straight blades
[39]	Full straight root
[40]	Long convex triangle total funnel root
[41]	Squat convex root
[42]	Total funnel root curved cone
[43]	Medium 1/2 concave root
[44]	Extra-long 3/4 total funnel bladed cone
[45]	Middle barb cone total root
[46]	Curved triangle 3/4 concave root
[47]	Convex cone 1/2 dome root
[48]	Major curve thin cone
[49]	1/2 dome root triangle
[50]	Long convex triangle
[51]	1/2 concave root
[52]	Medium straight bladed cone
[53]	3/4 root cone
[54]	Long convex triangle 3/4 concave root
[55]	Long 1/4 dome root
[56]	Convex 1/2 root flared blades
[57]	Convex triangle 1/2 vase root
[58]	Flat funnel root
[59]	Medium straight cone flared base
[60]	Small blade full root

Range chart key	Morphotype
[61]	Two part triangle
[62]	Extra-long curved two part straight tip
[63]	1/4 dome root cone no cap
[64]	Long straight striated cone
[65]	Convex triangle 1/2 total root
[66]	Lipped cone
[67]	Full root flared blades
[68]	1/2 straight root convex triangle
[69]	Flat full root
[70]	1/2 concave root flared blades
[71]	Convex 1/2 dome root
[72]	Two part triangular cone
[73]	Rootless medium triangle
[74]	Convex 3/4 root
[75]	Pot-bellied squat triangle
[76]	Straight triangle 1/2 funnel root
[77]	1/4 dome root curved cone
[78]	Flat right triangle big blade
[79]	Convex triangle 1/2 funnel root
[80]	1/2 root cone
[81]	1/2 total root cone
[82]	1/2 concave root cone
[83]	1/4 total root cone
[84]	Rootless long triangle
[85]	Elongated two part medium tip
[86]	Convex 1/2 root
[87]	Squat triangle 1/2 dome root
[88]	Squat convex triangle
[89]	Two part straight medium tip
[90]	Curved 1/2 total funnel root triangle

Range chart key	Morphotype
[91]	Asymmetric bladed cone
[92]	Asymmetric 1/2 vase root
[93]	Fingernail
[94]	Slinky christmas tree
[95]	Total root curved cone
[96]	Convex triangle full convex root
[97]	Extra-long straight cone
[98]	Full root convex triangle
[99]	Squat concave root
[100]	Curved full straight root
[101]	Two part squat triangle
[102]	Long minor recurved cone
[103]	Straight dome root
[104]	3/4 total funnel root
[105]	Straight triangle 1/2 total root
[106]	Two part convex squat tip
[107]	Curved 1/2 dome root triangle
[108]	Long 3/4 total root triangle
[109]	Rounded convex triangle
[110]	Squat curved convex cone
[111]	Squat flared bladed cone
[112]	1/4 dome straight blades
[113]	Curved deep triangle
[114]	Full-length straight root cone
[115]	Flared base 1/4 dome root
[116]	Rootless single bladed cone
[117]	Long full total root
[118]	Two part convex squat curved tip
[119]	Long 1/2 dome root triangle
[120]	Elongated curved bladed cone

Range chart key	Morphotype
[121]	Bladed recurved cone
[122]	Squat tucked base cone
[123]	Asymmetrical 3/4 funnel root
[124]	1/4 dome root convex cone
[125]	Curl-curved triangle 1/2 convex root
[126]	1/4 straight root cone
[127]	Flat extended root
[128]	Deep dome root flared blades
[129]	Mounding cone
[130]	1/4 total root cone no cap
[131]	Curved 1/4 barb
[132]	Elongated convex root cone
[133]	Funnel cone dome root
[134]	Major curve thin cone flared base
[135]	Curved funnel root cone
[136]	Long rootless cone
[137]	Curved two part curved tip
[138]	Squat 1/2 straight root cone
[139]	Long 1/4 total root cone
[140]	Elongated 1/2 total root cone
[141]	Cinched top cone
[142]	Convex triangle 1/2 convex root
[143]	Arrowhead triangle
[144]	flat 1/2 straight root flared blades
[145]	Extra-long spiraling striation
[146]	Elongated 1/2 total root cone no cap
[147]	Funnel triangle 1/2 convex root
[148]	Right triangle concave root
[149]	Tucked base cone
[150]	Domal bi-cusp

Range chart key	Morphotype
[151]	Straight many cusps
[152]	Long striated curved flared base cone
[153]	1/4 dome root concave triangle
[154]	Deep full straight root
[155]	Extra-long 1/4 total root cone
[156]	Curved long 1/4 dome root
[157]	Bicuspid long cone
[158]	Full root big blade barb
[159]	Asymmetrical flared triangle
[160]	Straight 3/4 barb
[161]	Concave root flared blades
[162]	Flat 1/2 straight root flared blades
[163]	Long curved two part bulbous tip
[164]	Squat total root
[165]	Curved triangle full concave root
[166]	Curved cone 1/2 total root
[167]	Funnel root cone
[168]	3/4 rounded root
[169]	Long deep 1/4 total root
[170]	Curved 1/2 barb
[171]	Middle bladed triangle
[172]	Flared base 3/4 funnel root
[173]	Long minor top curved cone
[174]	1/4 barb cone
[175]	Asymmetrical root right-angle cone
[176]	Convex 3/4 funnel
[177]	Long middle ridge triangle
[178]	Long curved tucked cone
[179]	Squat dome root cap tip
[180]	1/2 dome root lower barb
[181]	Convex cone total root
[182]	Long top curved cone 1/2 straight root

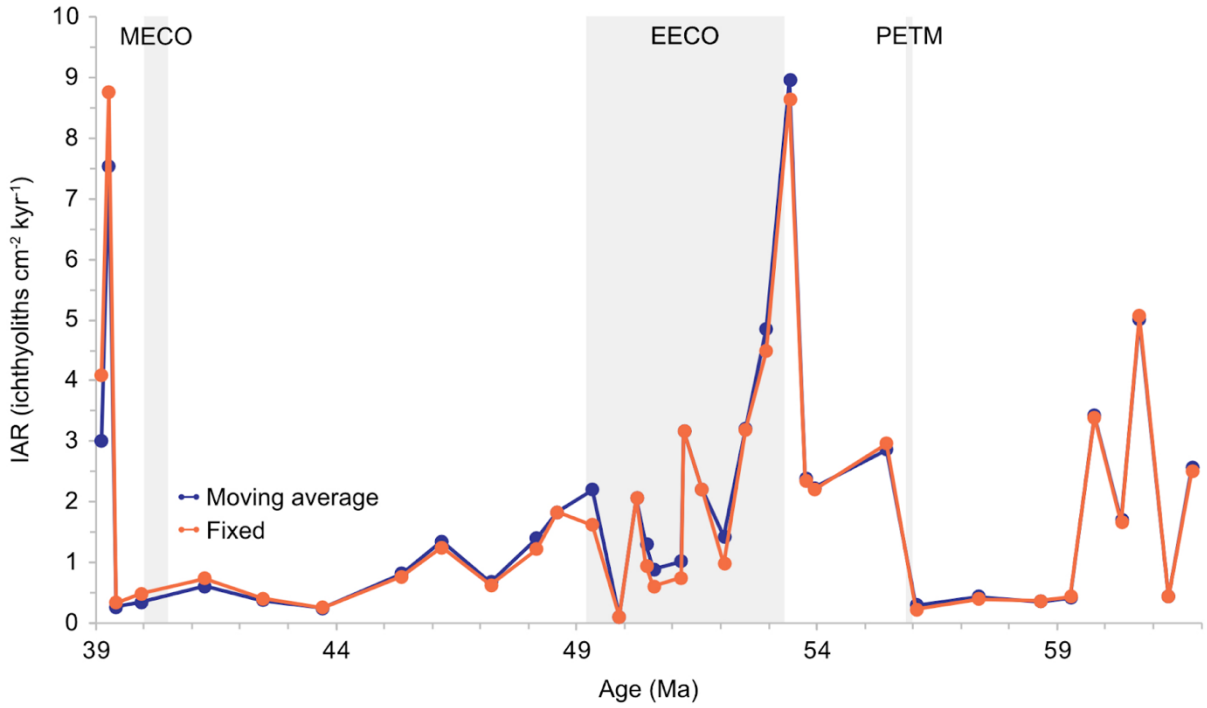

Appendix Figure 4.1. IAR calculated with moving average and fixed dry bulk density across Site U1514 sample interval.

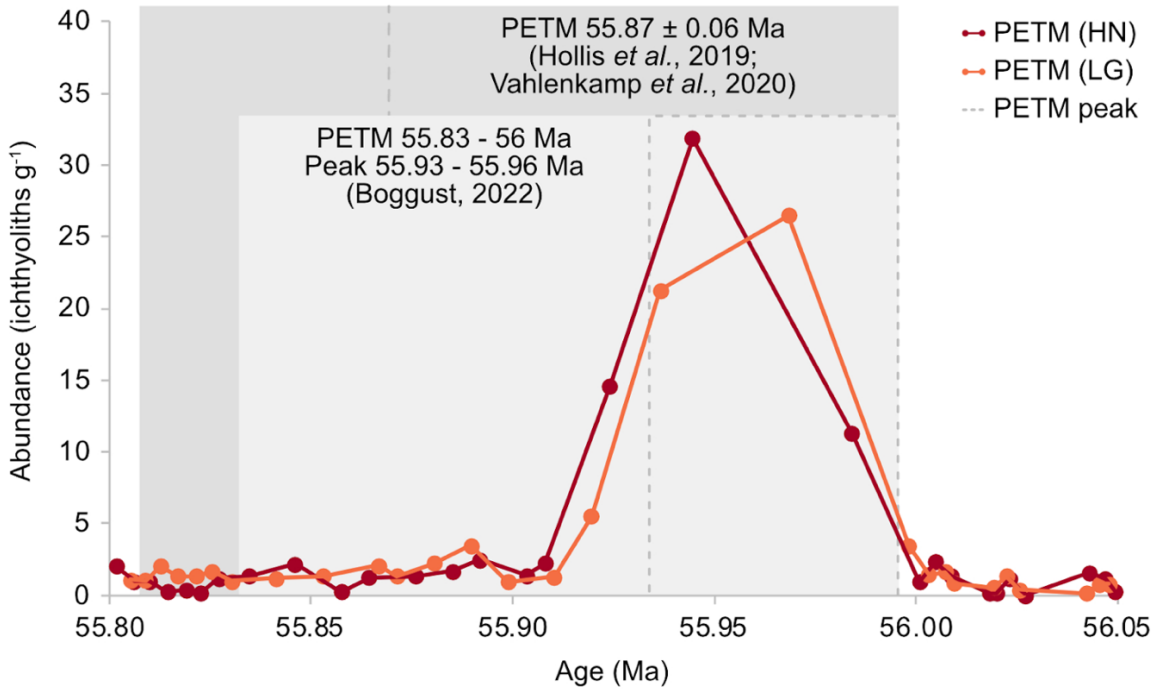

Appendix Figure 4.2. Ichthyolith abundance data for the PETM from undergraduate students (Haf Nawsath (HN) and Lily Goddard (LG)) which have significant increases in teeth and denticles during the peak of the PETM. Additionally, two age windows for the PETM are presented, that of Vahlenkamp *et al.* (2020) which uses Ca/Fe ratios to identify the PETM (the peak represented by the dashed line at 55.87 Ma), compared to Boggust's (2022) benthic foraminifera carbon isotope data, the peak of which (dashed grey box) matches the abundance data.

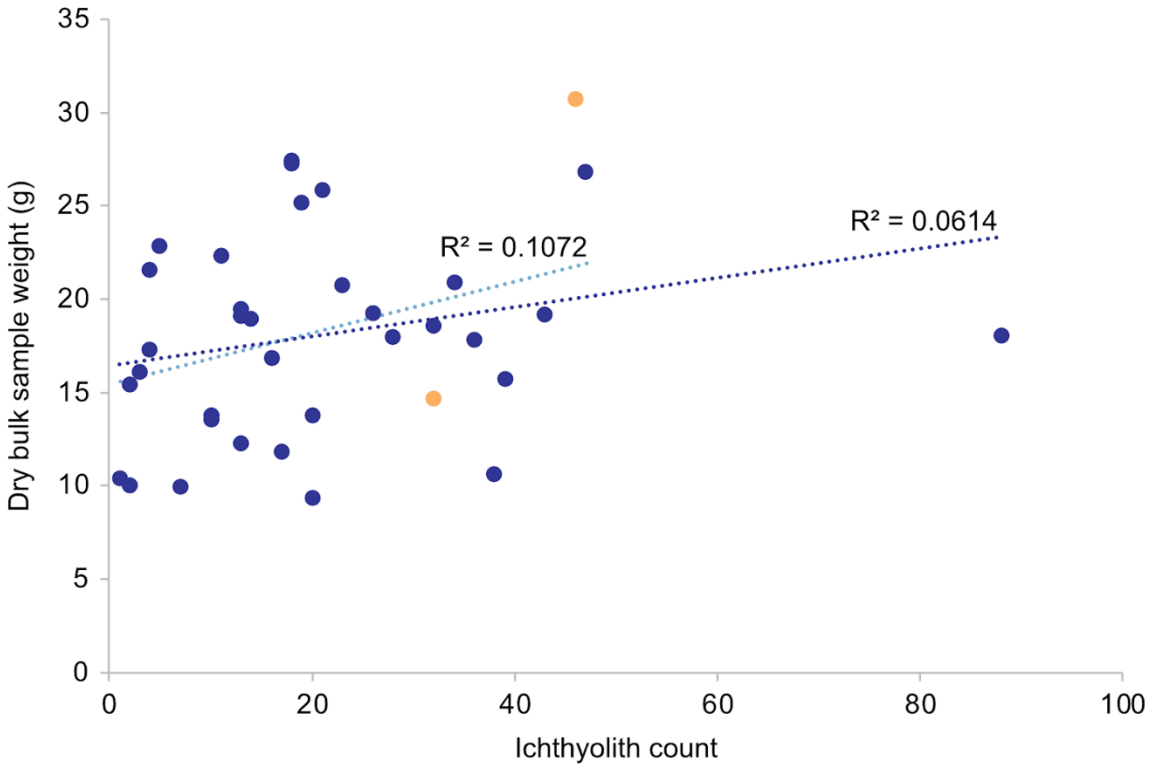

Appendix Figure 4.3. Crossplot of raw ichthyolith counts against dry bulk sample weight for the long-term late Palaeocene to middle Eocene dataset. The shorter trendline removes the effect of the one outlier sample of 88 ichthyoliths, and the two orange dots match to samples referenced in the text of Section 4.3.1 regarding discrepancies in abundance versus dry bulk sample weight.

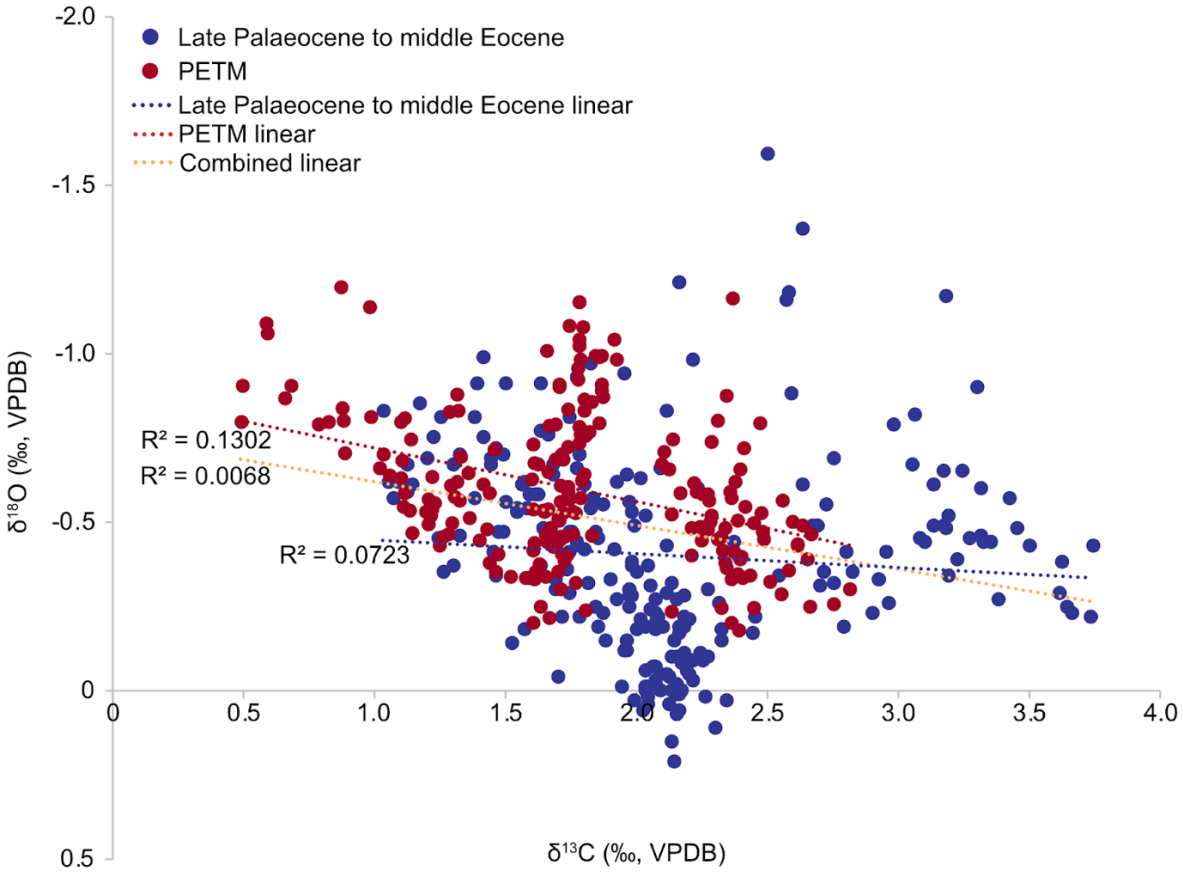

Appendix Figure 4.4. Crossplot of U1514 $\delta^{13}C$ and $\delta^{18}O$ isotopes (Edgar *et al.*, 2022; Boggust, 2022) across the study interval with linear trends and regression values.

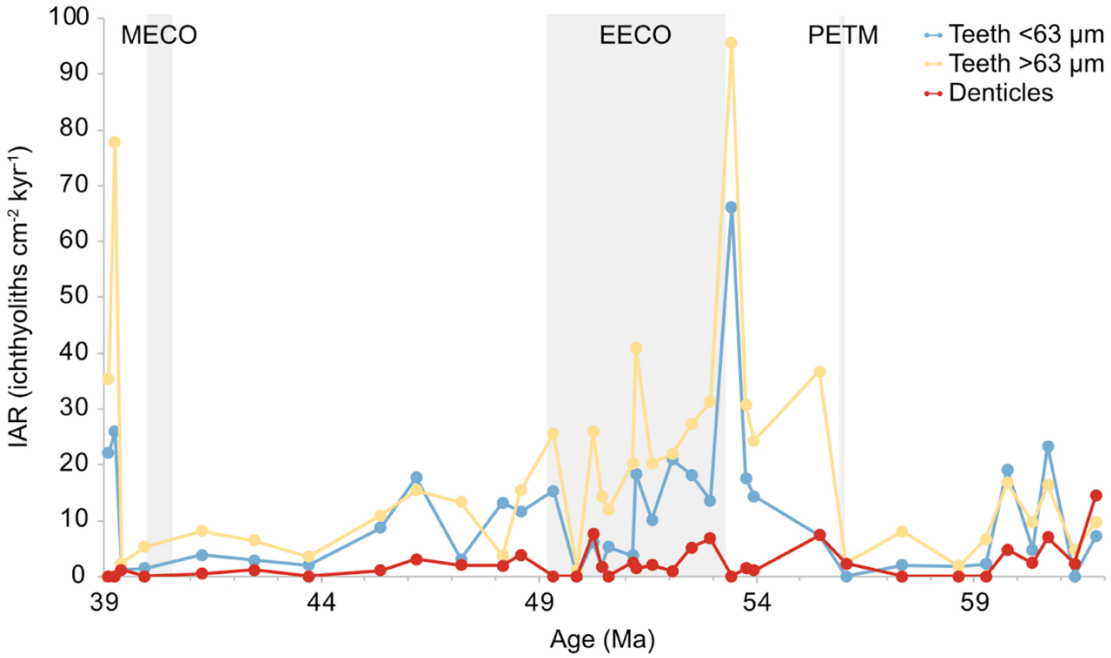

Appendix Figure 4.5. IAR for both tooth size fractions (38 to 63 µm and 63 to 250 µm) and denticles, calculated with moving average sample bulk density.

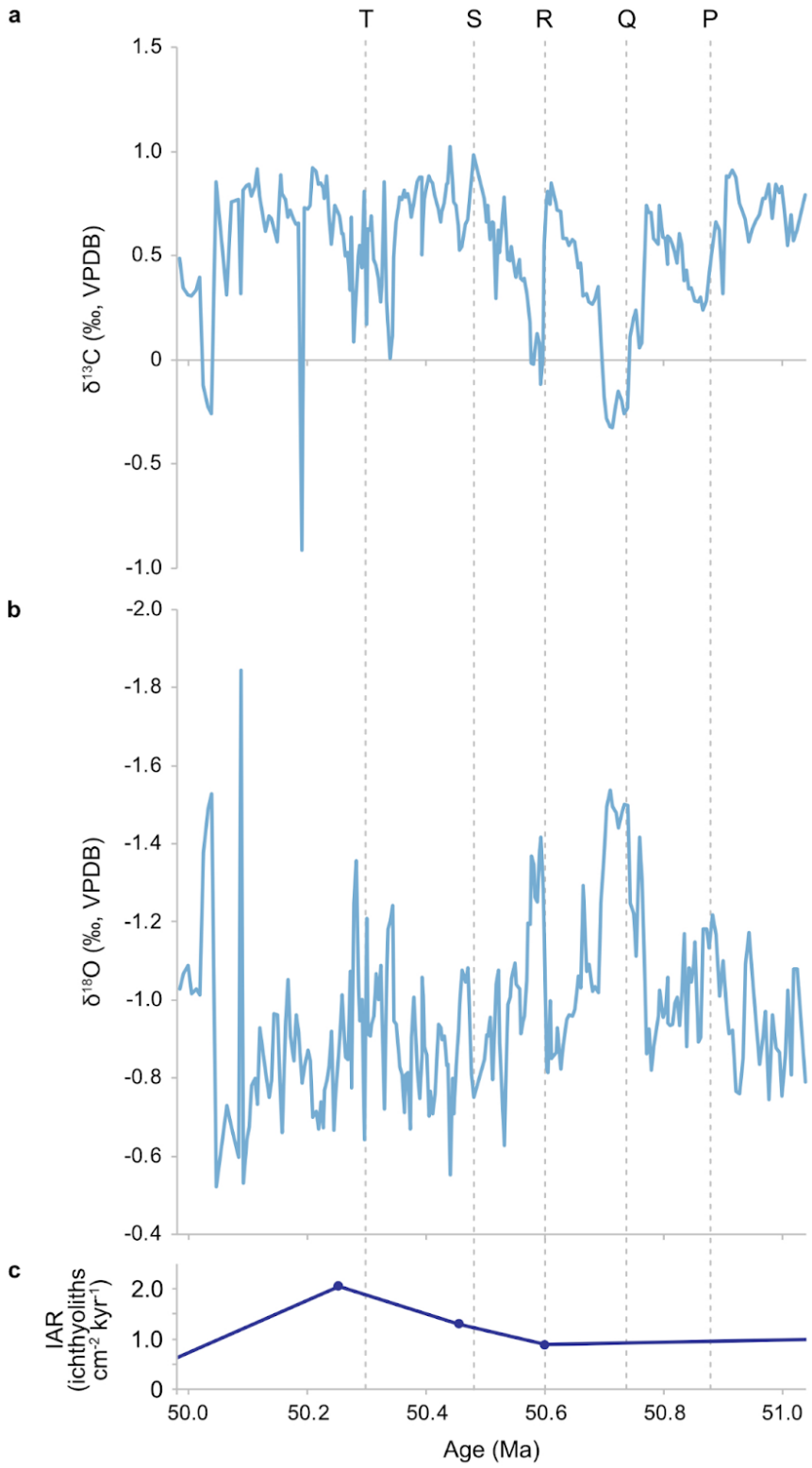

Appendix Figure 4.6. High resolution stable carbon (**a**) and oxygen (**b**) isotope data (Kirby, 2022) alongside IAR for long-term dataset (**c**, dots represent sample points) matched to hyperthermals, with timings as per Vahlenkamp *et al.* (2020).

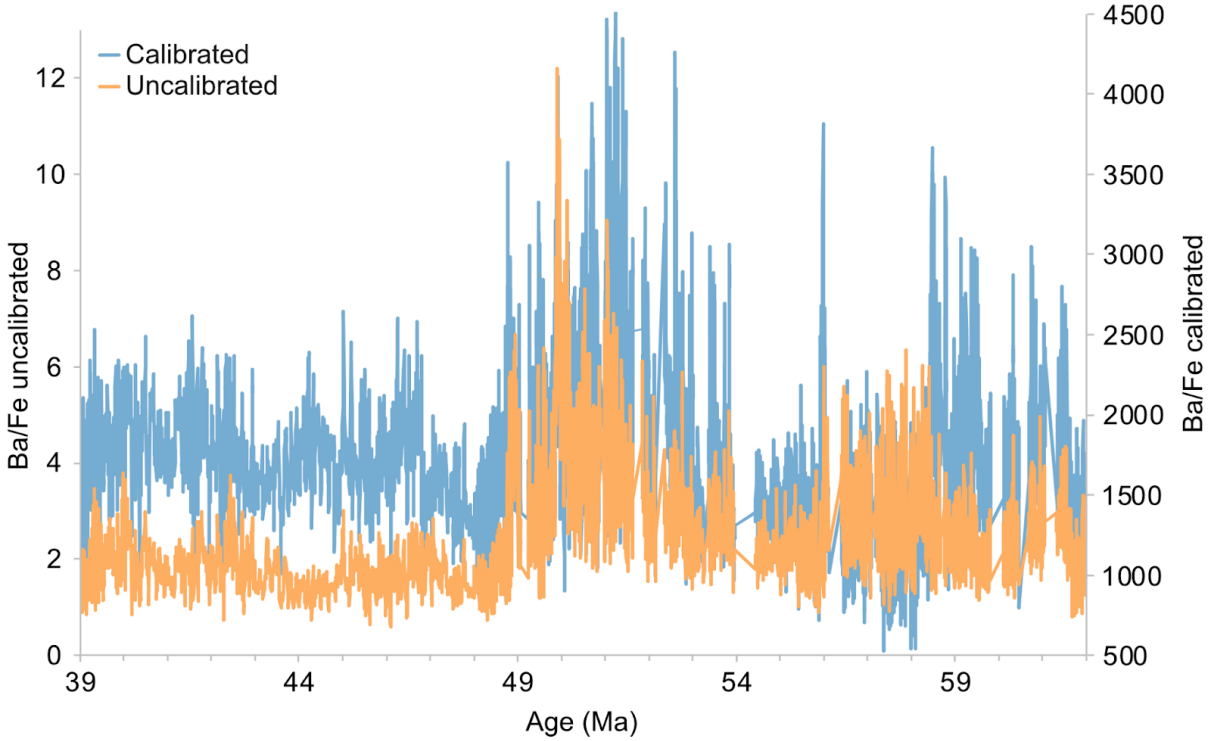

Appendix Figure 4.7. U1514 uncalibrated XRF Ba/Fe data alongside measurements calibrated using equation in Figure 2.2 of Kirby (2022) to correct for instrumental offset.

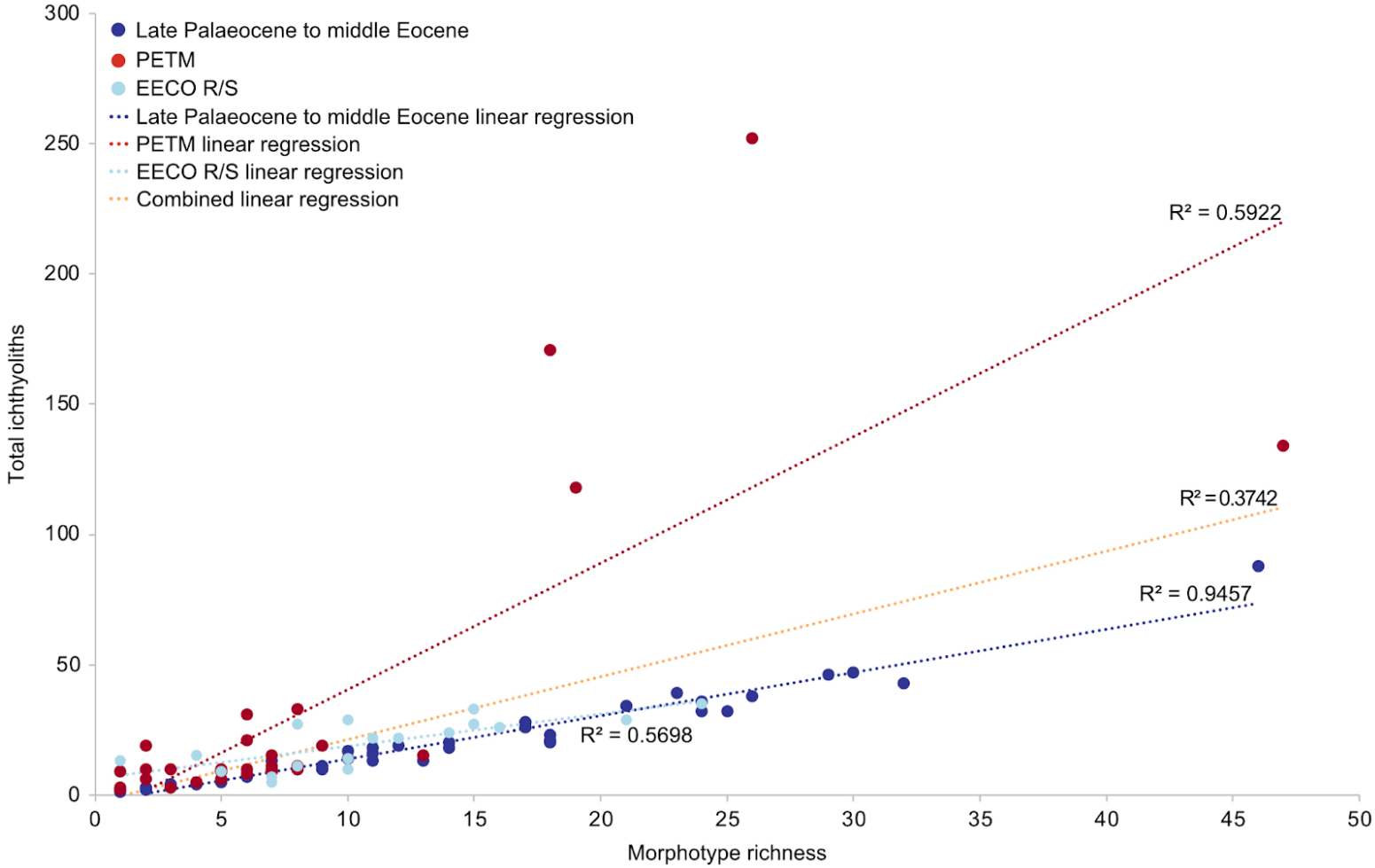

Appendix Figure 4.8. Crossplot to determine linear relationships between morphotype richness and increasing ichthyolith count, with regression values, for the late Palaeocene to middle Eocene dataset, the combined PETM data, the EECO R and S event data and the entire dataset together.

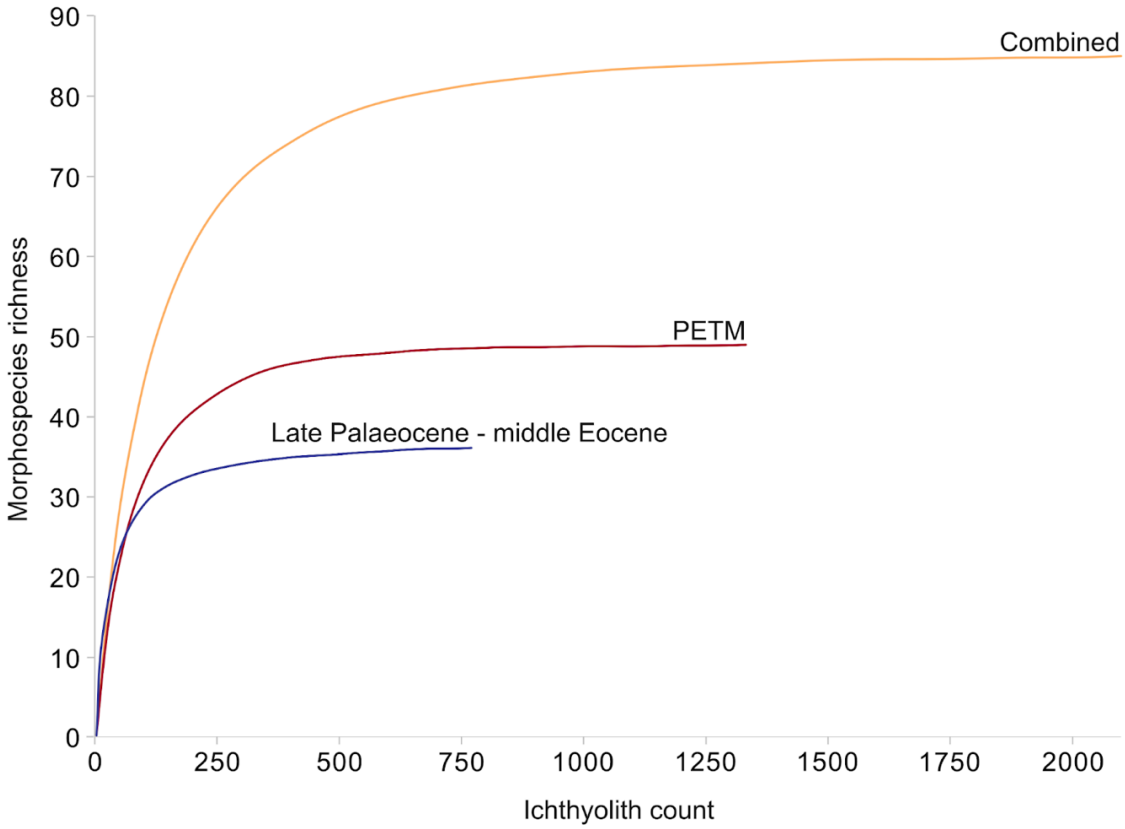

Appendix Figure 4.9. Rarefaction curves of morphospecies richness as ichthyolith count increases for the lower resolution late Palaeocene to middle Eocene dataset, the PETM data and all available U1514 data (combined).

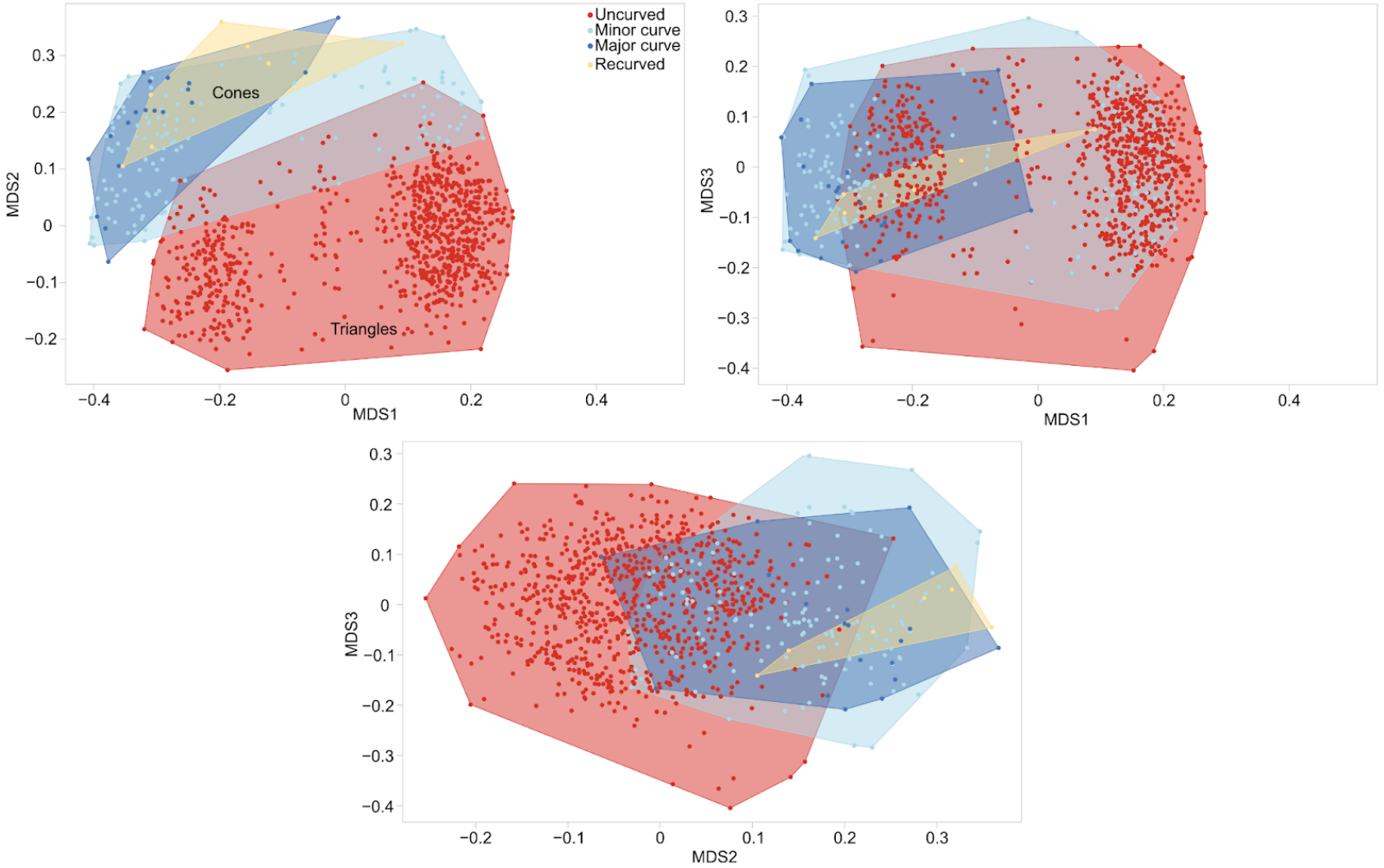

Appendix Figure 4.10. Morphospace ordination for tooth curvature in the entire U1514 dataset, presented in three orientations.

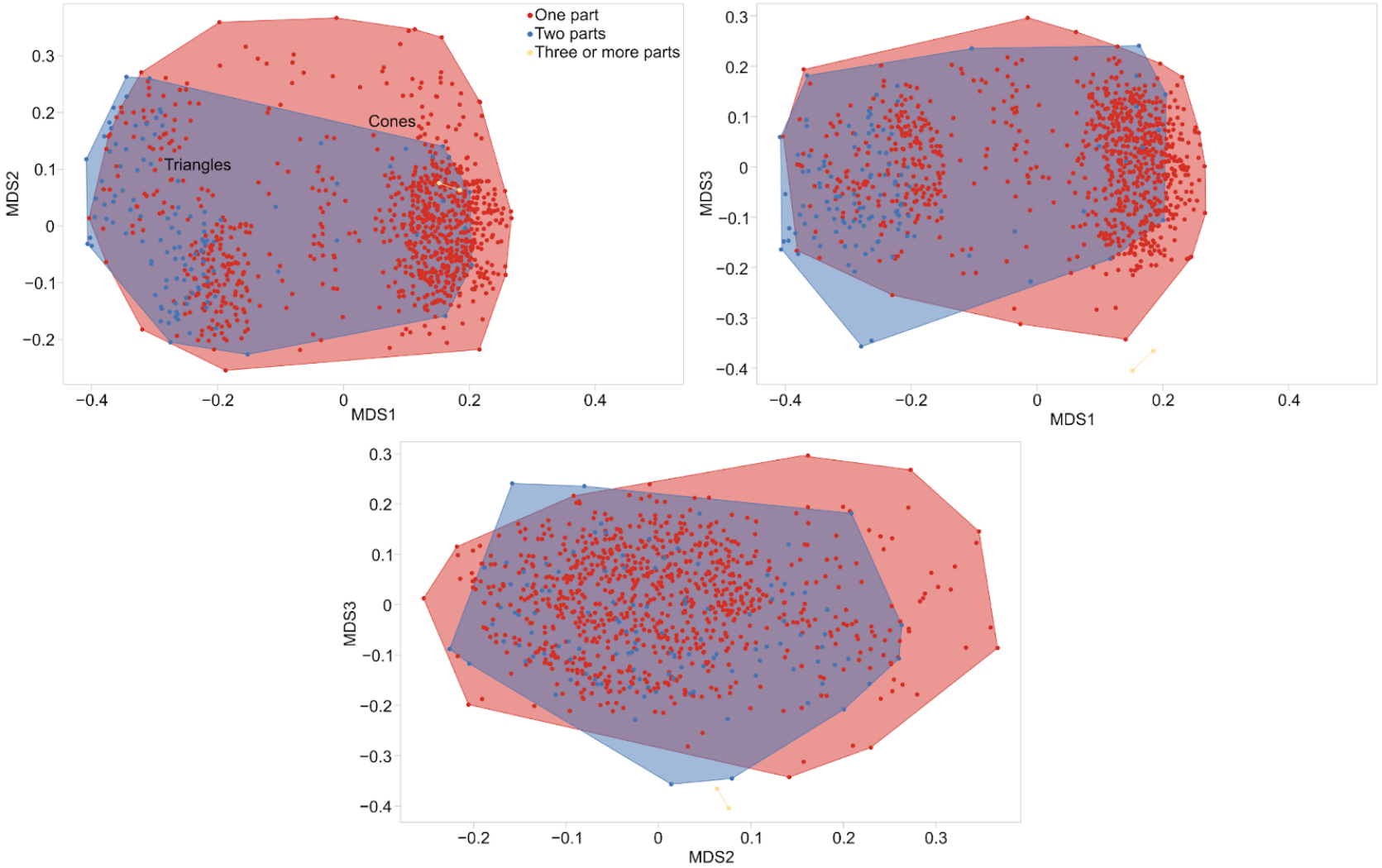

Appendix Figure 4.11. Morphospace ordination for number of tooth parts in the entire U1514 dataset, presented in three orientations.

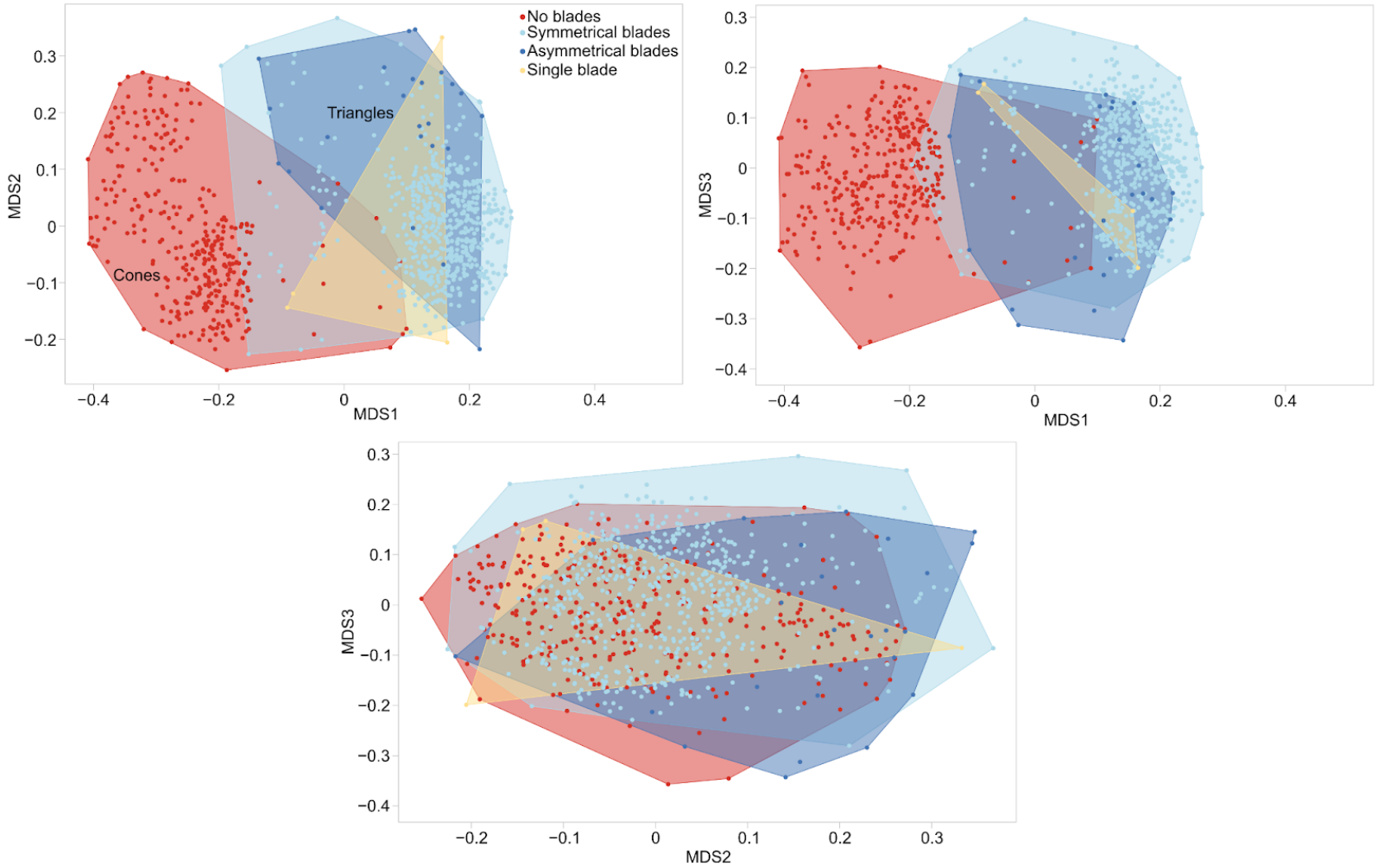

Appendix Figure 4.12. Morphospace ordination for presence of blades in the entire U1514 dataset, presented in three orientations.

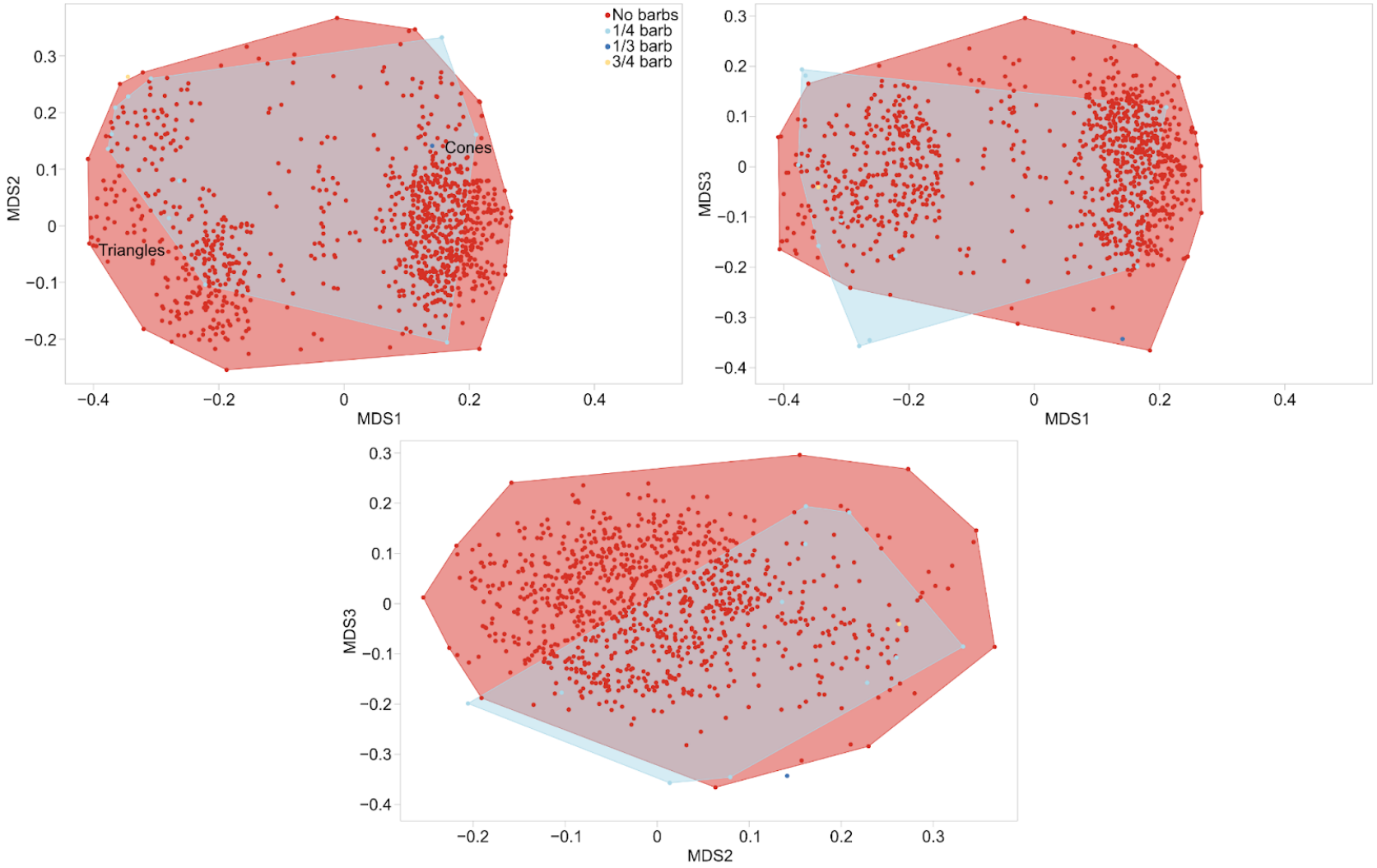

Appendix Figure 4.13. Morphospace ordination for presence of barbs in the entire U1514 dataset, presented in three orientations.

Appendix 3: Supplementary material for Chapter Five

Appendix Table 5.1. Ichthyolith morphotype coding for Sites 702 and 1263.

Due to the large file size, Appendix Table 5.1 has been deposited online within the University of Birmingham eData Repository titled: "Sites 702 and 1263 MECO ichthyolith morphotype coding (Appendix Table 5.1).xlsx", available within the repository titled "Bird, Hannah (2024) Research data supporting PhD thesis 'Actinopterygian and chondrichthyan palaeocommunity responses to early Cenozoic global warming'" (DOI: 10.25500/edata.bham.00001169).

Appendix Table 5.2. Ichthyolith morphotype key for range chart in Figure 5.10.

Range chart key	Morphotype
1	Horseshoe
2	Full straight root
3	Too broken to code
4	1/2 straight root convex triangle
5	Long 1/4 dome root
6	Long 3/4 straight root
7	Squat convex root
8	Pot-bellied squat triangle
9	Long rootless cone
10	Squat triangle 1/2 dome root
11	Extra-long curved cone
12	Medium 1/2 concave root
13	Convex triangle 3/4 dome root
14	1/4 dome root convex cone
15	1/4 total root cone
16	Elongated 1/2 straight root
17	Elongated 1/2 total root cone
18	Long 1/4 total root
19	Elongated 1/4 straight root cone
20	Two part triangle
21	1/4 dome root cone
22	1/4 dome root cone no cap
23	Convex 1/2 dome root
24	Generic con
25	Generic triangle
26	Long straight striated cone
27	Medium 3/4 straight root
28	Medium rootless cone
29	Squat rootless cone
30	Straight dome root
31	Squat dome root cap tip
32	Long minor recurved cone
33	1/4 dome root triangle
34	Extra-long curved two part straight tip
35	Medium 1/4 dome root
36	Medium cap tip cone flared base
37	Medium curved two part straight tip
38	Elongated two part squat tip
39	Long 3/4 straight root straight blades
40	Long minor curved cone
41	1/2 concave root
42	Convex 3/4 root
43	Convex rootless cone
44	Straight triangle 1/2 funnel root
45	Squat convex triangle dome root
46	1/4 straight root cone
47	Extended straight root
48	Tucked base cone
49	1/2 dome root triangle
50	Two part triangular cone
51	Convex cone total root
52	Two part convex squat tip
53	Elongated two part medium tip
54	Curved 2/3 convex root triangle
55	Funnel root cone
56	Straight triangle 3/4 concave root
57	1/2 root cone
58	Flared base 1/4 dome root
59	Squat convex triangle
60	1/2 straight root

Range chart key	Morphotype
61	1/4 straight root
62	Medium curved rootless cone
63	1/2 total root cone
64	Major curve thin cone
65	Long full total root
66	Extra-long curved middle barb cone
67	Medium straight bladed cone
68	Long 1/2 dome root triangle
69	Major curve tip-only two part cone
70	Elongated straight bladed cone
71	Middle barb cone total root
72	Long 1/4 total root cone
73	Medium 1/4 dome root cone no cap
74	3/4 total root cone
75	Curved cone 1/4 total root
76	Long striated cone curved tip
77	Curved distinct cap flared base
78	Bladed cone 1/3 dome root
79	Elongated side-curved bladed cone
80	Squat dome root cone
81	Curved triangle 3/4 concave root
82	Two part straight squat tip
83	Two part straight medium tip
84	Curved deep triangle
85	Flared base 3/4 funnel root
86	Full-length funnel root cone
87	Medium 3/4 funnel root
88	Long convex triangle
89	Squat convex cone 1/4 total root
90	Two part convex squat curved tip
91	Squat curved convex cone
92	Major bottom curved cone
93	Small blade full root
94	Major curve thin cone flared base
95	Curved two part curved tip
96	Medium triangle 3/4 concave root
97	Flat full root
98	Rounded convex triangle
99	Curl curved triangle 1/4 total root
100	Squat 1/2 straight root cone
101	Fingernail
102	Convex cone 1/2 dome root
103	Bladed recurved cone
104	Curved 1/2 dome root triangle
105	Long spiraling striation
106	Straight many cusps
107	Convex triangle 3/4 funnel root
108	Bumpy bladed triangle
109	Long curved cone 1/2 total root
110	1/2 funnel root flared blades
111	Convex 1/2 root flared blades
112	Medium curved bladed cone
113	Straight triangle 1/2 total root
114	Long minor top curved cone
115	Mounding cone
116	Thin triangle full straight root
117	Wide base curved triangle
118	Extra-long straight cone
119	Upper 3/4 bladed triangle
120	Deep dome root flared blades

Appendix Table 5.3. Ichthyolith morphotype key for range chart in Figure 5.12.

Range chart key	Morphotype
1	Horseshoe
2	Squat dome root cap tip
3	1/2 concave root
4	Convex 3/4 root
5	Convex rootless cone
6	Tucked base cone
7	Curved 2/3 convex root triangle
8	Funnel root cone
9	Straight triangle 3/4 concave root
10	Long full total root
11	Straight triangle 1/2 funnel root
12	Major curve tip-only two part cone
13	Full straight root
14	Bladed cone 1/3 dome root
15	Elongated side-curved bladed cone
16	Squat dome root cone
17	Curved deep triangle
18	Flared base 3/4 funnel root
19	Full-length funnel root cone
20	1/2 dome root triangle
21	Curved triangle 3/4 concave root
22	Two part convex squat curved tip
23	Squat curved convex cone
24	Curved two part curved tip
25	Medium triangle 3/4 concave root
26	1/2 root cone
27	Flared base 1/4 dome root
28	1/4 straight root
29	Major bottom curved cone
30	Curl curved triangle 1/4 total root
31	Squat 1/2 straight root cone
32	Too broken to code
33	Flat full root
34	Fingernail
35	Two part triangular cone
36	Elongated straight bladed cone
37	Middle barb cone total root
38	Two part straight squat tip
39	Bladed recurved cone
40	Curved 1/2 dome root triangle
41	Long spiraling striation
42	1/2 straight root convex triangle
43	Long 1/4 dome root
44	Long 3/4 straight root
45	Squat convex triangle dome root
46	Squat convex root
47	Extra-long curved middle barb cone
48	Medium 3/4 funnel root
49	Small blade full root
50	Straight many cusps
51	Bumpy bladed triangle
52	Long curved cone 1/2 total root
53	Pot-bellied squat triangle
54	Long minor recurved cone
55	Convex cone total root
56	Two part convex squat tip
57	Medium curved rootless cone
58	Long 1/4 total root cone
59	Medium 1/4 dome root cone no cap
60	Convex 1/2 root flared blades
61	Medium curved bladed cone
62	Straight triangle 1/2 total root
63	Long rootless cone
64	Squat triangle 1/2 dome root
65	Medium straight bladed cone
66	3/4 total root cone
67	Curved cone 1/4 total root
68	Long convex triangle
69	Rounded convex triangle
70	Convex cone 1/2 dome root
71	Extra-long curved cone
72	Medium 1/2 concave root
73	1/2 funnel root flared blades
74	Long minor top curved cone
75	Mounding cone
76	Convex triangle 3/4 dome root
77	1/4 dome root triangle
78	Extra-long curved two part straight tip
79	1/2 total root cone
80	Long 1/2 dome root triangle
81	Convex triangle 3/4 funnel root
82	Thin triangle full straight root
83	1/4 dome root convex cone
84	1/4 total root cone
85	Elongated 1/2 straight root
86	Elongated 1/2 total root cone
87	Long 1/4 total root
88	Squat convex triangle
89	Long striated cone curved tip
90	Elongated 1/4 straight root cone
91	Two part triangle
92	Medium 1/4 dome root
93	Medium cap tip cone flared base
94	Medium curved two part straight tip
95	1/2 straight root
96	Major curve thin cone
97	Curved distinct cap flared base
98	Two part straight medium tip
99	Squat convex cone 1/4 total root
100	Major curve thin cone flared base
101	Extra-long straight cone
102	Upper 3/4 bladed triangle
103	1/4 dome root cone
104	1/4 dome root cone no cap
105	Convex 1/2 dome root
106	Generic cone
107	Generic triangle
108	Long straight striated cone
109	Medium 3/4 straight root
110	Medium rootless cone
111	Squat rootless cone
112	Straight dome root
113	Elongated two part squat tip
114	Long 3/4 straight root straight blades
115	Long minor curved cone
116	1/4 straight root cone
117	Extended straight root
118	Elongated two part medium tip
119	Wide base curved triangle
120	Deep dome root flared blades

Appendix Table 5.4. Ichthyolith morphotype key for range chart in Appendix Figure 5.3.

Range chart key	Morphotype
1	1/4 total root cone
2	Extra-long curved cone
3	Horseshoe
4	Long 1/4 total root
5	Medium 1/2 concave root
6	Squat convex root
7	Full straight root
8	Too broken to code
9	1/2 straight root convex triangle
10	1/4 dome root convex cone
11	Elongated 1/2 total root cone
12	Long 1/4 dome root
13	Long 3/4 straight root
14	Pot-bellied squat triangle
15	Long rootless cone
16	Squat triangle 1/2 dome root
17	Convex triangle 3/4 dome root
18	Elongated 1/2 straight root
19	Elongated 1/4 straight root cone
20	Two part triangle
21	1/4 dome root cone
22	1/4 dome root cone no cap
23	Convex 1/2 dome root
24	Generic cone
25	Generic triangle
26	Long straight striated cone
27	Medium 3/4 straight root
28	Medium rootless cone
29	Squat rootless cone
30	Straight dome root
31	1/2 concave root
32	Convex 3/4 root
33	Convex rootless cone
34	Straight triangle 1/2 funnel root
35	Squat convex triangle dome root
36	1/4 straight root cone
37	Extended straight root
38	Curved 2/3 convex root triangle
39	Flared base 1/4 dome root
40	Funnel root cone
41	Straight triangle 3/4 concave root
42	Two part convex squat tip
43	1/2 root cone
44	1/2 straight root
45	Long minor recurved cone
46	Squat convex triangle
47	Medium 1/4 dome root
48	1/4 dome root triangle
49	Extra-long curved middle barb cone
50	Long full total root
51	Medium straight bladed cone
52	Long 1/2 dome root triangle
53	Elongated two part squat tip
54	1/2 dome root triangle
55	Bladed cone 1/3 dome root
56	Curved triangle 3/4 concave root
57	Elongated side-curved bladed cone
58	Squat dome root cone
59	Two part straight squat tip
60	Long 3/4 straight root straight blades
61	Long minor curved cone
62	Convex cone total root
63	Two part straight medium tip
64	Curved deep triangle
65	Flared base 3/4 funnel root
66	Full-length funnel root cone
67	Medium 3/4 funnel root
68	Squat convex cone 1/4 total root
69	Medium curved two part straight tip
70	Medium 1/4 dome root cone no cap
71	Long convex triangle
72	Elongated two part medium tip
73	Curved two part curved tip
74	Medium triangle 3/4 concave root
75	Curl curved triangle 1/4 total root
76	Middle barb cone total root
77	Squat 1/2 straight root cone
78	Flat full root
79	Fingernail
80	Long 1/4 total root cone
81	Convex cone 1/2 dome root
82	Extra-long curved two part straight tip
83	Rounded convex triangle
84	3/4 total root cone
85	Curved cone 1/4 total root
86	Long striated cone curved tip
87	1/2 total root cone
88	Convex triangle 3/4 funnel root
89	Thin triangle full straight root

Appendix Table 5.5. Ichthyolith morphotype key for range chart in Appendix Figure 5.4.

Range chart key	Morphotype
1	Squat dome root cap tip
2	1/4 dome root triangle
3	1/2 straight root convex triangle
4	Long 1/4 dome root
5	Long rootless cone
6	Extra-long curved two part straight tip
7	Long minor recurved cone
8	1/4 dome root cone
9	Long 1/4 total root
10	1/4 dome root cone no cap
11	Elongated two part squat tip
12	Generic cone
13	Generic triangle
14	Long 3/4 straight root straight blades
15	Long minor curved cone
16	Long straight striated cone
17	Medium 1/4 dome root
18	Medium 3/4 straight root
19	Medium cap tip cone flared base
20	Medium curved two part straight tip
21	1/4 straight root cone
22	Tucked base cone
23	1/2 dome root triangle
24	Convex triangle 3/4 dome root
25	Two part triangular cone
26	Convex 1/2 dome root
27	Extended straight root
28	Convex cone total root
29	Elongated two part medium tip
30	Two part convex squat tip
31	Elongated 1/4 straight root cone
32	1/4 total root cone
33	1/4 straight root
34	1/2 total root cone
35	Medium curved rootless cone
36	Major curve thin cone
37	Curved cone 1/4 total root
38	Major curve tip-only two part cone
39	Squat convex triangle dome root
40	Straight triangle 1/2 funnel root
41	3/4 total root cone
42	Long 3/4 straight root
43	Elongated straight bladed cone
44	Middle barb cone total root
45	Long 1/4 total root cone
46	Medium 1/4 dome root cone no cap
47	Pot-bellied squat triangle
48	Long striated cone curved tip
49	Curved distinct cap flared base
50	Two part convex squat curved tip
51	Two part straight squat tip
52	Extra-long curved middle barb cone
52	1/2 straight root
54	Two part straight medium tip
55	Curved triangle 3/4 concave root
56	Squat curved convex cone
57	Straight dome root
58	Major bottom curved cone
59	Small blade full root
60	Elongated 1/2 total root cone
61	Major curve thin cone flared base
62	1/2 root cone
63	Flared base 1/4 dome root
64	Flat full root
65	Long convex triangle
66	Medium rootless cone
67	Rounded convex triangle
68	Extra-long curved cone
69	1/4 dome root convex cone
70	Bladed recurved cone
71	Convex triangle 3/4 funnel root
72	Curved 1/2 dome root triangle
73	Long spiraling striation
74	Straight many cusps
75	Elongated 1/2 straight root
76	Bumpy bladed triangle
77	Long curved cone 1/2 total root
78	Medium 3/4 funnel root
79	Squat convex root
80	1/2 funnel root flared blades
81	Squat convex cone 1/4 total root
82	Convex 1/2 root flared blades
83	Medium curved bladed cone
84	Squat rootless cone
85	Straight triangle 1/2 total root
86	Long minor top curved cone
87	Medium 1/2 concave root
88	Mounding cone
89	Squat convex triangle
90	Extra-long straight cone
91	Upper 3/4 bladed triangle

Appendix Table 5.6. Ichthyolith morphotype key for range chart in Appendix Figure 5.6.

Range chart key	Morphotype
1	1/4 total root cone
2	Extra-long curved cone
3	Horseshoe
4	Long 1/4 total root
5	Medium 1/2 concave root
6	Squat convex root
7	1/2 concave root
8	Convex 3/4 root
9	Convex rootless cone
10	Straight triangle 1/2 funnel root
11	Curved 2/3 convex root triangle
12	Flared base 1/4 dome root
13	Funnel root cone
14	Straight triangle 3/4 concave root
15	Two part convex squat tip
16	1/2 root cone
17	1/2 straight root
18	Extra-long curved middle barb cone
19	Long full total root
20	Full straight root
21	1/2 dome root triangle
22	Bladed cone 1/3 dome root
23	Curved triangle 3/4 concave root
24	Elongated side-curved bladed cone
25	Squat dome root cone
26	Long minor recurved cone
27	Convex cone total root
28	Curved deep triangle
29	Flared base 3/4 funnel root
30	Full-length funnel root cone
31	Medium 3/4 funnel root
32	Squat convex cone 1/4 total root
33	Two part straight squat tip
34	Curved two part curved tip
35	Medium triangle 3/4 concave root
36	Curl curved triangle 1/4 total root
37	Middle barb cone total root
38	Squat 1/2 straight root cone
39	Too broken to code
40	Squat convex triangle
41	Two part straight medium tip
42	Medium curved two part straight tip
43	Flat full root
44	Fingernail
45	1/2 straight root convex triangle
46	1/4 dome root convex cone
47	Elongated 1/2 total root cone
48	Long 1/4 dome root
49	Long 3/4 straight root
50	Pot-bellied squat triangle
51	Squat convex triangle dome root
52	Medium 1/4 dome root cone no cap
53	Long 1/4 total root cone
54	Long rootless cone
55	Squat triangle 1/2 dome root
56	Medium 1/4 dome root
57	Medium straight bladed cone
58	Long convex triangle
59	Convex cone 1/2 dome root
60	Rounded convex triangle
61	3/4 total root cone
62	Curved cone 1/4 total root
62	Long striated cone curved tip
64	Convex triangle 3/4 dome root
65	Elongated 1/2 straight root
66	1/4 dome root triangle
67	Long 1/2 dome root triangle
68	Extra-long curved two part straight tip
69	1/2 total root cone
70	Convex triangle 3/4 funnel root
71	Thin triangle full straight root
72	Elongated 1/4 straight root cone
73	Two part triangle
74	1/4 dome root cone
75	1/4 dome root cone no cap
76	Convex 1/2 dome root
77	Generic cone
78	Generic triangle
79	Long straight striated cone
80	Medium 3/4 straight root
81	Medium rootless cone
82	Squat rootless cone
83	Straight dome root
84	1/4 straight root cone
85	Extended straight root
86	Elongated two part squat tip
87	Long 3/4 straight root straight blades
88	Long minor curved cone
89	Elongated two part medium tip

Appendix Table 5.7. Ichthyolith morphotype key for range chart in Appendix Figure 5.7.

Range chart key	Morphotype
1	Squat dome root cap tip
2	1/4 straight root cone
3	Tucked base cone
4	Curved cone 1/4 total root
5	Major curve tip-only two part cone
6	Squat convex triangle dome root
7	Straight triangle 1/2 funnel root
8	1/2 dome root triangle
9	Two part convex squat curved tip
10	Curved triangle 3/4 concave root
11	Squat curved convex cone
12	Straight dome root
13	1/4 dome root triangle
14	1/4 straight root
15	3/4 total root cone
16	Long 3/4 straight root
17	Major bottom curved cone
18	1/2 root cone
19	Flared base 1/4 dome root
20	Flat full root
21	Long convex triangle
22	Medium rootless cone
23	Rounded convex triangle
24	1/2 straight root convex triangle
25	Long 1/4 dome root
26	Convex triangle 3/4 dome root
27	Two part triangular cone
28	1/2 total root cone
29	Elongated straight bladed cone
30	Middle barb cone total root
31	Two part straight squat tip
32	Bladed recurved cone
33	Convex triangle 3/4 funnel root
34	Curved 1/2 dome root triangle
35	Long spiraling striation
36	Long rootless cone
37	Convex 1/2 dome root
38	Extended straight root
39	Extra-long curved middle barb cone
40	Small blade full root
41	Straight many cusps
42	Bumpy bladed triangle
43	Long curved cone 1/2 total root
44	Medium 3/4 funnel root
45	Squat convex root
46	Extra-long curved two part straight tip
47	Long minor recurved cone
48	Convex cone total root
49	Elongated two part medium tip
50	Two part convex squat tip
51	Medium curved rootless cone
52	Long 1/4 total root cone
53	Medium 1/4 dome root cone no cap
54	Pot-bellied squat triangle
55	Convex 1/2 root flared blades
56	Medium curved bladed cone
57	Squat rootless cone
58	Straight triangle 1/2 total root
59	Elongated 1/4 straight root cone
60	Extra-long curved cone
61	1/2 funnel root flared blades
62	Long minor top curved cone
63	Medium 1/2 concave root
64	Mounding cone
65	1/4 dome root cone
66	Long 1/4 total root
67	1/4 total root cone
68	Long striated cone curved tip
69	Elongated 1/2 total root cone
70	1/4 dome root convex cone
71	Elongated 1/2 straight root
72	Squat convex triangle
73	1/4 dome root cone no cap
74	Elongated two part squat tip
75	Generic cone
76	Generic triangle
77	Long 3/4 straight root straight blades
78	Long minor curved cone
79	Long straight striated cone
80	Medium 1/4 dome root
81	Medium 3/4 straight root
82	Medium cap tip cone flared base
83	Medium curved two part straight tip
84	Major curve thin cone
85	Curved distinct cap flared base
86	1/2 straight root
87	Two part straight medium tip
88	Major curve thin cone flared base
89	Squat convex cone 1/4 total root
90	Extra-long straight cone
91	Upper 3/4 bladed triangle

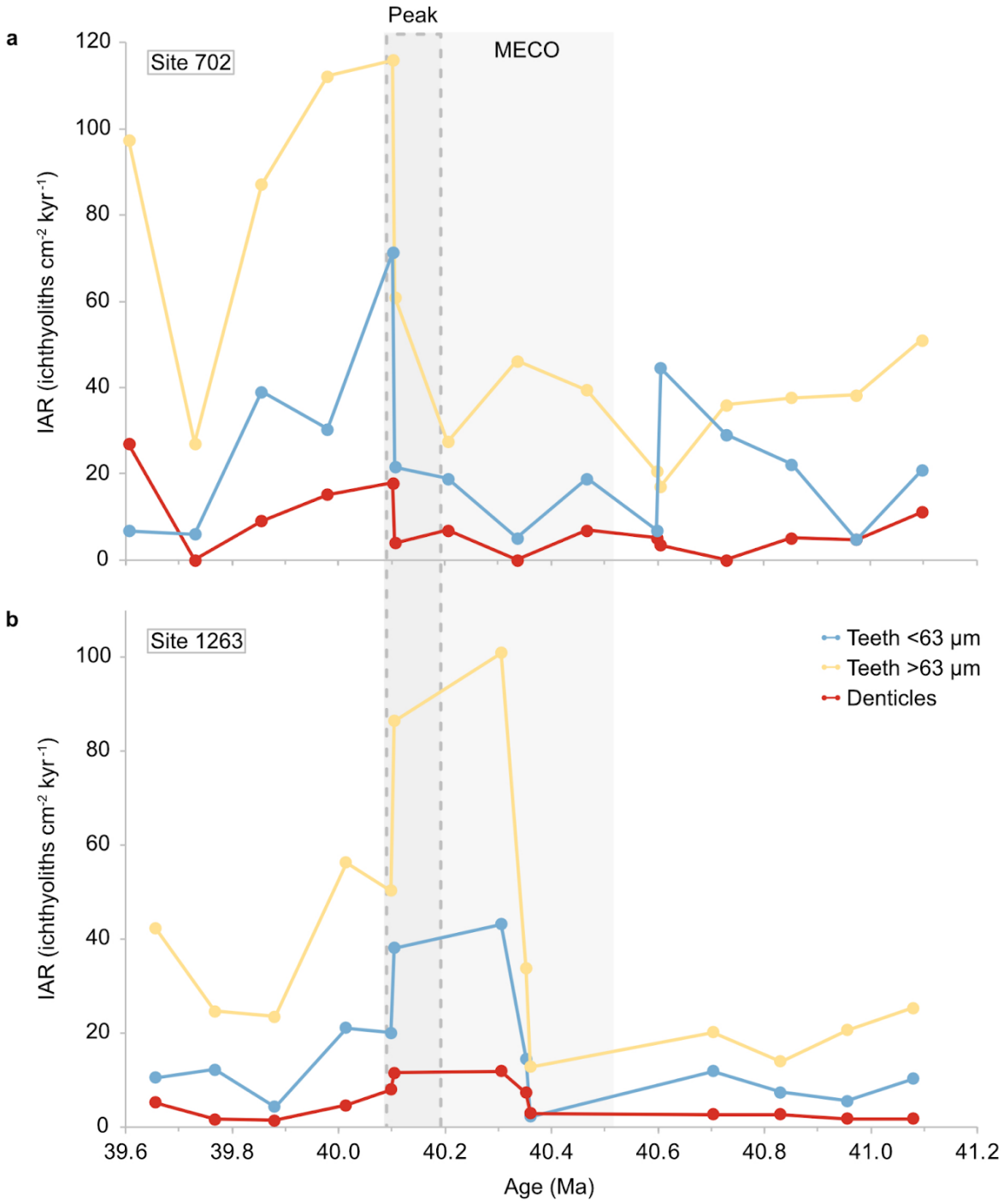

Appendix Figure 5.1. IAR for both tooth size fractions (38 to 63 µm and 63 to 250 µm) and denticles, calculated with fixed dry bulk density per core for Site 702 (**a**) and 1263 (**b**).

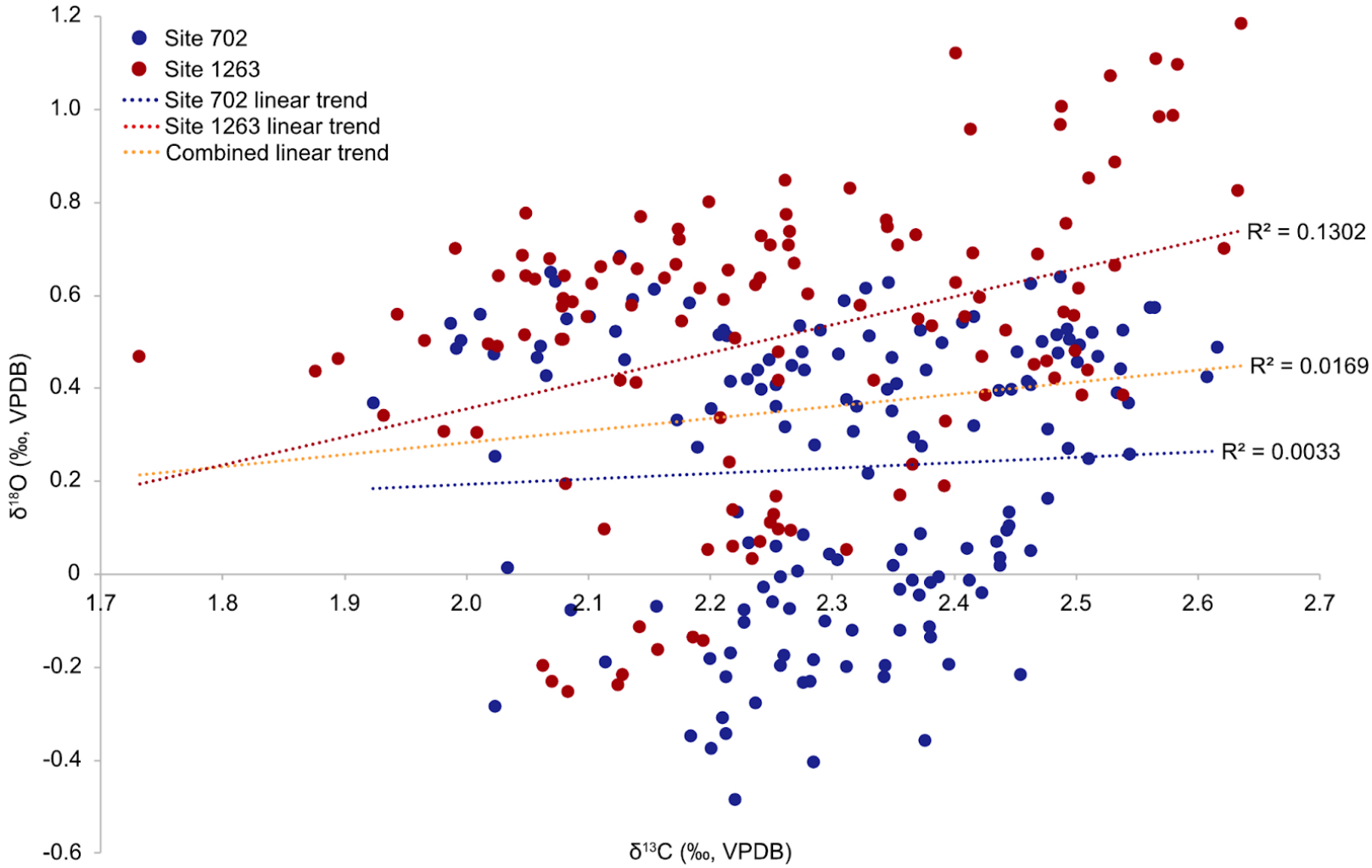

Appendix Figure 5.2. Crossplot of Sites 702 and 1263 $\delta^{18}O$ and $\delta^{13}C$ isotopes (Bohaty *et al.*, 2009) across the MECO, with linear trends and regression values.

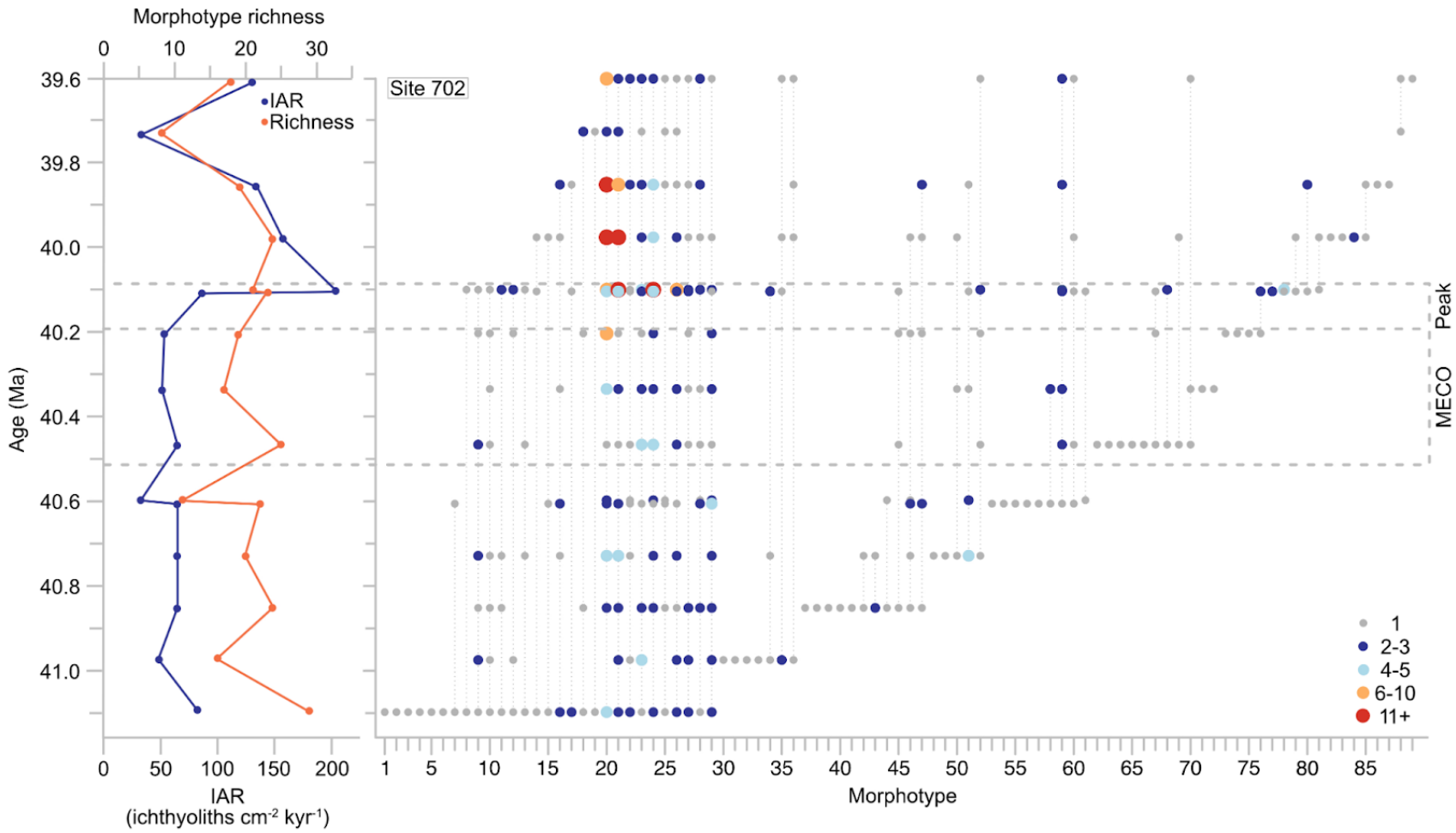

Appendix Figure 5.3. Morphotype range chart for Site 702 ordered by first appearance, alongside IAR and richness. Dot colour and size indicates morphotype abundance within a time slice and the morphotype key is available in Appendix Table 5.4.

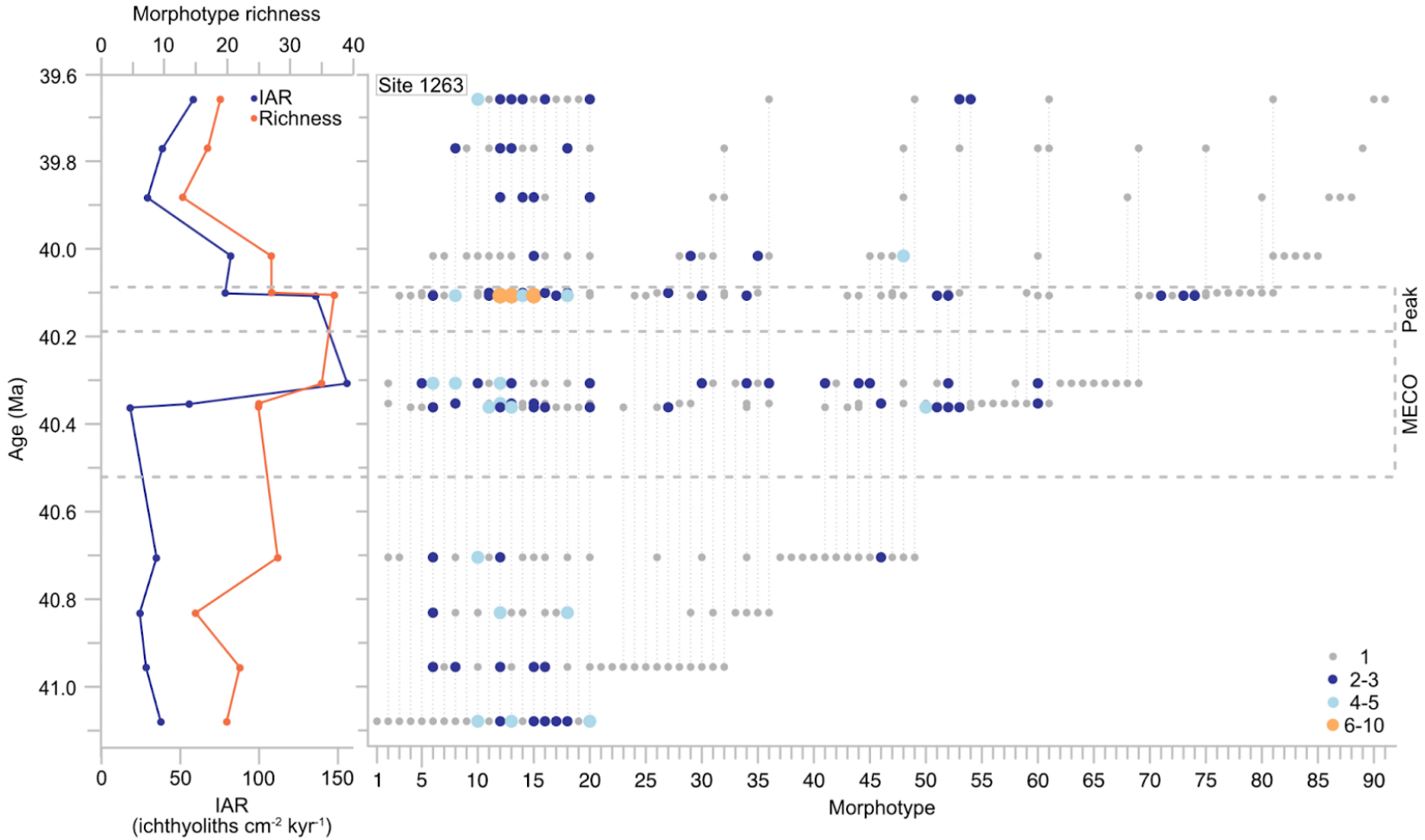

Appendix Figure 5.4. Morphotype range chart for Site 1263 ordered by first appearance, alongside IAR and richness. Dot colour and size indicates morphotype abundance within a time slice and the morphotype key is available in Appendix Table 5.5.

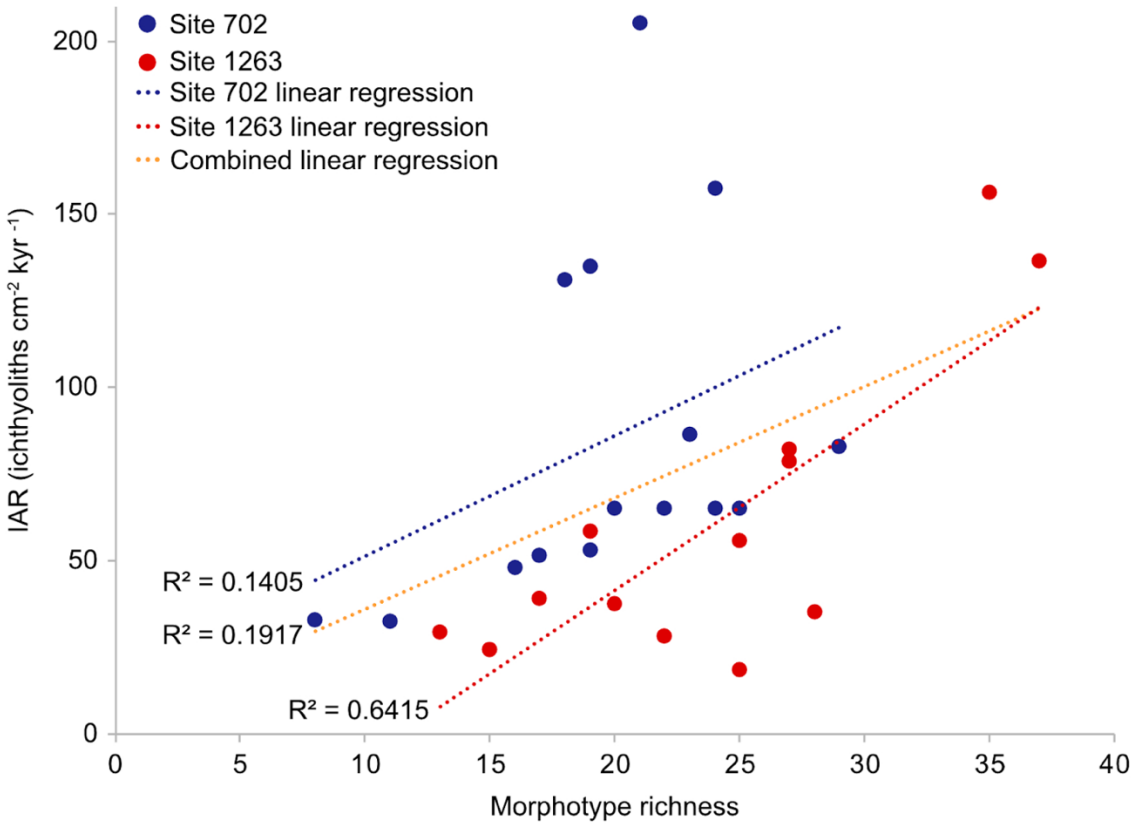

Appendix Figure 5.5. Crossplot to determine linear relationships between IAR and morphotype richness, with regression values, for both sites across the MECO.

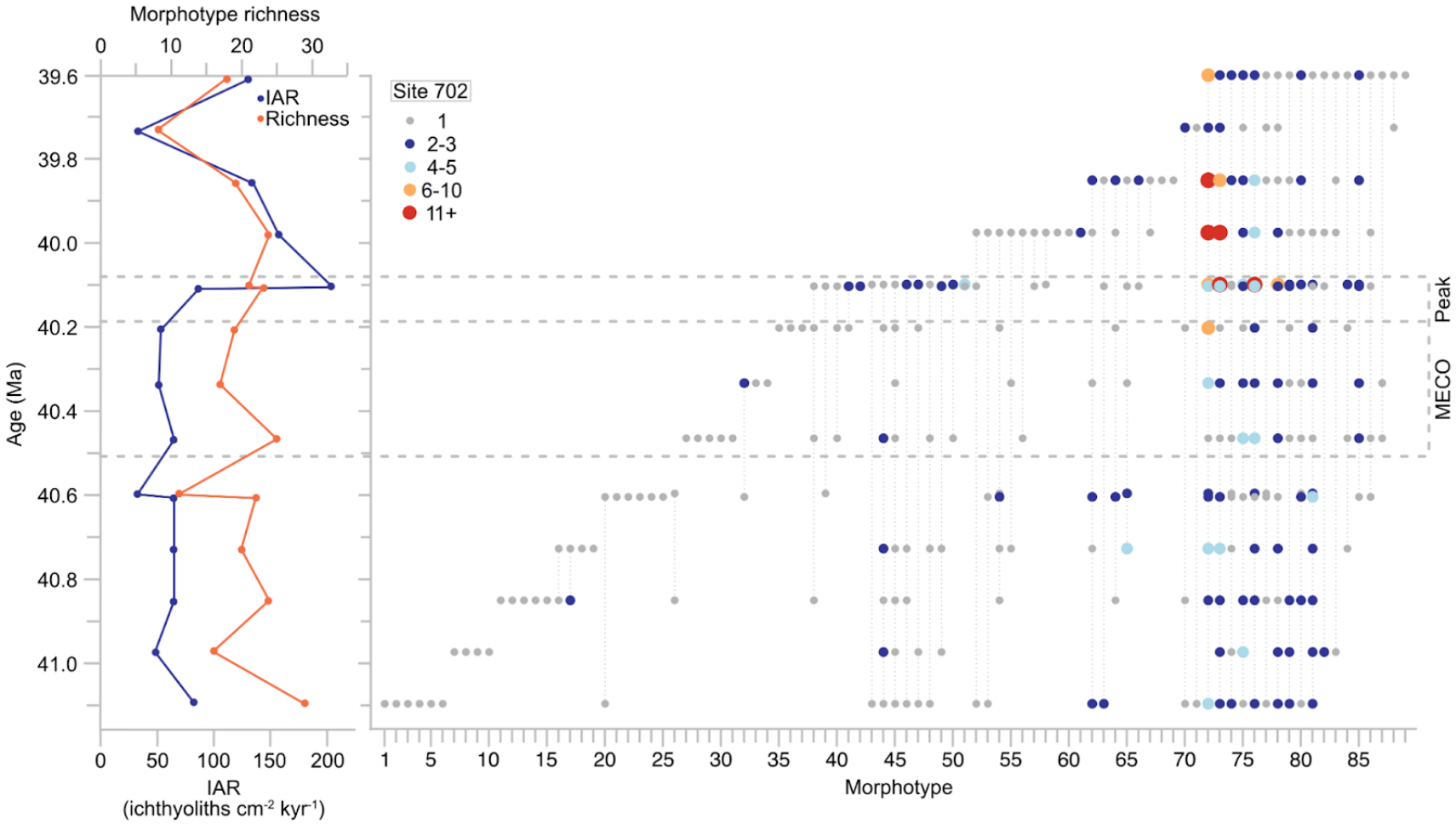

Appendix Figure 5.6. Morphotype range chart for Site 702 ordered by last appearance, alongside IAR and richness. Dot colour and size indicates morphotype abundance within a time slice and the morphotype key is available in Appendix Table 5.6.

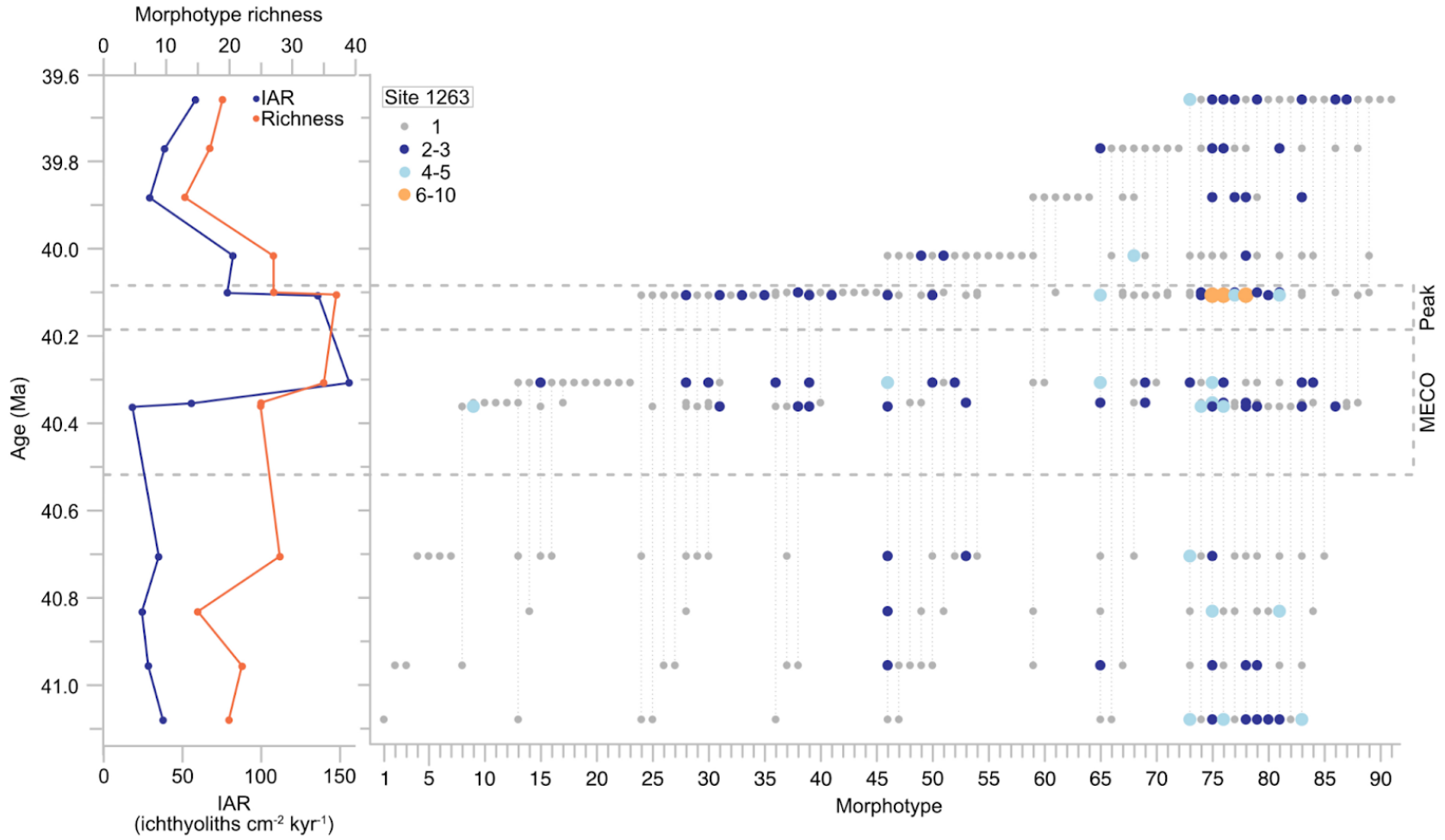

Appendix Figure 5.7. Morphotype range chart for Site 1263 ordered by last appearance, alongside IAR and richness. Dot colour and size indicates morphotype abundance within a time slice and the morphotype key is available in Appendix Table 5.7.

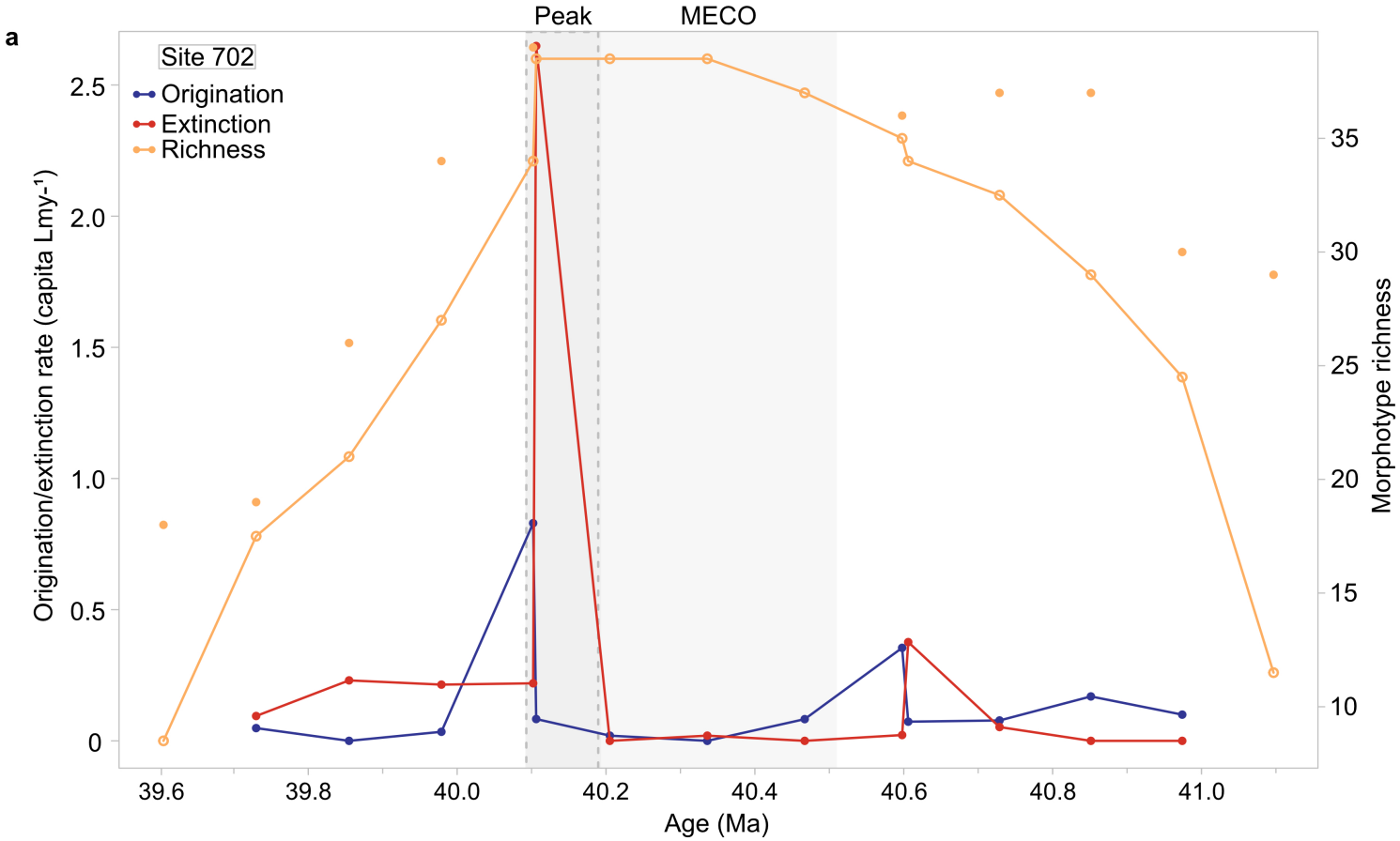

Appendix Figure 5.8. Per capita origination and extinction rates per lineage million years (Foote 2000), alongside morphotype richness for Sites 702 (**a**) and 1263 (**b**). Part **b** is overleaf.

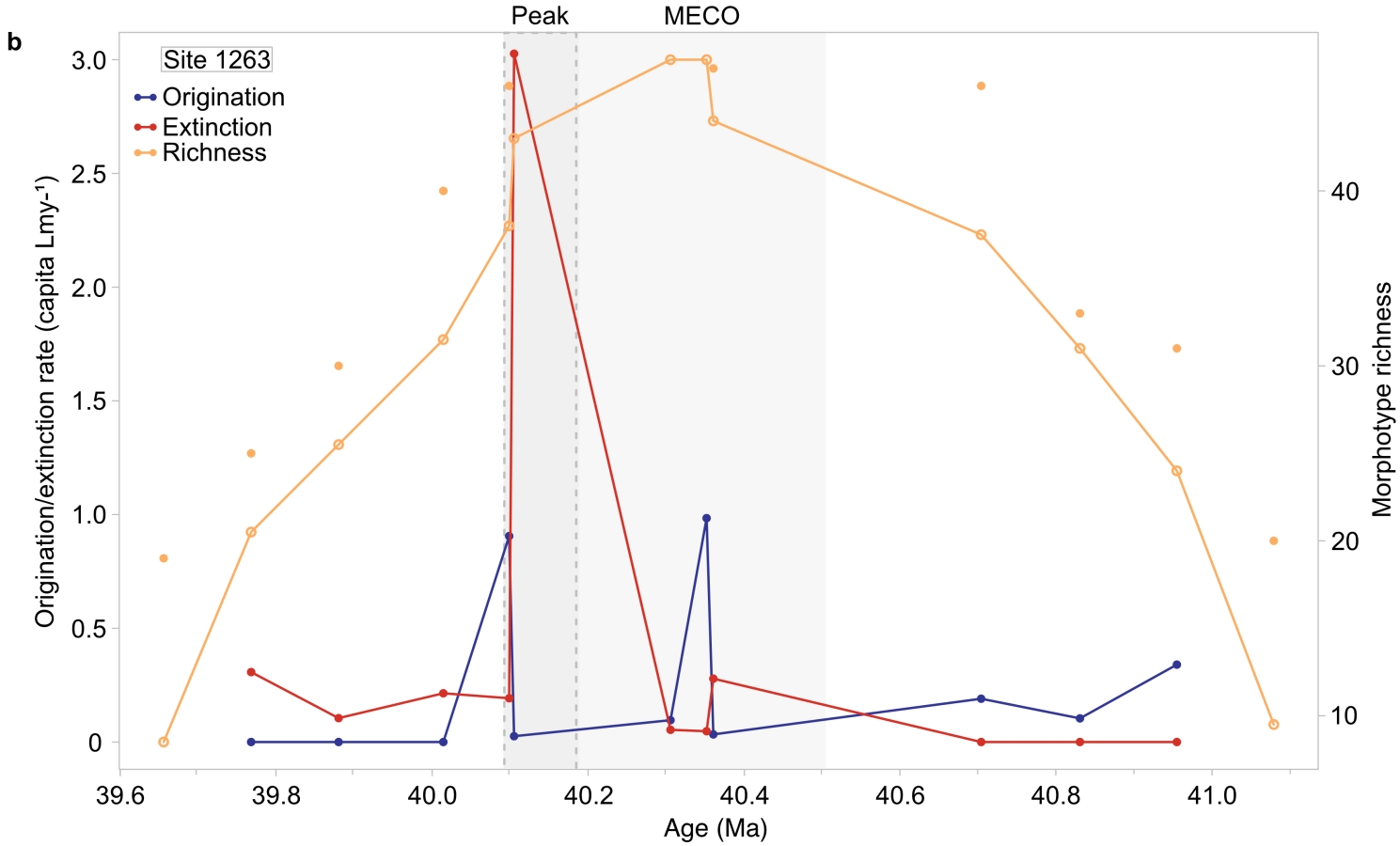
b
Peak
MECO
Site 1263
Origination
Extinction
Richness
Origination/extinction rate (capita Lmy-1)
Morphotype richness
Age (Ma)
3.0
2.5
2.0
1.5
1.0
0.5
0
40
30
20
10
39.6
39.8
40.0
40.2
40.4
40.6
40.8
41.0